TECHNISCHE UNIVERSITÄT GRAZ
INSTITUT FÜR
THERMISCHE TURBOMASCHINEN UND MASCHINENDYNAMIK

Development and Application of Interferometric Measurement Techniques for Multi-Flame Gas Turbine Combustion

Dissertation

zur Erlangung des akademischen Grades eines
Doktors der technischen Wissenschaften,
eingereicht an der
Fakultät für Maschinenbau der Technischen Universität Graz

von

Dipl.-Ing. Stefan Köberl

Erstbegutachter: Ao.Univ.-Prof. Dipl.-Ing. Dr. techn. Jakob Woisetschläger

Zweitbegutachter: Univ.-Prof. Dr. rer. nat. Michael Pfitzner

Graz, März 2011

Gefördert durch den Fonds zur Förderung der wissenschaftlichen Forschung (FWF)
Projekt P19955

EIDESSTATTLICHE ERKLÄRUNG

Ich erkläre an Eides statt, dass ich die vorliegende Arbeit selbstständig verfasst, andere als die angegebenen Quellen/Hilfsmittel nicht benutzt und die den benutzten Quellen wörtlich und inhaltlich entnommenen Stellen als solche kenntlich gemacht habe.

Graz, am …… ……..
(Unterschrift)

Englische Fassung:

STATUTORY DECLARATION

I declare that I have authored this thesis independently, that I have not used other than the declared sources / resources and that I have explicitly marked all material which has been quoted either literally or by content from the used sources.

…… ……..
date (signature)

Acknowledgements

This thesis was written during my time as a research associate at the Institute for Thermal Turbomachinery and Machine Dynamics at Graz University of Technology. I would like to thank the head of the Institute, Mr. Univ.-Prof. Dr.-Ing. Franz Heitmeir, for the opportunity to write this thesis at the Institute and the convenient working atmosphere.

I would like to express my special gratitude to my supervisor, Mr. Ao.Univ.-Prof. Dipl.-Ing. Dr. Jakob Woisetschläger, whose encouragement, guidance and support enabled me to get an understanding of the subject. I will keep the discussions with him and his advices always in positive memory.

I also wish to acknowledge Mr. Univ.-Prof. Dr. Michael Pfitzner for the review of my thesis.

Special thanks go to Mr. Univ.-Doz. Dipl.-Ing. Dr. Fabrice Giuliani for his support and his suggestions.

Also thanks to my former diploma students, Mr. Dott.-mag. Fabrizio Fontaneto, Mr. Dipl.-Ing. Martin Heimel and Mr. Dipl.-Ing. Daniel Neubauer, who supported me in the test rig constructions, during the measurement campaigns and in the software design. The work of these students is gratefully acknowledged.

Last but not least I would like to thank my colleagues and staff at the Institute for the convenient working atmosphere and the cheerful coffee breaks.

This work was funded by the Austrian Science Fund (FWF) in grant P19955-N19 (Experimental investigation of flame–flame interaction in a gas turbine model combustor with forced flow instabilities).

Graz, März 2011 Stefan Köberl

Kurzfassung

Die Forderung nach einem geringeren Ausstoß an Emissionen durch Turbomaschinen führt unweigerlich hin zu neuen Verbrennungskonzepten. Unglücklicherweise sind gerade diese Niedrigemissionskonzepte besonders anfällig für Verbrennungsinstabilitäten, die in weitere Folge zu beträchtlichen Einschränkungen im Betrieb führen. Obwohl der Hauptmechanismus für diese thermo-akustischen Instabilitäten, die Kopplung zwischen unstetiger Wärmefreisetzung und Druckschwankungen, schon seit langer Zeit bekannt ist, sind diese Instabilitäten, aufgrund komplexer Wechselwirkungen zwischen dem Strömungsfeld, der Reaktionskinetik, dem Druckfeld und der Wärmefreisetzung, noch immer nicht ausreichend kontrollierbar.

Für die experimentelle Untersuchung dieser Phänomene kommt eine Vielzahl von Messtechniken zum Einsatz um möglichst viele Messgrößen zu erfassen. Dabei sind Dichtemessungen von besonderem Interesse, da insbesondere die Dichteschwankung als Marker für Verbrennungsinstabilitäten dienen kann.

In dieser Arbeit werden deshalb interferometrische Methoden zur Messung von Dichte und Dichtefluktuation in Verbrennungsvorgängen angewandt, wobei das Hauptaugenmerk auf orts- und frequenzaufgelösten Messungen der Dichtefluktuation liegt. Für diese Messungen werden zwei Laservibrometer verwendet und deren Strahl gekreuzt. Da diese interferometrischen Messgeräte nur integrale Dichtefluktuationen entlang des Messstrahls detektieren, müssen lokale Daten erst mittels Korrelationsfunktionen auf Basis von Kreuzspektren gewonnen werden.

Diese Messtechnik wurde an drei verschiedenen Verbrennungsexperimenten mit jeweils zunehmender Komplexität getestet. Die Versuche umfassten eine Methan-Jet Flamme, eine vorgemischte, drallstabilisierte Flamme und eine Mehrflammenbrennkammer mit selbsterregten Verbrennungsinstabilitäten. Diese Experimente zeigten das Potential der Messtechnik für die Untersuchung von Verbrennungsprozessen und Verbrennungsinstabilitäten. Bei allen Experimenten wurde zusätzliche optische- und laser-optische Messtechnik eingesetzt.

Abstract

To meet the objective of reduced emissions in turbomachinery, new combustion technologies have to be applied. Unfortunately these low-emission concepts are particularly prone to combustion instabilities and limit the operational range of gas turbine engines significantly. The main mechanism for thermo-acoustic instabilities, the coupling between unsteady heat release and pressure fluctuations has been known for a long time, although thermo-acoustic instabilities are far from being fully controlled yet, because of complex interactions between the flow-field, chemical kinetics, pressure fluctuations and heat release.

For the investigation of unstable combustion processes a vast number of measurement techniques are used to gain information on a multitude of quantities, but density measurements are of great interest, since density fluctuations serve as a marker for combustion instabilities.

In this work interferometric techniques for density and density fluctuation measurements are introduced to combustion processes, with a special focus on frequency- and space-resolved measurements of density fluctuations. Therefore two laser vibrometer systems are used, crossing their laser beams. Since laser vibrometry is based on interferometric techniques, the derived signals are path-integrals along the measurement beam. To obtain local frequency spectra of density fluctuations, long-time-averaged measurements from each of the two systems are performed using correlation functions and cross-spectra.

This measurement technique was applied to three different combustion processes with increasing level of complexity. The experiments included the investigation of an unconfined methane-jet flame, an unconfined premixed, swirl-stabilized flame and a multi-flame combustion chamber with self-induced combustion instabilities. The experiments showed the potential of the measurement technique for the investigation of combustion processes and unstable combustion. Additionally all experiments were accompanied by optical- and laser-based measurement techniques.

Table of contents

List of figures

Abbreviations and Symbols

Latin symbols

A_c	effective measurement area
ART	algebraic reconstruction technique
$\vec{B}$	magnetic field
c_0	speed of light
C	constant
C_2*	radical intermediate species
CO_2*	radical intermediate species
CCD	charged coupled device
CH*	radical intermediate species
$C(x_0,y_0,f)$	cross-spectrum
DFT	discrete Fourier transform
DIF	differential interferometry
DNS	direct numerical simulation
D_P	particle diameter
E	potential Energy
$\vec{E}$	electric field
f	frequency
$F_A(U)$	window function
F_d	Fourier transform of the first derivative in time of local density fluctuations $\partial\rho' / \partial t(x,y,t)$
FFT	fast Fourier transform
FT	Fourier transform
f_g	fundamental frequency
f_{NY}	Nyquist frequency
f_s	sampling frequency
$F(f)$	discrete Fourier transform of a time signal
$F_t(f)$	continuous Fourier transform of a time signal
$f(r, \varphi)$	spatial distribution from integral data $h(p,\theta)$
$F(x,y,f)$	local spectra of density fluctuations
$F_1(x_0,f)$, $F_2(y_0,f)$	integral spectra of density fluctuations
G	Gladstone-Dale constant
h	Planck constant
$h(p,\theta)$	integral data distribution
$H_{R,3\text{-}D}$	'local' rate of heat release [Wm^{-3}] (tomographic reconstruction)
$H_{R,local}$	local rate of heat release [Wm^{-2}] (projection data)
$H_{R,overall}$	overall heat release rate
i	imaginary unit
I_1 , I_2	laser beam intensities
$I_{3\text{-}D}$	'local' data of chemiluminescence emissions [Wm^{-3}] (tomographic reconstruction)
I_λ	spectral radiant emittance
I_{local}	local chemiluminescence emissions [Wm^{-2}] (projection data)
$I_{overall}$	overall chemiluminescence emissions
$I_{Raman,i}$	intensity of the vibrational Raman signal
$I_{Rayleigh}$	intensity of the Rayleigh signal

k	Boltzmann constant
k	vibrometer calibration factor
$K(f)$	relative correlation
l	characteristic diameter of density structures
LCAO	linear combination of atomic orbitals
LIF	laser induced fluorescence
l_{opt}	optical beam path length
LV	laser vibrometer
m	modulation depth
M	number of projections
MO	molecular orbitals
n	refractive index
N	sample values
OH^*	radical intermediate species
p	spatial coordinate
p	pressure
$P(t)$	polarization density
P	discrete power density spectrum (also called power spectrum)
P_t	continuous power density spectrum
$q_A(u)$	convolution function
R	radius
R_{12}	cross-correlation function
s	spatial coordinate
T	temperature
T	period time
T	sample length
u	velocity
V	volume
x, y, z	Cartesian coordinates
Δx	distance between adjacent interference fringes
$X(t)$	time signal
X_k	discrete form of $X(t)$
Y_i	molar species fraction

Greek Symbols

α	dimensionless exponent
α	polarizibility
α	particle size parameter
β	angle
γ	ratio of specific heat capacities
δ	shear
Δ	difference
ε_0	permittivity
ε_x , ε_y	deflection angles
ζ	coordinate along beam axis
$\eta_{Rayleigh}$	total effectiveness of the detection system (Rayleigh-scattering)
θ	projection angle
κ	coefficient of extinction
λ	wavelength

$\lambda^{(k)}$	relaxation parameter
μ_0	permeability
ν	vibrational state, frequency
ρ	density
σ	variance of the time signal
$\left.\frac{\partial\sigma}{\partial\Omega}\right\|_{Raman,i}$	Raman-scattering cross-section
$\left.\frac{\partial\sigma}{\partial\Omega}\right\|_{Rayleigh,i}$	Rayleigh-scattering cross-section
τ	time lag
φ	phase of a lightwave
φ_0	reference phase
$\Delta\varphi$	phase difference between two waves
ϕ	phase
χ	susceptibility
Ω	angle of detection

Superscripted symbols

*	radical intermediate species
*	conjugate complex function
-	time-averaged mean value
'	turbulent, fluctuating value

1 Introduction

1.1 Motivation

The desire of modern society for fast transportation and the worldwide increasing demand for permanent availability of energy led to a wide range of use for thermal turbomachinery. The field of applications for gas turbines ranges from aviation, the propulsion of helicopters and planes (see figure 1), special propulsion applications in ships and tanks, to the generation of electricity in power plants. In stationary applications as well as in propulsive applications the combustion process plays a key role, since the energy conversion and the pollutant emissions are influenced considerably by the combustion process. Especially for propulsive applications in aviation, the combustion chamber has to meet a great number of requirements over a large operational range.

In the early days of the turbomachinery research the main task was to provide a stable combustion for all operating conditions in the gas turbine but in recent years combustion research in turbomachinery has additionally focused on the reduction of pollutant emissions and the optimum use of fuel due to environmental policies. To achieve these goals the implementation of new combustion concepts was necessary. Among these concepts, lean premixed combustion is one of the most promising in reducing emissions.

Operating combustors under lean premixed conditions decreases nitrous oxides emissions considerably, but the lean premixed combustion is particularly prone to instabilities in the form of thermo-acoustic pulsations caused by a closed-loop coupling between unsteady heat release and pressure fluctuations.

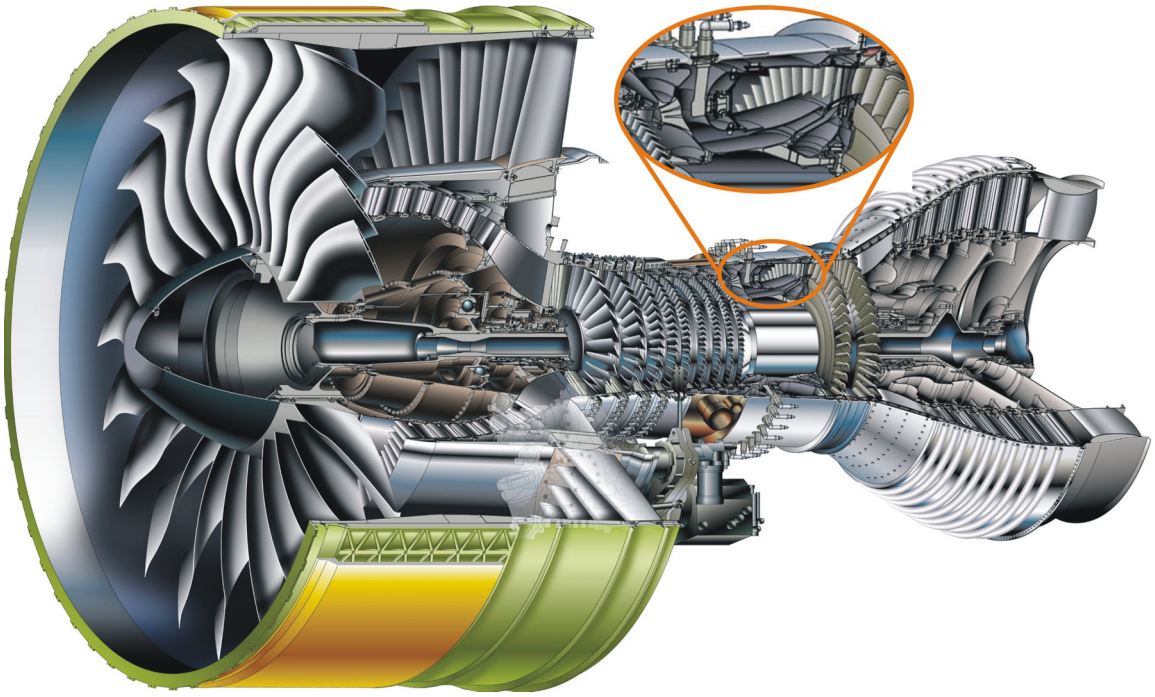

Figure 1: GP7000 turbofan engine (Engine Alliance, bypass ratio 9:1, pressure ratio 43.9:1 and 340 kN of thrust) for the Airbus A380. The combustion chamber of the engine (marked orange) is enlarged for a better visibility (Source: http://www.pw.utc.com).

These self-sustained combustion oscillations limit the operational range of gas turbine engines, as they lead to an increased deterioration of the system or might even result in severe mechanical damage due to the pulsed heat release. Although the main mechanism for thermo-acoustic pulsations, the coupling between unsteady heat release and pressure fluctuations, has been known for a certain time, thermo-acoustic instabilities are even today far from being fully controlled, because of the complex interactions between unsteady flow structures, acoustic field, chemical kinetics, pressure fluctuations and unsteady heat release.

For the investigation of thermo-acoustic instabilities in turbulent gas turbine combustion, a vast number of different measurement techniques are employed to gain information on the combustion process and intensive experimental research is focused on the understanding, prediction and control of combustion instabilities. In most cases detailed experimental studies are performed including extensive use of laser diagnostics, since optical techniques provide non-intrusive investigations of the combustion process and the flow-field.

High frequency-response pressure transducers are used to measure the magnitude, phase and frequency of the pressure fluctuations (e.g. Lieuwen 2002; Lieuwen 2003), while laser Doppler velocimetry (LDV) and/or particle image velocimetry (PIV) are often applied to characterize the unsteady flow-field velocity (e.g. Barbosa et al. 2009; Meier et al. 2010). Information on species concentration and temperature can be provided by Raman- and Rayleigh-scattering (Meier et al. 2010), whereas planar laser fluorescence measurements (PLIF) are often used to determine heat release rates and mixture fractions in the combustion process (Ayoola et al. 2006). Another useful technique to measure heat release rates or concentrations of electronically excited species in unstable combustion processes is that of the naturally occurring flame chemiluminescence (e.g. Lee and Santavicca 2003; Ayoola et al. 2006; Steinberg et al. 2010).

To get a deeper understanding in the dynamics of combustion instabilities, single feature measurements are not enough and complex, simultaneous measurements of a multitude of quantities are indispensable, where especially the determination of quantitative heat release rates requires measurement techniques with a high level of complexity e.g. planar laser induced fluorescence PLIF (Giezendanner et al. 2005; Meier et al. 2010; Steinberg et al. 2010).

The interaction between unsteady heat release q, pressure p' and density is discussed in detail in Dowling and Morgans, 2005, resulting in the following equation relating these important quantities

$$\frac{\partial \rho'}{\partial t} = \frac{1}{\bar{c}^2} \cdot \frac{\partial p'}{\partial t} - \frac{(\gamma - 1) \cdot q}{\bar{c}^2} \tag{1}$$

with the speed of sound and the ratio of specific heat capacities denoted by c and γ, where a mean value is denoted by an over bar, a fluctuating value by a prime. This equation intimates that laser interferometry is of special interest for the investigation of combustion instabilities, as pressure fluctuations and unsteady heat release lead to density fluctuations in the flow according to equation (1), which can be recorded directly using a special type of interferometer called laser vibrometer (LV).

1.2 Project tasks and goals

The goal of this work was the development and application of interferometric measurement techniques for the investigation of combustion instabilities in a multi-flame gas turbine model combustor. An analysis of the unstable combustion processes should be performed based on spatially- and frequency-resolved density fluctuations recorded by two commercial laser vibrometer systems. Spatially- and frequency-resolved measurements of density fluctuations, using two laser vibrometer systems, had already been successfully applied to an isothermal circular free jet flow (Hampel and Woisetschläger 2006), but the dual laser vibrometry was applied in a combustion process for the first time in this work.

In the first part of the work presented, this dual laser vibrometer technique was tested in a methane-fired reference burner. This burner was operated at atmospheric pressure conditions and provided a lifted, circular flame without limitations concerning the optical access. A quantitative calibration and validation of the density fluctuations recorded in the flame was planned by accompanying measurements of the density and density fluctuations using differential interferometry in combination with tomographic reconstruction techniques. The main purpose of these experiments was the validation of the dual laser vibrometry measurement technique for combustion processes.

In the second part of this work, the tests for the dual laser vibrometry were extended to an unconfined, premixed and swirl-stabilized burner that provided a complex-shaped methane flame with a higher level of turbulence due to the swirled flow. These experiments served as preliminary tests for the application of the novel measurement techniques in combustion chambers and should reveal their capability for the investigation of flame types normally used in turbomachinery combustion (high level of turbulence, swirl-stabilized combustion). Additionally the relation between pressure fluctuations, fluctuations of the local heat release rate and their impact on the time derivative of density fluctuations was investigated, according to equation (1).

In the last part of this work, the relevance of dual laser vibrometry for the investigation of combustion instabilities in a gas turbine model combustor was shown. Therefore measurements were performed in the combustion test rig using a multi-flame gas turbine model combustor that exhibited strong thermo-acoustic oscillations at a certain operating point. Those tests showed the capability of the dual laser vibrometry for combustion diagnostics under challenging environmental conditions like pollution of the optical accesses and forced vibrations of the measurement setup due to the unstable combustion process. The dual laser vibrometry experiments were accompanied by measurements of the chemiluminescence emissions to analyse the relation between pressure fluctuations, unsteady heat release and time derivative of density fluctuations qualitatively in an unstable combustion process.

1.3 Research at Graz University of Technology

The Institute for Thermal Turbomachinery and Machine Dynamics at Graz University of Technology focuses on the research and education in the field of turbomachinery. Large experimental facilities are available for research activities at the Institute, including a 3 MW compressor station supplying compressed air to several test rigs, e.g. a two-shaft transonic test turbine and a transonic wind tunnel. The Institute participated in a number of projects within the last decade, focusing on the investigation of turbulent flows through turbomachinery components. Therefore a number of non-intrusive, laser optical measurement techniques were developed and applied at the Institute.

In 2004 the research activities were extended to the field of combustion and a work group for gas turbine combustion was installed. For the combustion test rig additional experimental facilities were connected to the 3 MW compressor station, including a 5 MW thermal air heater (see figure 2) and a versatile air system (figure 3) with up to 3 lines for multi-injection sectors, secondary air, by-pass air and mixing capability. The test rig is shown in figure 4. The electrical driven compressor station consists of two radial compressors and one double screw compressor and enables highly flexible operation of the individual compressors so that air can be provided continuously from 2.5 kgs^{-1} to 15 kgs^{-1} with a pressure ratio up to 2.9 and up to 2.5 kgs^{-1} with a pressure ratio of 10. Together with the thermal air heater, the combustion test rig can be supplied with compressed air heated up to temperatures of 550°C, depending on the mass flow rate of compressed air and the heat input (Leitgeb et al. 2009).

The research activities of the combustion group cover the analysis of turbulent combustion, the interaction between flame dynamics and its environment, and especially combustion instabilities. Therefore the Institute participates in a number of projects funded by the Austrian Science Fund or the European Union (e.g. FWF grant P19955-N19 "Experimental investigation of flame–flame interaction in a gas turbine model combustor with forced flow instabilities" or NEWAC SP6 WP6.2 "Advanced Injection System & Fuel Spray technology Development"). Further research topics include the investigation of atomization- and spray-behaviour of conventional and alternative fuels (e.g. FWF grant P20530-N13 "Evaluation of active control strategies regarding airblast atomization") and preliminary studies of future combustion concepts such as pulse detonation engines or constant volume combustion (NEWAC SP2 "Future Innovative Core Configuration").

Figure 2: Picture of the 5 MW thermal air heater at the Institute for Thermal Turbomachinery and Machine Dynamics, Graz University of Technology.

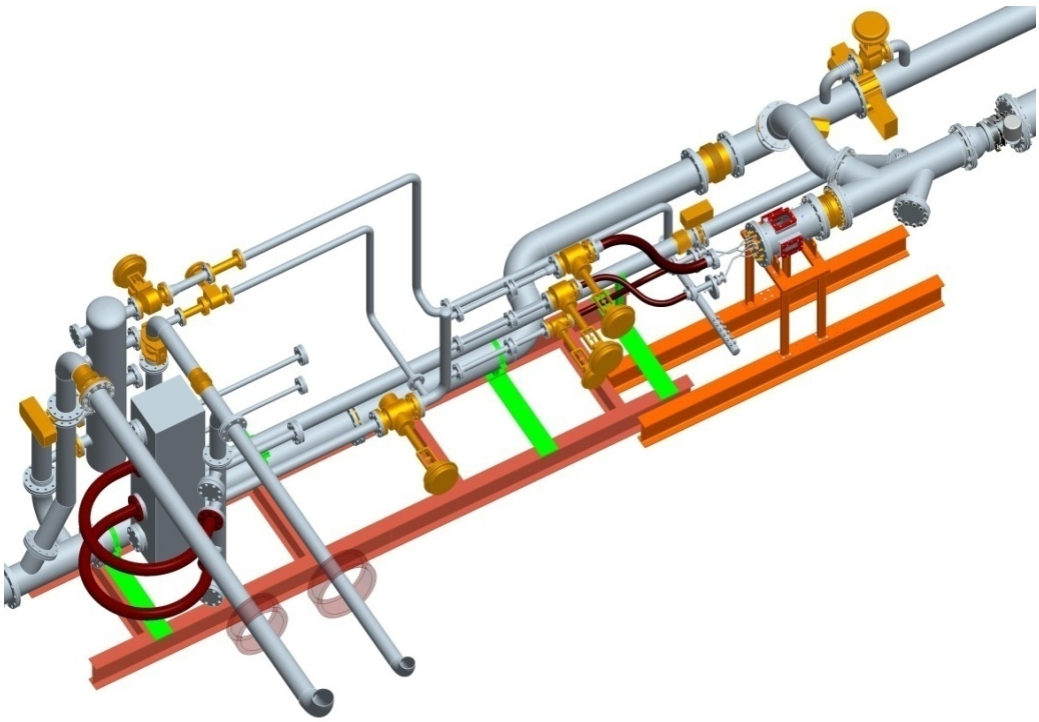

Figure 3: Air distribution system and combustion test rig at the Institute (Leitgeb 2009).

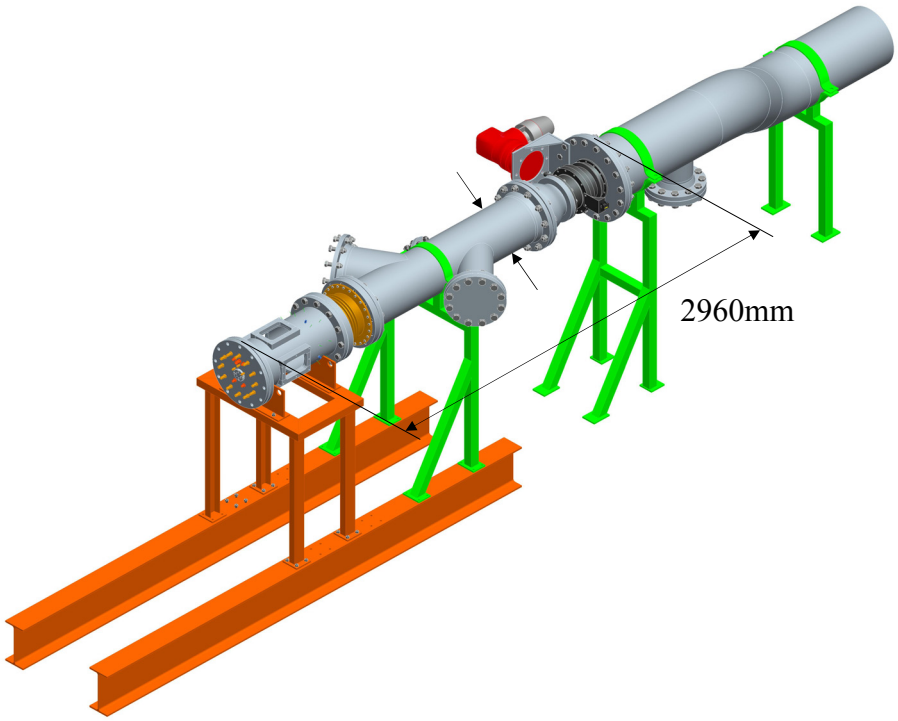

Figure 4: Combustion test rig at the Institute (Leitgeb 2009).

2 Literature overview

At the Institute for Thermal Turbomachinery and Machine Dynamics (ITTM) laser vibrometer were used for the first time to record density fluctuations. The number of published literature in this field of research is rather low, and therefore most of the literature presented here is attributed to the ITTM. Representative for research activities of other institutions in the field of flow investigations by laser vibrometry, the work of Zipser is outlined in this chapter.

The first part of the literature overview consists of a chronological listing of publications, where laser vibrometers have been applied for the recording of density fluctuations in flow-fields. The overview starts with literature of integral density fluctuation measurements in a turbine wake flow and ends with spatially- and frequency-resolved measurements of density fluctuations in a circular isothermal air jet.

The second part of the literature overview is dedicated to combustion and combustion processes. The first publication by Dowling and Morgans presented here discusses the relationship between the pressure, heat release rate and density fluctuations in combustion processes and has a high relevancy for laser vibrometry. The second publication by Kawanabe refers to the burner used for the validation of the dual laser vibrometry. The literature overview in this section ends with two more publications, one by Giuliani et al., dealing with experimental investigations of the relations between pressure fluctuations, heat release rate fluctuations and density fluctuations in an excited flame and another one by Giezendanner et al., describing experimental investigations of combustion instabilities in a gas turbine combustion chamber.

2.1 Laser vibrometer

N. Mayrhofer, H. Lang, J. Woisetschläger (2000): "Experimental investigations of turbine wake flow by interferometrically triggered LDV-measurements"

In this publication the laser vibrometer is applied to a flow-field for the first time. The laser vibrometer is used to trigger two-dimensional velocity measurements by laser Doppler velocimetry (LDV) in a turbine wake flow. The experiments are carried out behind a linear cascade of turbine profiles and density fluctuations of the shedding vortices behind the trailing edge of a profile are measured by the laser vibrometer. For this purpose the laser vibrometer is not used to detect surface vibrations, but changes in the optical path caused by density fluctuations. The recorded density fluctuations in the vortex street are used to trigger the LDV-measurements, thus phase-resolved measurements of velocities in the wake of the profile are derived. This work demonstrates the capability of laser vibrometry for the recording of density fluctuations in turbine flows.

N. Mayrhofer, J. Woisetschläger (2001): "Frequency analysis of turbulent compressible flows by laser vibrometry"

A detailed analysis of the frequency-resolved recording of local density fluctuations from integral measurements using laser vibrometers, velocity decoders and tomographic reconstructions is given including an error analysis. The tomographic reconstruction of local density fluctuations with only one laser vibrometer and single integral data assumes a radial symmetry of the jet used as test object.

L. Zipser, S. Lindner, R. Behrendt (2002): "Interferometrische Messung und Visualisierung von Schallwellen und Turbulenz"

In contrast to the laser vibrometer systems utilized at the ITTM a scanning vibrometer is used in this publication to measure and visualize turbulences and acoustic sound waves in gases. A scanning vibrometer allows the automatic and phase-resolved recording of vibrations from a predefined measurement grid. Here, the background plane is a solid wall and the vibrometer detects the density changes between vibrometer and background wall. The measuring principle is described in the publication and the influence of temperature- and pressure-fluctuations on the refractive index and therefore the impact on the measurement results are outlined. Several test objects are investigated including the sound fields of an ultra sonic wave, the sound field of an activated "T-vibrator", and the turbulence for a pulsating flow in a pipe.

The measurement results presented in the publication are of integral nature, but due to the simple geometries of the investigated objects a 2-dimensional interpretation of data is given.

Additionally, the recording of sound fields with scanning laser vibrometers can make use of the phase relation between the phase of the sound wave in single positions and the trigger or a microphone signal. The minimal detectable pressure fluctuations for the laser vibrometer operating in the displacement mode and the velocity mode are determined in this work and the advantage of the velocity mode at higher frequencies is discussed briefly.

J. Woisetschläger, N. Mayrhofer, B. Hampel, H. Lang, W. Sanz (2003): "Laser-optical investigation of turbine wake flow"

In this publication multi-feature measurements are performed in a vortex street of a turbine blade profile mounted in a linear cascade. The employed measurement techniques include laser vibrometry to gain information on the frequency of density fluctuations in the wake and around the profile, and particle image velocimetry (PIV) to investigate the vortex shedding process. In this work the principle setup for integral density fluctuation measurements is illustrated and the mathematical processing of the obtained data in order to receive quantitative data is described. The laser vibrometer data are used to detect the position of the boundary layer transition at the suction side of the turbine blade profile and to investigate the vortex shedding near the trailing edge of the turbine blade. Additionally, the vortex shedding is investigated for different flow conditions and analysed with respect to the frequency recorded by the laser vibrometer. To clarify the vortex shedding process the laser vibrometer measurements are supported by PIV-measurements.

B. Hampel, J. Woisetschläger (2006): "Frequency- and space-resolved measurement of local density fluctuations in air by laser vibrometry"

This publication reports on the measurement of spatially- and frequency-resolved density fluctuations by laser vibrometry. The test object investigated is a fully developed turbulent free jet. To receive spatially- and frequency-resolved measurements two laser vibrometer systems are used together with a correlation technique. To obtain local spectra of density fluctuations, long-time averaged measurements from each laser vibrometer system are recorded and a correlation function is used in the frequency domain to reveal the common part of both laser vibrometer signals.

The mathematical processing of data and the geometrical considerations of the dual laser vibrometry are discussed in this work and the validation process to receive quantitative data of local density fluctuations is shown. The validation of the dual laser vibrometry technique is done by a comparison of the laser vibrometry data with local pressure measurements, using a

fast pressure transducer. The pressure spectra recorded by the transducer are therefore converted into spectra of density fluctuations. (This validation method could not be used in this thesis due to the high temperatures in the combustion process.)

Furthermore, useful quantities for the judgement of obtained measurement results are identified and discussed, and strategies to improve the measurement results and to suppress artefacts are presented. This publication represents the initial point for the dual laser vibrometry measurements in combustion processes performed in this thesis.

2.2 Combustion

A. P. Dowling, A. S. Morgans (2005): "Feedback control of combustion oscillations"

Dowling and Morgans deal with combustion oscillations and the control strategies for the suppression of these instabilities. At the beginning the physics of combustion oscillations is discussed and the most common mechanism, the coupling between acoustic waves and the unsteady heat release are explained in detail. Therefore the stability of the combustion system is described through a generalized energy equation, where the stability depends on the energy exchanged from the heat release to the acoustic waves and the acoustic energy loss across boundaries. The acoustic energy in the system tends to increase, when the pressure and the heat release have a component that is in phase and the acoustic pressure will increase in magnitude when the growth of the acoustic energy exceeds the energy losses across the boundaries.

For the application of laser vibrometry in combustion processes equation (1) in this publication (and in the thesis here) is of special interest. This equation describes the relation between the time derivative of pressure fluctuations, the unsteady heat release rate and the time derivative of density fluctuations. According to equation (1) laser vibrometry is of special interest for the investigation of combustion instabilities, as this technique allows density fluctuations to be measured directly, which are an indicator for instabilities.

In the second part of the publication control strategies for the suppression of combustion oscillations are discussed and a demonstration of active feedback control for full-scale combustion systems are described.

H. Kawanabe, K. Kawasaki, M. Shioji (2000): "Gas-flow measurements in a jet flame using cross-correlation of high-speed-particle images"

This publication reports the measurement of gas-flow velocities in a jet flame. Particle image velocimetry is applied to a methane-jet flame to investigate the flow velocities and the turbulence characteristics in the flame. The distributions of ensemble-averaged velocities and turbulence intensities are presented and compared to measurement results obtained in a non-reactive jet. The comparison between the non-reactive jet and the methane-jet flame reveals an increase of the velocity gradient in the shear layer of the flame due to the local acceleration caused by buoyancy. Furthermore the turbulent length scales are estimated and it is shown that the characteristic length scales of the methane-jet flame are greater than those of a non-reacting jet. Temperature measurements in the methane-jet flame at several heights complete the characterization of the burner.

The type of burner used in this publication is the same that was used in this thesis to validate the dual laser vibrometry in a combustion process and therefore the publication has a high relevance for the thesis. The author acknowledges the support by Dr. Kawanabe by providing the blue prints of the burner.

F. Giulinai, T. Leitgeb, D. Durox, T. Schuller (2010): "Analyse des variations de densité dans une flamme de référence en présence de couplage thermoacoustique"

These authors performed an experimental study to analyze the relations between the acoustic pressure, the rate of unsteady heat release and the density fluctuations in the reaction zone of a laminar flame with enforced combustion oscillations. The investigated flame has a M-shaped form and is excited to oscillations using a loudspeaker at a frequency of 51 Hz. The sound pressure is measured by a microphone, variations in the heat release rate are determined from the light emission from the flame and the density fluctuations are recorded by a laser vibrometer. The mechanisms involved in the response of the flame to the modulations in the flow caused by the loudspeaker is investigated, using the time signals of the sound pressure (microphone), the heat release rate (photomultiplier) and the time signal of the density fluctuations recorded by the laser vibrometer. The signals are compared to each other and investigated with respect to their phase relationships.

R. Giezendanner, P. Weigand, X. R. Duan, W. Meier, U. Meier, M. Aigner, B. Lehmann (2005): "Laser-based investigations of periodic combustion instabilities in a gas turbine model combustor"

This work reports on an experimental study of periodic combustion instabilities in a swirl-stabilized non-premixed model combustor operated at atmospheric pressure conditions. The investigated flame exhibits strong thermo-acoustic oscillations at 290 Hz. This periodic combustion instabilities are studied by a number of phase-resolved laser-based measurement techniques, including laser Doppler velocimetry for velocity measurements, planar laser induced fluorescence measurements for the imaging of *CH* and *OH* radicals, and Raman-scattering for the determination of species concentrations, temperature and mixture fractions.

These phase-resolved measurement techniques enable a qualitative description of the arising combustion instability. Furthermore the correlations between the heat release rates, axial velocity at the nozzle exit, mixture fraction and temperature in the periphery of the flame and their phase relationship are discussed and the mechanism of the combustion oscillation is explained.

The publication is an example for a vast number of publications in this area of research and shows the high experimental effort and the massive application of laser-based measurement techniques needed for the investigation of combustion instabilities.

3 Optical measurement techniques for combustion diagnostics

3.1 Introduction

In this chapter a brief theoretical overview of all optical measurement techniques applied in this work is given. The measurement techniques discussed here include shadowgraph- and schlieren-visualization, scattering measurement techniques (laser Doppler velocimetry and Rayleigh/Raman-scattering), chemiluminescence emission measurement techniques and interferometric measurement techniques (differential interferometry and laser vibrometry). At the beginning the physical properties of matter and light and their interaction are discussed, since all the measurement techniques are based on these properties.

3.1.1 Methane-Molecule

A molecule can be defined as a group of atoms bound together by electrons. It consists of a group of nuclei surrounded by electrons in such a way that covalent bonds are formed. The electrons are arranged around the nuclei according to the laws of quantum mechanics. In fact the inner electrons remain attached to their original nuclei almost undisturbed. Only the outermost electrons, so-called valence electrons, constitute the chemical binding and are responsible for most physical and chemical properties of the molecule.

The probability density of the binding valence electrons in space is given by molecular orbitals. These molecular orbitals form across the atoms by superposition of orbits from the single atomic partners leading to covalent bonds. The orbitals correspond to different energetic states, and may have complex shapes due to their combination of different atomic orbitals.

In figure 5(a) the molecular structure for methane with the molecular bonds is presented. The methane molecule consists of a central C-atom bonded to the four surrounding H-atoms by four sp^3-hybridized orbitals. The H-atoms are arranged symmetrically around the C-atom leading to bond angles of 109.5° and a tetrahedron molecular shape. Figure 5(b) presents the methane molecule schematically and presents the van der Waals sphere that corresponds to the "effective" volume of the molecule.

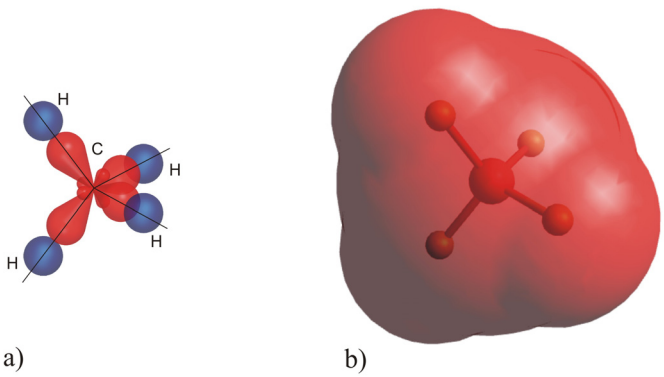

Figure 5: Molecular structure of methane with (a) localized carbon sp^3- and hydrogen s-orbials and (b) the van der Waals sphere for methane

The electronic potential energy E for molecular bonds as a function of the interatomic distance r can be described by the Morse potential and is presented for a diatomic molecule in figure 6. For large values of r the electronic potential energy for the electron tends to a constant value, in the ground state this is value D, which is the energy required to separate or dissociate the molecule. Different energetic states for the binding electron can be found by linear combination of atomic orbitals (LCAO theory) and present molecular orbitals (MO). Excited states correspond to Morse potentials above the ground state with different interatomic distances.

Additionally to the electronic states, relative nuclear motions - as vibration and rotation - take place in molecules. For the diatomic molecule in figure 6, only vibrational modes were taken into account. Bound together by the electrons, the nuclei can be in relative oscillatory motion against each other. For vibrational modes, the quantum mechanic laws are valid as well, leading to additional vibrational states that are superimposed to the electronic state, as shown in figure 6. These vibrational energy levels are spaced equally, with the ground state of vibration having a minimum energy.

For the methane molecule four different vibrational modes can be identified (see figure 7), but only the two vibrational modes ν_1 and ν_3 are of interest for temperature and concentration measurements using Raman-scattering technique.

Due to the different electronic and vibrational states, a large number of energy transitions are theoretically possible in molecules. The probabilities for certain energy transitions are limited according to the Franck-Cordon-principle, a selection rule for simultaneous changes in electronic and vibrational energy levels (Alonso and Finn 1968).

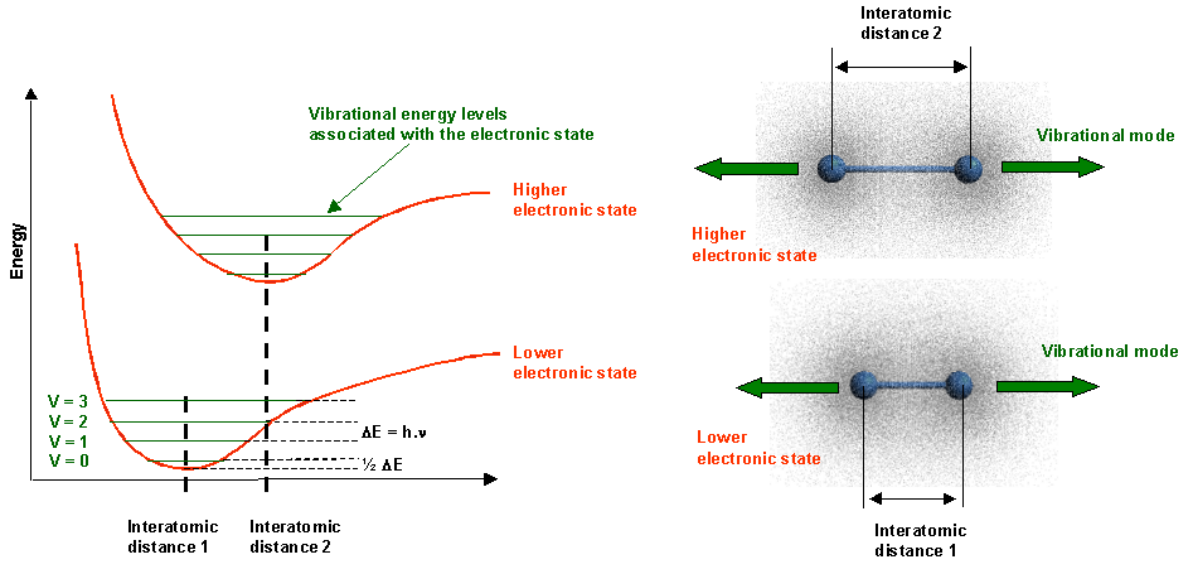

Figure 6: Electronic potential energy in a diatomic molecule described by Morse potentials. Superimposed are the energy levels for molecular vibrations (left). Molecular orbitals presented by the relative probability (dotted cloud) to find the binding electron in different places (right) (Woisetschläger 2010).

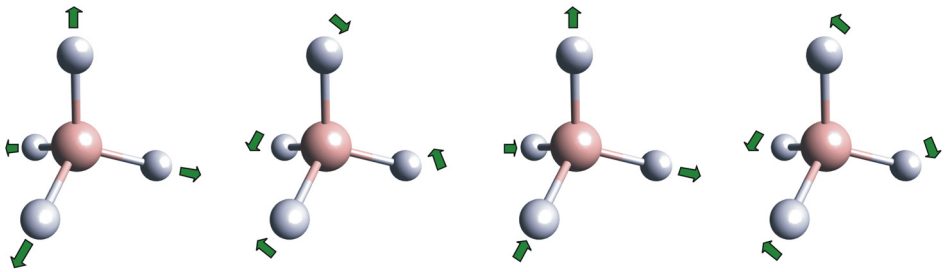

Figure 7: Vibrational modes for the methane molecule.

When energy is transferred to the molecule, e.g. by absorption of photons, the binding electrons can move to higher energetic states, if the input energy equals the energy difference between two energy levels in accordance to this selection rule. A quantum of electromagnetic energy is then released again as a photon, if the electron again drops back into a lower energy level. The energy difference ΔE between two levels is related to the photons frequency ν according to equation (2), where the Planck constant is denoted by h.

$$\Delta E = h\nu \qquad h = 6{,}626068 \cdot 10^{-34}\, Js \tag{2}$$

The frequency ν is linked to the wavelength λ via the speed of light c_0 by

$$\lambda = \frac{c_0}{\nu} \tag{3}$$

Now the wavelength for any energy transition can be determined, e.g. for a transition from the ground level to an excited level (absorption of light waves) or from the ground level to a 'virtual' level (light scatter processes), to discuss the interaction between molecules and light waves (Alonso and Finn 1968).

3.1.2 Interaction of light with matter

Light can be described as an electromagnetic wave that propagates through empty space (vacuum) with a fixed phase velocity c_0. The origin and the interaction of light with matter are basically influenced by the light's electromagnetic nature and the electric charges in atoms and molecules. Furthermore, important phenomena like absorption, emission, polarization, reflection and refraction are explained by this theory. As most optical measurement techniques are based on the aforementioned phenomena, a short overview of electromagnetic wave theory is given in this chapter and the interaction of light with matter is described.

The nature of electromagnetic waves obeys the Maxwell's equations, a set of four partial differential equations. According to these equations a time varying electric field vector generates a time varying magnetic field vector and vice versa. Thus an oscillating electric field generates an oscillating magnetic field and this magnetic field in turn generates an oscillating electric field. The oscillating magnetic and electric fields together form a propagating electromagnetic wave (see figure 8).

The mathematical formulation for the electromagnetic wave can be written either in terms of the electric field $\vec{E}$ or the magnetic field $\vec{B}$ and derives from the Maxwell equations. In the free space the electromagnetic wave equation can be written in terms of the electric field as

$$\frac{\partial^2 \vec{E}}{\partial t^2} = \frac{1}{\mu_0 \varepsilon_0} \Delta \vec{E} \tag{4}$$

with

$$c_0 = \frac{1}{\sqrt{\varepsilon_0 \mu_0}} = 299722458 \frac{m}{s} \tag{5}$$

the phase velocity for the propagating wave. In this equation the phase velocity, the permittivity and the permeability are denoted by c_0, ε_0 and μ_0. In empty space the phase velocity c_0 equals the vacuum speed of light. In matter the velocity of propagation of electromagnetic waves is different from the velocity of propagation in vacuum. The ratio between the phase velocity in vacuum and the velocity in matter is specified by the refractive index n (also called index of refraction):

$$n = \frac{c_0}{c} = \frac{1}{\sqrt{\varepsilon_0 \mu_0}} \sqrt{\varepsilon \mu} \tag{6}$$

Discussing the wave equation, equation (4), reveals that electromagnetic waves propagating through non-conducting media (insulators) are transverse, with the electric field $\vec{E}$ and the magnetic field $\vec{B}$ perpendicular both to each other and to the direction of propagation of the waves. The electric and magnetic field are also in phase and the amplitudes are proportional to each other. The coupling between the electric and magnetic field allows a complete description of the wave in terms of one parameter, either the electric field $\vec{E}$ or the magnetic field $\vec{B}$. Typically the equation is written in terms of the electric field, as the direction of the electric field defines the polarisation direction of the light (see figure 8) (Alonso and Finn 1967; Oertler sen. and Oertler jun. 1989).

If an electromagnetic wave propagates in dielectric matter, it interacts with the atoms or molecules and induces an electric dipole and oscillations of this dipole. Thus, a dielectric is an insulator with atoms or molecules that will be polarized by the electromagnetic wave, and an electric dipole moment will be induced. (In case a permanent dipole already exists in the molecule the light wave will induce an additional dipole moment).

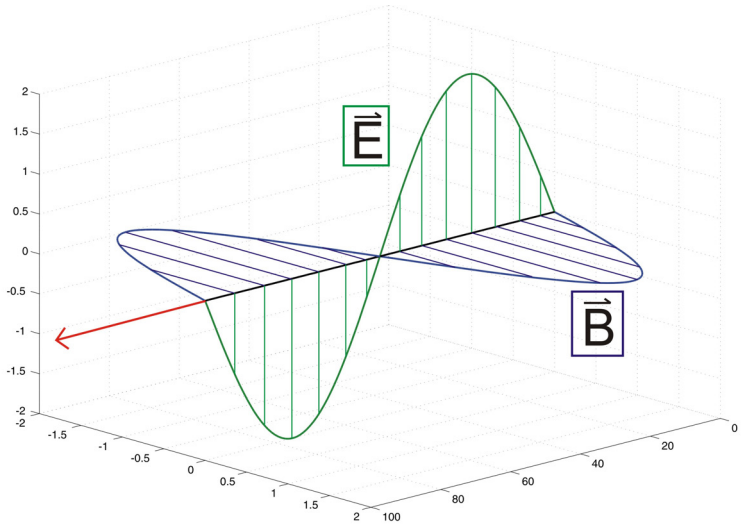

Figure 8: Electromagnetic wave. The electric field and magnetic field are perpendicular to each other, the wave is transverse. The polarisation direction is defined by the electric field vector.

During this interaction the electrons in the atoms or molecules are slightly moved relatively to the nuclei by the incoming electromagnetic wave and therefore the centres of positive and negative charges are slightly displaced against each other in the molecules. This induced dipole moment is defined by a displacement *x(t)* pointing from the negative charge *–q* to the positive charge *+q*, the polarizibility of the molecules is denoted by α:

$$\vec{p}(t) = \varepsilon_0 \alpha \vec{E}(t) = q\vec{x}(t) \tag{7}$$

With *N* the number density of molecules or atoms per volume unit, this leads to the polarization density *P(t)* with χ the susceptibility of the medium. The electric susceptibility now is a quantitative measure of the extent to which an electric field applied to a dielectric material causes polarization.

$$\vec{P}(t) = \varepsilon_0 N\alpha \vec{E}(t) = \varepsilon_0 \chi \vec{E}(t) \tag{8}$$

In a dielectric medium the susceptibility is a complex number and consists of the real and imaginary part χ_1 and χ_2.

$$\chi = \chi_1 + i\chi_2 \tag{9}$$

Both parts of the susceptibility, real part and imaginary part, strongly depend on the frequency of the incident electromagnetic wave and on the molecule's resonance frequency (see figure 9). Near the resonance frequency - at this frequency the light wave will be absorbed by the atom or molecule, the electrons will transit from ground level to an excited level - the imaginary part of the susceptibility reaches a maximum, the real part has a turning point at the resonance frequency and changes sign (Alonso and Finn 1967). Mechanically speaking we observe the behaviour of a forced oscillator.

The index of refraction *n* and coefficient of extinction κ are related to the real and imaginary part of the susceptibility according to equation (10) and (11); hence they strongly depend on the frequency too.

$$n^2 + \kappa^2 = 1 + \chi_1 \tag{10}$$

$$2n\kappa = \chi_2 \tag{11}$$

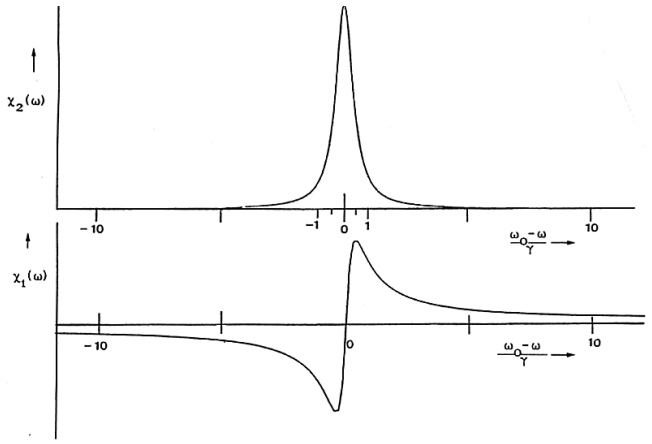

Figure 9: Real and Imaginary part of the electric susceptibility (Woisetschläger 2010)

A few line widths away from the resonance frequency ω_0 the dielectric medium is transparent, hence κ is very small and therefore the refractive index n depends on χ_1 only (see equation (10)). In a gas the refractive index n is close to 1, thus leading to equations (12) and (13).

$$2(n-1) \cong \chi_1 \tag{12}$$

$$2\kappa \cong \chi_2 \tag{13}$$

For the interaction of matter with light, it is important to notice that atoms and molecules posses a number of resonance frequencies. When the frequency of the incident electromagnetic light wave equals a resonance frequency, κ becomes large leading to absorption of the light wave, as shown in figure 9 and by equation (13). Beside these resonance frequencies only forced dipole oscillations are induced by the electromagnetic light wave. The oscillating dipoles now emit a secondary wave, interfering with the primary wave. The interference of the primary and secondary wave lead to a new resultant wave with a phase lag compared to the primary wave, figure 10. This explains the slower propagation of a light wave through a medium and therefore the larger refractive index.

Figure 11 presents absorption coefficients for different atmospheric gases, including methane, as a function of the wavelength of the incoming electromagnetic waves. For methane two peaks can be identified in the infrared range, where the absorption coefficient has maximal values. These peaks denote two resonant states for the methane molecule, where infrared radiation is absorbed. Beside these resonance frequencies the methane gas is transparent and the light propagates in the medium with a phase velocity c defined by the refractive index n according to equation (6) (Alonso and Finn 1967; Oertler sen. and Oertler jun. 1989).

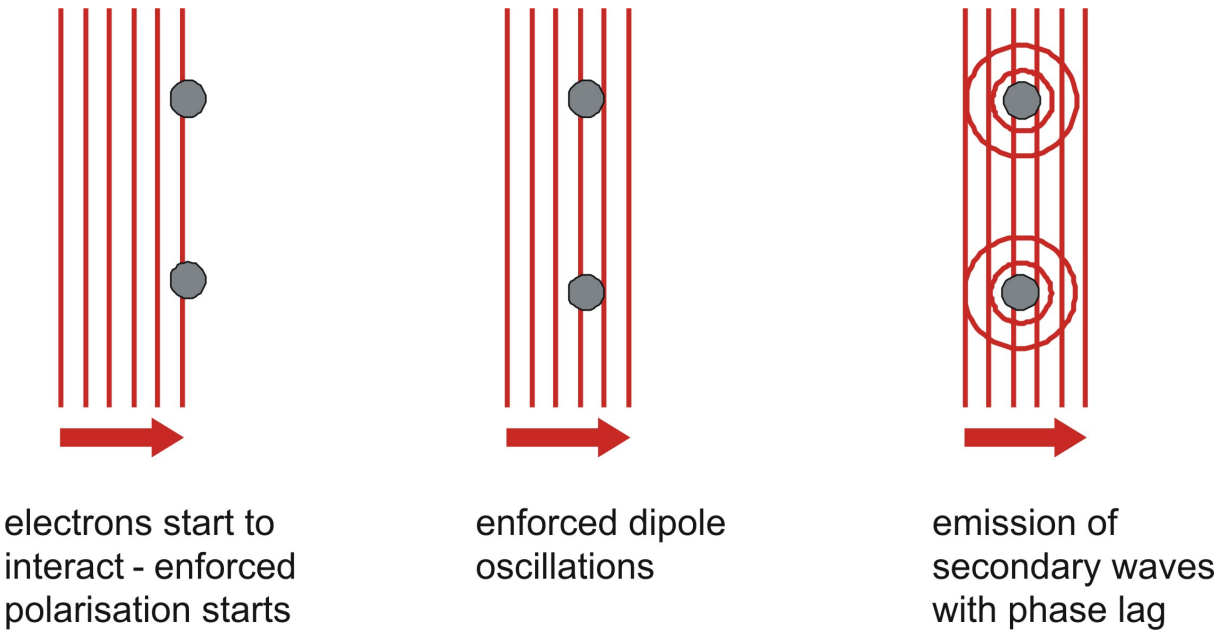

Figure 10: Interaction of light with matter. Forced dipole oscillations are induced by the electromagnetic wave. The interference of the primary and secondary wave lead to a new resultant wave with a phase lag compared to the primary wave (Woisetschläger 2010).

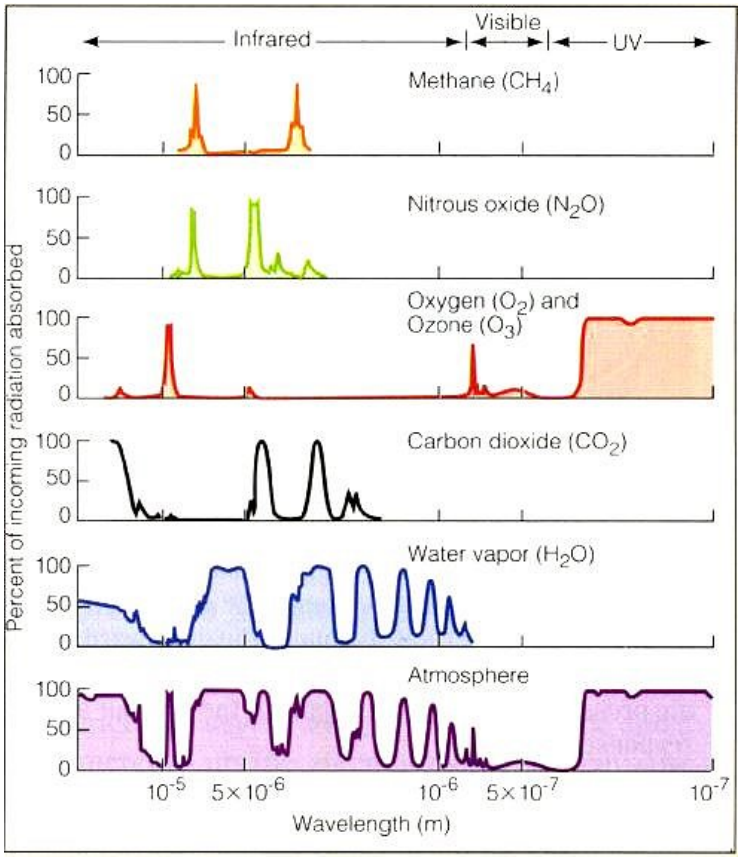

Figure 11: Absorption coefficients as function of frequency of the electromagnetic wave for some atmospheric gases. (Source: www.fe-lexikon.info/images/AtmosAbsorption.jpg)

3.1.3 Methane combustion

Generally, combustion is referred to as a chemical exothermic reaction of a fuel and an oxidant accompanied by the production of heat and the conversion of chemicals. For all experimental setups presented in this work, methane was employed as fuel and air was used as an oxidant. In a complete combustion reaction methane (CH_4) and oxygen (O_2) is converted to carbon dioxide (CO_2) and vapour of water (H_20).

$$CH_4 + 2O_2 \rightarrow CO_2 + H_2O \qquad (14)$$

In reality complete combustion is almost impossible to achieve and the combustion process can not be characterized by one simple reaction equation. Methane and oxygen are not converted to carbon dioxide and water steam directly; in fact a complex system of reaction equations is needed to cover all the radical intermediates involved in the combustion process (Joos 2006).

The reaction mechanism for a laminar methane-air flame, including radical intermediates, is shown in figure 12 (top). These intermediates are of great interest for measurement purposes, as their appearance is spatially limited to a certain zone in the flame. Most reactions take place within this thin zone, called reaction zone, where the reactants are converted to final products via radical intermediate species like CH^*, OH^*, CO_2^* or C_2^*(the asterisk indicates an excited species). Due to their limited appearance these species often serve as a marker for the reaction zone. Normalized concentration profiles for different species in a methane-air flame are presented in figure 12 (bottom).

Especially *CH** and *OH** are suited for the indication of the flame front due to their steep increase in the reaction zone. According to figure 12 (bottom) the *CH** concentration characterizes the flame front best due to the steep increase and decrease within the reaction zone. The *OH** concentration on the other hand provides information to distinguish pre- and post-flame regions due to a steep increase in the reaction zone and a persistent high concentration in the post-flame region (Kee et al. 1996).

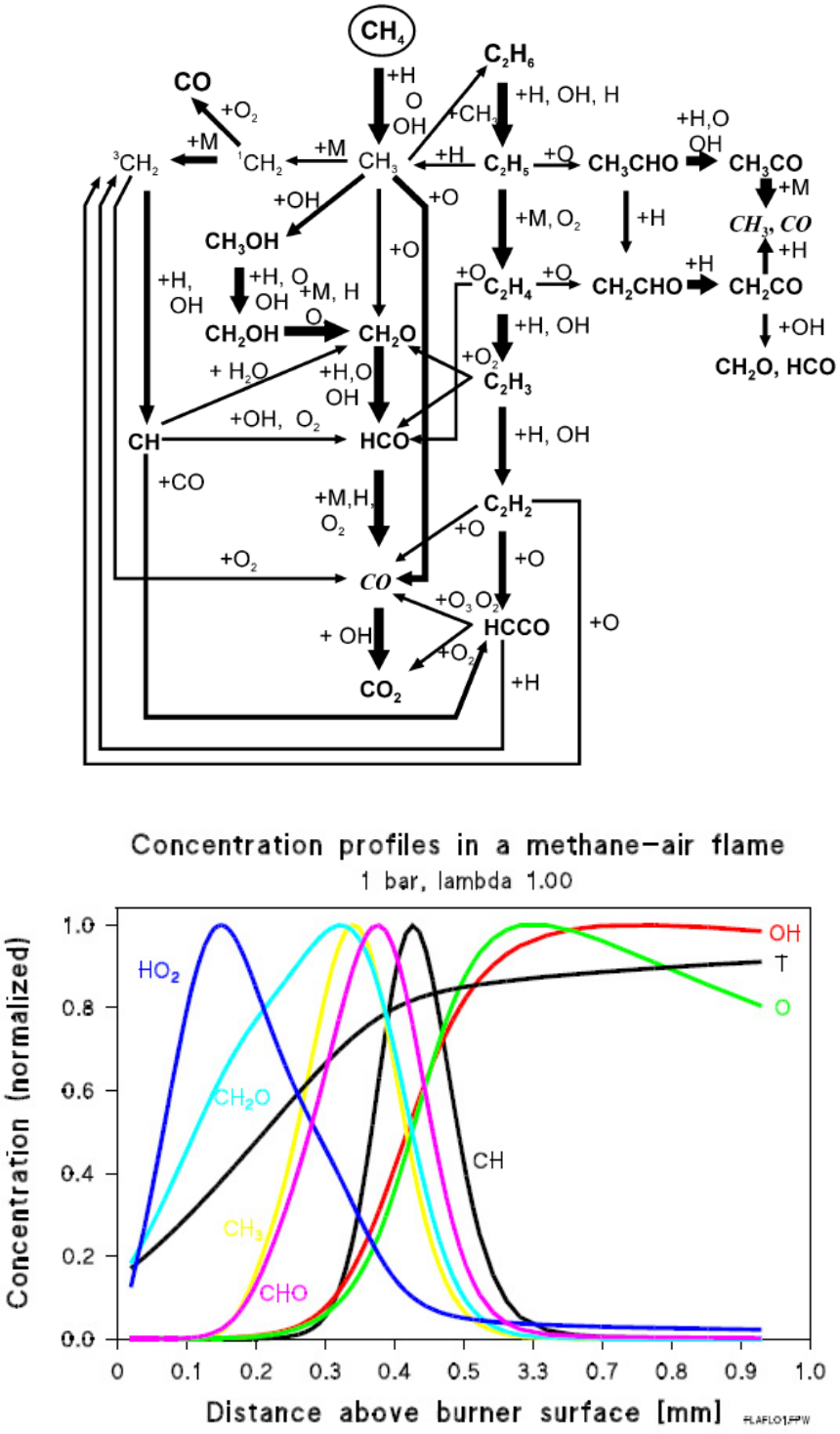

Figure 12: Reaction mechanism (Joos 2006) (top) and concentration profiles (bottom) in a laminar methane-air flame (Kee et al. 1996).

3.2 Shadowgraph- and schlieren-visualization

Shadowgraph- and schlieren-method are visualization techniques that provide qualitative information on the fluid flow by visualizing refractive index gradients. These gradients of refractive index are caused by changes of the fluid density. Hence shadowgraph- and schlieren-visualization may be applied to investigate compressible flows, e.g. to visualize shock waves, convective heat transfer, or the mixing of two or more fluids of different density. In a combustion process all three former effects are involved, therefore shadowgraph- and schlieren-visualization were applied in this work for characterization and visualization purposes.

For shadowgraph and schlieren-visualizations light beams passing through the test zone are disturbed due to the distribution of the refractive index in the test zone and two phenomena occur. The light is deflected from the original direction and the phase of the disturbed light wave is shifted with respect to the undisturbed light wave, according to changes in the density in the test zone, see figure 13.

In gases the refractive index n is linked to the density via the Gladstone-Dale constant G. The refractive index of a gas mixture is given by equation (16), where G_i denotes the Gladstone-Dale constants and ρ_i the partial densities of the mixture components.

$$n - 1 = G\rho \tag{15}$$

Values of G for different gases can be found in the literature (Merzkirch 1987) and especially for combustion gases (Gardiner et al. 1981).

$$n - 1 = \sum G_i \rho_i \tag{16}$$

For shadowgraph- and schlieren-visualization the light ray deflection in an inhomogeneous field is treated in terms of geometrical optics. The deflection ε_x and ε_y of a light ray as a function of the Gladstone-Dale constant, the density gradients and the length ζ_2-ζ_1 is given by equation (17a) and (17b) and can be seen in figure 14 (Oertler sen and Oertler jun. 1989).

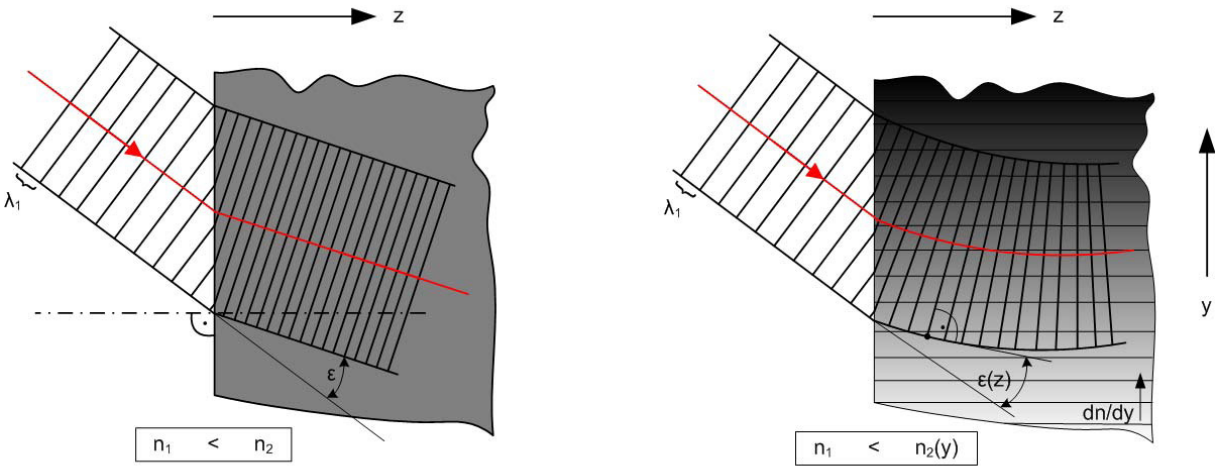

Figure 13: Refraction of light at the interface between two media of different refractive indices (left). Continuous refraction of light due to a density gradient in media 2 (right) (Heimel 2010).

$$\varepsilon_x = \frac{G}{1+G\rho}\frac{\partial \rho}{\partial x}(\varsigma_2 - \varsigma_1) \qquad (17a)$$

$$\varepsilon_y = \frac{G}{1+G\rho}\frac{\partial \rho}{\partial y}(\varsigma_2 - \varsigma_1) \qquad (17b)$$

The shadowgraph now visualizes the displacement QQ*, the schlieren-method visualizes the deflection angles ε_x and ε_y. Therefore the shadowgraph-technique is sensitive to changes in the second derivation of the refractive index, whereas the schlieren technique visualizes changes in the first derivative of the refractive index.

The shadowgraph method is the simplest technique for flow visualization. The setup consists of a point-shaped light source, a lens system to provide parallel light through the test field and a screen or a camera to visualize the shadows, see figure 15. A light ray passing through the measurement area is deflected by the inhomogeneous refractive index in the field and arrives at a different point of the recording plane compared to an undisturbed light ray. This alters the distribution of the light intensity in the recording plane, visualizing all changes in the density gradients integrated along the line of sight.

The setup for the schlieren visualization is similar to the shadowgraph setup. Again a point-shaped light source together with a lens system is used to provide parallel beam of light through the test field. Additionally an aperture, e.g. a knife edge, is placed in the focal plane of the second lens, to cut off a part of the light source. Now, depending on the chosen schlieren stop (aperture), either all undisturbed light rays are blocked and only deflected light rays pass the aperture generating the resulting image on the screen, or vice versa. If all undisturbed light rays are blocked the method is referred to as the dark-field schlieren technique, otherwise the method is called bright-field schlieren technique (see figure 16).

Additional information on the test field can be gained, if directionally sensitive schlieren systems are applied. Therefore a colour source filter is often used to get information on the direction of the density gradient. Increasing density gradients in different spatial directions are then marked by different colours in the schlieren image (Merzkirch 1987; Settles 2006).

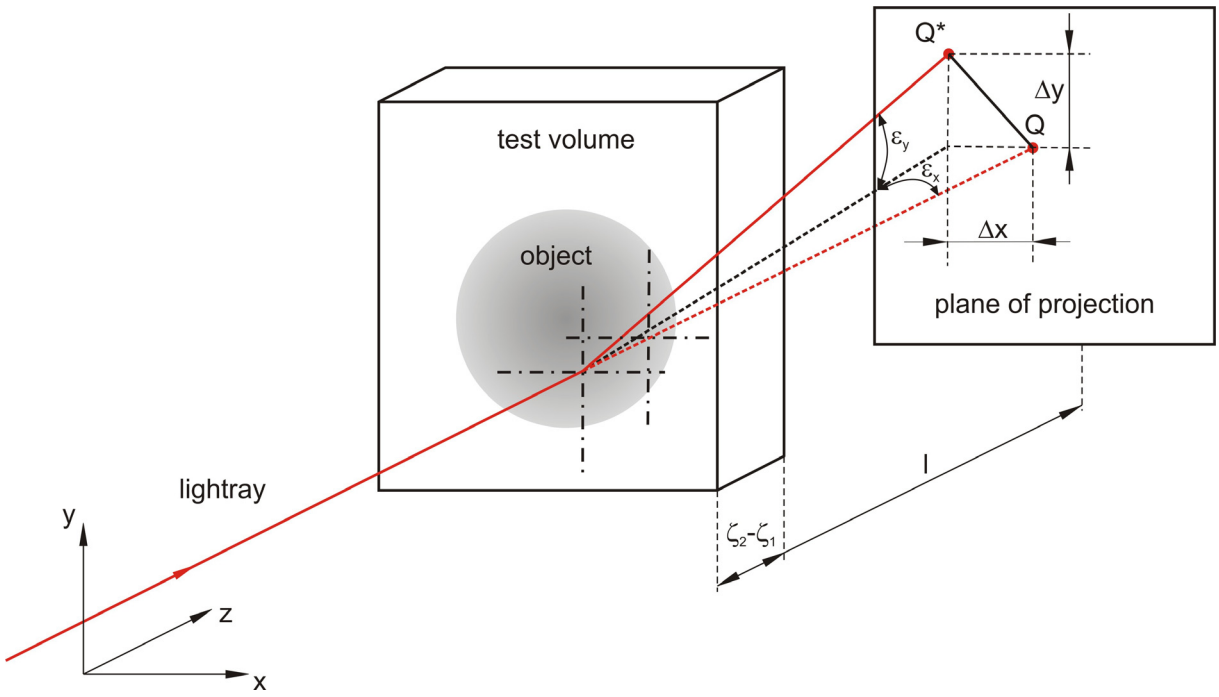

Figure 14: Deflection of a light ray in an inhomogeneous test object (Heimel 2010).

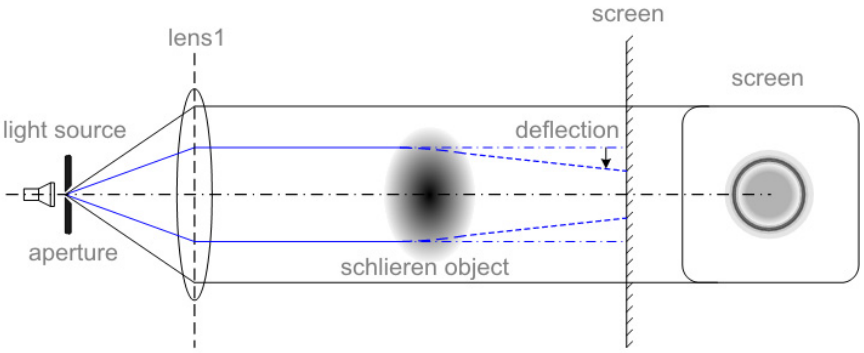

Figure 15: Shadowgraph system with parallel light through the test zone (Heimel 2010).

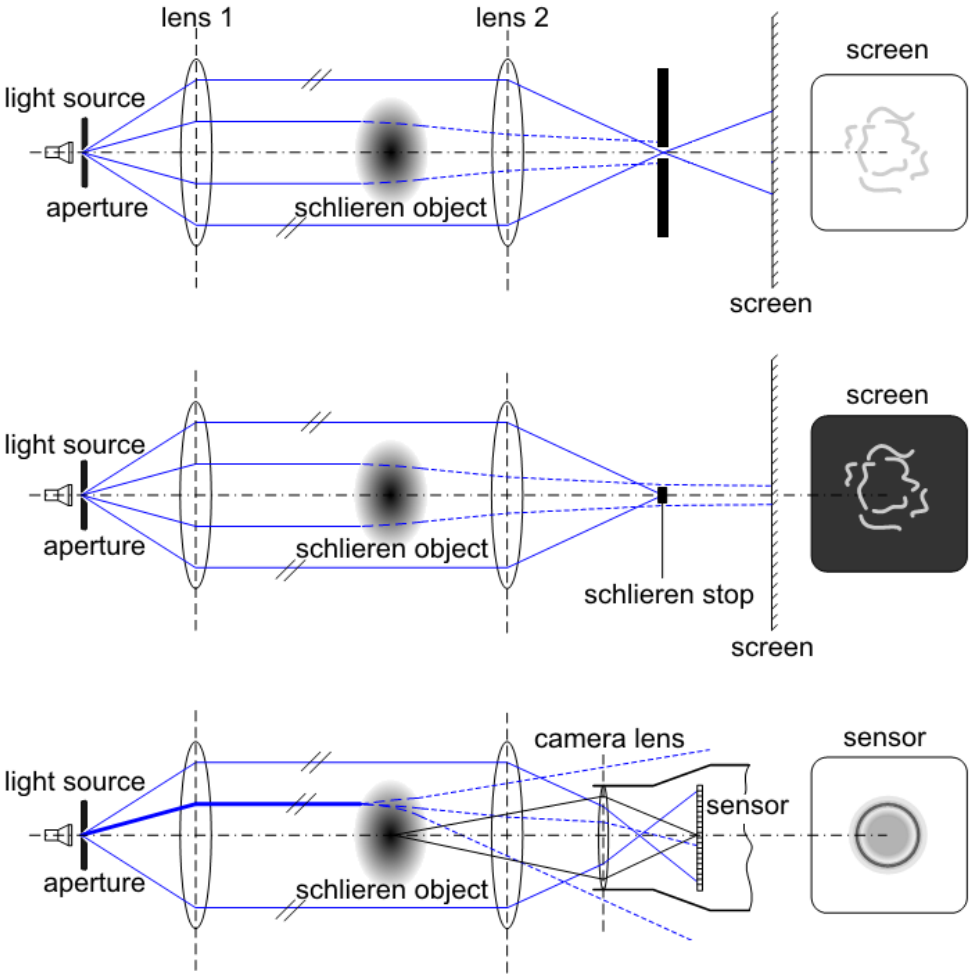

Figure 16: Bright-field schlieren system (top). Dark-field schlieren system, only deflected light rays are imaged at the screen (middle). Schlieren system with the camera objective acting as a schlieren stop (bottom) (Heimel 2010).

3.3 Scattering measurement techniques

In this chapter measurement techniques based on the scattering of light are discussed. The two scatter-based measurement techniques applied in this work to investigate combustion processes are laser Doppler velocimetry (LDV) for velocity measurements and Rayleigh/Raman-scattering for temperature and concentration measurements. Both methods are based on the detection and signal analysis of scattered light, but one uses elastic, the other inelastic scatter processes.

Commonly scattering describes the collision especially that of waves and particles. This general statement on scattering also includes light that propagates through the matter, since light can be described as an electromagnetic wave. The basic interaction of light with matter was discussed at the beginning in the chapter "*Optical measurement techniques for combustion diagnostics*". During this basic interaction of a plane light wave with atoms or molecules, the interference of the primary light wave with light waves emitted by the forced dipole oscillations of the atoms and molecules results in a plane secondary wave front without lateral scatter of light. Lateral scatter of light is observed if randomly, widely spaced scatterers (droplets or particles) are present in the matter, which emit secondary waves (figure 17) independently of the waves scattered by other particles (Born and Wolf 1980; Donges and Noll 1993).

Light scattering can be divided into elastic scattering, e.g. Rayleigh- or Mie-scattering, or inelastic scattering, e.g. Raman-scattering. Elastic scattering is characterized by scattered light having the same frequency then the incident light wave, whereas inelastic scattering is specified by a difference in the frequency of the incident light wave and the scattered light.

The Lorenz-Mie theory now describes the elastic scattering modes for spherical particles. Originally Gustav Mie derived a solution for the scattering of a plane light wave by one single conducting sphere. This solution also applies to scattering by any number of spheres, as long as they feature the same diameter and composition, as long as these spheres are distributed randomly and as long as these spheres are separated by distances that are large compared to the wavelength of the incident light. Provided that these conditions are satisfied there are no coherent phase relationships between the scattered light from different spheres and the total scattered energy equals the energy scattered by one sphere multiplied by the total number of spheres. Additional information on the Mie theory can be found in (Born and Wolf 1980).

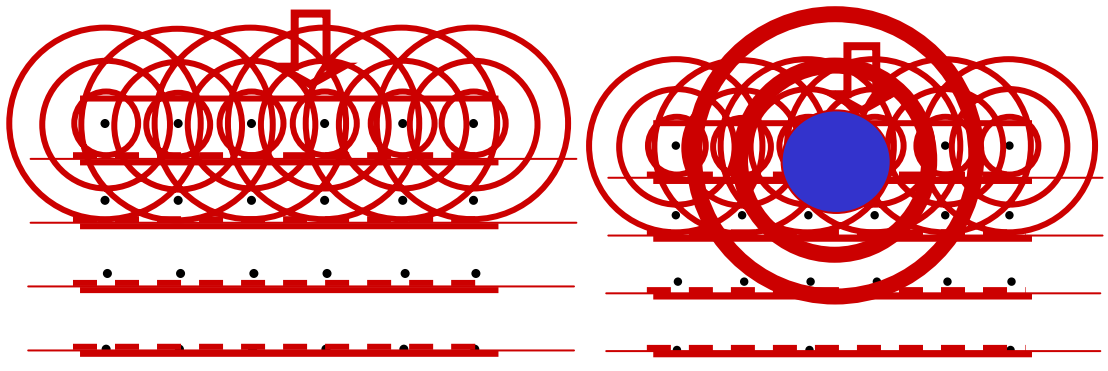

Figure 17: Comparison between the interaction of light with atoms or molecules and scattering of light due to a single particle (Woisetschläger 2010).

This theory holds to limiting cases. One is for very small particles, smaller than the wavelength of light used, this scattering is named Rayleigh-scattering (named after John William Strutt, 3rd Baron Rayleigh). The other is for very large scatter objects, e.g. rain drops, where geometrical optics can also be used to calculate the scatter. This case is generally called the geometric optics case.

So, in current language usage the elastic scattering is divided into three domains based on the size parameter α, which is a dimensionless measure for the relation between the diameter D_P of the particle and the wavelength λ of the incident light.

$$\alpha = \frac{D_P}{\lambda} \tag{18}$$

For spherical scatterers with a diameter D_P being small compared to the wavelength λ, hence $\alpha << 1$, only enforced dipole oscillation, so called Rayleigh-scattering, is observed. This mode is characterized by a strong scatter in the forward and backward direction, but no scatter in the direction of the enforced dipole oscillations.

For larger diameters of scatterers the Rayleigh-scatter mode changes into the Mie-scatter mode. According to equation (18) the diameter of the scatter now gets in the order of the wavelength leading to multipole-oscillations with complex surface currents on the scatter particle. The Mie-scattering is still strongest in forward and backward direction, but the scattered intensity distribution gets much more complex due to the complex surface currents.

If $\alpha >> 1$**,** the particles or droplets are large enough for a wave front to form inside and phenomena well known from geometrical optics like reflection and refraction are observed. In this case geometrical optics can be used to explain a number of scattering effects within these particles.

3.3.1 Laser Doppler velocimetry (LDV)

Laser Doppler velocimetry (LDV) is a technique for measuring local flow velocities based on the detection and analysis of light scattered by particles in the flow. The most common setup for LDV is the so-called cross-beam arrangement. Therefore two beams of monochromatic, coherent laser light are crossed in the focus of a lens, providing an interference pattern in the probe volume of the two crossing laser beams (figure 18).

Tracer particles suspended in the fluid flow now scatter the laser light from the regions of constructive interference, while moving through the probe volume. This scattered light, fluctuating in intensity while the particle passes the measurement volume, is collected by a photo detector and the particle's velocity can be calculated due to the signal recorded by the detector (figure 18).

The distance Δx between two adjacent interference fringes as a function of the wavelength λ of the utilized laser light and the angle β between the two laser beams is given by

$$\Delta x = \frac{\lambda}{2 \sin \beta} \tag{19}$$

and the frequency f of the intensity oscillations from the recorded signal is linked to the particle velocity u and distance Δx via equation (20).

$$f = \frac{u}{\Delta x} \tag{20}$$

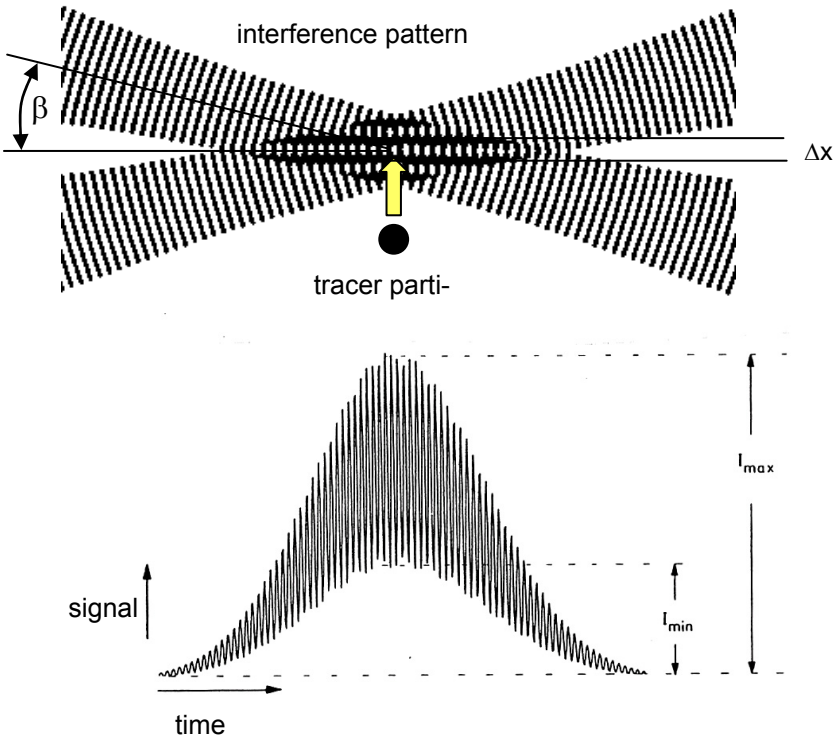

Figure 18: Interference pattern in the probe volume of a LDV in the cross-beam arrangement (top), and Doppler burst of the scattered signal (bottom) caused by a particle passing through an interference pattern (Woisetschläger 2010).

Combining the previous equations, the particle's velocity u can be written in terms of the wavelength λ, the angle β and the frequency f, equation (21):

$$u = f \frac{\lambda}{2 \sin \beta} \tag{21}$$

In the simple setup discussed so far the sign of the velocity is not available. From the recorded signal it is not possible to determine which way the particle passes the probe volume. To overcome this sign ambiguity one of the two laser beams is frequency shifted by a Bragg-cell (compare to chapter "*Density measurement techniques using laser interferometry*"). Introducing a fixed frequency shift to one beam leads to a linear change in the phase of one beam with respect to the other beam and this finally results in a fringe pattern system moving at constant velocity (40MHz for the employed LDV-system) (Lading et al. 1994). Figure 19 illustrates a LDV-system with an integrated Bragg-cell.

For particles not moving in the probe volume a beat frequency, which equals the frequency shift caused in the Bragg-cell is observed at the detector. If the direction of the moving fringe pattern system and the direction of the moving particle coincide, the detector frequency is reduced. If the particle moves in the opposite direction, compared to the direction of the moving fringe pattern, the detector frequency is increased. By means of this frequency shift the way the particle passes the probe volume is now determined (Lading et al. 1994).

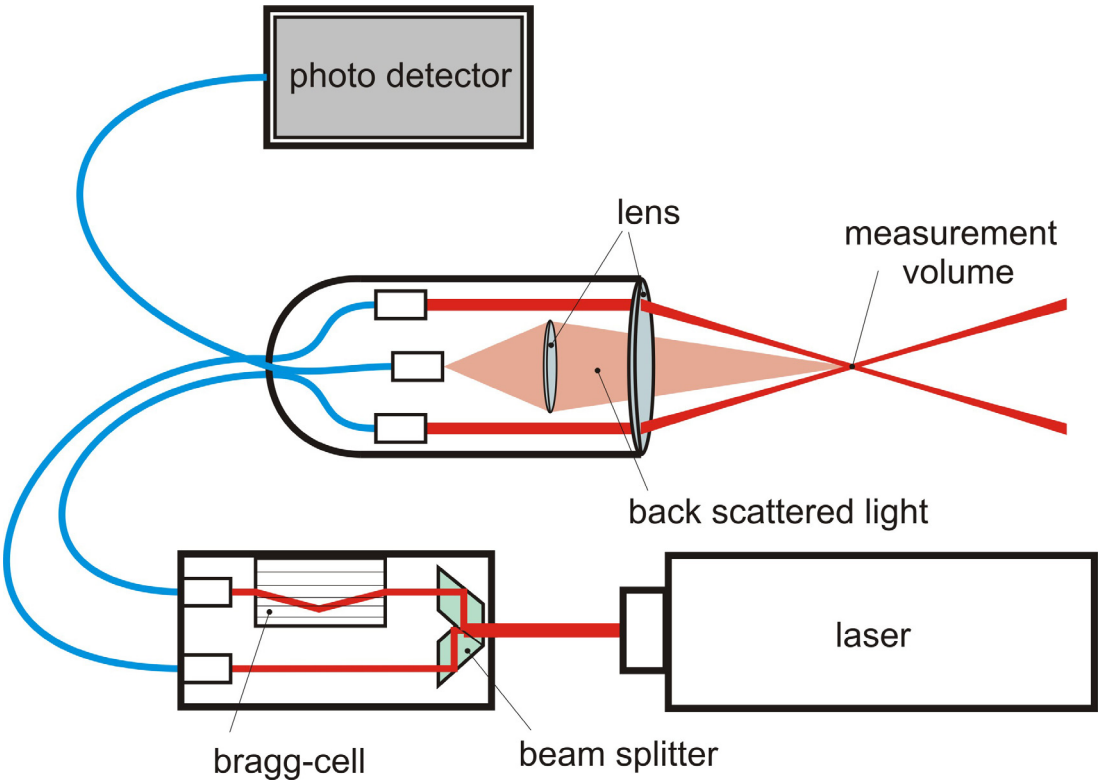

Figure 19: LDV-system with integrated Bragg-cell to overcome the sign ambiguity of the measured particle velocity. The figure illustrates a LDV-system that uses a signal recorded from the back scattered laser light to evaluate the velocity.

A disadvantage of LDV measurements is the fact that the fluid velocity is not measured directly, but the velocity of the seeded particles. Typical diameters of seeded particles are in the µm-range. These particles should follow the flow without a lag, but depending on their diameter and weight, they can not follow too high turbulence frequencies or circulation frequencies and therefore act as a low-pass filter. For this reason seeding particles should be small in the diameter. The scattering intensity of the seeding particles on the other hand strongly depends on their size and the angle between the light source and the detector. The scattering intensity gets stronger with an increasing particle diameter; therefore particles should have a larger diameter. Generally strongest signals are reached in the forward direction (Mie-scatter mode since the wavelength of laser light typically is in the range of 400-600 nm, and particle diameters in the range of µm), but modern, compact LDV-systems often collect the light scattered in the backward direction (Hassel and Linow 2000).

It should be mentioned that the above description of the system can also be given in terms of the Doppler shift of the light from the two inclined laser beams scattered at the tracer particle. This led to the appreciation of Christian Doppler in naming this measurement system.

In this work all velocity measurements were performed with a two-component LDV (DANTEC Fiber-Flow with DANTEC Burst Spectrum Analyser, DANTEC Dynamics, Roskilde, Denmark) fed by an argon ion laser (Coherent Inc., Santa Clara, CA) with wavelengths $\lambda = 488$ nm and 514.5 nm. The positioning of the optical head was done with a DANTEC Lightweight traverse. For control, acquisition and analysis of the collected data, DANTEC BSA Flow Software 1.2 was used.

3.3.2 Rayleigh- and Raman-scattering

Rayleigh- and Raman-scattering is often applied to determine temperatures and concentrations in combustion processes. Both scattering modes are non-resonant effects, in contrast to the often used laser induced fluorescence (LIF). Rayleigh-scattering is an elastic process, whereas Raman-scattering is an inelastic process at molecules, causing energy transitions and changes in the relative nuclear motions within a molecule (molecular rotations and vibrations). During Raman-scattering internal energy redistributions between the vibrational and/or rotational states of the molecules take place leading to a different quantum state of the molecules at the end of the process compared to the initial quantum state. Therefore the scattered light emitted by the molecules is shifted to either longer wavelengths, so called Stokes-Raman, or shorter wavelengths, so called Anti-Stokes-Raman (illustrated in figure 20).

The intensity of the Rayleigh signal $I_{Rayleigh}$, which appears at the same frequency as the incident light wave (elastic scattering), can be written in terms of the intensity of the incident laser light I_L, the Rayleigh-scattering cross-section $\left.\frac{\partial\sigma}{\partial\Omega}\right|_{Rayleigh,i}$ of species i and the molar fraction Y_i of species i:

$$I_{Rayleigh} = I_L \eta_{Rayleigh} V \rho \sum_i Y_i \left.\frac{\partial\sigma}{\partial\Omega}\right|_{Rayleigh,i} \qquad (22)$$

Additionally the Rayleigh-signal depends on the measurement volume V and the density ρ as well as $\eta_{Rayleigh}$, the total effectiveness of the detection system, see equation (22). The Rayleigh-signal can be used to determine the temperature if the averaged cross-section $\bar{\sigma}$ of a gas mixture

$$\bar{\sigma} = \sum_i Y_i \left.\frac{\partial\sigma}{\partial\Omega}\right|_{Rayleigh,i} \qquad (23)$$

is known.

If the dependence of the total Rayleigh-cross-section on the gas composition in the measurement volume is weak, the temperature can be estimated from the Rayleigh-signal only. Assuming ideal gas law, the molecular density is inversely proportional to the temperature at constant pressure and since the molecular density is connected to the Rayleigh-signal via equation (24), the intensity of the Rayleigh-signal is inversely proportional to the temperature too. If the signal intensity $I_{Rayleigh,0}$ is calibrated for a known temperature T_0, the temperature T can be calculated easily from the signal $I_{Rayleigh}$ (equation (24)).

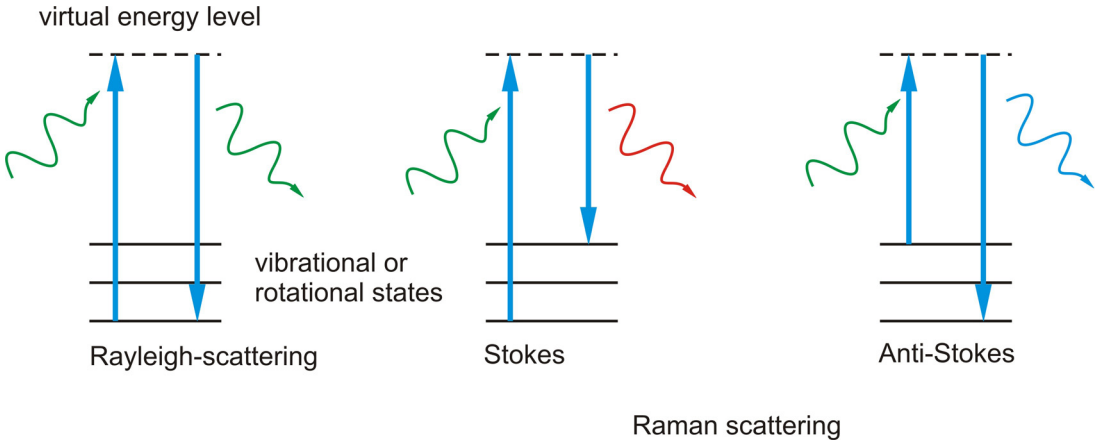

Figure 20: Rayleigh and Raman-scattering at a molecule.

$$\frac{T}{T_0} = \frac{\bar{\sigma}}{\bar{\sigma}_0} \frac{I_{Rayleigh,0}}{I_{Rayleigh}} \tag{24}$$

with

$$\bar{\sigma} = \sum_i Y_i \left.\frac{\partial \sigma}{\partial \Omega}\right|_{Rayleigh,i} \quad \text{and} \quad \bar{\sigma}_0 = \sum_i Y_{i,0} \left.\frac{\partial \sigma}{\partial \Omega}\right|_{Rayleigh,i,0} \tag{25}$$

In combustion processes, where the cross-section of fuels and oxidizer differs strongly, the gas composition in the measurement volume must be determined simultaneously to calculate temperatures correctly. Therefore Rayleigh-scattering is often combined with simultaneous measurements of Raman-scattering to evaluate the species concentration within the measurement volume (Hassel and Linow 2000).

Compared to Rayleigh-scattering the inelastic Raman-scattering is approximately three orders of magnitude weaker, but many signals are detected additionally to the incident laser light at lower and higher wavelength (Anti-Stokes and Stokes-Raman-signals). The internal energy redistribution in the molecule during Raman-scattering leads to wavelength-shifts characteristic for each kind of molecule, since molecular rotations and vibrations have discrete energy levels, varying for each species of molecules due to differences in the molecular bindings. Figure 21 presents vibrational Raman shifts for a number of molecules.

The intensity of the vibrational Raman-signal $I_{Raman,i}$ for a molecule species i depends on the Raman-scattering cross-section $\left.\frac{\partial \sigma}{\partial \Omega}\right|_{Raman,i}$, the molar fraction Y_i, and the laser intensity I_L (equation (26)). In this equation $A = \eta_i \Omega V$ denotes the apparatus performance and consists of the efficiency of the optics η_i, the angle of detection Ω, and the sample volume V. The Raman intensity additionally depends on the density of the scattering molecules ρ, which includes the temperature and the pressure. Additionally the Raman cross-section is temperature-dependent too.

$$I_{Raman,i} = A I_L \rho Y_i \left.\frac{\partial \sigma}{\partial \Omega}\right|_{Raman,i} \tag{26}$$

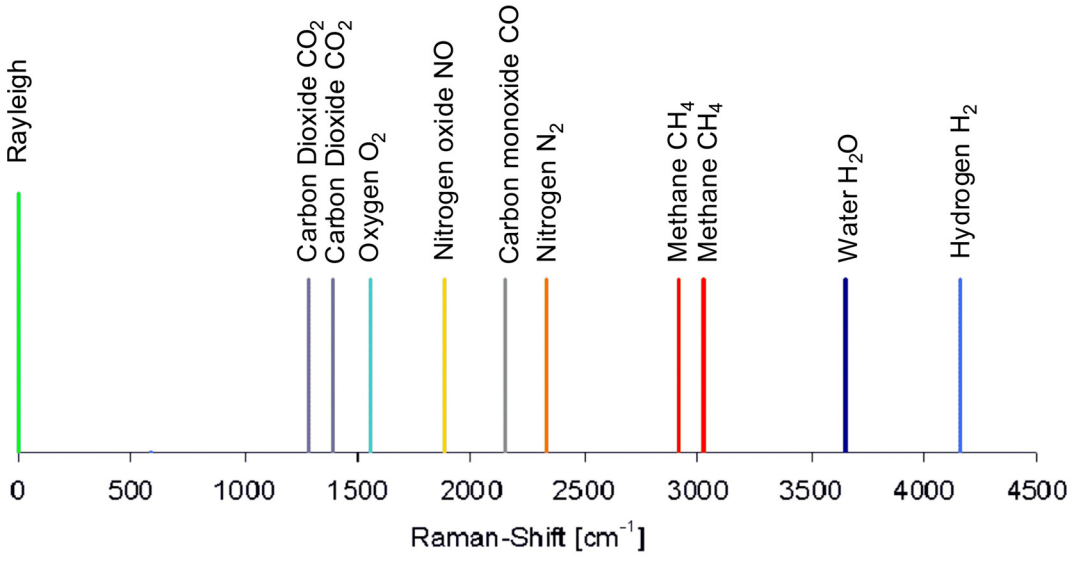

Figure 21: Vibrational Raman shifts for a number of gas molecules (Kirchweger 2007).

This temperature sensitivity of the Raman-signal enables the evaluation of the temperature via the ratio of the Stokes- and Anti-Stokes-Raman lines. However, at room temperature only the vibrational ground energy level of the molecules is populated and therefore the Anti-Stokes signal is very small or vanishes completely. In this case the temperature can not be calculated via the ratio between the Stokes- and the Anti-Stokes-intensities (Hassel and Linow 2000).

The measurement system applied in this work evaluates the temperature and species concentrations based on the combination of Rayleigh- and Raman-scattering processes. From the Raman-signals only the vibrational modes of the Stokes-signals are analysed in the evaluation process. The intensity of the recorded Rayleigh-signal is used to estimate the temperature by comparison to a reference spectrum of air. With the help of the estimated temperature molar fractions of the species within the measurement volume are calculated roughly due to the recorded Raman-intensities. Afterwards, the temperature is calculated again with the molar fractions provided by the Raman-intensities. This process is repeated until the temperature and concentrations from Rayleigh- and Raman-scattering are in good agreement, i.e. the iterative process converges (Hayashida et al. 2006).

The signal intensity of both scatter-modes, Rayleigh- and Raman-scattering, strongly depends on the wavelength of the applied laser light and is proportional to $1/\lambda^4$. For this reason the application of a laser emitting light in the ultra-violet range (UV) is advantageous, but the use of UV-light is crucial in diffusion flames, since it might lead to a broad and intense background noise caused by soot precursors. Changing the polarization direction of the laser beam and recording the spectrum with two different laser polarizations enables the separation of these background emissions from the Raman-signal as Raman-signals are highly polarized and background emissions are not polarized (Hassel and Linow 2000; Hayashida et al. 2006).

The Raman system applied in this work consisted of a single pulsed Nd-YAG laser (InnoLas, SpitLight 600, InnoLas Systems GmbH, Krailling, Germany) that emitted light at a frequency-tripled wavelength of 355 nm with a pulse duration of 7 ns, a spectrograph (PI/ACTON Spectra Pro-2300i, Princeton Instruments, Trenton, NJ) and an Intensified CCD camera (Nano Star S25, LaVision, Göttingen, Germany). For the measurements the laser beam was slightly focused into the flame by an achromatic lens (f = 500 mm). The scattered light was collected perpendicular to the laser beam by another achromatic lens with a focal length of f = 150 mm and imaged onto the entrance slit of the spectrograph passing a bandpass filter (LaVision, Göttingen, Germany) designed to transmit scattered light in the range of 370-450 nm only.

The setup is illustrated in figure 22. Data collection was done with DAVIS Flowmaster 7.1.1 (Lavision, Göttingen, Germany) and images were taken at each measurement position with the Nanostar camera for two different polarization directions of the laser beam, using a polarisation rotator (LaVision, Göttingen, Germany). Additionally an energy monitor (LaVision, Göttingen, Germany) was used to check the output power of the laser beam.

The data evaluation process, including averaging and calibration of the recorded images and the calculation of species concentrations and temperatures was done with DAVIS Flowmaster 7.1.1 as well. Since Raman signals are generally low in intensity the recording of a number of images for each measurement position is indispensable and averaging over a number of images has to be performed. Figure 23 shows an image of Rayleigh- and Raman-scattering recorded in a methane-air jet. In this case an averaged image is presented obtained from 50 single images and major species like O_2, N_2 and CH_4 can be identified. Additionally the Rayleigh signal can be seen in this figure.

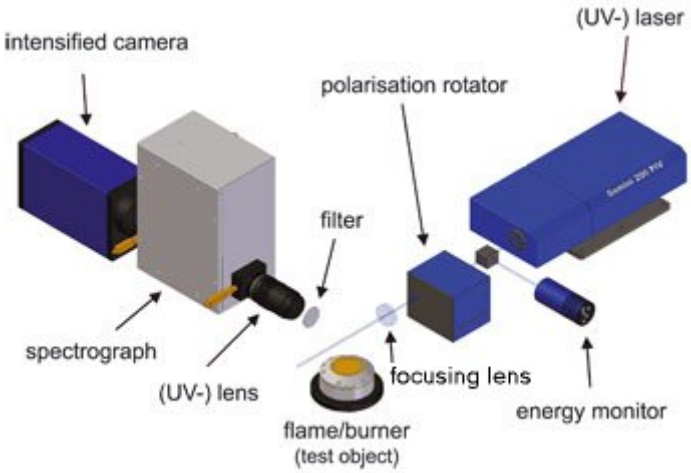

Figure 22: Rayleigh/Raman-scattering system. (Source: www.lavision.de)

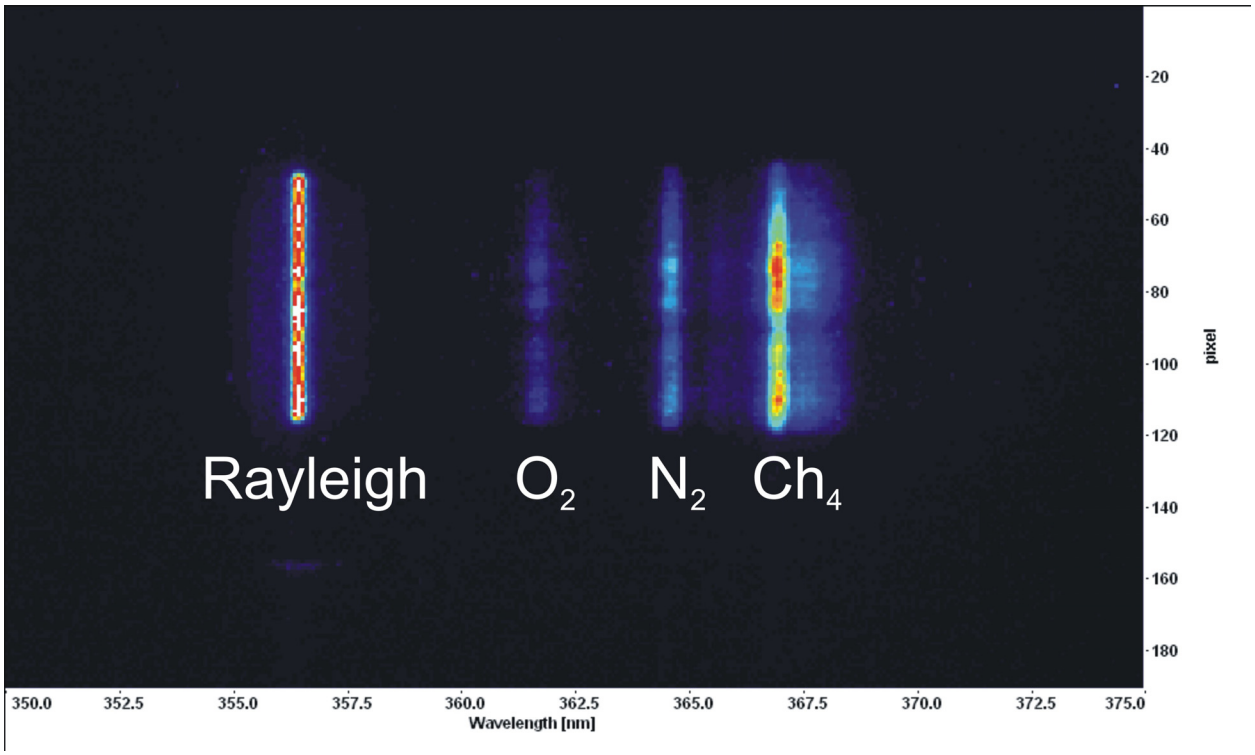

Figure 23: Image of Rayleigh- and Raman-scattering recorded in a methane-air jet. The image presents averaged data, calculated from 50 single images. The image is not calibrated to Raman-shifts yet, although major species can be identified using figure 21.

3.4 Chemiluminescence measurements

Measurements of flame chemiluminescence represent an interesting technique for combustion diagnostics. Chemiluminescence is the emission of light from electronically excited species generated by chemical reactions (e.g. radicals, see chapter 3.1.3 "*Optical measurement techniques for combustion diagnostics*"). The light is emitted, if the excited species relax to a lower energy state. The intensity of the chemiluminescence emission is a function of the concentration of the excited species, which is determined by the ratio of the production rate of the species to the collisional quenching reactions.

In hydrocarbon flames, e.g. methane, significant chemiluminescence emissions are due to CH^*, OH^*, CO_2^* and C_2^* and can be found at different characteristic wavelengths, depending on the excited species. The chemiluminescence emission from CH^* (431 nm), OH^* (309 nm), and C_2^* (519 nm) occur at distinct narrow wavelength intervals, whereas the CO_2^* (350-600 nm) chemiluminescence emissions extend over a broad wavelength interval (Lee and Santavicca 2003).

In a candle-flame, light is emitted in the visible range from colours blue to yellow, see figure 24. The emitted blue light can be ascribed to the CH^* emission and is found at the bottom region near the wick as indication of the flame front. Radiative emissions in the visible green range of the spectrum are due to the C_2^* radicals, but they are rather weak in a candle-flame. In most zones in the candle-flame, light is emitted ranging in colours from orange to yellow or almost white. These emissions are due to solid soot particles, resulting from incomplete combustion in the flame. The solid particles act like a blackbody radiator and emit light according to Planck's law (equation (27)), where I_λ denotes the spectral radiant emittance [1] ($Wm^{-2}\mu m^{-1}$) as a function of the temperature T, the wavelength λ and the constants h (Planck constant), c (speed of light) and k (Boltzmann constant).

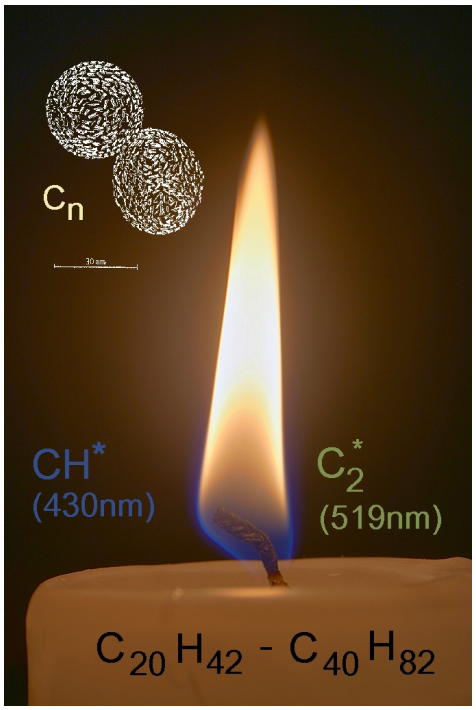

Figure 24: Radiative emission from a candle-flame in the visible range. While the faint blue and green radiation is from chemiluminescence, the orange-reddish gloom is blackbody radiation from soot particles (Heimel 2010).

The emittance of the soot particles is superimposed to the chemiluminescence emissions in the visible spectrum of CH^* and C_2^* and covers these emissions. To gain information on the combustion process, filters have to be applied to separate the emissions from the soot particles and emissions from the radicals in the flame.

[1] The term "Irradiance" is used when an incoming electromagnetic radiation hits a surface. "Radiant emittance" is used when the radiation emerges from a surface, both with dimension W/m^2). Here, the radiant emittance is integrated over all angles. $I_\lambda(T)[Wm^{-2}\mu m^{-1}] = \pi\, I_\lambda(T)[Wm^{-2}\mu m^{-1}sr^{-1}]$. It is also a "spectral radiant emittance", e.g. it depends on the wavelength.

$$I_\lambda(T) = \frac{2\pi hc^2}{\lambda^5\left(e^{\frac{hc}{\lambda kT}} - 1\right)} \cdot 10^{-6} \tag{27}$$

For combustion diagnostics the spatial distribution of the radiative emission intensity from the radicals is of great interest. The spatially-resolved intensity of chemiluminescence emissions can be used to localize the flame front (see chapter 3.1.3 "*Methane combustion*"). Furthermore the intensity of the chemiluminescence emissions may be used to estimate local and overall heat release rates, or for equivalence ratio sensing in flames (Lee and Santavicca 2003; Kojima et al. 2005; Nori and Seitzmann 2009).

The relationship between the local chemiluminescence emission I_{local} [Wm^{-2}] and the local rate of heat release $H_{R,local}$ [Wm^{-2}] is characterized by a power law, where the exponent α depends on the flame temperature and on the effects of unsteady strain and flame curvature (Lee and Santavicca 2003).

The flame temperature itself is a function of the equivalence ratio, unburned gas temperature, dilution, and radiation losses in the flame.

$$I_{local} \propto \left(H_{R,local}\right)^{\alpha} \tag{28}$$

Thus, α is a positive number and depends on the flame temperature as determined by the equivalence ratio[2], unburned gas temperature, dilution and radiative losses. For a fixed equivalence ratio and negligible effects of strain and flame curvature, the overall intensity of chemiluminescence emissions from a flame increases linearly with the fuel flow rate. In this case the overall chemiluminescence emissions $I_{overall}$ can be written in terms of a constant C and the overall heat release rate $H_{R,overall}$, equation (29) (Lee and Santavicca 2003).

$$I_{overall} = CH_{R,overall} \tag{29}$$

The pre-condition constant flame temperature limits the application of chemiluminescence emissions for heat release measurements more or less to premixed flames. In partially premixed turbulent flames the equivalence ratio generally varies over the flame area and affects the flame temperature. This temperature distribution leads to a varying exponent α over the flame area and affects the relationship between the local heat release rate and local chemiluminescence emissions according to equation (28). The overall heat release rate in a partially premixed flame can only be evaluated based on the overall chemiluminescence emissions if an averaged equivalence ratio over the flame area is estimated (Lee and Santavicca 2003).

Furthermore the dependency on the equivalence ratio is critical if the overall chemiluminescence emissions are used to investigate the overall heat release rate in an unstable combustion process. Changes in the fuel flow rate and changes in the equivalence ratio alter the chemiluminescence emissions independently, but only a varying fuel flow rate alters the overall heat release rate. For example, if only the airflow fluctuates in a combustion chamber, but the fuel flow remains constant, the overall heat release rate does not change, but the overall chemiluminescence emissions fluctuate due to changes in the equivalence ratio. If the airflow and the fuel flow oscillate, fluctuations in the chemiluminescence emissions derive in part from changes in the overall heat release rate and in part from changes in the equivalence ratio. In an unstable combustion process the overall chemiluminescence emissions can be attributed solely to the overall heat release only, when the equivalence ratio does not change (e.g. premixed flames).

[2] ratio of the fuel-to-oxidizer ratio to the stoichiometric fuel-to-oxidizer ratio

Therefore, in this work chemiluminescence emissions were used as a qualitative measure of local heat release and to characterize temporal fluctuations in the overall heat release rate qualitatively in combustion processes in terms of frequency spectra.

3.4.1 Analysis of flame dynamics by means of chemiluminescence emission

Using a high-speed camera to visualize the combustion process is a simple and convenient technique to analyse the flame dynamics by means of chemiluminescence emissions. To describe the flame dynamics in premixed methane flames qualitatively, it suffices to record the chemiluminescence emissions in the visible blue spectrum only. For combustion analysis periodical fluctuations in the chemiluminescence emissions are of great interest as they are related to combustion instabilities, which might occur at certain frequencies.

Therefore the chemiluminescence emission intensity is recorded by a high-speed CCD-camera (figure 25) and the overall intensity is calculated for each single frame, leading to a time signal of overall emission intensities. In a next step a Fourier analysis is applied to the time signal and a frequency spectrum of the fluctuating emissions due to the combustion process is obtained. Since combustion instabilities emerge also at high frequencies, the applied camera must be capable to record at a high frame rate. According to the Nyquist sampling theorem the sampling frequency must be at least twice of the maximum component frequency of the signal being sampled, and additionally the camera has to be sensitive enough to record small differences in the intensity (radiant emittance) between the single frames (Heimel 2010).

At this point a short excursion to signal theory, especially to the principles of the Fourier transform and Fourier analysis, is given, since these tools are fundamental for the measurement technique described here and some of the measurement techniques discussed in the subsequent chapters.

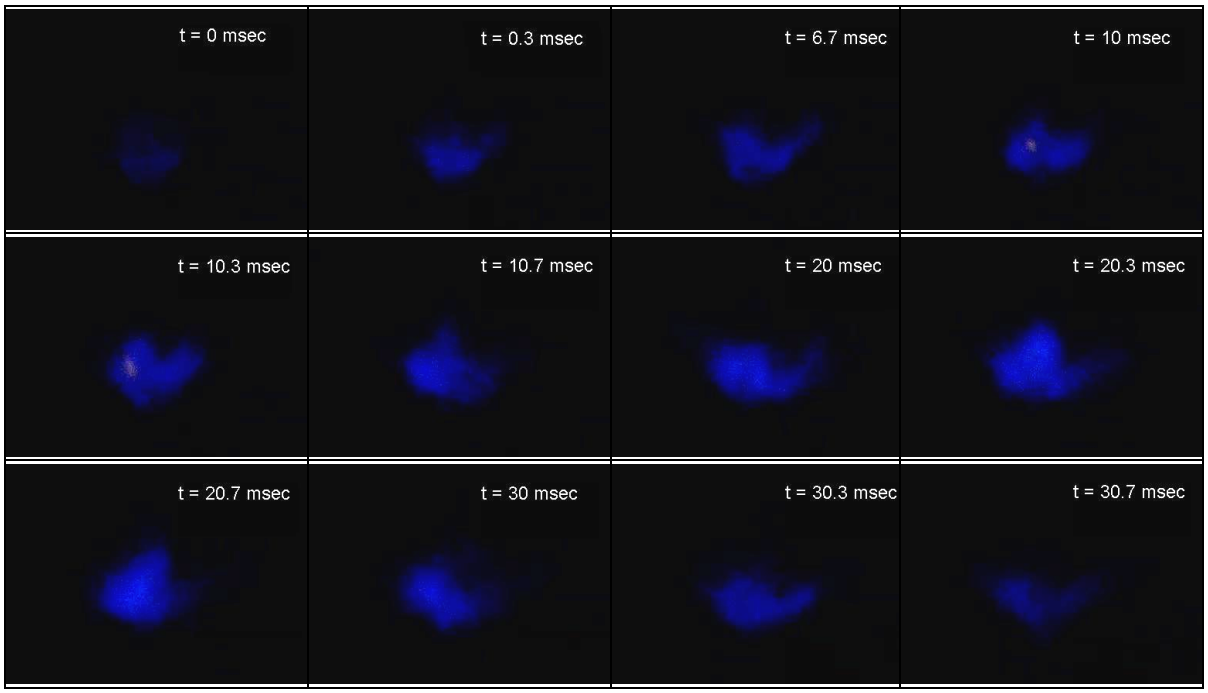

Figure 25: Fluctuations of chemiluminescence emissions in a premixed swirl-stabilized methane-air flame recorded by a high-speed CCD-camera (Heimel 2010).

Fourier transform and Fourier analysis

Applying a Fourier transform, the time domain representation of a signal is transformed to its frequency domain representation. The Fourier transform thereby decomposes a signal into oscillatory functions by correlation of the time signal with complex oscillations $e^{-i2\pi ft}$, according to equation (30).

$$F_t(f) = \int_{-\infty}^{\infty} X(t) \cdot e^{-i2\pi ft}\, dt \tag{30}$$

Applying this algorithm to a time signal *X(t)*, a complex number $F_t(f)$ is calculated for each frequency *f*, leading to the complex amplitude spectrum. Its magnitude denotes the strength of the oscillation and the complex angle denotes the phase of the oscillation. The original time signal *X(t)* can be reconstructed from $F_t(f)$ by the inverse transform in equation (31).

$$X(t) = \int_{-\infty}^{\infty} F_t(f) \cdot e^{i2\pi ft}\, df \tag{31}$$

In reality the Fourier transform can not be applied to infinite time signals. Therefore the Fourier transform is performed with time signals of a finite length and period time *T*, so called samples, leading to equation (32). The magnitude of this spectrum now depends on the sample length *T*.

$$F_t(f,T) = \int_{0}^{T} X(t) \cdot e^{-i2\pi ft}\, dt \tag{32}$$

The power density spectrum (also called power spectrum) P_t, defined according to equation (33), characterizes the strength of the respective oscillations and is rather taken into account than the amplitude spectrum. The power density spectrum is determined by the product of the Fourier transform $F_t(f,T)$ and the complex conjugate of $F_t(f,T)$*, which is marked by the asterisk. The division by *T* in equation (33) eliminates the dependency of the power density spectrum P_t on the sample length and leads to a power density spectrum with the physical unit [PUT^2 Hz^{-1}] in accordance to the physical unit of the respective time signal [PUT], e.g. [Wm^{-2}].

$$P_t(f) = \frac{1}{T}\left|F_t(f,T)\right|^2 = \frac{1}{T} F_t(f,T) \cdot F_t(f,T)^* \tag{33}$$

For a single frequency, no relevant physical analogy can be found for the power density spectrum, but the integral over a certain region of frequencies corresponds to the power of the standard deviation (also known as the rms-value) for a time signal *X(t)* (equation (34)). The relationship between the power density spectrum, the integral of the power spectrum over a certain region and the corresponding time signal are presented in figure 26.

$$\sigma^2 = \int_{f_1}^{f_2} P_t(f)\, df \tag{34}$$

For most experimental measurements the recorded time signals are digitalized by an A/D-converter. Therefore the numerical calculation of the Fourier transform is done by a discrete Fourier transform (DFT) algorithm. Generally the fast Fourier transform algorithm (FFT) is chosen. The FFT algorithm transforms a sequence of N values from a discrete time series into a complex spectrum of N values in the frequency domain and is optimized for sample lengths $N=2^m$. A detailed description of the FFT algorithm can be found in (Newland 1975).

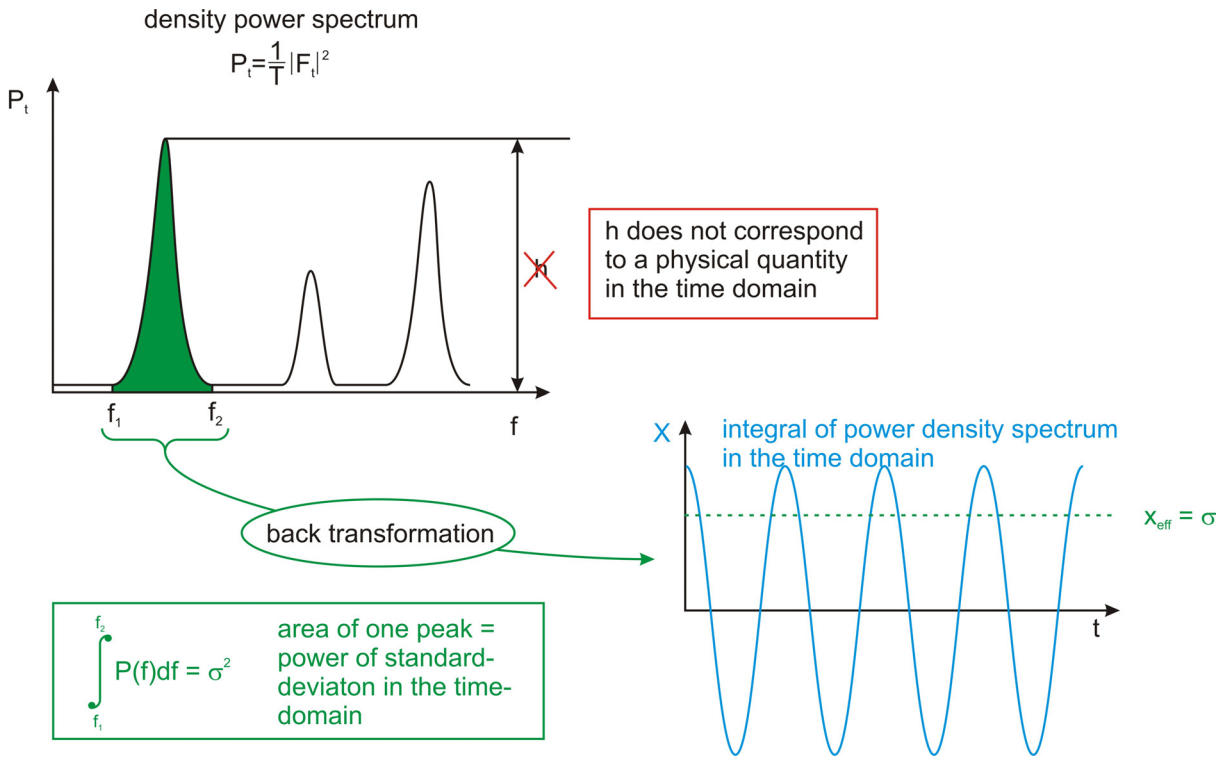

Figure 26: Information on the power spectrum. The area of one peak, the integral over a frequency range from f_1 to f_2 corresponds to the power of the standard deviation (Hampel 2005).

Figure 27 presents a flowchart for a discrete Fourier transform. First the analogue measurement signal is digitalized; i.e. measurement values are sampled at a regularly spaced time interval t. Performing an FFT with a discrete time series of a certain length T results in a complex spectrum with the same length. The first entry in the complex frequency spectrum expresses the average value of the sample. The second entry indicates the strength of the oscillation at the fundamental frequency f_g, which is linked to the sample length by $f_g = 1/T$. The following entries in the spectrum describe the strength of the oscillations for certain frequencies f_g *n with n=1, 2, 3…

The Nyquist frequency f_{NY} indicates the highest frequency that can be detected, and equals half of the sampling frequency f_s. This is important if measurement techniques based on frequency analysis are applied. The sampling frequency must be high enough to cover the complete frequency range of the time series; otherwise the calculated spectrum will differ from the true spectrum because of aliasing (Newland 1975).

For a time signal $X(t)$ in its discrete form

$$X_k = X(t_k) \qquad t_k = k\Delta t \qquad k = 0,\quad 1,\quad 2,\ldots,\quad (N-1) \tag{35}$$

with N sample values, the frequency spectrum with N frequency bins of strength F_n and frequency f_n, where f_n is defined by

$$f_n = \frac{n}{N\Delta t} \tag{36}$$

is calculated according to equation (37) and the inverse transformation is calculated according to equation (38).

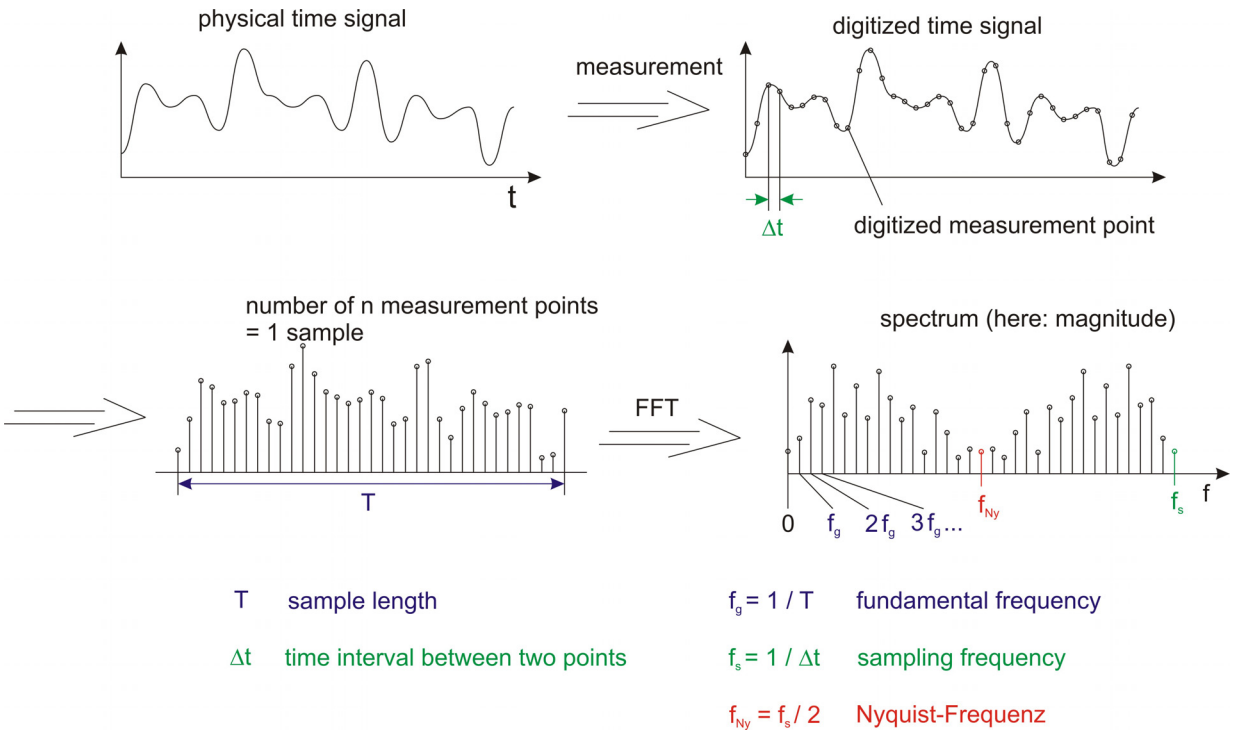

Figure 27: Discrete Fourier transform for a digitalized physical time signal. Characteristic frequencies for the Fourier transform are illustrated.

$$\text{DFT:} \qquad F_n = \frac{1}{N}\sum_{k=0}^{N-1} X_k e^{-\frac{2\pi k n}{N}} \tag{37}$$

Furthermore it is important to notice that the FFT algorithm operates with number series and does not take into account the fundamental frequency f_g. Therefore the physical units for the continuous and the discrete power spectrum differ, according to table 1.

$$\text{IDFT:} \qquad X_k = \sum_{n=0}^{N-1} F_n e^{\frac{2\pi k n}{N}} \tag{38}$$

Table 1: Comparisons of continuous and discrete Fourier transform.

continuous	⇔	discrete
t	time parameter	k
f	frequency	n or f
$F_t(f,T)$	complex spectrum	$F(f)$
$P_k(f) = \frac{1}{T}\lvert F_k(f,T)\rvert^2$	power spectrum	$P(f) = \lvert F(f)\rvert^2$
[PUT^2 Hz^{-1}]	$P_k \approx T \cdot P(f) = \frac{P(f)}{f_g}$	[PUT^2]
$\sigma^2 = \int_{f_1}^{f_2} P_t(f)df$	power of rms-value	$\sigma^2 = \sum_{n=0}^{N-1} P(f)$

3.4.2 Local chemiluminescence emissions for local heat release indication

Besides using chemiluminescence emissions to characterize temporal fluctuations in the overall heat release rate, chemiluminescence emissions are also considered as a measure of the local heat release rate under the restrictions discussed at the beginning of this chapter. Therefore local data of chemiluminescence must be linked to the local heat release rate via equation (28). Since chemiluminescence emissions measurement is a line-of-sight measurement technique it can only provide local data in combination with tomographic reconstruction techniques. A local distribution of chemiluminescence is reconstructed from integral line-of-sight chemiluminescence emissions data, applying these techniques.

However it should be noticed that 'local' data of chemiluminescence emissions $I_{3\text{-}D}$ [Wm^{-3}] obtained by the tomographic reconstruction technique from within a volume do not actually equal the 'local' chemiluminescence intensity I_{local} [Wm^{-2}], as defined by (Lee and Santavicca 2003). Both can be related by the integral of all emissions along the line of sight (here defined by a s-coordinate).

$$I_{local} = \int_{s} I_{3-D}\, ds \tag{39}$$

The rate of heat release $H_{R,3\text{-}D}$ is defined in the same way (equation (40)).

$$H_{local} = \int_{s} H_{3-D}\, ds \tag{40}$$

The relationship between the local chemiluminescence emissions $I_{3\text{-}D}$ and the local heat release rate $H_{R,3\text{-}D}$ can be written in terms of the constant C (with help of equation (28), (39), and (40)). C again depends on the flame temperature in the emission zone and all effects that alter the flame temperature.

$$\int_{Volume} I_{3-D} = C \int_{Volume} H_{R,3-D} \tag{41}$$

Therefore the intensity of the local chemiluminescence emissions by tomographic reconstruction can be used to estimate the rate of heat release but with the aforementioned constraints discussed at the beginning of this chapter.

Tomographic reconstruction techniques

For reconstruction purpose there are several different reconstruction algorithms available, but most of them are based on the Radon transform. The so called Radon transformation describes the relation between an integral data distribution $h(p,\theta)$, also called projection data, and the corresponding local distribution $f(r, \varphi)$ (see figure 28). The projection data for a distinct viewing direction can be calculated for a given spatial distribution according to equation (42), by integrating the local data along the line-of-sight.

Equation (42) exactly describes the transaction that takes place during the measurement of the chemiluminescence emissions. The local chemiluminescence emissions $I_{3\text{-}D}$ are integrated along the viewing direction and recorded by a detector, e.g. a spectrograph or a CCD-camera.

$$h(p,\theta) = \int_{-\infty}^{\infty} f\left(\sqrt{p^2+s^2}, \arctan\left(\frac{s}{p}\right)+\theta\right)\cdot ds \tag{42}$$

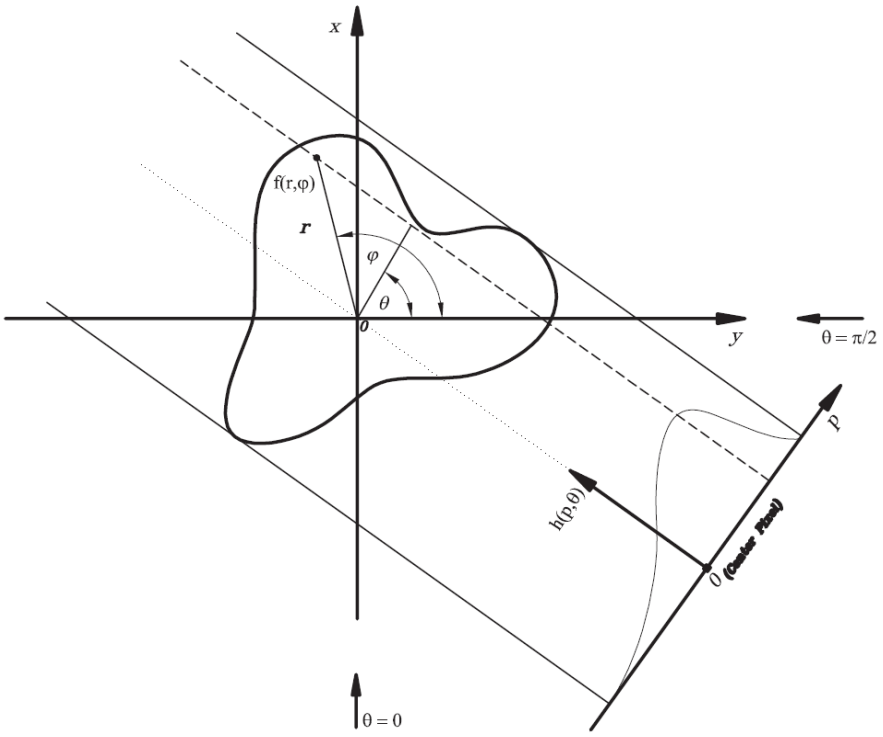

Figure 28: Relation between integral data distribution h(p,θ), also called projection data, and the local distribution f(r,φ) for one specific viewing direction (Hipp and Reiterer 2003).

So projection data are measured directly, but no information on the spatial distribution is gained. In this case the inverse Radon transform, that reconstructs the spatial distribution *f(r, φ)* from the projection data *h(p,θ)* is of greater interest. According to equation (43), the application of the Radon inversion to determine the spatial distribution exactly would require an infinite number of projections from different viewing directions in the range between 0° and 360°; hence this transform can not be applied directly to the measurement data. Therefore a number of different numerical approaches have been developed to solve this problem.

$$f(r,\varphi) = \frac{1}{2\pi^2} \int_0^{\pi} \int_{-\infty}^{\infty} \frac{1}{r \cdot \cos(\theta - \varphi) - p} \frac{\partial h(p,\theta)}{\partial p} \cdot dp \cdot d\theta \qquad (43)$$

In this work two different methods, the convolution method and the algebraic reconstruction technique (ART), have been used to obtain spatially distributed data of chemiluminescence emissions.

Convolution method

The convolution method approximates the Radon inversion by applying a mathematical operation called convolution to eliminate the calculation of the derivation within the integral, which is critical for discrete measurement data. This method is also known as "*Filtered back projection with Convolution*", since the convolution itself always has a filtering effect on the data. The procedure for this method consists of:

- a differentiation of the projection data *h(p,θ)* to *h'(p,θ)*.
- an Hilbert transformation of *h'(p,θ)*
- finally a back-projection

The differentiation and the Hilbert transformation are approximated by a convolution of projection data (equation (44)),

$$f^*(r,\varphi) = \lim_{A\to\infty} \int_0^{\pi} d\theta \int_{-\infty}^{\infty} h(p,\theta) q_A(r\cos(\theta-\varphi)-p)dp \tag{44}$$

with a fixed convolving function (equation (45)).

$$q_A(u) = 2\int_0^{A/2} UF_A(U)\cos(2\pi Uu)dU \tag{45}$$

$F_A(U)$ refers to a function window, that has to satisfy the following restrictions:

$$\begin{aligned} &0 < F_A(U) < 1 \quad \text{for } U < A/2 \\ &F_A(U) = 0 \qquad \text{for } U \geq A/2 \\ &\lim_{A\to\infty} F_A(U) = 1 \end{aligned} \tag{46}$$

In the IDEA software[3] (Hipp et al. 2004; Hipp et al. 1999) deployed in this work the following generalized Hamming window function is implemented for $F_A(U)$ (Hipp and Reiterer 2003):

$$F_A(U) = \alpha + (1-\alpha)\cos\left(\frac{2\pi U}{A}\right) \text{ for } 0{,}5 < \alpha < 1 \tag{47}$$

If the convolution method is applied some restrictions must be taken into account. The algorithm needs equidistant projection angles between projection data from different viewing directions. Additionally the quality of the back-projected data strongly depends on the number of projection data.

Equation (48) provides a simple estimation for the number M of projections necessary to receive the same bandwidth of spatial frequencies $\Delta\nu$ within an area of radius R for the tomographic reconstruction as for the projection data.

$$M = 2\pi R\Delta\nu + 1 \tag{48}$$

Another restriction results from the fact that the tomographic reconstructions using integral line data as projection input need uniform boundary values in all projections and in the reconstructed field. A limited field of view therefore inhibits tomographic data reconstruction, which is often the case in combustors.

Algebraic reconstruction technique (ART)

The second reconstruction-method, called ART, features a completely different approach to approximate the Radon inversion. The Radon inversion is therefore simplified to a linear equation system (equation (49)), where y denotes a vector of the measured projection data (image vector), x the data to reconstruct, and the matrix R_{ij} containing intersections of the probing beam with the j^{th} pixel in the image vector, hitting the i^{th} element of y. The error-vector e represents the deviation of real data from approximated data.

$$y_i = R_{ij}x_j + e_i \tag{49}$$

The equation system is solved using an iterative procedure called the relaxation method for inequalities (Hipp and Reiterer 2003). The mathematical background of this approach exceeds the scope of this work and a detailed description can be found in (Herman 1980). The final relations used for the ART in the IDEA-software are presented in equation (50) and (51).

[3] Download from http://optics.tugraz.at

$$x_i^{(k+1)} = x_i^{(k)} + vc_i^{(k)} r_i$$
$$u_i^{(k+1)} = u_i^{(k)} + c_i^{(k)}, \; u^{(0)} = 0 \tag{50}$$

Here, i refers to the index for a data element within a single projection and k denotes the number of overall iteration, while r_i denotes a vector including all intersections for a beam on its way to the i^{ths} data in this certain projection with pixels included in x. The vector product of r_i with x equals the length of the beam's path through the reconstruction beam, λ denotes the relaxation parameter, and ε is a positive infinite small number. The denominator in equation (51) includes the squared norm of r_i, which is the sum off all squared element values, and v is a constant representing relation of variances of x and e.

$$c_i^{(k)} = \lambda^{(k)} \frac{v\left(y_i - \left\langle r_i x^{(k)} \right\rangle\right) - u_i^{(k)}}{1 + v^2 \left\| r_i \right\|^2} \tag{51}$$

with

$$0 + \varepsilon \le \lambda^{(k)} \ge 2 - \varepsilon$$

Compared to the Convolution method the ART is not restricted to equidistant projection angles, but the computing time for the ART-algorithm exceeds the computing time required for the convolution method. Detailed information on both methods can be found in (Herman 1980; Hipp and Reiterer 2003; Hipp et al. 2004).

3.5 Density measurement techniques using laser interferometry

3.5.1 Interferometry basics

Laser optical interferometric measurement techniques are common tools in experimental fluid dynamics. These measurement systems are based on the ability of laser light to interfere, i.e. two or more laser light waves can combine with each other, either constructively or destructively in accordance to their relative phase to each other. For two laser beams the intensity I of the resultant wave depends on the intensities I_1 and I_2 of the respective waves as well as the phase difference $\Delta\varphi$ (equation (52)) between the two waves.

$$I = I_1 + I_2 + 2\sqrt{I_1 I_2}\cos(\Delta\varphi) \tag{52}$$

According to equation (52), maximum (I_{max}) or minimum (I_{min}) intensities can be identified within the interference field. Thus a modulation depth m can be defined, with m serving as a degree for the relative strength of the interference (equation (53)).

$$m = \frac{I_{\max} - I_{\min}}{I_{\max} + I_{\min}} = \frac{2\sqrt{I_1 I_2}}{I_1 + I_2} \tag{53}$$

To perform experimental investigations based on interference phenomena, a coherent source of light is needed. Generally coherence describes a correlation between physical quantities of a wave. Here a phase correlation between different wave packets is understood, enabling temporally and spatially constant interference. Thus coherent light is characterized by a fixed relation of the phase between different wave packets during interference. Light, defined as an electromagnetic wave, is regarded to be coherent, if a more or less strong correlation between the instantaneous values of the electric field on the same place at different times (temporal coherence) or at the same time at different places (spatial coherence) can be found.

To produce interference for the experiments in this work it was necessary that the interfering beams stem from the same source and were generated by wave front division after being emitted from the light source by a beam splitter. The maximal delay distance and the maximal delay time between two laser beams (generated by wave front division), for which interference is still observed, are called coherence-length and coherence-time, respectively. Some typical values for coherence-time and coherence-length for different laser light sources can be found in (Oertler sen. and Oertler jun. 1989). Contrary to sunlight, which is practically incoherent (coherence length in the µm range), laser light possesses the aforementioned characteristics and emits coherent wave packets with long coherence-lengths, usually in the centimetre range.

Measurement systems relying on these characteristics of the laser light are called interferometers. The light is emitted by a laser and split into two beams by a beam splitter. Then both beams pass a certain distance and are superimposed afterwards. According to the difference in the path length between the two beams, constructive or destructive interference takes place, according to figure 29. If the path length of a single beam changes by one wavelength compared to the path length of the other beam, a complete period of the amplification- and annihilation-cycle takes place. Measuring the intensity of the superimposed wave then allows the determination of changes in the geometrical beam length with high precision.

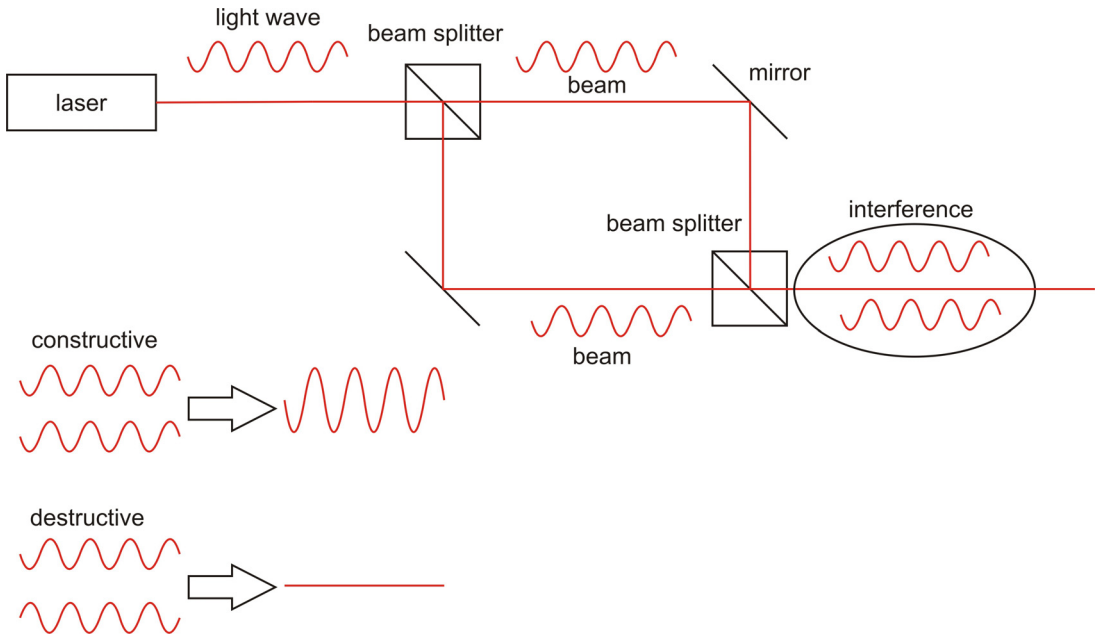

Figure 29: Interferometry basics. Constructive or destructive interference takes place according to the difference in the path length between the two laser beams.

The measured phase difference between both beams is not only dependent on changes in the geometrical beam path; furthermore it is affected by changes in the light propagation characteristics along the beam path. Thus the optical beam path length l_{opt} is defined, which takes into account the geometrical beam path z and changes in the refractive index $n(z)$ along the beam path (equation (54)).

$$l_{opt} = \int_z n(z)dz \tag{54}$$

Now the phase for a light wave φ with a fixed wave length λ_0 can be calculated for a certain distribution of the refractive index $n(z)$ according to equation (55).

$$\varphi = \frac{2\pi}{\lambda_0} l_{opt} = \frac{2\pi}{\lambda_0} \int_z n(z)dz \tag{55}$$

The phase difference $\Delta\varphi$ between both beams from equation (52) written in terms of l_{opt} leads to equation (56).

$$\Delta\varphi(t) = \frac{2\pi}{\lambda_0}\left[\int_{object} n(z,t)dz - \int_{reference} n(z)dz\right] \tag{56}$$

In gases the refractive index n is linked to the density via the Gladstone-Dale constant G (equation (16), chapter 3.2 "*Shadowgraph- and schlieren-visualization*"). Substituting the optical path length in equation (56) by the Gladstone-Dale equation then relates the phase difference to the density (equation (57)).

$$\Delta\varphi(t) = \frac{2\pi}{\lambda_0}\left[\int_{object} (G\rho(z,t)+1)dz - \int_{reference} (G\rho(z)+1)dz\right] \tag{57}$$

It must be noticed that the Gladstone-Dale relation is only valid for low to medium gas pressure levels. At high gas pressure levels the interaction between the molecules can not be neglected any more due to the small distances between the molecules and the Gladstone-Dale relation is not valid any more. Additionally the Gladstone-Dale constant depends on the gas composition and the utilized laser light. Therefore in gas mixtures the concentration of the

present gases must be known to determine the density distribution precisely (Oertler sen. and Oertler jun. 1989).

If the geometrical path lengths of both beams equal, equation (57) simplifies to

$$\Delta\varphi(t) = G\frac{2\pi}{\lambda_0}\int_z \Delta\rho(z,t)dz - \varphi_0 \tag{58}$$

where φ_0 includes all temporal constant parts of the phase, referenced to one beam usually called the reference beam, while the test or object beam contains the test or object zone.

Equation (58) indicates that interferometry is only capable to determine relative changes in the measured variable. To receive, for example, an absolute density distribution, the absolute density in a reference point must be known. According to equations (52)-(58) interferometry does not provide local data innately. To receive spatially-resolved data, interferometry has to be applied in combination with tomography either, or two special interferometers, so called laser vibrometers (LV), are used together with a correlation technique.

3.5.2 Differential interferometry (Shearography)

Differential interferometry (also referred to as shearography or shearing interferometry) is commonly used to measure density gradients in flows. The measurement technique is based on the detection of the phase shift by slightly displacing a wave against itself before or after passing through a transparent medium and comparing these two slightly displaced waves in an interferometer. Thereby a lateral change in density in the direction of the wave front shear is measured. Basically this could be accomplished by two different setups. One way is to send two slightly sheared waves through the measurement area and superimpose them afterwards. For the second setup, a single wave front passes the test object and is sheared against itself and superimposed afterwards in an interferometer. Setup 2 was used in all experiments performed in this work (figure 30).

For a single wave front passing the test object, the phase $\varphi(x,y)$ is linked to the density distribution $\rho(x,y,z)$ in the flow-field according to equation (59), with the x- and y-coordinate perpendicular to the beam direction z. In this derivation the Galdstone-Dale constant G is assumed to be constant in the measurement area, otherwise the different gas-component concentrations- and temperature-distributions are needed to calculate the distribution of the Gladstone-Dale constant in the flow-field.

$$\varphi(x,y) = \frac{2\pi}{\lambda_0}\int_{z_1}^{z_2}\left(G\rho(x,y,z)dz + 1\right)dz \tag{59}$$

For further evaluation only the y-direction, in which the wave front is sheared against itself is taken into account. The plane wave front of coherent light, emitted by a laser, is distorted due to the density distribution (distribution of the refractive index n) within the test object (figure 31).

The phase difference $\Delta\varphi(y)$ between two different positions y_0 and y_1 can be written in terms of the density distribution $\rho(y,z)$ along the beam path z according to equation (60).

$$\Delta\varphi = \varphi_0(y_0) - \varphi_1(y_1) = \frac{2\pi}{\lambda_0}\int_{z_1}^{z_2}\left(G\rho(y_0,z)dz + 1\right)dz - \frac{2\pi}{\lambda_0}\int_{z_1}^{z_2}\left(G\rho(y_1,z)dz + 1\right)dz \tag{60}$$

In a next step the distorted wave front is sheared against itself by the small distance δ. Now each point of the wave front interferes with a neighbouring point at distance δ and the phase difference $\Delta\varphi(y)$ can be written in terms of this distance δ (equation (61)).

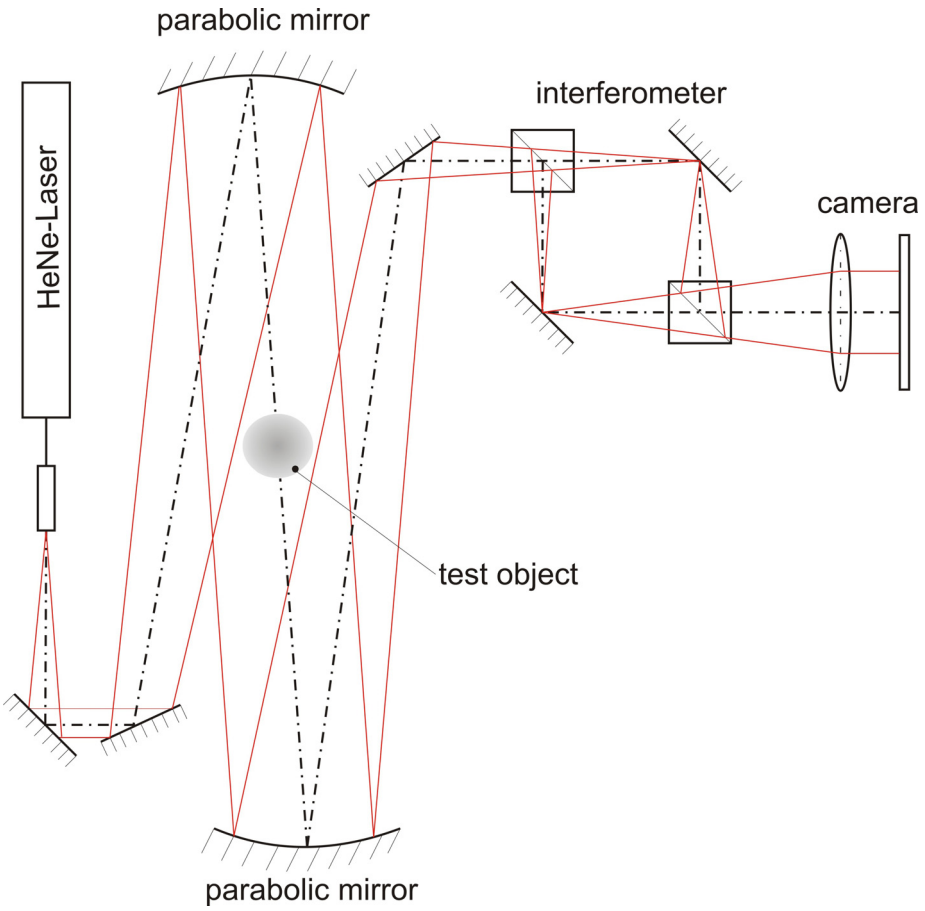

Figure 30: Experimental setup for differential interferometry.

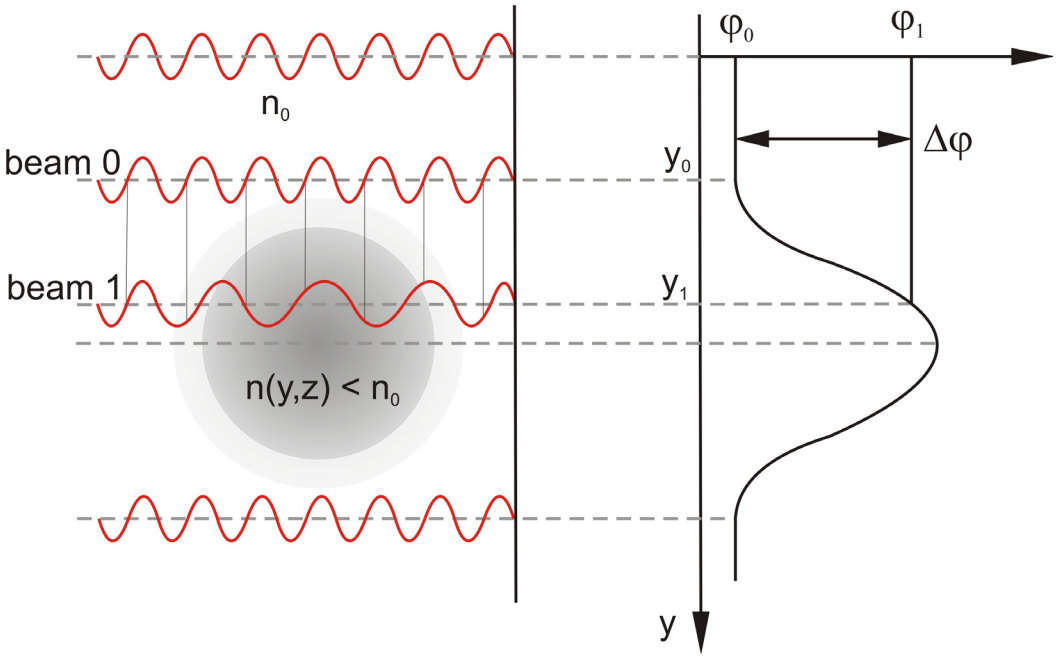

Figure 31: Phase difference between light waves due to changes in the refractive index in the measurement area.

$$\Delta\varphi(y) = \frac{2\pi}{\lambda_0} G \int_{z_1}^{z_2} \left(\rho\left(y - \frac{\delta}{2}, z \right) - \rho\left(y + \frac{\delta}{2}, z \right) \right) dz \tag{61}$$

As the measured phase difference is always related to the shear adjusted, dividing both sides of equation (61) by δ leads to equation (62).

$$\frac{\Delta\varphi(y)}{\delta} = \frac{2\pi}{\lambda_0} G \int_{z_1}^{z_2} \frac{\left(\rho\left(y - \frac{\delta}{2}, z \right) - \rho\left(y + \frac{\delta}{2}, z \right) \right)}{\delta} dz \tag{62}$$

Now it should be noted that the direction of the adjusted shear δ automatically defines the direction of the measured density gradient (in this case the *y*-coordinate). Therefore the shear on the right side of equation (61) is replaced by Δy (equation (63)),

$$\frac{\Delta\varphi(y)}{\delta} = \frac{2\pi}{\lambda_0} G \int_{z_1}^{z_2} \frac{\left(\rho\left(y - \frac{\Delta y}{2}, z \right) - \rho\left(y + \frac{\Delta y}{2}, z \right) \right)}{\Delta y} dz \tag{63}$$

and with Δy sufficiently small this phase shift is proportional to the first derivative of phase or density (equation (64)) (Woisetschläger et al. 1998; Pretzler et al. 1993).

$$\frac{\Delta\varphi(y)}{\delta} \approx \frac{2\pi}{\lambda_0} G \int_{z_1}^{z_2} \frac{\partial\rho}{\partial y} dz \text{ for } \delta << \tag{64}$$

The phase difference $\Delta\varphi(y)$ in this equation is directly obtained by analyzing the interferograms (figure 32), the displacement δ has to be evaluated separately.

The optical setup for differential interferometry is illustrated in figure 30. A parallel, expanded laser beam passes the measurement object and is focused on the mirrors of a small Mach-Zehnder interferometer afterwards. In the interferometer the two wave fronts are sheared against each other by tilting one of the mirrors (figure 33). The sensitivity of the interferometric system can be changed by adjusting the wave front shear δ, tilting one mirror. This variable sensitivity is the main advantage of differential interferometry.

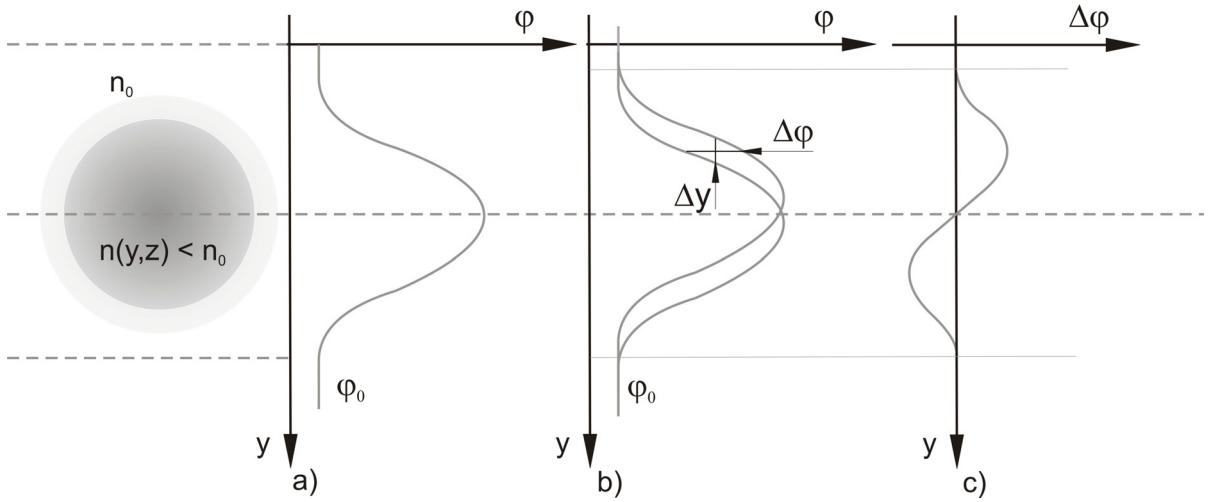

Figure 32: Basics of differential interferometry. The plane wave front is distorted by the object (a), and afterwards split into two beams and superimposed with a displacement Δy in the interferometer (b). This finally results in the phase difference distribution $\Delta\varphi$ (proportional to the first derivative of the density) (c).

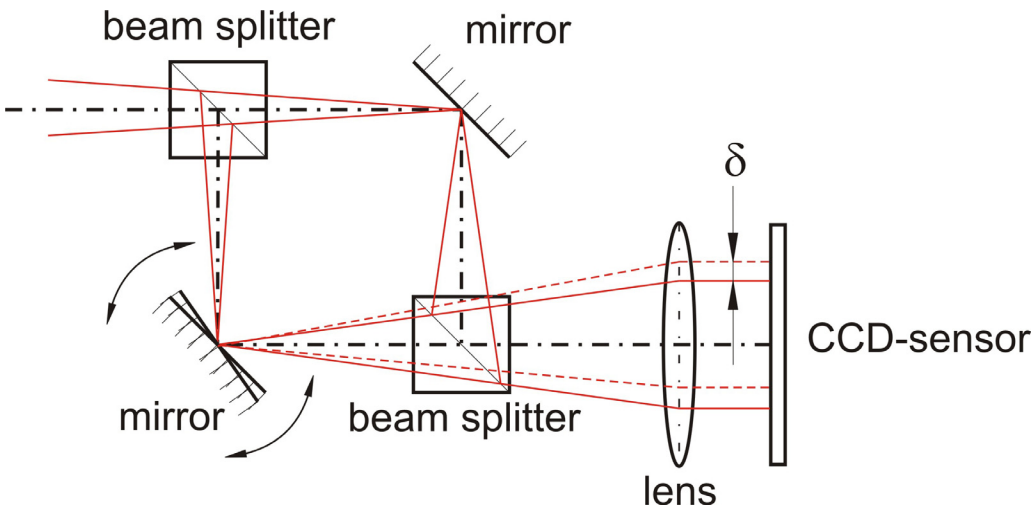

Figure 33: Detail of the shearing interferometer. The shear δ needed for the evaluation process is produced by tilting the mirror.

Additionally, one beam splitter is tilted to generate a carrier fringe system which is needed for the digital fringe evaluation process. Tilting the beam splitter inclines the wave fronts against each other by a certain angle α, heterodyning a carrier fringe system to the interferogram (figure 34). The carrier fringe system can be adjusted independently to the shear, either perpendicular for density gradient visualisation, or parallel or nearly parallel to the shear, which offers some advantages for the Fourier analysis performed in the data evaluation process. This carrier fringe system is then modulated by the basic fringe system caused by the object's density changes (Woisetschläger et al. 1998; Pretzler et al. 1993).

Data analysis is performed by a fringe evaluation software developed at Graz University of Technology (IDEA v.1.7) (Hipp et al. 1999; Hipp et al. 2004). In this evaluation process recorded interferograms are subject to a two-dimensional FFT. The intensity along a line in the interferogram is given by equation (65)

$$I(x,y) = I_0(x,y) + A(x,y) \cdot \cos \Delta\varphi(x,y) \qquad (65)$$

where $I_0(x,y)$ denotes the background intensity and $A(x,y)\cos\Delta\varphi(x,y)$ the interference fringes with their modulation.

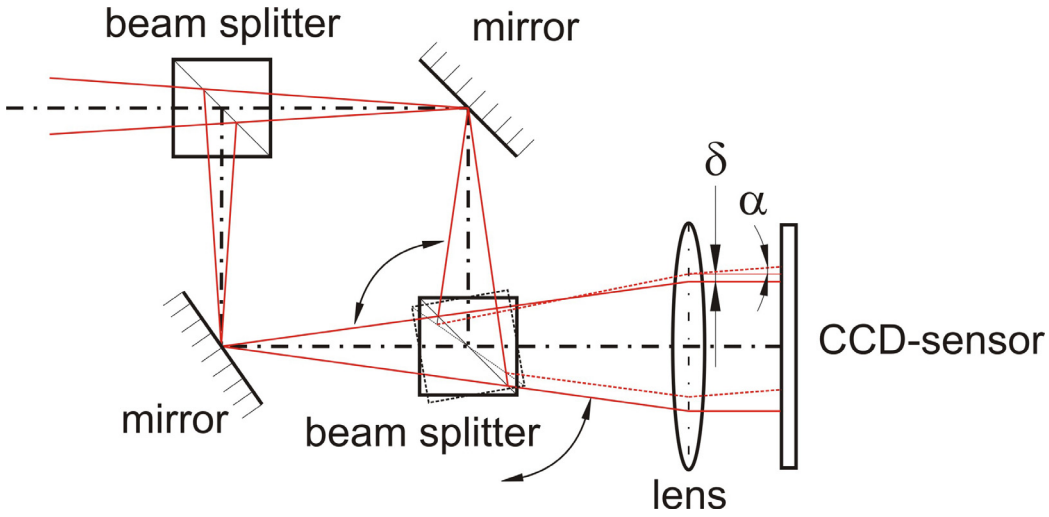

Figure 34: Tilting the beam splitter produces the inclination α necessary for heterodyning a carrier fringe system.

With the Euler identity, equation (65) can be written in terms of

$$I(x,y) = I_0(x,y) + G(x,y) + G^*(x,y) \tag{66}$$

with

$$G(x,y) = \frac{1}{2} A(x,y) \cdot e^{i\Delta\varphi(x,y)} \tag{67}$$

and

$$G^*(x,y) = \frac{1}{2} A(x,y) \cdot e^{-i\Delta\varphi(x,y)} \tag{68}$$

Applying a FFT to the signal $I(x,y)$ results in the intensity $j(\nu_x, \nu_y)$ in the Fourier domain with the frequency scales in x and y direction ν_x, ν_y, respectively (equation (69)).

$$j(\nu_x,\nu_y) = j_0(\nu_x,\nu_y) + g(\nu_x,\nu_y) + g^*(\nu_x,\nu_y) \tag{69}$$

The signal containing the interferometric information $G(y)$ is shifted towards higher frequencies in the Fourier domain because of the heterodyned carrier fringe system in the spatial domain. Due to this frequency shift, the signal $g(\nu_x, \nu_y)$, containing the information on the phase or density needed for the data reconstruction, is clearly separated from the low frequency background and modulation noise $j_0(\nu_x, \nu_y)$. Applying a rectangular filter window to the signal $g(\nu_x, \nu_y)$ and performing a back transformation of the filtered signal to the spatial domain leads to the phase distribution of the wave front calculated from the filtered signal (equation (70)) (Woisetschläger et al. 1998).

$$\Delta\varphi(x,y) = \arctan\frac{\mathrm{Im}(G(x,y))}{\mathrm{Re}(G(x,y))} \tag{70}$$

The FFT, the filtering process and the back-transformation as well as the subsequent demodulation of the modulo 2π distribution is illustrated in figure 35. For the demodulation an algorithm is used adding 2π whenever a phase jump is detected (Vukicevic et al. 1990). Figure 35(d), presents the phase distribution map calculated from the interferogram.

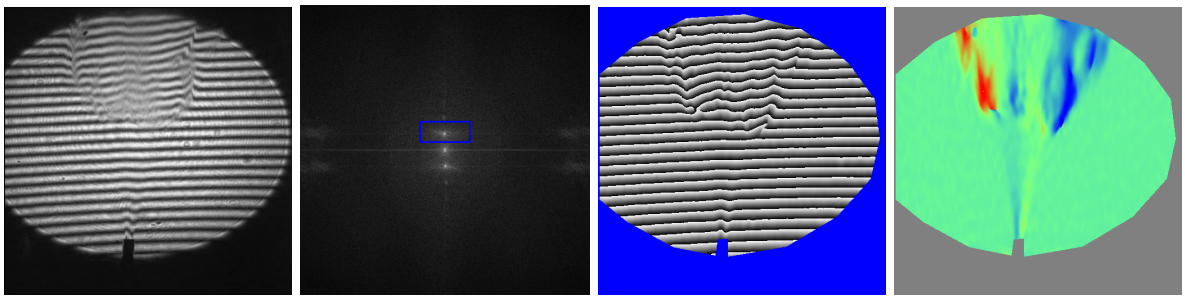

a) b) c) d)

Figure 35: Evaluation process for differential interferometry. The recorded interferogram with the heterodyned carrier fringe system (a) is Fourier transformed and filtered (b). Afterwards a back-transform is applied (c) and the phase distribution map is calculated (d) (Heimel 2010).

If the amount of shear is known, the density gradient map can be calculated directly from the phase distribution map $\Delta\varphi(x,y)$ (equation (64)). There are three different options to determine the adjusted shear:

- The unexpanded laser beam is projected on a screen far away from the interferometer and the tilt is measured by the shift between the two laser points and the distance towards the interferometer.
- The shear is evaluated in the plane of the CCD-camera by using an edge in the object's field of view and measuring the shear between the two images in terms of pixel of the CCD-camera. Therefore a precise length calibration of the pixeled image has to be recorded by placing a scale into the field of view.
- A calibration wedge with a well defined constant density gradient in the direction of the adjusted shear is applied to calculate the shear according to equation (64). The disadvantage of this method is the existing 2π uncertainty. The determined $\Delta\varphi(x,y)$ values might be larger or smaller by a multiple of 2π.

After the evaluation for the shear is done, the density gradient distribution can be calculated. To receive the data of the density distribution, it is necessary to integrate the density gradient distribution in the direction of the adjusted shear. This results in an integral density distribution along the beam path z. To obtain local density data a tomographic reconstruction method has to be applied. Unfortunately, tomographic reconstructions using integral line data as projection input need uniform boundary values in all projections and in the reconstructed field (Vest 1999; Philipp et al. 1992). A limited field of view or acoustic waves propagating through the flow-field therefore inhibit tomographic data reconstruction, which is often the case in combustors.

3.5.3 Laser vibrometer (LV)

Performing density measurements by differential interferometry has two main disadvantages. First data are not spatially-resolved, as mentioned before, and secondly differential interferometry does not provide frequency-resolved data. To perform a frequency analysis a continuously recorded time signal is needed, which can be recorded by modern, electronically controlled interferometers, so called laser vibrometers.

A laser vibrometer (LV) basically consists of a laser and a Mach-Zehnder interferometer. The laser beam is divided into an object-and a reference-beam. The reference-beam remains in the sensing head while the object-beam is focused by a lens on the object to be investigated. The reflected object beam re-enters the aperture and is superimposed to the reference beam in the sensing head. Distance changes in the geometrical beam path due to surface vibrations of the object now lead to intensity variations at the photo-detector (Lewin 1999).

In the same way a distance change at a constant refractive index can be used to detect surface vibrations, a change in the refractive index at a constant geometrical beam path can be used to identify flow and combustion processes. Therefore the vibrating surface is replaced by a rigidly fixed mirror, thus changes in the optical path length are solely due to density changes within the object to be investigated (figure 36).

A special feature of the laser vibrometers employed for the experiments presented in this work (model Polytec OVD 353 laser vibrometer, OFV-3001 controller and OVD-02 velocity decoder, Polytec GmbH, Germany) is the integrated Bragg-cell. This Bragg-cell operates as an acousto-optical modulator that diffracts and shifts the frequency of the reference-beam using sound waves. Therefore a piezo-electric transducer, attached to a crystal, is forced to vibrations by an oscillating electric signal, thereby creating sound waves in the crystal.

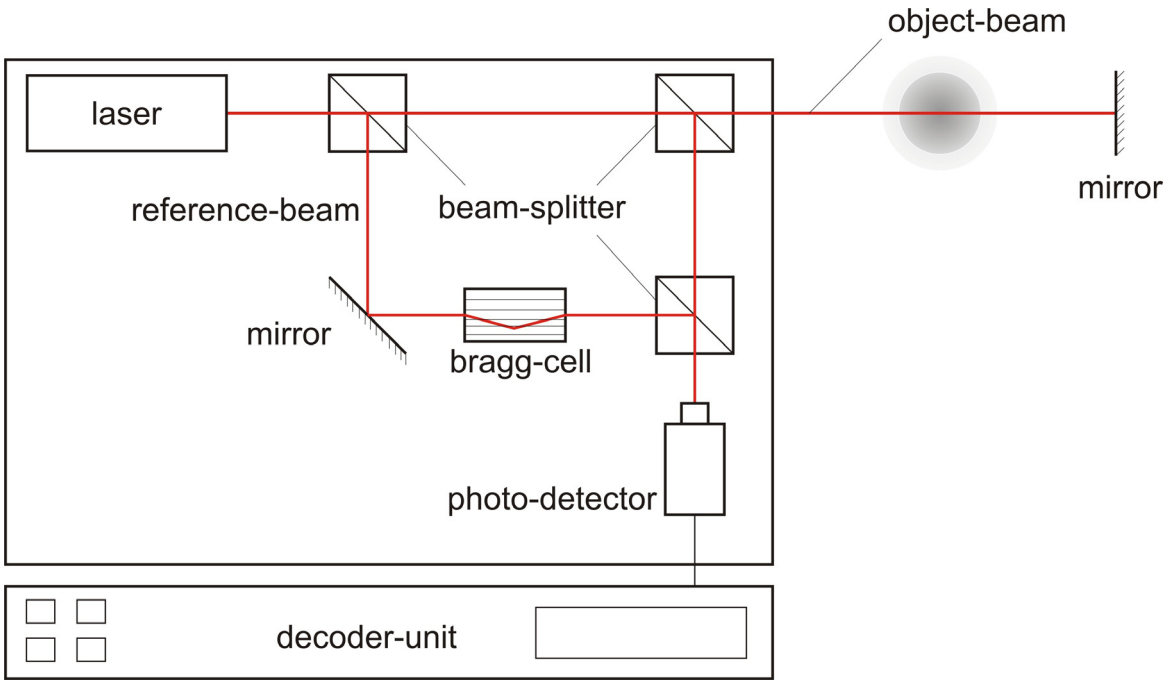

Figure 36: Laser vibrometer design. The vibrometer basically consists of the sensing head including a laser, a Mach-Zehnder interferometer with an integrated Bragg-cell and a photo detector, and a decoder-unit for signal demodulation.

Laser light passing the Bragg-cell is Doppler-shifted in frequency by the moving sound waves. When the frequency-modulated reference-wave and the unmodulated object-wave superimpose, a beat frequency is detected in the photo-detector, even if the optical path length of the object-beam remains constant. This beat frequency equals the frequency-shift caused in the Bragg-cell and acts as a carrier-frequency in the electric output signal of the photo-detector (40 MHz for the employed LVs).

The carrier-frequency is now modulated due to changes in the optical path length of the object beam, either caused by surface vibrations or density fluctuations along the object beam path (object wave is frequency-Doppler-shifted by the vibrating surface velocity, or object wave is frequency-Doppler-shifted by density fluctuations $\partial\rho' / \partial t$). This carrier-frequency modulation results in a frequency-modulated signal in the photo-detector and is demodulated in the de-coder-unit. In this mode the rate of change of the measure is recorded rather (first derivative in time) then the absolute value. Recording data in this mode, the so called vibrometer velocity mode, improves the signal-to-noise ratio by a $2\pi f$ factor (Mayrhofer and Woisetschläger 2001).

For laser vibrometer measurements in flows or combustion processes the difference in the optical beam path length (OPL) is defined again as

$$\Delta l_{opt} = \int_{\zeta_1}^{\zeta_2} n(\zeta, t) d\zeta \qquad (71)$$

With ζ the coordinate along the object beam axis. Applying the Gladstone-Dale relation, the OPL difference can be written in terms of the space integral of the density differences $\Delta\rho$ along the beam of laser light (equation (72)).

$$\Delta l_{opt} = G \int_{\zeta_1}^{\zeta_2} \Delta\rho(\zeta, t) d\zeta \qquad (72)$$

The time-dependent phase difference $\Delta\varphi(t)$ is now proportional to two times of the OPL difference, as the object beam is reflected by a mirror and passes the measurement area twice, see equation (73).

$$\Delta\varphi(t) = \frac{2\pi}{\lambda_0} \cdot 2\Delta l_{opt} = \frac{4\pi}{\lambda_0} \cdot G \int_{\zeta_1}^{\zeta_2} \Delta\rho(\zeta, t) d\zeta \tag{73}$$

For the further derivation of the equations the density difference $\Delta\rho$ is now split into a time-averaged mean value and a fluctuating time-dependent value, resulting in equation (74).

$$\Delta\rho(t) = \overline{\Delta\rho} + \Delta\rho'(t) = \overline{\rho} + \rho'(t) \tag{74}$$

For data recorded in the velocity mode, the vibrometer voltage output is proportional to the the time derivative of the density fluctuations along the beam of light (spatially integral data). The relation between this integral optical path change X along the path ζ and the time derivative of the density or the measured voltage signal $U(t)$ also contains the calibration factor k (mm/s/V) of the vibrometer and the Gladstone–Dale constant G (equation (75)) (Hampel 2005).

$$X(\zeta, t) = \int_{\zeta_1}^{\zeta_2} \frac{\partial\rho'}{\partial t}(\zeta, t) d\zeta = \frac{kU(t)}{G} = \frac{\Delta l_{opt}}{G} \tag{75}$$

In this mode the laser vibrometer is able to detect the density fluctuations in the test zone continuously, enabling a frequency analysis of the data by a FFT algorithm.

3.5.4 Dual laser vibrometry

According to equation (75) only integral data of density fluctuations are recorded using one vibrometer. To obtain spatially-resolved data a second vibrometer unit is needed. Using two laser vibrometers and crossing their laser beams can give spatially-resolved data if a signal correlation technique is used for data analysis. When this technique is employed, the two beams intersect in a certain position with both integral vibrometer signals containing local information on the density fluctuations in this position. To reveal this local information a correlation technique is needed. But, as the density fluctuations in the flows or combustion processes are turbulent and of stochastic nature, the use of statistical methods is necessary. A detailed description of the method and the underlying mathematical considerations can be found in (Hampel 2005; Hampel and Woisetschläger 2006).

The main approach of this tool is the calculation of the cross-correlation function R_{12} of two stochastic signals X_1 and X_2 in the time domain (equation (76)). The cross-correlation function is used to record the relationship of two signals X_1, X_2 as a function of the time-lag τ. For independent random signals the cross-correlation function will equal zero. In our application the numerical calculation of the cross-correlation is not performed in the time domain but in the frequency domain. Performing the cross-correlation calculation in the frequency domain on the one hand lowers the mathematical complexity and on the other hand provides frequency-resolved data on the density fluctuations.

$$R_{12}(\tau) = \frac{1}{T} \int_0^T X_1(t) X_2(t+\tau) dt \tag{76}$$

The experimental setup for dual LV measurements is illustrated in figure 37. The measurement plane is spanned by vibrometer beam 1 and 2, defining the coordinate system. In the measurement plane $\partial\rho'/\partial t(x, y, t)$ denotes the first derivative in time of density fluctuations for an arbitrary position. The scanning positions for the laser beams of vibrometer 1 and 2 are

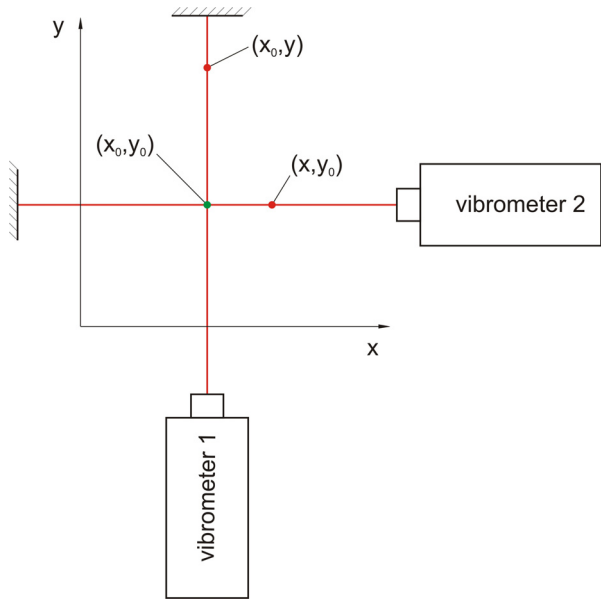

Figure 37: Coordinate system for dual laser vibrometry (Hampel 2005).

defined by the coordinates x_0 and y_0. Thus the coordinates for the point of intersection of both beams are fixed at (x_0,y_0). For arbitrary points along the laser beam path the coordinates for vibrometer 1 are described as a function of $f(x_0,y)$ and for vibrometer 2 as a function of $f(x,y_0)$. Since all the data analysis is done in the frequency domain, all time signals are Fourier-transformed first. Here F_d denotes the Fourier transform of the first derivative in time of local density fluctuations $\partial\rho' / \partial t(x,y,t)$ (equation (77)).

For practical use the spectrum of density fluctuations $\rho'(x,y,t)$ is of greater interest then the spectrum of the time derivative of density fluctuations. To calculate the density fluctuations from the first derivative in time, one must keep in mind that a Fourier-transform (FT) of a time derivative equals a simple multiplication of the complex spectrum by the factor $2\pi f i$, with i the imaginary unit (equation (78)).

$$F_d(x,y,f) = FT\left\{\frac{\partial\rho'}{\partial t}(x,y,t)\right\} \tag{77}$$

$$F(x,y,f) = FT\{\rho(x,y,t)\} = \frac{1}{2\pi f i}F_d(x,y,f) = \frac{1}{2\pi f i}FT\left\{\frac{\partial\rho'}{\partial t}(x,y,t)\right\} \tag{78}$$

The integral spectra for vibrometer 1 and 2 along the respective laser beam written in terms of the local spectra $F(x,y,f)$ lead to:

$$\begin{aligned} F_1(x_0,f) &= \int_x F(x_0,y,f)dy \\ F_2(y_0,f) &= \int_y F(x,y_0,f)dx \end{aligned} \tag{79}$$

Using equation (75) the integral spectra for vibrometer 1 and 2 can be calculated by a Fourier transform of the time signals X_1 and X_2 recorded by the respective vibrometer and a subsequent division by $2\pi f i$ (equals an integration in the time domain).

$$\begin{aligned} F_1(x_0,f) &= \frac{1}{2\pi f i}FT\{X_1(x_0,t)\} = \frac{1}{2\pi f i}\frac{k_1}{G}FT\{U_1(x_0,t)\} \\ F_2(y_0,f) &= \frac{1}{2\pi f i}FT\{X_2(y_0,t)\} = \frac{1}{2\pi f i}\frac{k_2}{G}FT\{U_2(y_0,t)\} \end{aligned} \tag{80}$$

The main idea of the process is to reveal local spectra of density fluctuations $F(x,y,f)$ from the integral spectra $F_1(x_0,f)$ and $F_2(y_0,f)$ obtained from the recorded vibrometer signals. Therefore the cross-correlation is performed in the frequency domain, calculating so called cross-spectra (equation (81)).

$$C(x_0,y_0,f) = F_1^*(x_0,f)\cdot F_2(y_0,f) = \int_x\int_y F^*(x_0,y,f)\cdot F(x,y_0,f)\cdot dxdy \tag{81}$$

This quantity $C(x_0,y_0,f)$ has the same physical unit as the power spectrum $((\mathrm{kg\,m^{-2}})^2)$. The cross-spectrum consists of the product of one spectrum and the complex conjugate of the other. The calculated cross-spectrum $C(x_0,y_0,f)$ is a degree for the average coupling strength of both spectra. Its magnitude denotes the power spectrum of the correlated fraction that is contained in both signals. The complex angle of the cross-spectrum is the phase difference of both signals according to the frequency-wise and averaged time delay of the equal parts within the two signals.

The main data analysis algorithm is illustrated in principle in figure 38, showing two different approaches to calculate the cross-spectrum. One way is to apply a FFT to the recorded time-signals X_1 and X_2 first. Afterwards the cross-spectrum is calculated by a simple multiplication in the frequency domain, which is the more efficient way compared to the calculation of the cross-correlation in the time domain. The second approach is to calculate the cross-correlation in the time domain first, and perform the FFT afterwards. In this work, the FFT was always performed first and the numerical calculation of the cross-spectrum was done in the frequency domain by a simple multiplication.

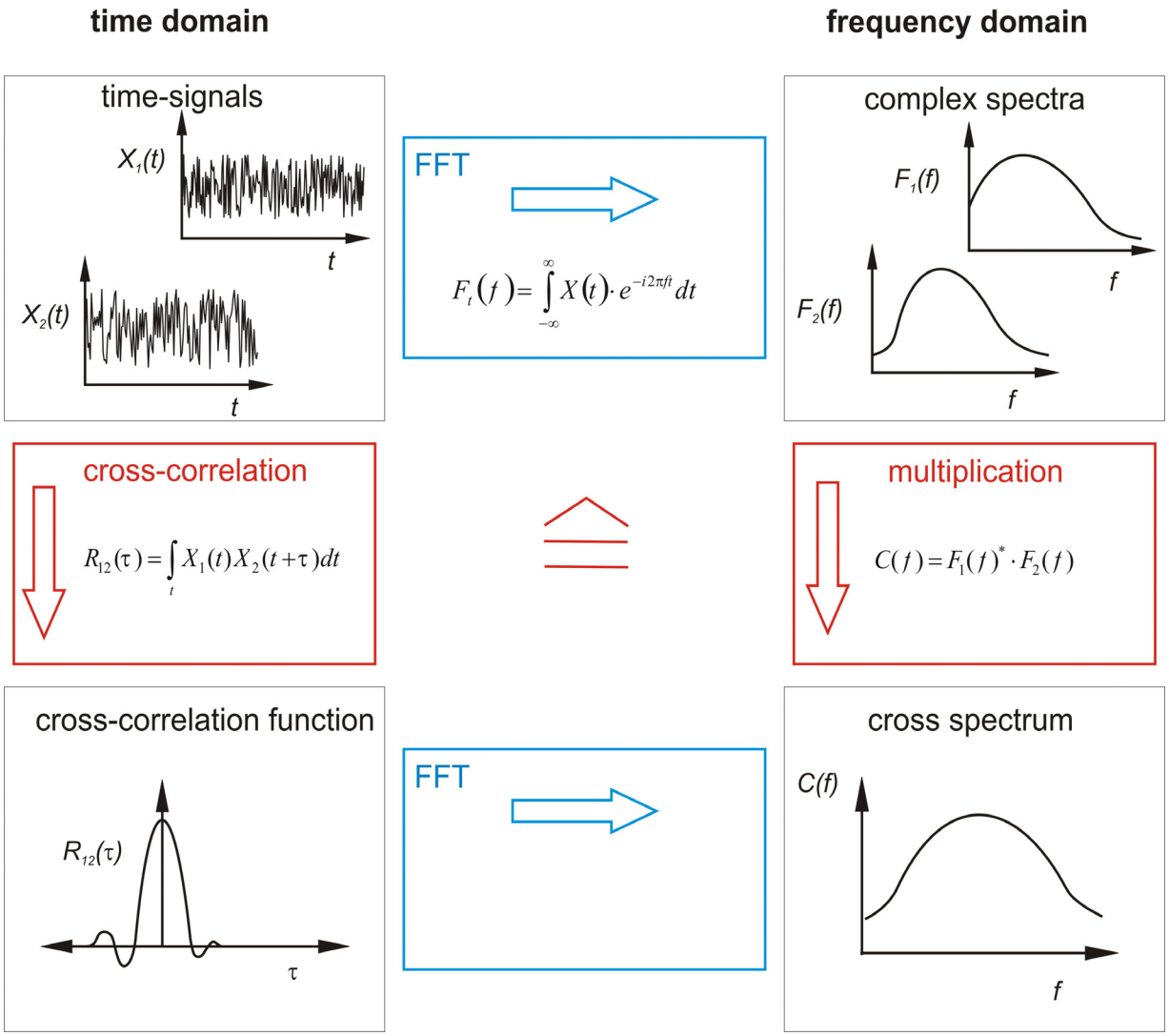

Figure 38: Principals of data analysis for dual LV (Hampel 2005).

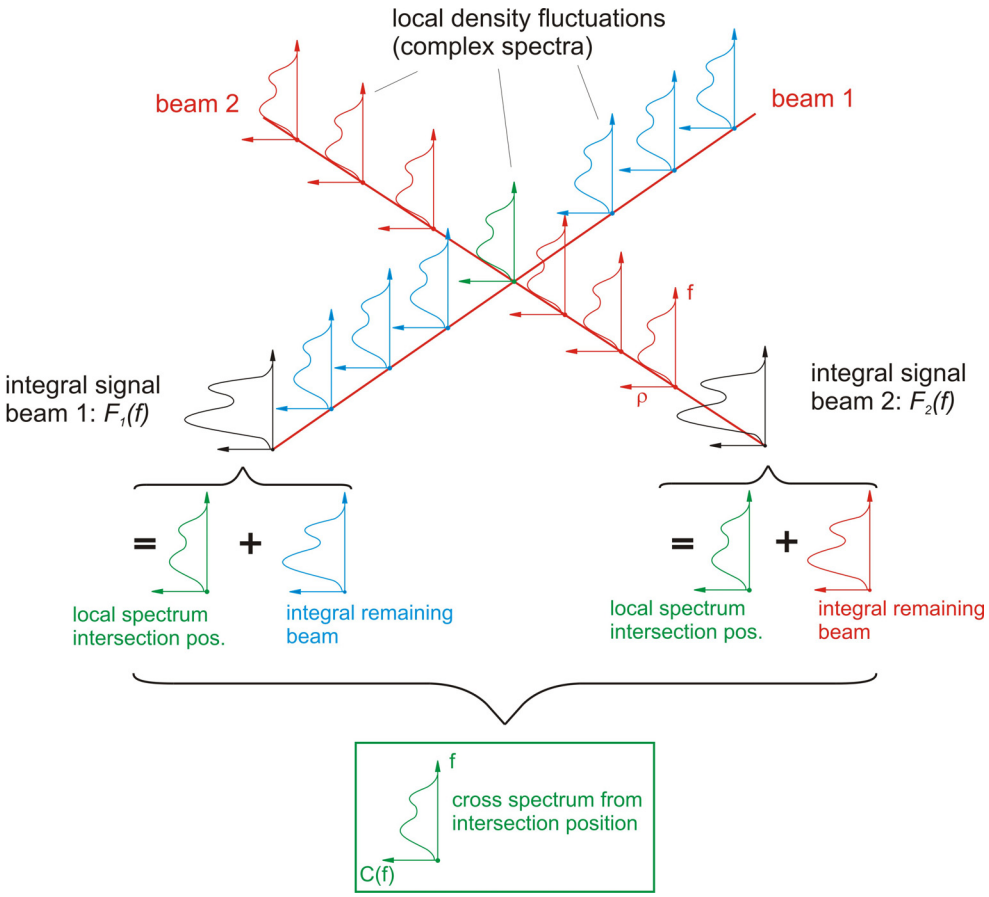

Figure 39: Visualisation of the mathematical data processing (Hampel 2005).

Figure 39 presents a visualisation of the mathematical data processing. All local density fluctuations are summed up along the beam path by the respective vibrometer leading to integral signals of density fluctuations. Both integral signals 1 and 2 now contain local information on the density fluctuations in the point of intersection of the two laser beams. Performing a fast Fourier transform leads to integral spectra of density fluctuations for beam 1 and 2. Finally the calculation of the cross-spectrum reveals the information on the density fluctuations contained in both signals.

If both signals are completely random, the magnitude and the phase of the cross-spectrum will average to zero. In turbulent (chaotic) signals a single observation is not sufficient. An average process over a large number of time records is always needed to extract the deterministic part in the signal (equation (82)).

$$\overline{C(x_0, y_{0,} f)} = \overline{FT\{R_{12}(\tau)\}} = \overline{F_1^*(x_0, f) \cdot F_2(y_0, f)} \qquad (82)$$

To obtain local power spectra of density fluctuations $|F(x_0,y_0,f)|^2$, it is necessary to correct the cross-spectra by an effective measurement area A_c which is a function of frequency (equation (83)). A_c describes an area that is related to the size of turbulent, coherent structures, e.g. vortices, in the flow-field and usually is not the size of the overlapping volume of the two laser beams. As these structures possess a physical correlation within their dimensions, not only does the intersection volume of the two laser vibrometers contribute to the cross-spectrum, but the cross-spectrum is elevated by all other points along the laser beams within the size of the structure as well (figure 40).

$$\overline{|F(x_0, y_0, f)|^2} = \frac{\left|\overline{C(x_0, y_0, f)}\right|}{A_c(f)} = \frac{1}{4\pi^2 f^2} \cdot \overline{\left|FT\left\{\frac{\partial \rho'}{\partial t}\right\}\right|^2} \qquad (83)$$

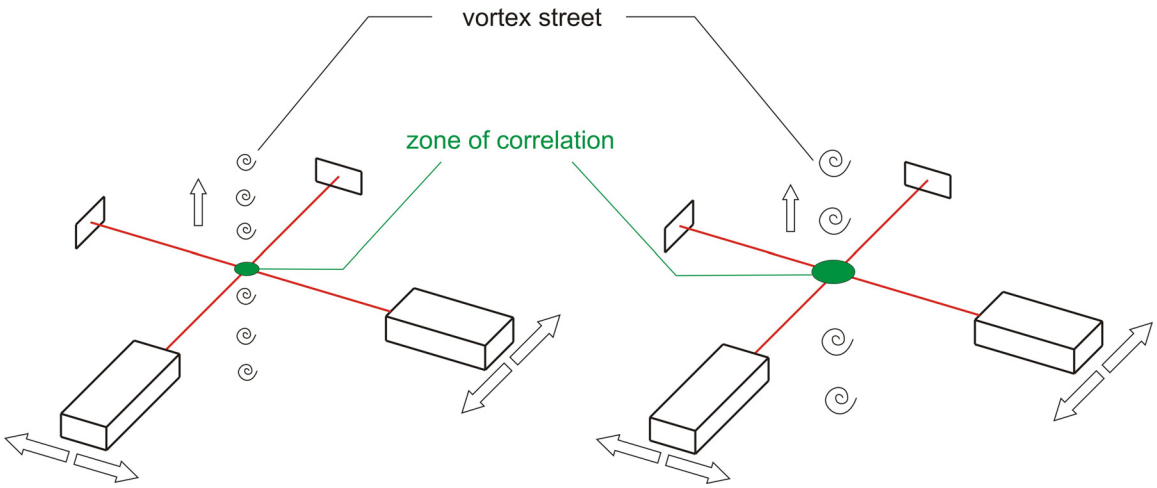

Figure 40: Zone of correlation in dependence on the size of the density structures, e.g. vortices, passing the laser beam intersection volume (Hampel 2005).

Values for A_c can be obtained through a reasonable theoretical model or an experimental calibration, for example by comparison of the results with local pressure measurements (Hampel and Woisetschläger 2006). In the experiments presented in this thesis, local pressure measurements could not be performed as no fast pressure sensor was available that could resist environmental conditions in the flame and due to the fact that density fluctuations are proportional to pressure fluctuations and heat release in a flame.

Previous research showed that if turbulent structures are thought to be spherical, i.e. have the same diameter in all three dimensions, and are transported with the flow at flow speed u, the frequency f of their signal is of the order of u/l, with l the diameter of the structures. As the area is of the order l^2, a simple approximation is (Hampel and Woisetschläger 2006):

$$A_c(f) = l^2 = \left(\frac{u}{f}\right)^2 \tag{84}$$

Furthermore, a number of coherent structures can create physical correlations in the flow-field. Even if these coherent structures do not emerge at the intersection between the two probing laser beams, they will elevate the cross-spectrum and artefacts can emerge in this way. But if these coherent structures influence the two beam paths from distant positions, not from the overlapping volume (measurement volume), a phase lag can be observed. Such artefacts can therefore be identified by a nonzero phase of the cross-spectrum since this phase angle corresponds to the time delay of the correlated parts within the two signals. In this case a Gaussian filter function can be used to correct the cross-spectrum (equation (85)).

$$\left|C_F(x_0, y_0, f)\right| = \left|C(x_0, y_0, f)\right| \cdot \exp\left[-\left(\frac{\varphi(x_0, y_0, f)}{\Delta\varphi(f)}\right)^2\right] \tag{85}$$

Especially when the phase lag is too small, additional artefacts could be caused by correlated shedding of large vortices, but in different sections of the laser beams, and might be falsely attributed to the measurement position tested (crossing point of the two laser beams). If the same position is scanned from different viewing angles, these special artefacts can be damped.

Figure 41 illustrates flow phenomena that falsify the measurement result and lead to artefacts in the intersection point of the two laser beams. One origin of artefacts are sound waves within the flow-field. Sound waves, causing pressure fluctuations, are highly correlated within their dimensions and therefore sound wave fronts passing through both laser beams are attributed to the measurement point (correlated points along the respective laser beams that con-

tribute to the cross-spectrum due to the sound wave fronts passing the laser beams are marked in purple in figure 41).

These artefacts can be damped using the aforementioned phase filter function, since the wave fronts generally reach the laser beams at different times, whenever the source of the sound wave does not coincide with the intersection point of the laser beams. The only problem with this kind of phase filter is the 2π uncertainty. A phase difference between the correlated fractions of both signals of exactly 2π is equivalent to a phase difference of zero and therefore the filter function does not correct the measurement result in this case.

Another source of artefacts are spatially separated but correlated density fluctuations, e.g. vortex shedding. If these correlated fluctuations pass through both beams at the same time, the filter function does not work due to the zero-phase between the two spatially separated fluctuations. In this case the measurement setup needs to be rotated and an additional measurement scan must be performed. The artefact is still present as soon as each laser beam passes through the correlated fluctuations, but the position of the artefacts in the measurement plane changes (figure 41) according to the viewing angle. These artefacts are damped now if the measurement area is scanned from different directions and the obtained results are averaged. The attenuation factor for this kind of artefacts equals the number of measurement scans performed for different viewing directions.

To judge the obtained measurement results, the relative correlation $K(f)$ defined in equation (86) is helpful, as it quantifies the fraction of correlated power in the cross-spectrum $C(f)$ compared to the product of the power spectra $P_1(f)$ and $P_2(f)$ obtained from each integral vibrometer signal. If there is a physical correlation outside the measurement volume in the flow-field caused by sound waves or large correlated structures, the measured signal obtained from the cross-spectrum could be elevated in the whole measurement area and therefore the relative correlation $K(f)$ would be elevated too in the whole flow-field. Thus, a high correlation over a large measurement area indicates a high probability of artefacts or an artificially elevated signal level.

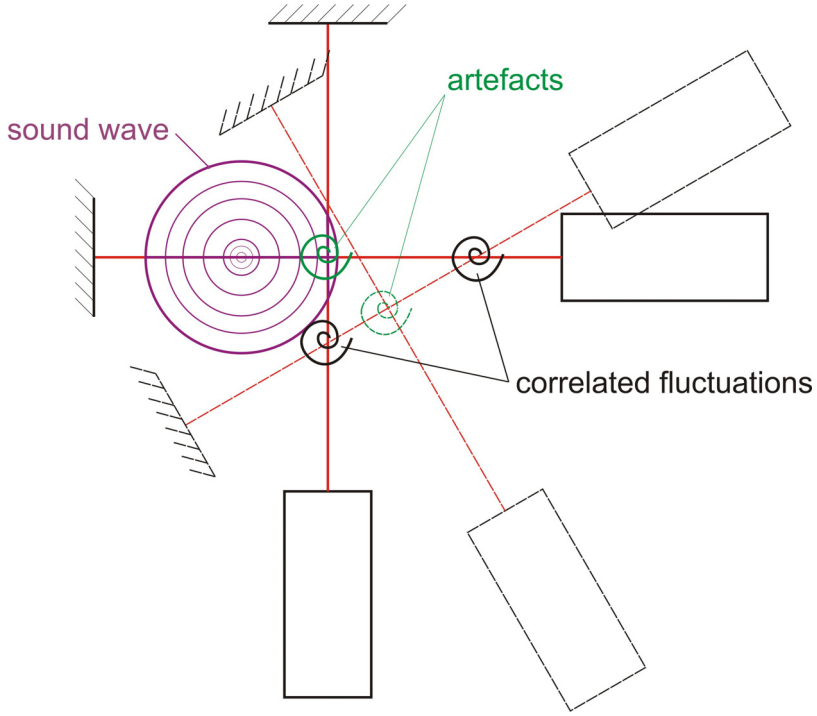

Figure 41: Flow phenomena causing artefacts in the measurement zone. Two different sources causing artefacts are identified, sound waves within the flow-field and spatially separated but correlated fluctuations.

$$K(f) = \frac{\left|\overline{C(f)}\right|}{\sqrt{\overline{P_1(f)} \cdot \overline{P_2(f)}}} = \frac{\left|\overline{C(f)}\right|}{\sqrt{\overline{|F_1(f)|^2} \cdot \overline{|F_2(f)|^2}}} \tag{86}$$

Since artefacts occur when large coherent structures are present in the flow and as these are normally produced by large density fluctuations or sound waves, they show a narrow band spectrum and appear at local peaks in the spectrum together with a high relative correlation. Thus unwanted surface vibrations or electronic noise from the power supply system in the 50 or 100 Hz range can be identified easily since these erroneous frequencies are generally present for all scanned positions resulting in an elevated cross-spectrum and a high relative correlation for these single frequencies.

4 Validation of dual laser vibrometry in a reference flame

This chapter presents the validation process of the dual laser vibrometry measurement technique for combustion processes. Since dual laser vibrometry measurements had already been successfully performed in an isothermal circular free jet in a previous work (Hampel and Woisetschläger 2006), but had not been applied to record spatially-resolved density fluctuations in combustion processes before, it was necessary to validate the measurement technique for combustion processes by a comparison of results recorded with the dual laser vibrometry technique in a reference flame, to data obtained using established, calibrated measurement techniques. The reference flame used for this validation process was designed and tested by (Kawanabe et al. 2000). The validation process and some results of this work can be found in (Köberl et al. 2010), but the process and all setups are described in all details in this section.

Besides the validation measurements additional experiments were performed, using the same reference burner in two more setups. To show the potential of the dual laser vibrometry technique for the detection of combustion instabilities, the fuel mass-flow of the reference burner was forced to oscillations in a second setup to simulate an unstable combustion process. Finally the burner was used in a third setup to gain experimental data for a comparison with numerical data obtained by a direct numerical simulation (DNS), which is performed at the Institute for Fluid Mechanics and Heat Transfer at Graz University of Technology.

4.1 Reference burner design and operating conditions

4.1.1 Setup 1

To verify the recording of density fluctuations by two laser vibrometers and subsequent correlation techniques in a reactive flow, a reference burner, designed, developed and tested by (Kawanabe et al. 2000) was used as test setup 1. For this burner (figure 42), velocity and temperature data are available (Kawanabe et al. 2000). The burner was operated under atmospheric pressure conditions during all the experiments performed in this work, used gaseous fuel and provided a lifted flame which was emitted from a central nozzle with an exit diameter of 4 mm. This central fuel jet was surrounded by an annular air jet emerging from a nozzle with a diameter of 50 mm. The fuel was supplied from gas bottles through a hose with 4 mm inner diameter. A settling chamber with 100 x 70 x 60 mm^3 inner dimensions was placed 700 mm in front of the burner to damp down pressure fluctuations in the fuel flow.

The air supply for the annular jet was ensured by an in-house pneumatic system. Before entering the exit nozzle, the airflow passed a settling chamber filled with steel balls of diameter 3 mm to damp down inhomogeneities. Additionally, three wire mesh sieves were mounted further downstream to condition the turbulence in the airflow.

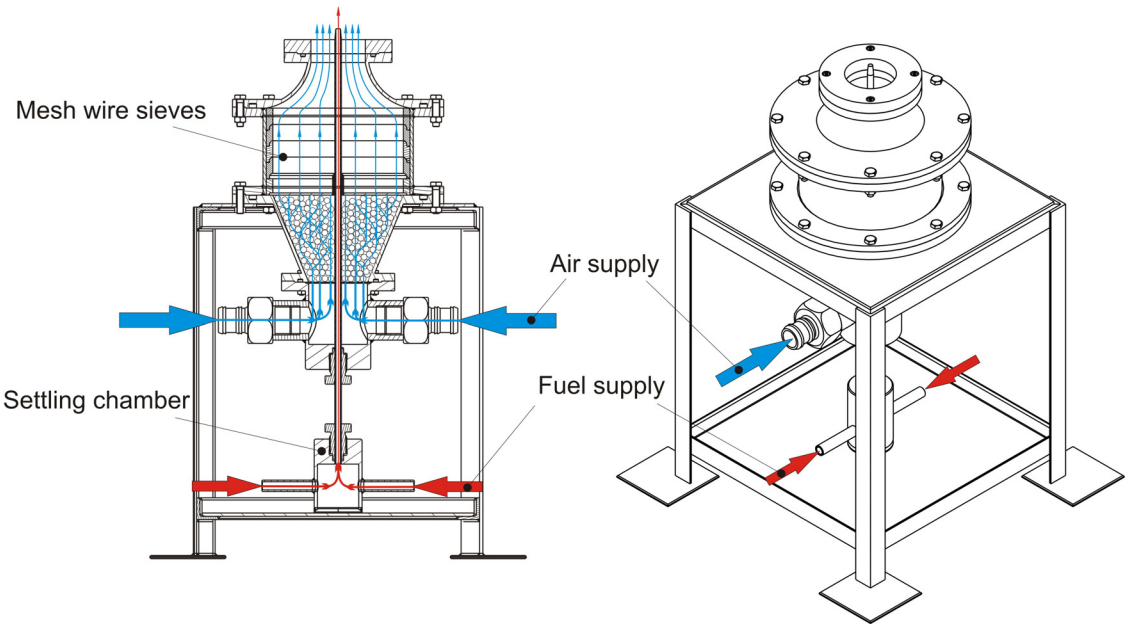

Figure 42: Cross-section of the reference burner (Kawanabe et al. 2000). Air-supply (blue) was ensured by an in-house pneumatic system, the fuel was supplied from gas bottles.

During the experiments performed for the validation of the dual laser vibrometry technique, pure methane was used as a fuel. The methane was emitted from the central nozzle with an exit velocity of 17.6 ms^{-1} at a temperature of 21°C, thus yielding a mass flow of 0.15 gs^{-1} and a Reynolds number of approximately 4300, based on the exit nozzle diameter.The exit velocity of the airflow was 0.5 ms^{-1} and its temperature was 21°C leading to a mass flow of 1.30 gs^{-1} and a Reynolds number of approximately 1800 at the air nozzle exit.

4.1.2 Setup 2

In a second setup the settling chamber was replaced by a chopper system to enforce controlled fluctuations in the fuel-flow. The chopper system consisted of a choked nozzle and a toothed, rotating wheel in front of the nozzle, embedded in a sealed casing. The rotation of the toothed wheel caused a periodic blockage and generated fluctuations in the fuel-flow at a certain frequency. In these experiments this frequency was set to 30 Hz. The mass-flow for fuel and air were not changed compared to setup 1.

4.1.3 Setup 3

For the third setup, the air mass-flow was set to zero and the air nozzle was sealed to prevent any air flow from the nozzle caused by the stack effect of the flame; additionally the fuel was changed from pure methane to a methane-nitrogen blend. The methane mass flow was set to 0.061 gs^{-1} and the nitrogen mass flow was set to 0.054 gs^{-1}, thus yielding an exit velocity of 11.3 ms^{-1} and a Reynolds number of approximately 2700. Experiments at setup 3 were carried out to provide a data base for a comparison of experimental data with numerical data obtained by a direct numerical simulation (DNS) performed at the Institute of Fluid Mechanics and Heat Transfer at Graz University of Technology. Table 2 presents an overview of the operating conditions for all setups.

Table 2: Operating conditions of the reference burner for different setups.

Setup 1	Fuel nozzle	Co-flow (air-nozzle)
fluid	methane	air
v_{exit}	17.6 ms^{-1}	0.5 ms^{-1}
mass flow	0.15 gs^{-1}	1.30 gs^{-1}
Re-number	4300	1800
Setup 2	Fuel nozzle	Co-flow (air-nozzle)
fluid	Methane (pulsed at 30 Hz)	air
v_{exit}	17.6 ms^{-1}	0.5 ms^{-1}
mass flow	0.15 gs^{-1}	1.30 gs^{-1}
Re-number	4300	1800
Setup 3	Fuel nozzle	Co-flow (air-nozzle)
fluid	methane/nitrogen	-
w_{exit}	11.3 ms^{-1}	-
mass flow	0.061/0.054 gs^{-1}	-
Re-number	2700	-

4.2 Burner characterization by optical- and laser-optical measurement techniques

Different optical and laser-optical measurement techniques were applied to the reference burner in the distinct setups. The reference burner was characterized extensively in setup 1, including visualizations of the density gradients in the flame using the schlieren-technique, velocity measurements by a laser Doppler velocimetry (LDV), temperature and concentration measurements with a Raman-scattering system, and density measurements by differential interferometry (DIF), to validate the dual laser vibrometry technique for the measurement of local and frequency-resolved density fluctuations in reactive flows.

In setup 2 the schlieren visulization technique and the dual laser vibrometry was applied to the oscillating flame to compare qualitative data of the density gradients to quantitative data recorded by the dual laser vibrometry.

Measurements for setup 3 included visualization of density gradients by a schlieren-visualization, investigations of the chemiluminescence emissions using a high-speed camera and measurements of density fluctuations by dual laser vibrometry. A complete overview of the measurement techniques applied in the different setups is given in Tab. 3.

Table 3: Measurement techniques applied to the different setups for the investigations of the reference burner

	Setup 1	Setup 2	Setup 3
Schlieren visualization	**x**	**x**	**x**
Chemiluminescence emissions meas.	**x**		**x**
Laser Doppler velocimetry (LDV)	**x**		
Differential interferometry	**x**		**x**
Raman-scattering	**x**		
Dual laser vibrometry	**x**	**x**	**x**

4.2.1 Chemiluminescence emissions

To characterize the shape of the flame and the local heat release rates, integral data of chemiluminescence emissions recorded by a CCD-camera were used for tomographic reconstructions. The recording of the integral projection data was done using a CCD-camera (Canon EOS 300D, Tokyo, Japan) with defined settings (ISO 800, aperture 22, exposure time 1.3 s). Since the flame was almost symmetrically shaped, integral projection data from only one direction was used to perform a tomographic reconstruction. This tomographic reconstruction provided a detailed map of the local heat release rate (averaged data).

4.2.2 Laser Doppler velocimetry (LDV)

In setup 1 velocity measurements were performed at three different heights (Y = -10, 20 and 90 mm) with a two-component LDV (DANTEC Fiber-Flow with DANTEC Burst Spectrum Analyser, DANTEC Dynamics, Roskilde, Denmark) fed by an argon ion laser (Coherent Inc., Santa Clara, CA) with wavelength λ_{laser} = 488 nm and 514.5 nm to characterize the flow and compare to previously published data (Kawanbe et al. 2000). Positioning of the optical head was done with a DANTEC Lightweight traverse. TiO_2 tracer particles with a characteristic diameter of 1 μm were added to the methane-jet and oil droplets (di-ethyl-hexyl-sebacat, DEHS) with a diameter about 0.3 μm were used to seed the air-flow. For control, acquisition and analysis of the collected data DANTEC BSA Flow Software 1.2 was used. At each measurement position 30000 bursts were recorded to measure the velocity.

4.2.3 Differential interferometry

With differential interferometry (shearography), density gradients were recorded in the methane-jet flame for setup 1 to reference the density fluctuation data obtained by dual laser vibrometry, and in the methane-nitrogen flame for setup 3. A parallel laser beam expanded to a diameter of 200 mm and emitted by a 25 mW HeNe laser (NEC, Tokyo, Japan) with wavelength of λ = 632.8 nm, crossed the flame and entered a small Mach-Zehnder interferometer, consisting of two beam splitters and two mirrors. The two wavefronts were sheared against each other by tilting one of the mirrors. Additionally one beamsplitter was tilted to generate a carrier fringe system which is needed for the digital fringe evaluation process. Afterwards the laser beam entered the aperture of a Panasonic 3CCD NV-DX100 camcorder. The details of this technique and the data evaluation are given by (Woisetschläger et al. 1998; Hipp et al. 1999).

The fringe evaluation software used was developed at Graz University of Technology (IDEA v.1.7 (Hipp et al. 1999)). With the filter width chosen during evaluation a spatial resolution of 2 mm was provided. To obtain local density information from these interferograms a tomographic reconstruction technique was applied, also implemented in the IDEA software (algebraic reconstruction technique, ART (Gordon and Herman 1974; Hipp et al. 1999)). Compared to the correlation technique used for the dual laser vibrometry this ART needs zero density change at the boundary of the reconstructed density field, therefore atmospheric conditions and no field limitations by windows. The density fluctuations needed for reference and for equation (1) were obtained from statistical evaluation of 800 interferograms.

4.2.4 Raman-scattering

Concentration and temperature measurements were done only for setup 1 using Raman-scattering technique. The Raman system consisted of a single pulsed Nd-YAG-laser (InnoLas, SpitLight 600, InnoLas Systems GmbH, Krailling, Germany), a spectrograph (PI/ACTON Spectra Pro-2300i, Princeton Instruments, Trenton, NJ) and an intensified CCD camera (Nano Star S25, Lavision, Göttingen, Germany). The laser emitted light at a frequency-tripled wavelength of 355 nm with a pulse duration of 7 ns. For the measurements the laser beam was slightly focused into the methane-jet flame by an achromatic lens (f = 500 mm). The scattered light was collected perpendicular to the laser beam by another achromatic lens with a focal length f = 150 mm and imaged onto the entrance slit of the spectrograph.

Using UV-laser in partially premixed flames of hydrocarbons can lead to a broad and intense background scatter caused by soot precursors. Change of polarization direction of the laser light was used to separate background emissions and Raman signals, as Raman-scattering is highly polarized and background emissions are depolarized. Data collection was done with DAVIS Flowmaster 7.1.1 (Lavision, Göttingen, Germany) and 50 images with 30 bursts per image were taken at each measurement position with the Nanostar camera for two different polarization directions of the laser beam. Before data evaluation was done, the background scatter was subtracted to obtain more reliable results (Hassel and Linow 2000; Hayashida et al. 2006).

4.2.5 Dual laser vibrometry setup

For all setups two laser vibrometers were used, both model POLYTEC OFV-353 with an OFV 3001 controller (Polytec GmbH, Waldbronn, Germany). The calibration factor k was calibrated to 5 mm/s/V and a low-pass filter of 20 kHz was chosen throughout all the measurements. Both laser vibrometer were fixed on a DANTEC Lightweight traversing system (Dantec Dynamics, Roskilde, Denmark) in a way that the two laser beams crossed orthogonally in a plane perpendicular to the jet axis. The complete measurement setup can be seen in figure 44. The laser beam (diameter 1.5 mm) of each vibrometer was collimated by a diverging lens (f = -40 mm), passed through the measurement area and was reflected by a flat aluminium surface mirror, passed through the measurement area again and re-entered into the aperture of the vibrometer. Each mirror was mounted at a distance of 1 m away from the respective laser vibrometer. Both mirrors were fixed using vibration insulation and a solid frame to avoid surface vibrations. The measurement plane was placed perpendicular to the air and methane flow direction at a distance of 90 mm above the methane nozzle exit for setup 1 and 2, for setup 3 the measurement plane was placed 110 mm above the nozzle exit.

The burner was pivot-mounted on the vibration-insulated table to allow measurements from different viewing angles. As large coherent structures in the flame could lead to artefacts, measurements were performed from seven different directions. The viewing angles for the measurements varied from 0° to 90° with an increment of 15°.

The voltage signals from both vibrometers were digitalized by a National Instruments PXI-1033 chassis and a NI 4452 A/D converter board (National Instruments Germany GmbH, München, Germany). The PXI-chassis was connected to a 1.8 GHz standard PC for data acquisition. Both vibrometer signals were recorded simultaneously by a user-defined routine developed using National Instruments LABVIEW 8.0. This software was also used to control the traversing system and automate the laser vibrometer measurements. After the desired measurement position was reached the software waited four seconds before starting the data acquisition. In this time vibrations, caused by the traversing, damped down. A sample rate of 40.96 kHz and a recording duration of 100 seconds per measurement point were chosen.

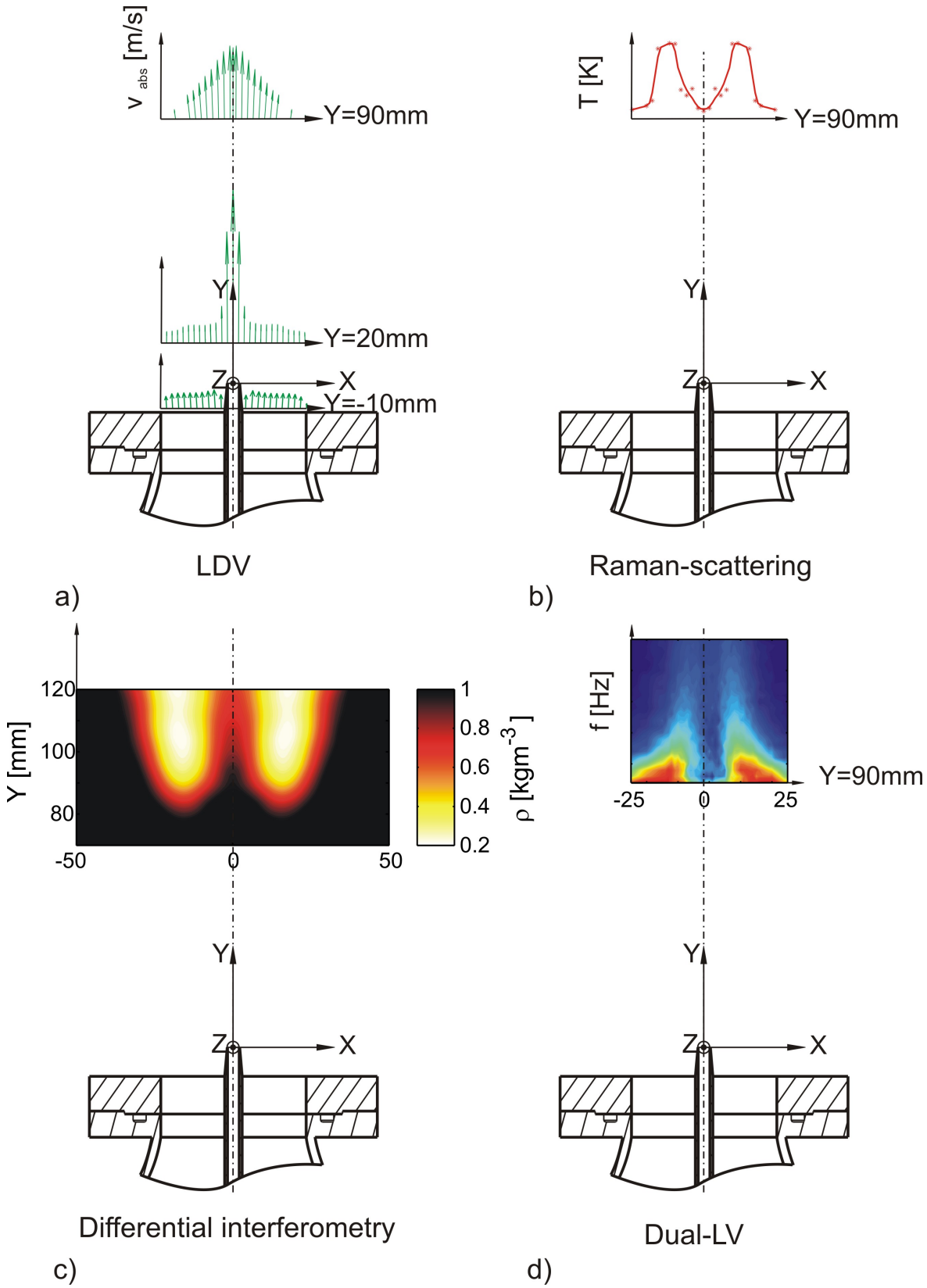

Figure 43: Measurement positions and measurement techniques applied to the reference burner for setup 1. LDV-measurements were performed at three different heights (a), Raman-scattering (b) and laser-vibrometry (d) was done at one fixed height at Y = 90 mm, and interferometric data was recorded according to (c).

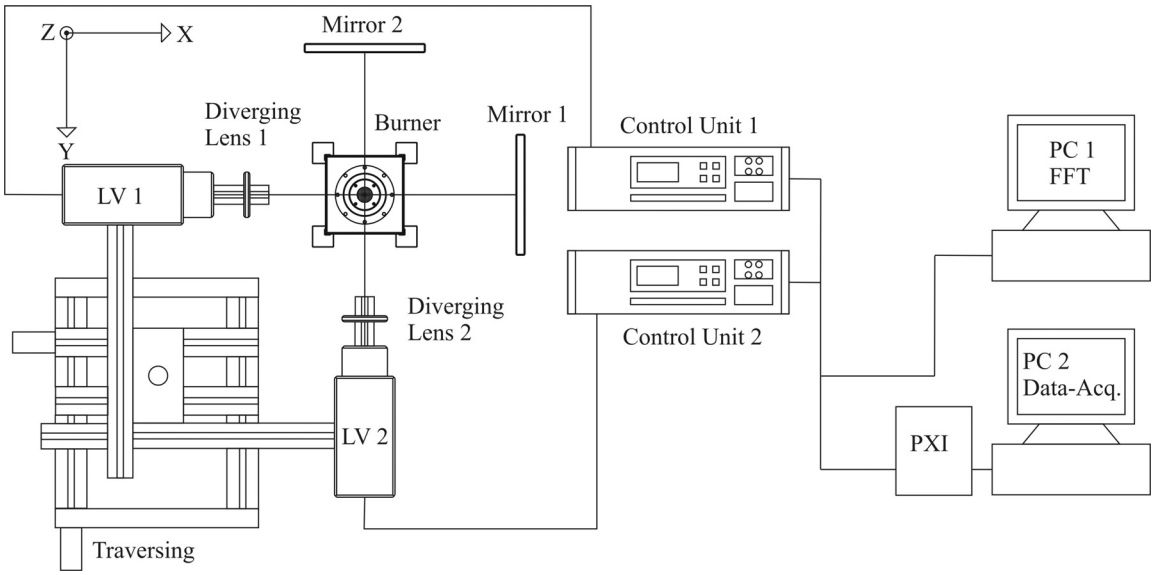

Figure 44: Principal experimental setup of the laser vibrometer for the investigations of density fluctuations in the methane-jet flame. Both vibrometers were fixed on a traversing system and the burner was pivot-mounted to allow measurements from several directions.

Performing a fast Fourier transform (FFT) with time samples containing 4096 values resulted in 1000 spectra with a frequency resolution of 10 Hz. The FFT, the calculation and the averaging of the cross-spectra was done in MATLAB vR2007b (The MathWorks, Natick, MA). The NI 4452 A/D converter board was mounted in a second standard PC, to observe the FFT of both laser vibrometer signals online during measurement.

4.3 Results and discussion

4.3.1 Setup 1

Figure 45 presents a schlieren visualization of the methane-jet flame with the respective dimensions, recorded at high shutter speed (1/1000), whereas local data of chemiluminescence emissions, obtained from a tomographic reconstruction of integral chemiluminescence emissions data recorded by a CCD-camera (Canon EOS 300D, Tokyo, Japan) at defined settings (ISO 200, aperture 5.6, exposure time 1.3 s) is shown in figure 46.

From the schlieren visualization only qualitative data on the combustion process can be revealed, but no quantitative data can be extracted, although, some general statements on the flame can be drawn from the schlieren image. The burner provided a lifted flame in this setup and the flame was located at a height of approximately 80 mm above the nozzle exit. In the lower third, where no combustion takes place, the cone-shaped methane-jet, emitted from the central nozzle is clearly visible and is characterized by small, fine structures in the schlieren image.

At approximately 80 mm height, the visible appearance of the methane-jet suddenly changes and the structures become significantly larger, which indicates the initial point of the combustion zone. At this height two different zones can be identified, one near the centre-region, where the methane-jet is still present and no combustion takes place, and a second zone, outside of a radius of approximately 20 mm, where large structures were found, which are buoyancy driven and move upwards slowly. These structures emerge due to the thermal expansion of the gases caused by the heat release of the flame. The main combustion zone can not be seen directly in the schlieren image, but the presence of small structures in the centre-region, surrounded by large structures, implies that the main combustion process takes place in the boundary layer between the centred methane-jet and theses large structures. The central methane-jet diminishes in the flame with increasing height and finally only the large, buoyancy-driven structures are visible in the upper third of the image.

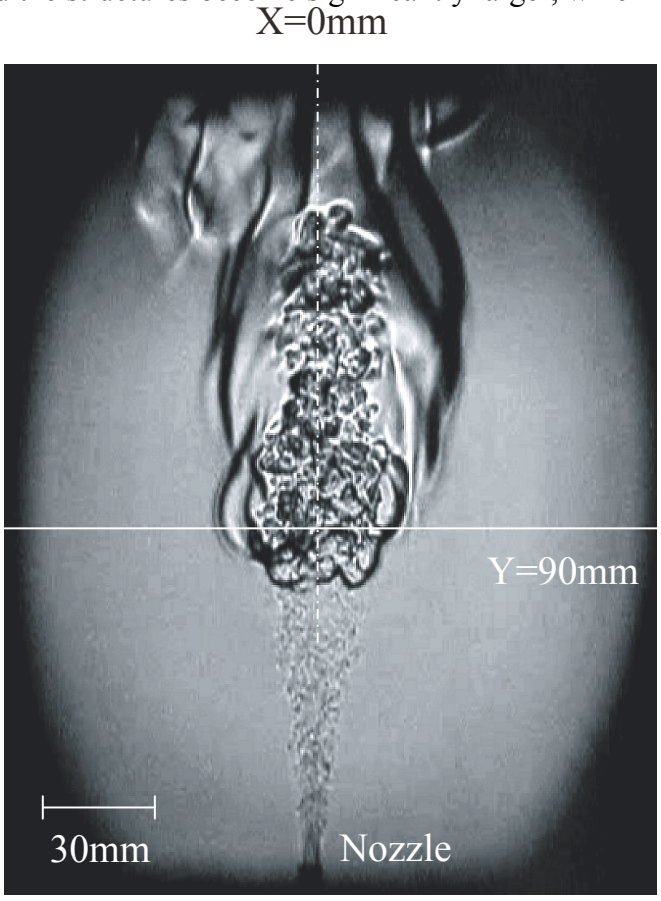

Figure 45: Schlieren visualization of the methane-jet flame. All data evaluations were done at 90 mm height above the nozzle in setup 1.

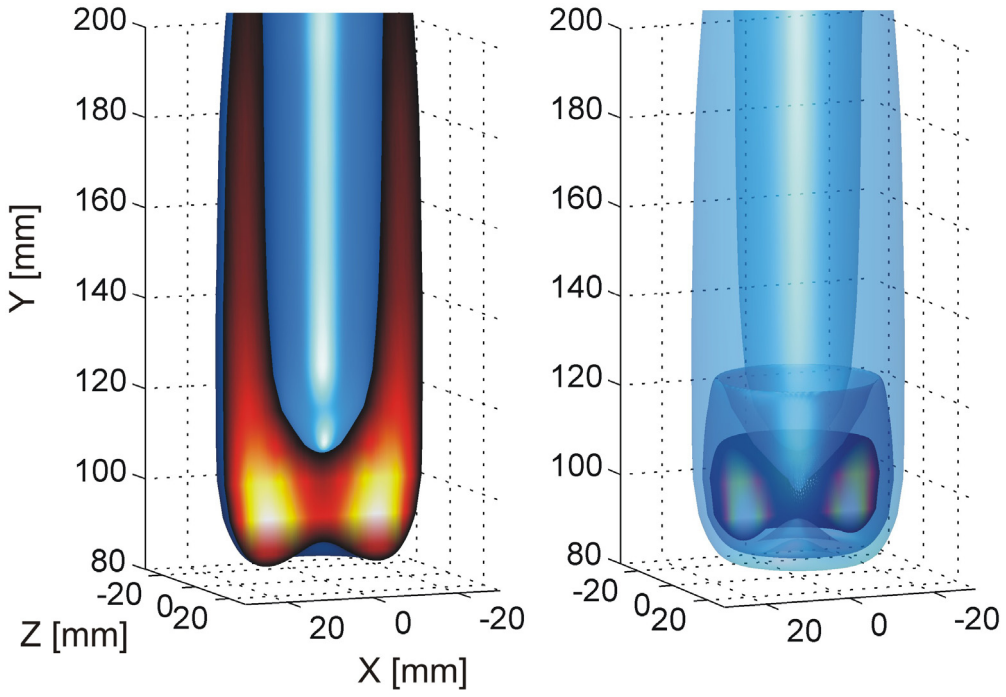

Figure 46: Visualizations of the tomographic reconstruction of chemiluminescence emission data. Isosurface of chemiluminescence emissions and local distribution of chemiluminescence emission in a cross section through the centre axis (left) indicate the position of the main combustion zone. On the right side isosurfaces of chemiluminescence emissions and a cross section of the main combustion zone and the local distribution of chemiluminescence emissions within this zone are shown.

To receive additional information on the combustion process and the zones of major heat release, the spatially-resolved and averaged chemiluminescence emissions of the flame (figure 46) were taken into account. Figure 46 shows a tomographic reconstruction of *CH** chemiluminescence data. Since *CH** chemiluminescence emissions are regarded as a qualitative measure for heat release rates - with some restrictions – the local data of chemiluminescence emission intensity were used to detect the main combustion zones. According to figure 46 (left), the burner provided a cylindrically shaped, tubular flame, where highest values of chemiluminescence emission intensity were found in two regions in the cross-section, located at a height between 80-100 mm and at a radial distance between 10-20 mm away from the centre axis of the flame. This indicates that the main combustion process takes place in a toroidally-shaped region at the bottom of the flame. In this zone the reaction rate reaches a maximum and the main part of the fuel is oxidized, thus resulting in high heat release rates. With increasing height, a decrease of chemiluminescence emissions in intensity as well as in the spatial dimensions of chemiluminescence emissions is observed. This implies that the reaction rates and heat release rates are reduced in the upper region of the flame. All the aforementioned information on the combustion process are only of qualitative nature and have to be handled with care, since the relationship between the local chemiluminescence emissions and the local rate of heat release is characterized by a power law (see equation (28)) with dependencies on the flame temperature, the effects of unsteady strain and the flame curvature.

Especially the dependence on the flame temperature is critical in non-premixed or partially-premixed flames, which is true for the flame investigated here, if quantitative data should be obtained.

Nevertheless the distribution of chemiluminescence emission intensity corresponds quite well to the observations from the schlieren image, furthermore they complement one another. The location of the main combustion zone, according to the chemiluminescence emissions, coincides with the boundary layer between the visible methane-jet in the centre and the large buoyancy-driven structures surrounding the centre-jet from the schlieren image. The main reaction zones and regions of elevated heat release rates are determined by the visualization of the chemiluminescence emissions, whereas the impact of the combustion process on the flow-field is described due to the visualisation of density gradients recorded by the schlieren image. The combination of the schlieren technique together with a visualization of chemiluminescence emissions therefore provides an easy to apply tool for a first qualitative description of the flame.

In a next step a more quantitative measures was needed for a more detailed analysis of the flame behaviour and flame dynamics. Figure 47 presents the radial distribution of the time-averaged mean and fluctuating component of density for the methane-jet flame recorded by differential interferometry (DIF). The mean component of density starts to decrease significantly at Y = 85-95 mm and reaches lowest values at Y = 100-115 mm, located at a radial distance of approximately 15-20 mm from the centre axis. In this region the mean density drops to values around 0.22 kgm^{-3}, which corresponds to a ratio of approximately one to seven compared to air at standard conditions (p = 1.0132 bar and t = 20°C). Near the centre axis the mean density decreases as well at higher heights, but the decline is not so significant. This slower decrease in the mean density near the centre axis can be attributed to the persistent methane-jet that has been already identified in the schlieren image. Since no combustion takes place in the centre-region, the temperature rise in the central jet is caused by the heat transfer from the reaction zones to the centre-region due to conduction, convection and radiation, which takes some time.

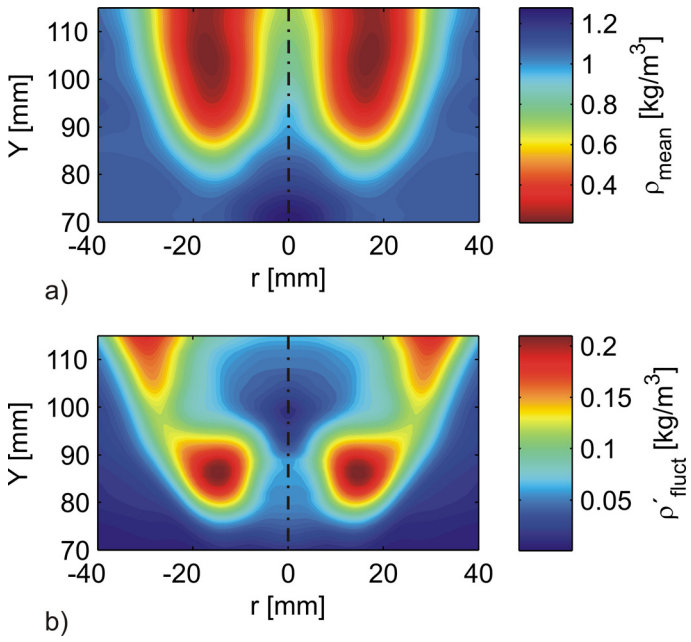

Figure 47: Radial distribution of time-averaged mean (a) and fluctuating (b) density. Data were derived from differential interferometry (800 interferograms recorded).

Highest values of the fluctuating component of density can be found at Y = 80-95 mm, located at a radial distance of approximately 15 mm from the centre axis. These density fluctuations are due to the combustion process initated at this height. The strong fluctuations in the density in this area are in part caused by the movement of the flame front between certain heights (oscillations), and in part by a general variation of the local heat release rate due to changes in the local air-to-fuel ratio caused by the mixing process between the central methane-jet and the surrounding co-flow of air.

Areas of elevated density fluctuations were also identified at Y = 105-115 mm, located at a

radial distance of about 30 mm from the centre axis. In these regions the absolute values of the fluctuating density component are lower compared to the density fluctuations near the main combustion zone, but still significantly higher than for the rest of the investigated area. These density fluctuations are caused by large buoyancy-driven density structures, which shed periodically (at low frequency) from the main combustion zone (for a comparison with a schlieren image see figure 45).

For the validation process of the dual laser vibrometer measurement technique, a detailed investigation of the main combustion zone in the methane-jet flame was performed along a horizontal line at a height of Y = 90 mm. In figure 48 the radial distribution of the time-averaged mean (a) and fluctuating (b) component of density, the time-averaged mean (c) and fluctuating (d) component of velocity, the methane-concentration (e) and the temperature (f) are shown at Y = 90 mm. The velocity data were derived from the LDV measurements, density data from differential interferometry as well as temperature and methane-concentration data from Raman-scattering. The error bars are plotted except for temperature and concentration, where the absolute errors were ±64 K and ±2.2% respectively. For LDV 30000 burst were recorded for each position, therefore the error is below 1%. For all scans recording data on both sides of the jet axis, these data were averaged for the same radial distances to obtain radial symmetric data for all measurement techniques. From LDV and differential interferometry a discrepancy of ±7% was observed between radial symmetric and recorded data sets.

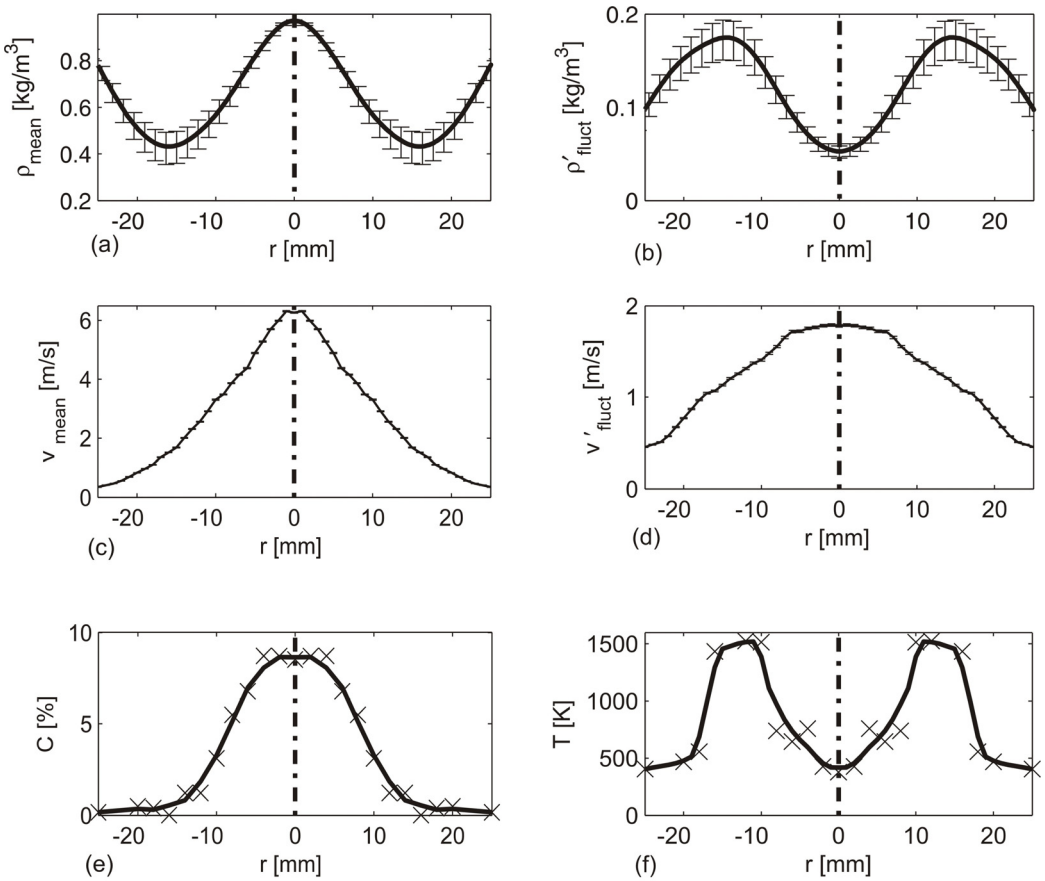

Figure 48: Characterization of the methane-jet flame at Y = 90 mm height about nozzle exit. Radial distribution of time-averaged mean and fluctuating density, in (a) and (b), time-averaged mean and fluctuating velocity, in (c) and (d), concentration of CH_4 in (e) and temperature in (f). Velocity data were derived from LDV, density data from differential interferometry measurements, concentration data from Raman-scattering.

Near the centre axis of the jet the absolute velocity, the absolute density and the methane-concentration have their maximum. The high absolute density and the low temperature in this zone indicate that no combustion takes place in the centre. This assumption is supported by the high values of methane-concentration in the same area. The methane-jet is still present near the centre and velocity and density fluctuations are mainly due to the methane-jet.

From these scans a cylindrical combustion zone can be located at a radial distance of approximately 12-15 mm from the centre axis at Y = 90 mm, indicated by low values of absolute density and high temperatures. Density fluctuations are also high in this zone. Recalling equation (1), the first derivative in time of density fluctuations is proportional to pressure fluctuations and heat release. As the burner was operated under atmospheric conditions, pressure fluctuations are thought to be small compared to the heat release, when combustion takes place. Thus high density fluctuations serve as an indicator for the combustion zone. As soon as density fluctuations start to increase, the methane-concentration decreases and converges towards zero, supporting this theory. Outside of a radius of approximately 20 mm the absolute density increases again and density fluctuations decrease. In this zone no combustion takes place, but from schlieren visualization large vortex structures were identified, which are buoyancy driven and move slowly upwards.

Figure 49 illustrates data of the physical cross-spectra in the methane-jet flame recorded from different scanning directions. For the methane-jet burner the same measurement points at one line along the flame diameter at Y = 90 mm were scanned from different directions and the results obtained from these scans were averaged afterwards to damp down artefacts. In figure 49 results for three different directions from 0° to 45° are presented. The measurement unit in the plots is (kgm^{-2}), this implies that the voltage signal of the vibrometer has already been converted to the unit of a density integrated along the beam path, but has not been calibrated yet. According to equation (81), chapter 3.5.4 "*Dual laser vibrometry*", the cross-spectrum *C(f)* has the physical unit((kgm^{-2})^2), but to improve the visibility at higher frequencies, the square-root of the cross-spectrum is displayed in figure 49, which is equal to an amplitude spectrum. However the plots already present local, frequency-resolved distributions of density fluctuation data, but to receive the absolute values for each frequency the cross-spectra need to be corrected by the frequency-dependent, effective measurement area A_c, which is related to the size of the recorded density structures and corresponds to the area of the physical correlation within the dimensions of these structures.

Values for A_c can be obtained through a reasonable theoretical model or an experimental calibration, for example by comparison of the results with local pressure measurements (Hampel and Woisetschläger 2006). In the experiments presented here local pressure measurements could not be performed, as no fast pressure sensor was available that could resist environmental conditions in the flame and due to the fact that density fluctuations are proportional to pressure fluctuations and heat release in the flame, according to equation (1).

For this evaluation local data obtained by tomographic reconstruction of integral data recorded by a single laser vibrometer were compared to the local correlation data recorded by the dual laser vibrometer technique for radial positions between -25 and 25mm and values for A_c were estimated, see figure 50(a). In case of the atmospheric methane-jet burner this is possible since no windows limit the view and tomographic as well as correlation techniques can be applied simultaneously.

As mentioned above, the low frequency density fluctuations located in the outer sections are buoyancy driven and move slowly upwards (1.5 ms^{-1}), while the high frequency oscillations are caused by the methane jet rising at high speed (6.5 ms^{-1}). At intermediate frequencies the velocity depends strongly on the structure size and therefore on the frequency (see also equation (84), chapter 3.5.4 *Dual laser vibrometry*).

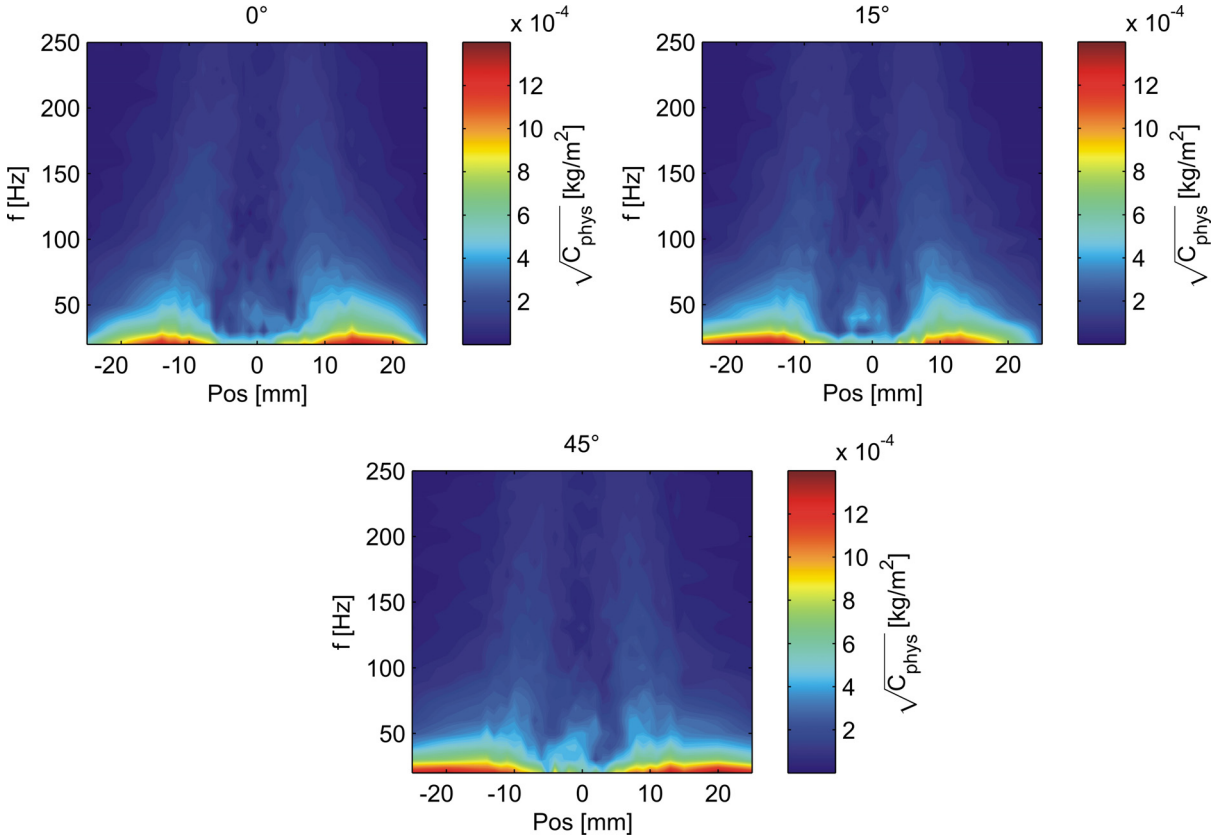

Figure 49: Distribution of physical cross-spectra in the flame according to laser vibrometer measurements at a height of Y = 90 mm above the exit nozzle and recorded from different scanning directions. A total number of seven scanning directions was used to damp artefacts in the investigated flow-field.

Such dependence can be investigated by placing two laser vibrometer beams parallel to each other and perpendicular to the jet axis at a few mm distance to each other. From the phase lag between the correlated signals a frequency dependent ensemble averaged velocity can be estimated (Giuliani et al. 2010).

Figure 51 presents the phase lag along the Y-axes for the 60 Hz frequency. For density fluctuations at this frequency a uniform phase lag or velocity of 1.8 ms^{-1} was observed. When compared to the LDV velocity data this indicates that these structures were localized at radial positions 12 mm away from the jet axis. This was also confirmed from the dual laser vibrometry recordings (see figure 49). The structures present in a flame are not necessarily of rotational symmetry in all directions, which can be seen in the schlieren visualization in figure 45, therefore the characteristic length l (equation (84)) describes the spatial dimension of these structures in flow direction only.

From evaluations similar to the one presented in figure 51 the ensemble averaged velocity of frequencies 10-50 Hz was also estimated. This was necessary since in this low frequency range not only high amplitude density fluctuations occur, but background noise (e.g. vibrations) is also significant. Since uncorrelated integral data from single laser vibrometer recordings were used for tomographic reconstruction, these data might well contain vibrational noise at low frequencies.

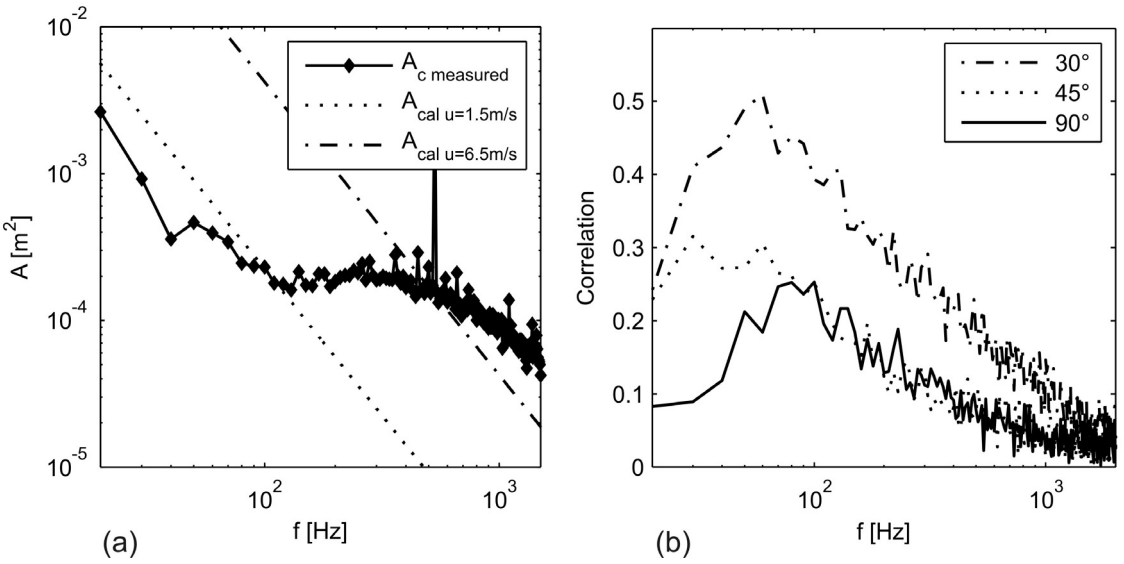

Figure 50: Effective measurement area A_c (a) estimated by comparing the tomographic reconstruction and the dual laser vibrometer correlation technique. The influence of changing the intersecting angle between the two laser beams (b) between 30° to 90° can be seen from the correlation (correlated power K *averaged for all scanned position) plotted versus the frequency.*

So, for these frequencies the effective measurement area was verified by equation (84) and the recording of ensemble averaged velocities was tested by placing two laser vibrometer beams parallel to each other and perpendicular to the jet axis. These recordings indicated, that the effective measurement area obtained by tomographic reconstruction of integral data from a single vibrometer, had to be corrected at low frequencies from 10-50 Hz, since these structures move upwards much slower than 1.5 ms^{-1}.

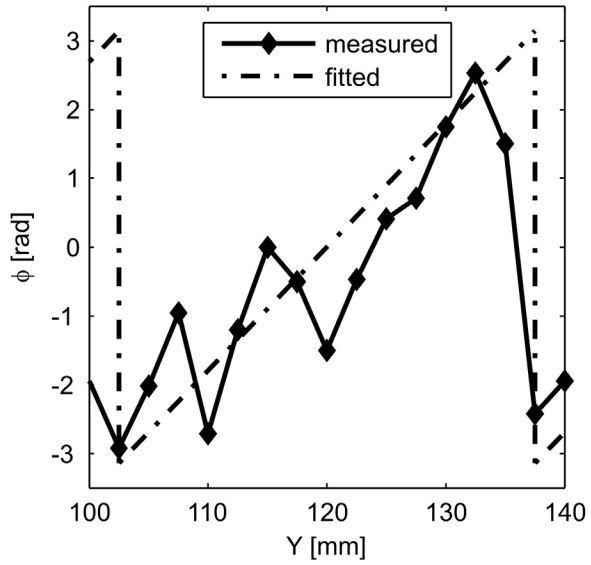

Figure 51: Characteristics of the phase lag between two parallel laser vibrometer beams perpendicular to the jet axis at 60 Hz, recorded with one fixed vibrometer at Y = 90 mm and the second vibrometer scanning along the Y-axes. From the phase lag an averaged velocity for density structures can be estimated.

In combustion chambers the optical access is limited and a change in the intersecting angle between the two laser beams might become necessary when a dual laser vibrometer technique is applied to record local data. Additional measurements with intersecting angles other than 90° were performed to observe the influence of the angle on the effective measurement area A_c and the measurement result. The influence of this intersecting angle can be seen from figure 50(b) and the correlation (correlated power K averaged for all scanned position) plotted versus the frequency. A sudden increase in correlation first at low

frequencies and then for all frequencies indicates that the measurement regime starts to change towards the integral line-of-sight measurement of a single laser beam interferometer when the intersection angle narrows. Since this loss in local information involves the large density structures first, it will become noticeable in the correlation at low frequencies first. When both laser beams overlap completely the correlation will become one for all frequencies, all local information will be lost, the data will present integral line-of-sight measurements only. If the relative correlation is high in the whole flow-field and at all frequencies, the intersecting angle is too small and the measurement results are not valid. At 30° the values for the correlation were significantly elevated (about two times) compared to values obtained by measurements performed at 45°, 75° and 90° which were quite similar when compared to each other. Since the reference burner provided complete optical access all the measurements were performed with an intersecting angle of 90° between the two laser beams.
According to equation (75) the measured integral signal along the beam path is proportional to a calibration factor, the voltage signal and the Gladstone-Dale constant. As the Gladstone-Dale constant changes along the beam path according to the varying gas composition in the flame, the gas composition must be known to get absolute data of density fluctuations. In this work the Gladstone-Dale constant was calculated, using concentration data from the Raman measurements.

Figure 52(a) presents the radial distribution of spatially- and frequency-resolved density fluctuations in the frequency domain from 20-250 Hz recorded by the dual laser vibrometer technique discussed in chapter 3.5.4 ”*Dual laser vibrometry*”. Seven different scan directions were used. The highest values of density fluctuations can be found in the low frequency range and density fluctuation amplitudes decline significantly when frequency increases. Along the central flow axis a region of small amplitude density fluctuations is present especially at frequencies above 100 Hz. In this zone near the centre and 90 mm above the orifice no combustion takes place and this area corresponds to the methane-jet (see figure 47(e)).

This central region is surrounded by ring-like areas with higher values of density fluctuations, which become narrower at higher frequencies. As high values of density fluctuations are mainly due to heat release under atmospheric conditions, these areas indicate that a combustion process takes place. If it is assumed that turbulent structures in the flow have the same diameter in all three dimensions and are transported with the flow, additional information on the distribution of these structures can be revealed from laser vibrometer data (figure 52(a), amplitude spectrum), as the frequency can be linked to the size of the structures by the recorded velocity values. High values of density fluctuations at very low frequency indicate big structures located annularly around the centre, which move upward slowly. Near the centre, structures get smaller indicated by higher frequencies and the narrower ring-shaped areas of maximum density fluctuations.

If there is physical correlation outside the measurement volume in the flow-field caused by sound waves or large correlated structures, the measured signal obtained from the cross-spectrum could be too high. Thus, high correlation can indicate a high probability of artefacts, or an artificially elevated signal level. To judge measurement results, the relative correlation defined in equation (86) is helpful, as it quantifies the fraction of correlated power in the cross-spectrum.

Artefacts occur when large coherent structures are present in the flow. As these structures are normally produced by large density oscillations or sound waves, they show a narrow band spectrum and appear as local peaks in the spectrum together with a high relative correlation. This is also true for unwanted surface vibrations or electronic noise in the 50 or 100 Hz range, but these erroneous frequencies will be present for all scanned positions and therefore can be identified easily. None of these vibrations or electronic noise is present in the results shown in figure 52.

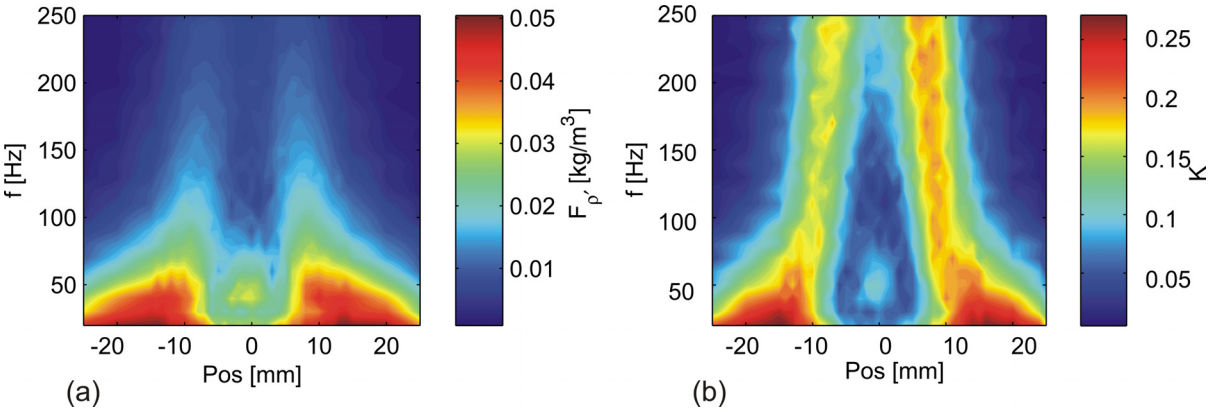

Figure 52: Density fluctuations in the flame according to dual laser vibrometer measurements at Y = 90 mm (a) and relative correlation K at the same position (b). At a frequency of 40–70 Hz a result with high physical correlation in the core region is present.

In figure 52(b) the relative correlation *K(f)* is shown. The shape of the relative correlation *K(f)* corresponds to the spectrum of density fluctuations in figure 52(a) and high relative correlation is only present at certain regions where the density fluctuations are strong itself, which indicates good results. Only in the centre-region between 40-60 Hz and between +/-5 mm a local peak can be found in figure 52(a) and (b). In this area no combustion takes place, but density fluctuations and relative correlation are high. So it is very likely that the measurement results in this area are elevated by artefacts, e.g. sound waves caused by the methane-jet emerging from the nozzle or correlated ring like structures in the combustion zone producing artefacts in the centre.

Another possibility to identify artefacts is the phase of the cross-spectrum, as mentioned in chapter 3.5.4 "*Dual laser vibrometry*". Figure 53 presents the phase distribution for two different scanning directions at 0° and at 45°. The value of the phase is close to zero for the main parts of the section, which implies that the magnitude of the cross-spectrum in these areas stems from the intersection volume between the two laser beams, thus the cross-spectrum is not falsified due to artefacts and can be attributed directly to density fluctuations in the measurement volume. At the centre-region in the range from 20-140 Hz and at higher frequencies in exterior areas the phase values differ from zero significantly.

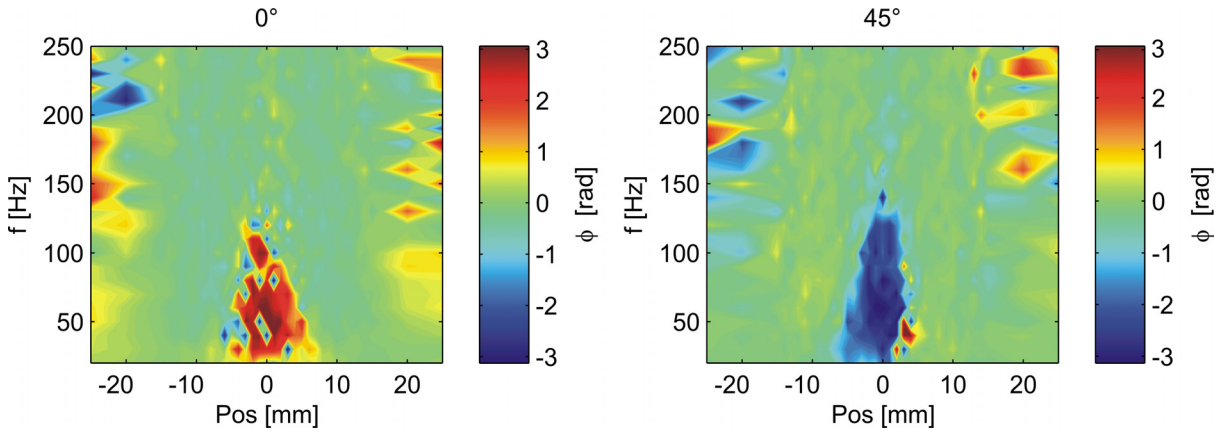

Figure 53: Phase distribution for two different scanning directions at 0° and at 45°. The value of the phase is close to zero for the bigger parts of the section, except in the centre-region from 20–120 Hz and at higher frequencies in exterior areas the phase values differ from zero significantly.

Phase values different from zero are due to the frequency-wise and averaged time delay of the equal parts of both vibrometer signals and could indicate a falsified measurement signal in this area. The non-zero phase values in the centre-region are caused by large, coherent density structures that develop in the combustion zone. Due to their large dimensions, it is likely, that theses structures are present in both laser beams beside the measurement volume (overlapping volume of both laser beams), and that the signal from these structures is attributed falsely to the measurement position tested. In this case, the application of phase filtering from equation (85) can help to reduce these artefacts. In figure 54 the phase-filtered cross-spectrum (filter width $\Delta\varphi$=1 rad) can be seen. As the cross-spectrum at 20-140 Hz and +/- 5mm is too high, most likely due to artefacts, the phase filtering reduces the magnitude of the results especially in this area, whereas the rest of the measurement result is barely changed. This indicates that the measured signal generally corresponded to effective density fluctuations and was not elevated by artefacts, apart from the area in the centre-region where the measured signal has to be corrected by the filter.

Figure 55 presents slopes of density fluctuations for certain frequencies selected from figure 54, where the scaling of the y-axis was adapted to the maximum amplitude of density fluctuations for each frequency to display the slopes at higher frequencies, which can not be seen in figure 54 due to their small amplitude compared to the density fluctuations at low frequencies. Besides the spatial resolution, which can be also provided for certain applications by differential interferometry combined with tomographic re-constructions techniques, this plot reveals another main advantage of the dual laser vibrometer technique, the frequency resolution of the density fluctuation data.

The maximal amplitudes of density fluctuations at low frequencies (represented by the 40 and 60 Hz plots) are located at almost the same distance from the centre axis as the maximal density fluctuations recorded by differential interferometry (see figure 47) and can therefore be referenced to the same source (movement of the flame front and variation in the local heat release rate causing large structures to move with corresponding density fluctuations). At higher frequencies the local maxima of density fluctuations are found at distances closer to the centre axis and the dip near the centre axis starts to decrease. At 540 and 570 Hz this dip has almost diminished and a plateau of elevated amplitudes of density fluctuations can be found between Pos =-10 to 10 mm. Additionally the amplitudes of density fluctuations at higher frequencies (540 and 570 Hz) are lowered by approximately one order of magnitude compared to the density fluctuations at 40 or 60 Hz.

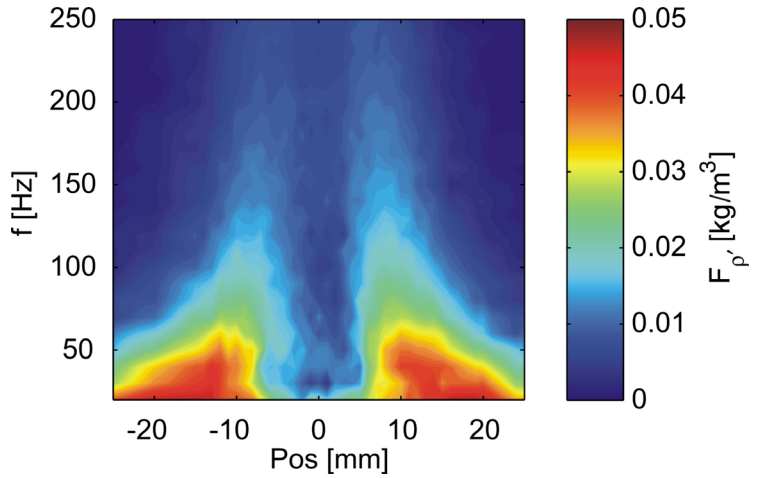

Figure 54: Local distribution of the density fluctuations in the flame according to dual laser vibrometer measurements at Y = 90 mm. A filter with bandwidth $\Delta\varphi$=1 rad was applied.

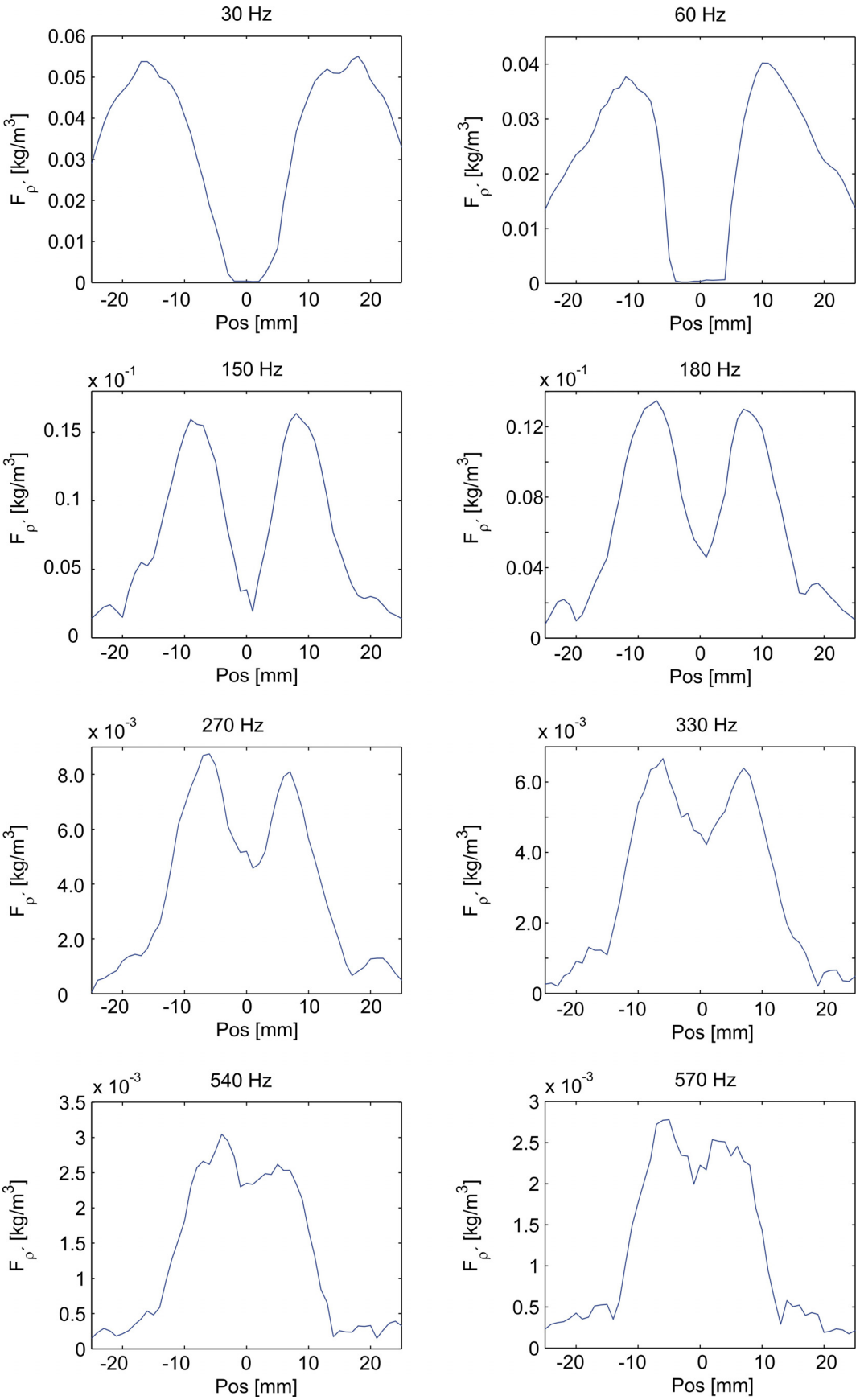

Figure 55: Local distribution of density fluctuations as recorded by dual laser vibrometry in the flame for different frequencies. Highest amplitudes of density fluctuations are found at low frequencies. Slopes of density fluctuations vary significantly with the frequency.

Validation of dual laser vibrometer data by differential interferometry

A validation of the laser vibrometer measurements was done by comparing the results recorded by the dual laser vibrometer technique (correlation method) and data of density fluctuations obtained from a tomographic reconstruction of the density field from a single projection recorded by differential interferometry (figure 48(d)). While density fluctuations at all frequencies contribute to the differential interferometer data, the laser vibrometer data always present frequency-resolved density fluctuations and had to be integrated for all frequencies numerically. This integration must be performed in the power spectrum. Figure 56 presents the comparison between the different measurements techniques, differential interferometer and correlated dual laser vibrometer data with and without phase filter.

Since the tomographic reconstruction from differential interferometry is based on only one observation direction, all data were symmetrised for comparison. Data were calculated with the concentration dependent Gladstone-Dale constant (equation (16), chapter 3.2 "*Shadowgraph- and schlieren-visualization*") according to the gas composition obtained from Raman-scattering. For the results obtained by differential interferometry no concentration correction was performed. The filtered dual laser vibrometer data show significant lower values especially in the centre of the distribution, where artefacts from ring-like correlated structures might easily form. In this case the filter function from equation (9), with parameter $\Delta\varphi$=1 rad was applied to the cross-spectrum to reduce the influence of sound waves propagating through the flow-field and vortex structures correlated over large areas of the field (see also figure 54).

The influence of artefacts in the central region is clearly seen, with a significant reduction of these artefact by application of a phase filter function ($\Delta\varphi$=1 rad). It must be also kept in mind that an up- and downwards oscillatory motion of the flame also caused a correlated density change and will result in a high correlation of the signals at these low frequencies with little or no phase shift between the laser vibrometer beams. From an experimental point these fluctuations must be attributed to 'real' density fluctuations, while they will not be found in any numerical simulation, where the flame lift position is numerically fixed.

On the other hand differential interferometry is always integral with a need for tomographic reconstruction, and both processes acting as low-pass filters, smoothing out high-frequency, small-sized structures. Nevertheless both techniques compared in figure 56 agree within less than 10%.

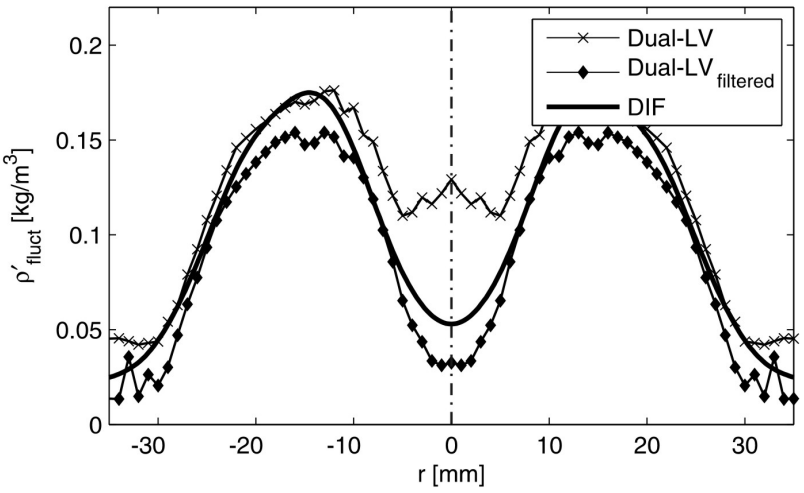

Figure 56: Comparison of density fluctuations between differential interferometer (integral data) and laser vibrometer measurements (tomographic reconstruction from integral data and local data obtained by the dual laser vibrometer correlation technique).

4.3.2 Setup 2

For the experiments performed in setup 2 (settling chamber replaced by a chopper system), combustion instabilities were forced by modulating the methane-flow at a certain frequency of 30 Hz. In figure 57, colour-schlieren images of the non-premixed methane-jet flame for this second configuration can be seen, providing phase-resolved images for one oscillation period at (a) 0, (b) $\pi/2$, (c) π and (d) $3/2\pi$. At the beginning of the oscillation period (figure 57(a)) no methane-flow is present in the core region, as the rotating toothed wheel blocked the choked nozzle in the chopper system at that time, thus only the large surrounding structures are visible. The methane-flow increases in figure 57(b) and reaches a maximum in figure 57(c). At that time the choked nozzle was completely unblocked. In figure 57(d) a decrease in the methane-flow can be seen. Compared to standard schlieren technique, the colour-schlieren technique benefits from information on the direction of the density gradient. Different colours in the image characterize increasing density gradients in different directions, with the direction of the density gradients indicated by an arrow.

Figure 58(a) presents the radial distribution of spatially-resolved cross-spectra in the frequency domain from 20 to 250 Hz recorded by the dual laser vibrometer technique at Y = 90 mm above the jet nozzle from one scanning direction. Measurements were performed for only one line along the flame diameter due to the almost axis symmetric shape of the flame, but this line was again scanned from seven different directions to average out artefacts. In figure 58(b) the corresponding phase distribution can be found. Values for the phase are generally close to zero and non-zero values of the phase are only present in a small area near the centre axis around 50 Hz and in the border regions of the image, where the cross-spectrum tends to zero.

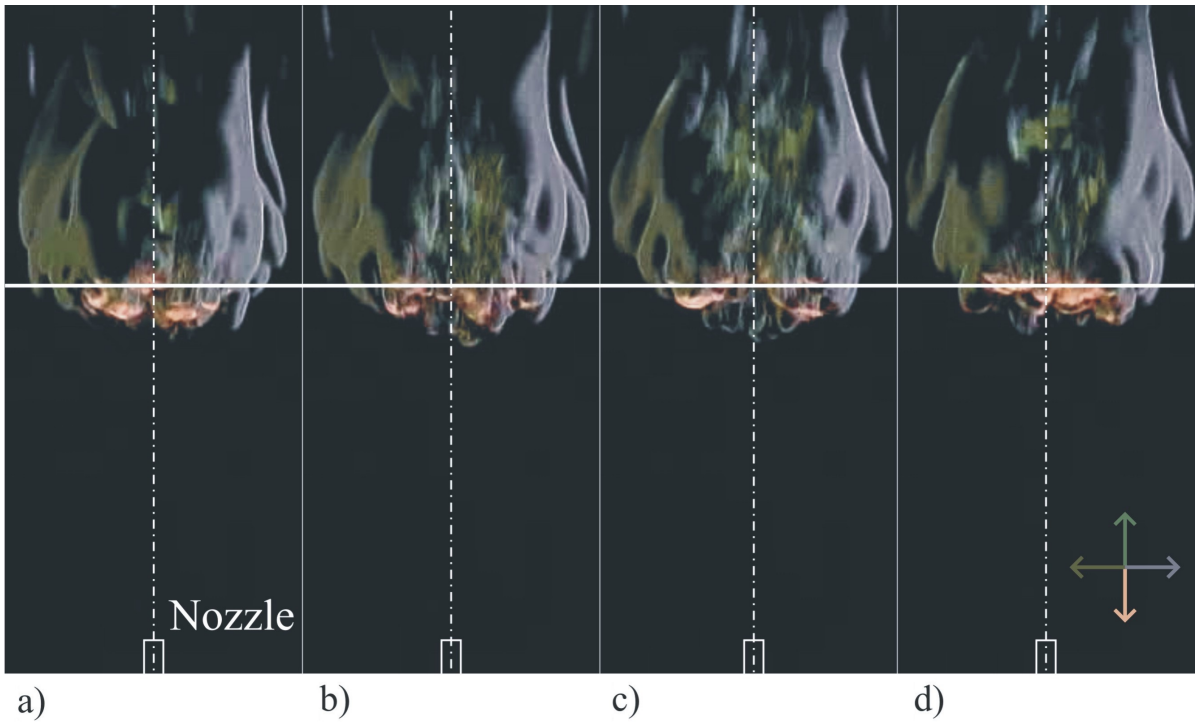

Figure 57: Colour-schlieren visualization methane-jet diffusion burner. A chopper system to enforce controlled flow oscillations in the methane-flow at a frequency of 30 Hz was used in this setup. Different phases at (a) 0, (b) π/2, (c) π and (d) 3/2π are shown.

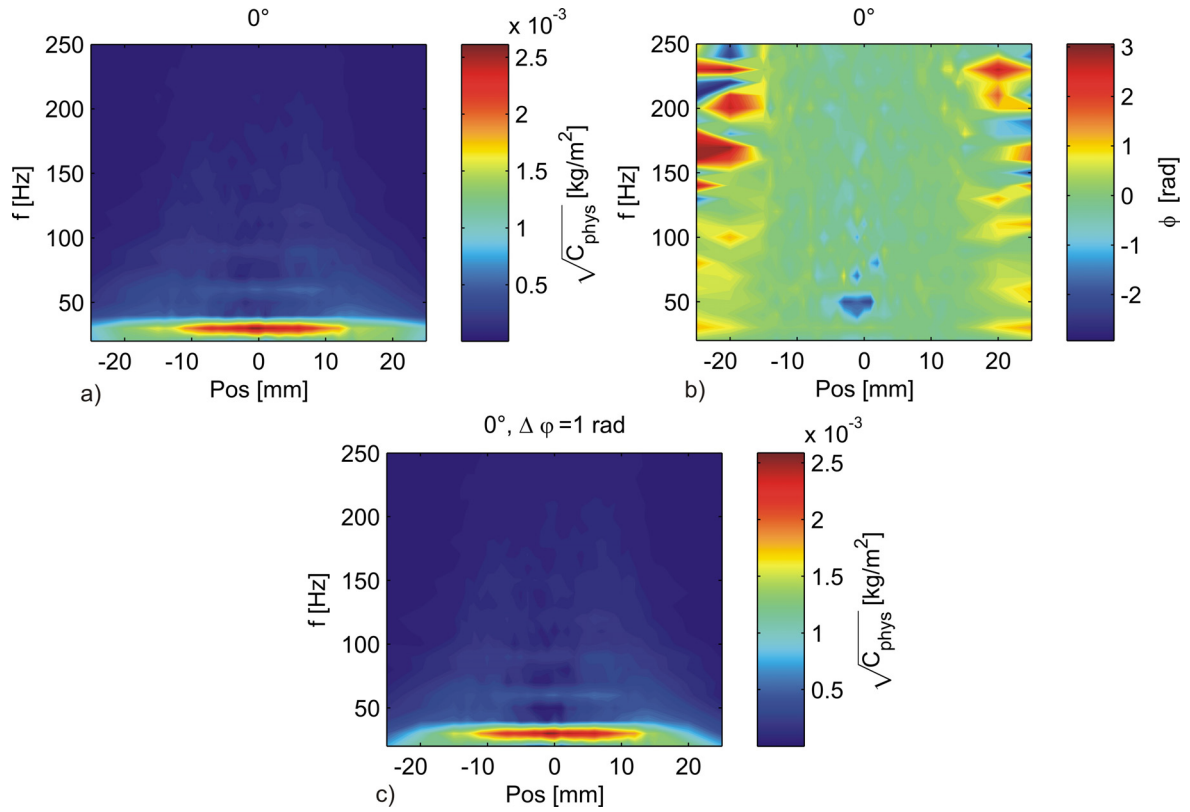

Figure 58: Magnitude of the physical cross-spectrum recorded in the pulsed flame (a) and corresponding phase distribution (b) for one scanning direction. In (c) a filter (bandwidth $\Delta\varphi$=1 rad) was applied to the data of the physical cross-spectrum from (a).

If the magnitude of the cross-spectrum tends to zero, the phase difference between the two vibrometer signals becomes more or less arbitrary and the phase values do not equal zero. In this case the phase does not provide any information on artefacts in these regions and even the appliance of the filter function does not change the results, due to the low magnitude of the cross-spectrum. A phase filter of $\Delta\varphi$=1 rad was used in figure 58(c) to obtain the filtered data of the cross-spectrum for all areas with sufficient magnitude. The differences between the unfiltered and filtered results are very small in this case and the magnitude of the cross-spectrum was affected by the phase filter only in a small area near the centre axis in the frequency range around 50 Hz, indicating that the measurement results for the unfiltered cross-spectrum were generally not influenced by artefacts in the flow.

The highest values for the magnitude of the cross-spectrum can be found at a frequency of 30 Hz at a radial distance from -10 to 10 mm. This peak corresponds to the oscillation frequency excited by the chopper system. The chopper system created a strong fluctuation in the methane-flow and exerted a significant influence on the combustion process by modulating the local equivalence ratio in the flame. The fluctuating fuel-flow resulted in combustion instabilities triggered at 30 Hz.

To receive quantitative data of spatially- and frequency-resolved density fluctuations the cross-spectra were corrected by the same effective measurement area A_c that was already used for the stable flame without forced combustion instabilities (figure 50(a)). Figure 59(a) shows the radial distribution of calibrated density fluctuations for the second experimental setup with the methane-flow modulated at 30 Hz. As combustion instabilities are characterized by elevated pressure fluctuations and heat release rates at certain frequencies, their identification can be easily done in density fluctuation plots.

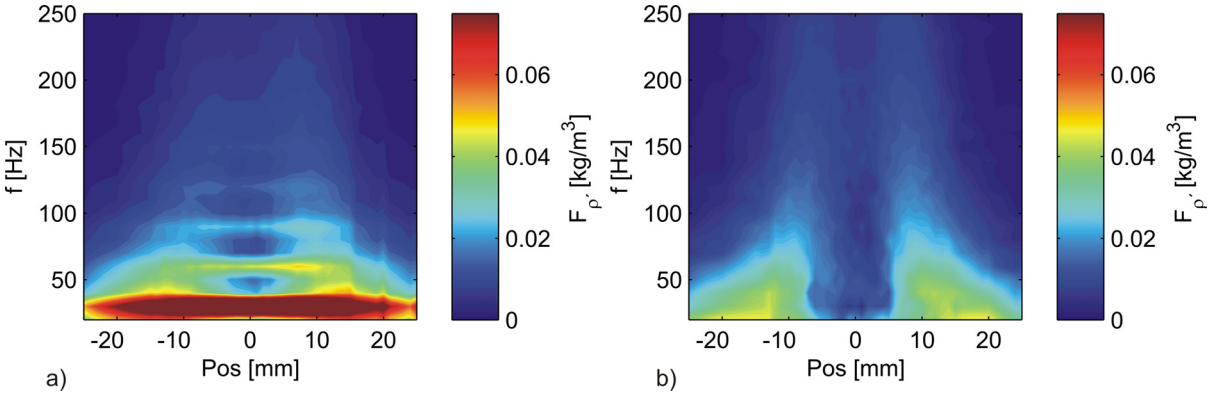

Figure 59: Local distribution of the density fluctuations at Z = 90 mm in the pulsed (a), and in the unpulsed flame (b). Radial coordinates are used.

Compared to figure 59(b), elevated values of density fluctuations are clearly visible at 30 Hz and at higher harmonics in figure 59(a). Increased values of density fluctuations are present all along the flame diameter at the frequency of excitation, also in the centre-region of the non-reacting methane-jet. This corresponds quite well to the colour-schlieren visualization (figure 57), where this fluctuating methane-flow is clearly visible. So on the one hand dual laser vibrometry can be used to investigate the combustion process itself on the other hand it offers a convenient opportunity to detect combustion instabilities. The additional advantage compared to other measurement techniques used to observe combustion instabilities, e.g. microphones or pressure probes, is the fact that dual laser vibrometry provides local data. Therefore the source of instabilities can be detected.

Figure 60 shows a comparison between local data of density fluctuations recorded in the pulsed flame and in the stable flame for different frequencies. The slopes between the pulsed and stable flame differ according to the observed frequencies. Density fluctuations at 30 Hz in the pulsating flame are nearly three times higher in amplitude then the density fluctuations at the corresponding frequency in the stable flame. Additionally the slopes show large differences, when compared to each other, since highest values of density fluctuations in the pulsating flame can be found in the centre-region, whereas maximal amplitudes of density fluctuations are located at a radial distance of -15 and 15 mm away from the centre axis in the stable flame. Moreover density fluctuations in the centre-region in the stable flame are almost zero at 30 Hz.

Aside of the excitation frequency, the recorded density fluctuations are in the same order of magnitude for the pulsed and the stable flame and the slopes are more or less similar in their appearance (see figure 60, 40 and 80 Hz). The peaks in the amplitude of the density fluctuations are located at nearly the same positions for the pulsed and the stable flame, only the amplitude of density fluctuations in the centre-region tend to be higher in the pulsating flame. The systematically higher amplitudes in the centre-region at the investigated frequencies indicate an increased level of turbulence in the methane-jet due to the flow excitation by the chopper system, which is also present in the excitation frequency. At the first harmonic frequency the amplitudes of the density fluctuations in the pulsed flame exceed the peak amplitudes for the stable flame only slightly but the slopes vary significantly. The largest deviations between the two slopes can be found again in the centre-region.

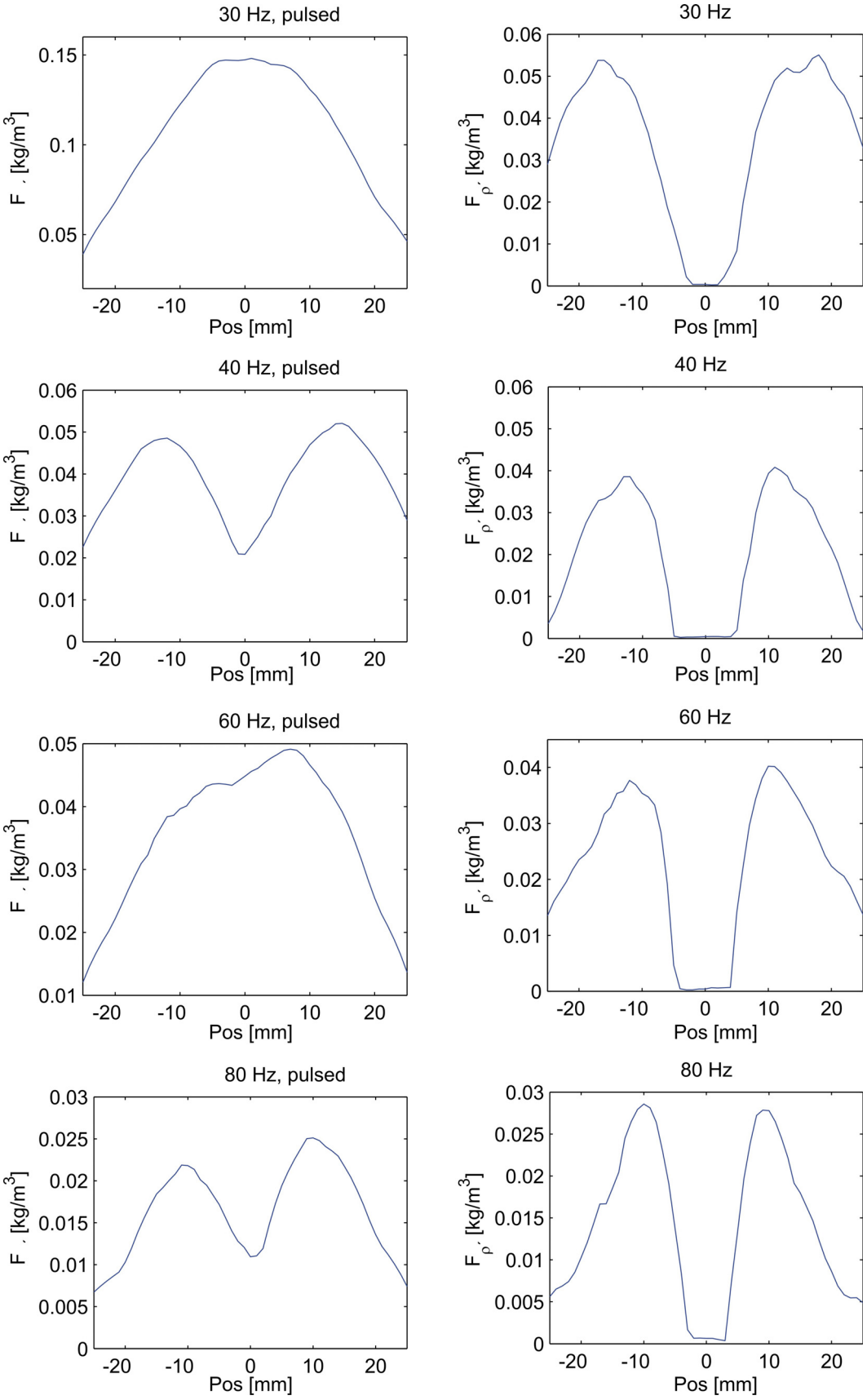

Figure 60: Comparison between local data of density fluctuations recorded in the pulsed flame and in the stable flame. Great deviations can be found at the excitation frequency and the corresponding first harmonic frequency, at 30 Hz and at 60 Hz respectively.

4.3.3 Setup 3

Changing the fuel from pure methane to a nitrogen-methane blend and setting the co-flow of air to zero at the same time led to some changes in the appearance of the flame discussed in setup 3. Due to the reduced mass-flow of fuel and the lower exit velocity at the fuel nozzle, the dimensions of the flame were reduced but the flame was still lifted in this configuration. This is confirmed by the cone-shaped fuel-jet emitted from the central nozzle that can be seen in figure 61. As soon as the fuel-blend reaches the combustion zone and ignites, the appearance of the flow-field in the schlieren image changes. The central fuel jet, now surrounded by large structures, persists in the flame for a while and diminishes with increasing height. The same flow-phenomena have been observed in the methane-jet flame, at the operating conditions from setup 1.

However, the change in fuel and the absence of the stabilizing co-flow of air also led to a less stable flame, with respect to the location of the main combustion zone. The series of schlieren images in figure 61 illustrates that the spatial location of the main combustion zone alternates significantly in terms of height, symbolized by the dashed lines.

To get a better idea on the flow-field dynamics and the evolution of density structures caused by the combustion process, a high-speed schlieren visualization was performed, recorded at a sampling speed of 150 fps. Compared to the methane-jet flame, the nitrogen-methane jet is laminar at the nozzle exit according to the schlieren images and transition from a laminar to a turbulent jet takes place 1-2 cm downstream of the nozzle exit. The position of the transition changes in time (see figure 62, dashed ellipse), which could be the source for the less stable combustion process in this setup.

Additionally the evolution and propagation of one large density structure is marked in the schlieren images (green lines). These large density structures develop due to the thermal expansion of the hot gases caused by the combustion process. For the thermal expansion of gases two main directions can be identified in the schlieren images. First, the hot combustion gases propagate outwards and at the same time downwards, reverse to the main flow direction. The downwards propagation decelerates very soon and comes to an end; meanwhile the structure still expands in the lateral direction. Afterwards the density structures starts to propagate in the main flow direction again, and the lateral expansion slows down as well. The structure propagates further in the flow direction and a new density structure evolves. The schlieren images presented in figure 62 cover a time period of approximately 0.05 s, indicating that the large density structures evolves at very low frequencies ranging from 10-30 Hz.

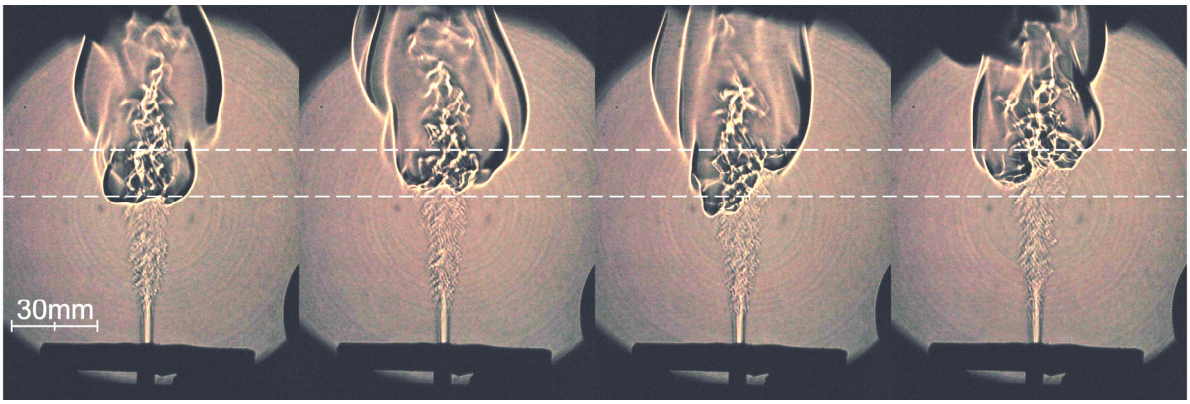

Figure 61: Series of schlieren images for the nitrogen-methane flame. At these operating conditions the main combustion zone alternates significantly in terms of the vertical location.

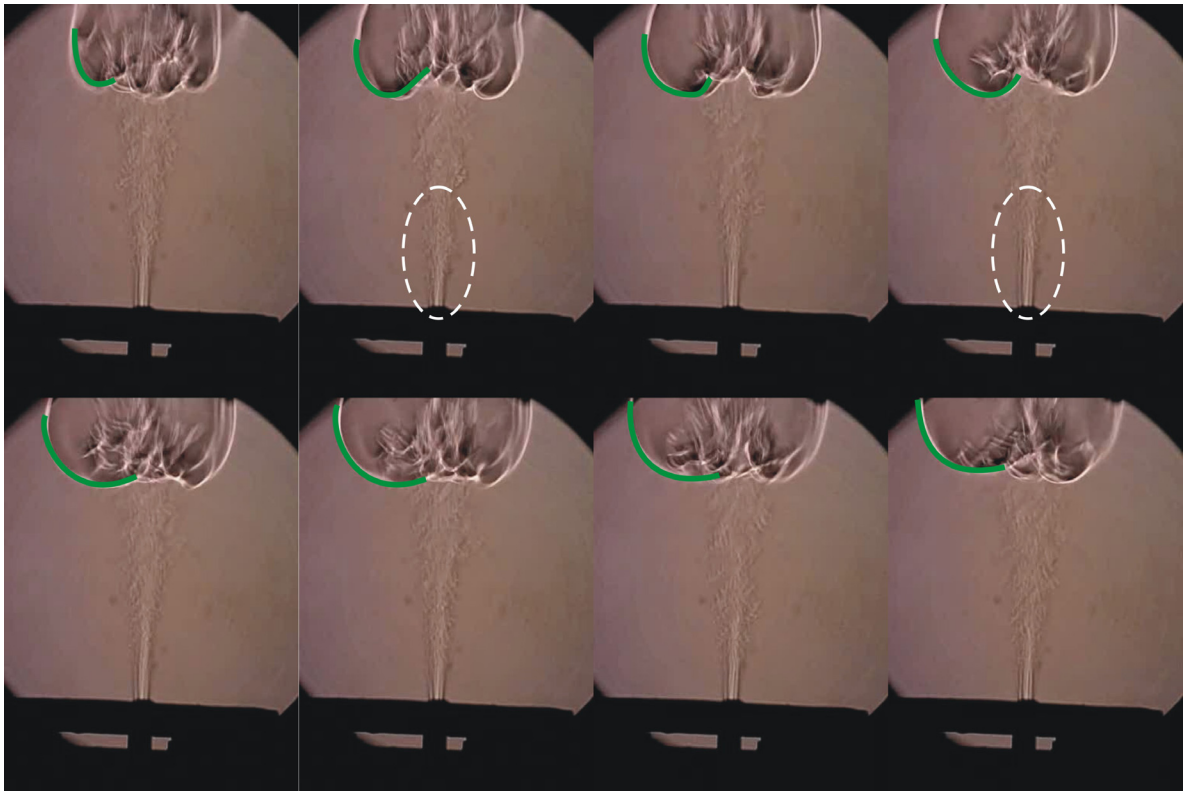

Figure 62: Series of schlieren images recorded at 150 fps, resulting in a time difference of 0.0067 s between the single frames. The time series presented covers a time period of 0.046 s. Movements of a hot bubble (green lines) and variations in the transition position from laminar to turbulent flow in the methane-nitrogen jet (white, dashed lines) are marked in the images.

Spatially-resolved and averaged data of chemiluminescence emissions of the flame, obtained by a tomographic reconstruction of integral data are presented in figure 63. The tomographic reconstruction data show a cylindrical shaped, tubular flame with peak areas in the local chemiluminescence emission intensity located at the bottom region of the flame at a radial distance between 10-15 mm away from the centre axis. In this main combustion zone the main part of the fuel is oxidized and local heat release rates are therefore maximal. With an increase in height, the chemiluminescence emissions start to decline and near the centre axis the chemiluminescence emission intensity is rather low.

Generally the appearance of the nitrogen-methane flame seems to be similar to the methane-jet flame with the co-flow of air. For a qualitative comparison between the two flames, the obtained chemiluminescence emission data were normalized for each flame and compared to each other in a cross-section along the centre axis in figure 64. Despite the differences in the flame dimensions, the variation in the intensity of the relative chemiluminescence emissions between regions of low emissions and regions of high emissions are much more pronounced in the methane-jet flame, e.g. the peak area of chemiluminescence emissions at the bottom of the flame significantly differs from the rest of the flame, whereas no such steep gradients are found in the nitrogen-methane flame. In the methane-jet flame most of the fuel seems to react with the oxygen in these peak areas at the bottom, whereas in the nitrogen flame the reaction of fuel and oxygen seems to be more distributed.

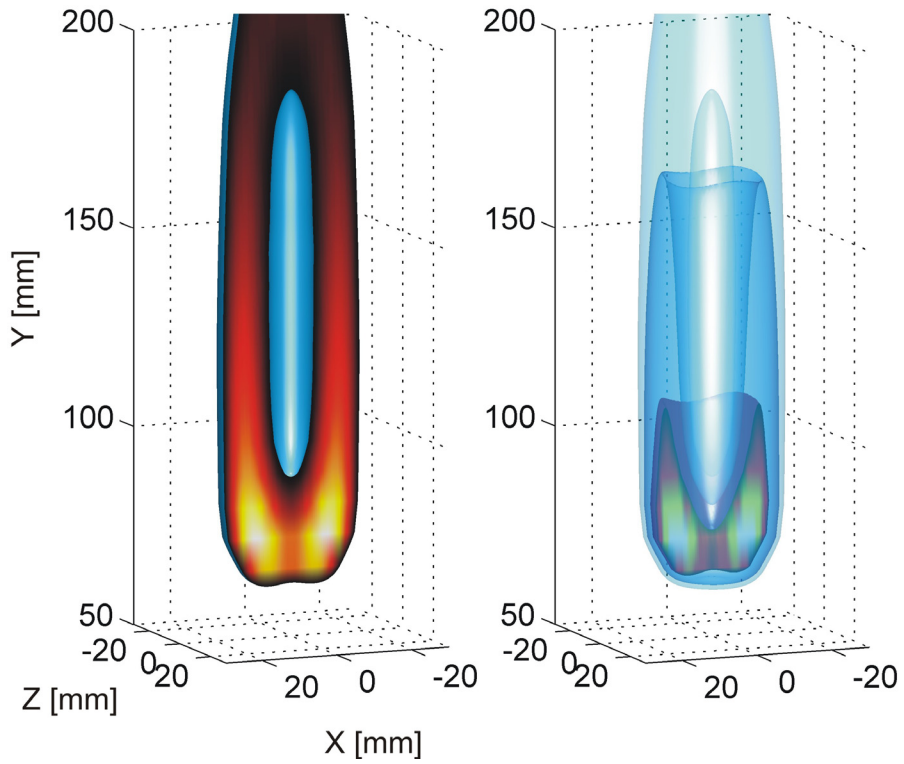

Figure 63: Visualizations of the tomographic reconstruction of chemiluminescence emission data for the nitrogen-methane flame.

A possible explanation for this phenomenon might be a better premixing of fuel and air in the methane-jet flame due to the higher exit velocity at the fuel nozzle and the larger density gradient between the pure methane and the co-flow of air. The methane-concentration from Raman-scattering measurements at Y = 90 mm in the methane-jet flame indicates already a good premixing at this height.

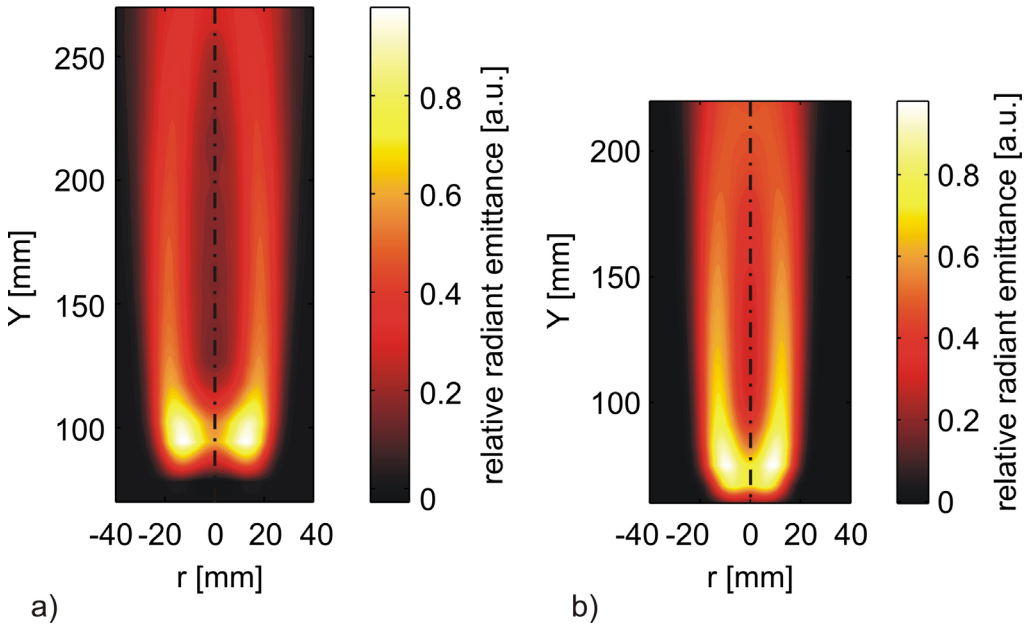

Figure 64: Comparison between relative chemiluminescence emission intensity in the methane-jet flame (a) and the nitrogen-methane flame (b).

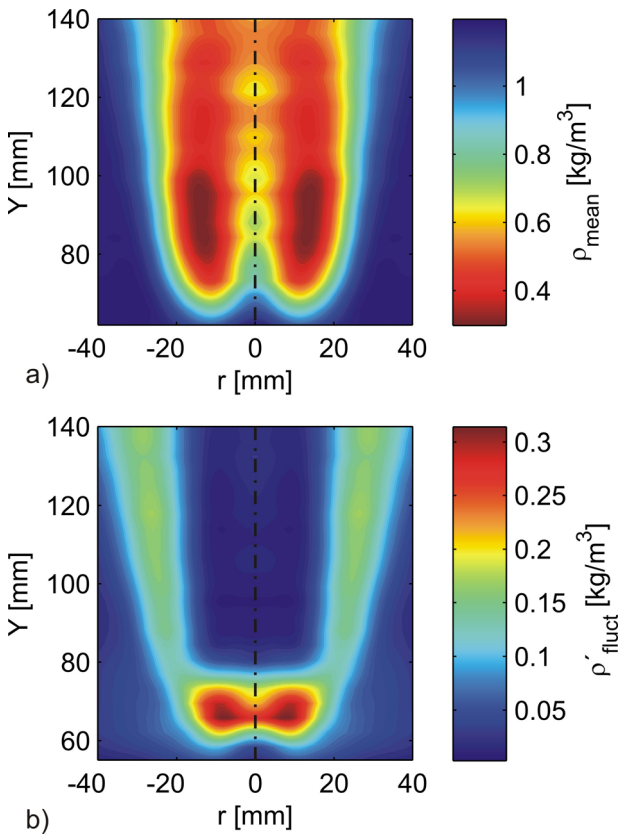

Figure 65 Radial distributions of time-averaged mean (a) and fluctuating (b) density for the nitrogen-methane flame. Data were derived from differential interferometry (800 interferograms recorded).

The fuel mixture, consisting of nitrogen and methane, could also contribute to the observed effect, as the nitrogen in the fuel acts as a coolant in the combustion process resulting in a lower flame temperature and reduced reaction rates. This will probably lead to reduced reaction rates in the bottom region of the flame, and therefore more unburned fuel (methane) is transported further downstream with the flow and burnt afterwards at higher heights.

Figure 65 illustrates the radial distribution of the time-averaged mean and fluctuating component of density for the nitrogen-methane flame. The mean component of density starts to decrease significantly at Y = 70-80 mm and reaches lowest values at Y = 80-100 mm, located at a radial distance of approximately 10-15 mm from the centre axis. In this region the mean density drops to values about 0.29 kgm^{-3} and is therefore higher than the lowest values in the methane-jet flame (0.22 kgm^{-3}). The density starts to increase slightly at higher heights but at the same time the diameter, where the density differs from the density of air at standard conditions becomes larger. This effect can be attributed to enhanced movements of the flame in the lateral directions at increased heights, which can be seen in the schlieren images as well (figure 61).

Peak values of the fluctuating component of density can be found at Y = 65-70 mm, located at a radial distance of approximately 5-10 mm from the centre axis. Density fluctuations in the nitrogen-methane flame are significantly higher then density fluctuations recorded in the methane-jet flame at the flame base (Y = 65-70 mm). There these density fluctuations are again caused by the combustion process that is initiated at this height, but in the nitrogen-methane flame density fluctuations are increased in this region additionally due to the stronger oscillations of the flame in the vertical direction. In contrast, density fluctuations in the centre-region from Y = 80-140 mm are very low in magnitude, whereas higher values of density fluctuations can be found further outside, starting at distances of approximately 20 mm from the centre axis. Density fluctuations in these regions can be attributed to the lateral oscillations of the flame.

Figure 66(a) presents the radial distribution of spatially-resolved physical cross-spectra in the frequency domain from 20 to 250 Hz recorded by the dual laser vibrometer technique at Y = 110 mm above the jet nozzle from one scanning direction. For the nitrogen-methane flame the line scan was performed only for one scanning direction, since the measurement

results recorded from one direction in the methane-jet flame did not differ a lot from the measurement results obtained by averaging the results from seven directions.

Additionally to the physical cross-spectrum, the corresponding phase distribution (figure 66(b)) and the filtered cross-spectrum (figure 66(c)) are illustrated. Differences between the filtered and the unfiltered cross-spectrum are generally small, but at very low frequencies around 20 Hz the filter function alters the cross-spectrum significantly. At 20 Hz non-zero phase values can be found almost at each measurement position along the line, only around +/-20 mm the phase values are almost zero. In the filtered cross-spectrum two regions of elevated density fluctuations can be found at 20-30 Hz with the peak values located at radial distances of -25 mm and 20 mm. If these low frequency density fluctuations are compared to the fluctuating component of the density at Y = 110 mm (figure 65) obtained from DIF measurements, the peak values almost coincide. This indicates that mainly the density fluctuations from very low frequencies (10-30 Hz) contribute to the overall density fluctuations. From 40 Hz to higher frequencies, increased values of density fluctuations are only found near the centre axis, but can not be found at distances more than 10 mm away from the centre axis. Density fluctuations at higher frequencies are mainly due to the nitrogen-methane jet that is still present at a height of Y = 110 mm in the flame.

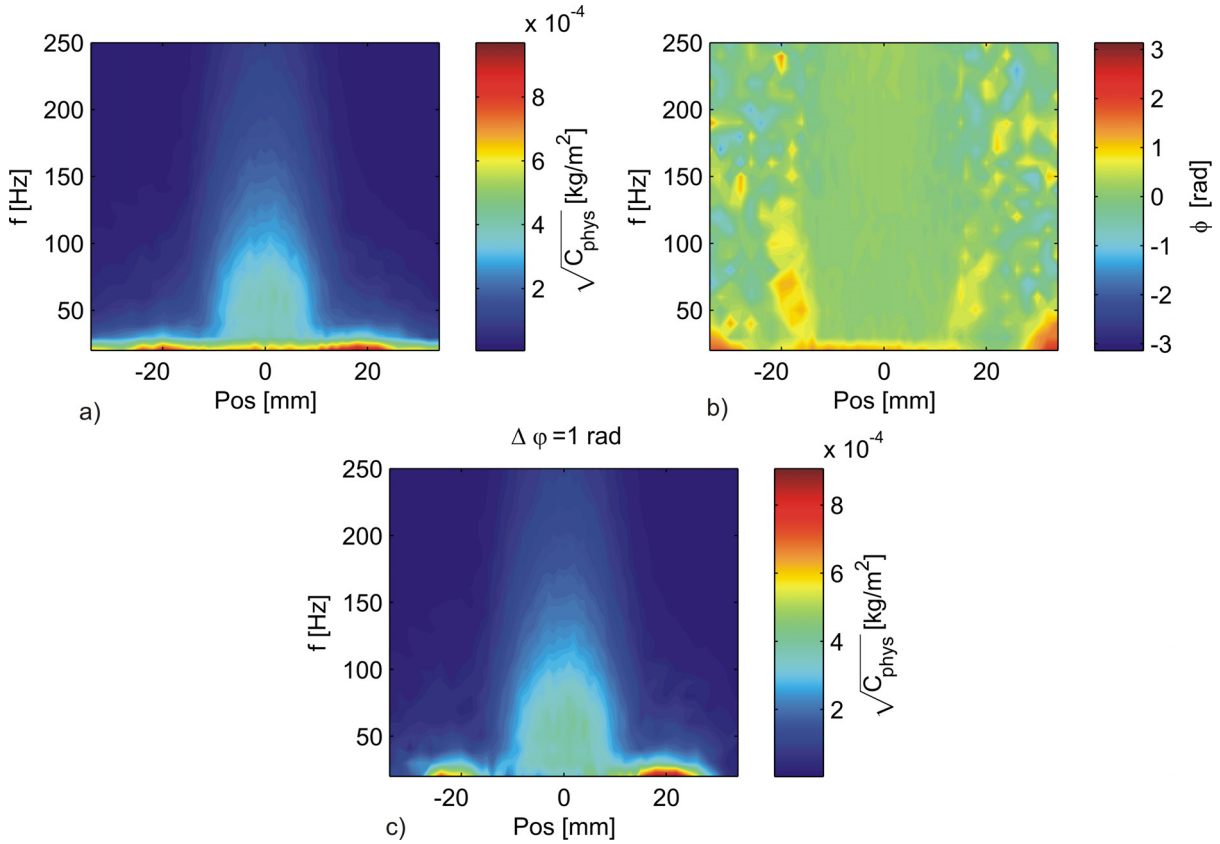

Figure 66: Magnitude of the physical cross-spectrum recorded in the CH_4-N_2-flame (a) and corresponding phase distribution (b) for one scanning direction at Y = 110 mm. In (c) a filter (bandwidth $\Delta\varphi$=1 rad) was applied to the data of the physical cross-spectrum from (a).

5 Experimental investigations of a swirl-stabilized premixed flame

In this chapter experimental investigations of an unconfined, swirl-stabilized premixed flame are discussed. It also presents measurement results obtained by different visualization- and measurement techniques. The main purpose of these experiments was on the one hand a preliminary characterization of the flame, and a discussion of the flame dynamics provided by the single-injection module operated for these experiments, since the same type of injection modules were used afterwards in the multi-flame gas turbine module combustor. On the other hand the tests demonstrated the capability of the dual LV measurement technique to resolve complex structures, since the burner provided a more complex, non rotational shaped flame, compared to the almost rotational symmetric reference burner investigated in the previous chapter.

5.1 Burner design and operating conditions

The premixed swirl-stabilized burner, designed at the Institute for Thermal Turbomachinery and Machine Dynamics, Graz University of Technology (Lang et al. 2008), was operated under atmospheric pressure conditions and provided a premixed methane-air flame. The methane was injected into the air-flow about 0.34 m upstream the swirler exit plane to ensure good premixing, figure 67. The mass flow for methane was 0.35 gs^{-1} and 3.6 gs^{-1} for air. The temperature of the methane-air mixture was 22°C and the axial velocity at the swirler exit plane was 16.8 ms^{-1}. A combination of an axial swirler and a Venturi nozzle generated a vortex-stabilized flame. The swirler consisted of three blades with an axial swirl angle of 30° and created a cone-shaped flame. The methane supply was ensured by gas bottles and air was supplied by the in-house pneumatic system.

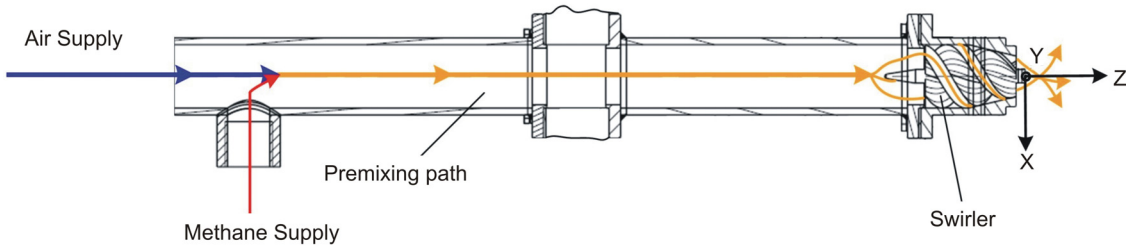

Figure 67: Premixed swirl-stabilized burner and coordinate system used for investigations.

5.2 Applied measurement techniques and experimental setups

For the characterization of the premixed swirl-stabilized flame schlieren-technique, chemiluminescence emission measurements and dual LV measurement technique were applied.

5.2.1 Chemiluminescence emissions measurements

To characterize the shape of the flame and the local heat release rates, integral data of chemiluminescence emissions recorded from 12 different directions, from 0° to 175°, were used for tomographic reconstructions.

The recording of the integral projection data was done using a CCD-camera (Canon EOS 300D, Tokyo, Japan) with defined settings (ISO 800, aperture 22, exposure time 1.3s). This tomographic reconstruction provided a detailed map of the local heat release rate (averaged data).

A high-speed camera (CASIO EXILIM F1, Casio, Tokyo, Japan) then visualized and analysed the flame dynamics qualitatively, recording high-speed movies with three different recording speeds of 300 fps, 600 fps and 1200 fps with respective resolutions of 512 x 384, 432 x 192 and 336 x 96 pixels. For the experiments presented in this work the chemiluminescence emission intensity emitted by the combustion in the premixed, swirl-stabilized flame was recorded by the high-speed camera at two recording speeds, 600 fps and 1200 fps. For the evaluation process only the blue colour separation of the recorded chemiluminescence emissions was processed (*CH** lines). For further data analysis two different evaluation processes were applied to these raw data.

In a first step the overall intensity of the chemiluminescence emissions was analyzed to gain information on the fluctuation of the overall heat release rate. Therefore, the overall intensity of chemiluminescence emissions was calculated for each single frame by adding up the single values of intensity for all pixels in the frame, leading to a time signal of overall emission intensities. Each data set consisted of intensity values calculated from 4096 sequent single frames. Performing a FFT with time samples containing 4096 values recorded at 600 fps then resulted in an amplitude spectrum with a frequency resolution of 0.147 Hz. The frequency resolution for time samples recorded at 1200 fps was 0.293 Hz. The calculation of the intensity for each frame, the colour separation of the blue channel and the FFT were performed in MATLAB vR2007b (The MathWorks, Natick, MA). The data obtained in this way provided information on the fluctuation of the overall heat release rate to a certain degree, but did not provide any information on the fluctuations of the local heat release rates.

To gain spatially-resolved data of the heat release rates, the intensities of the chemiluminescence emissions were now analyzed pixel-wise in the single frames. In this setup, the mean- and the rms-value of the chemiluminescence emissions were calculated from 6000 subsequent single frames recorded at 600 fps. This resulted in spatially-resolved mean and fluctuating values of the chemiluminescence emissions (local heat release rate) projections, integrating all emissions along the line of sight.

5.2.2 Dual laser vibrometry

The setup for the dual LV measurement technique almost remained unchanged, compared to the measurement setup employed for the investigation of density fluctuations in the reference flame discussed in the previous chapter. The calibration factor was set to 5 mm/s/V for both vibrometers and a low-pass filter of 20 kHz was chosen throughout all the measurements. The measurement plane was perpendicular to the main flow direction at a distance of 55 mm above the burner nozzle and measurements were performed from 6 different scanning directions to damp potential artefacts, therefore the angles for the individual scans varied from 0° to 75° with increments of 15°. Contrary to the reference burner, measurements along one line were not sufficient and field measurements were performed in the respective measurement plane, since the burner provided a non-symmetrical flame. The measurement grid consisted of a total number of 169 measuring positions arranged in a square, with a distance of 10 mm between adjacent positions. This resulted in a square grid with overall dimensions of 120 x 120 mm^2 at a height of Z = 55 mm above the nozzle exit.

For data acquisition, the setup remained unchanged compared to the setup used for the reference burner, but due to the increased total number of measurement positions (169 for the swirl-stabilized flame, compared to 51 positions for the reference burner for each direction) the recording duration was reduced to 37 s for each position at a sample rate of 40.96 kHz. Performing a FFT with time samples containing 4096 values resulted in 366 spectra with a frequency resolution of 10 Hz. The complete data analysis was done in Matlab vR2007b again.

5.3 Results and discussion

The premixed, swirl-stabilized flame was first visualized by schlieren-technique. The line of sight density gradients in the premixed, swirl-stabilized flame are considerably higher compared to the line of sight density gradients in the reference flame, due to the higher power density in the burner. For a light ray passing the measurement area, the beam deflection is significantly higher and therefore no schlieren stop was needed, since the camera aperture itself acted as a schlieren stop preventing strongly deflected rays to reach the camera detector. Figure 68 presents a series of schlieren images recorded by a high-speed camera (CASIO EXILIM F1) at a recording speed of 300 fps. To reveal temporal changes in the flame in terms of density gradients more clearly, only every second single frame is shown in figure 68, which resulted in a time difference between two adjacent frames of 0.0066 s. Thus, the series of Schlieren images covers a total time period of approximately 0.01 s.

In contrast to the previously discussed schlieren-visualization of the reference flame, no distinct zones can be determined and the size distribution of the visible structures is much more uniform due to the premixing of fuel and air, and because of the higher turbulence level due to the induced swirl in the flow-field. Therefore it is harder to draw conclusions from the schlieren-visualization in this case.

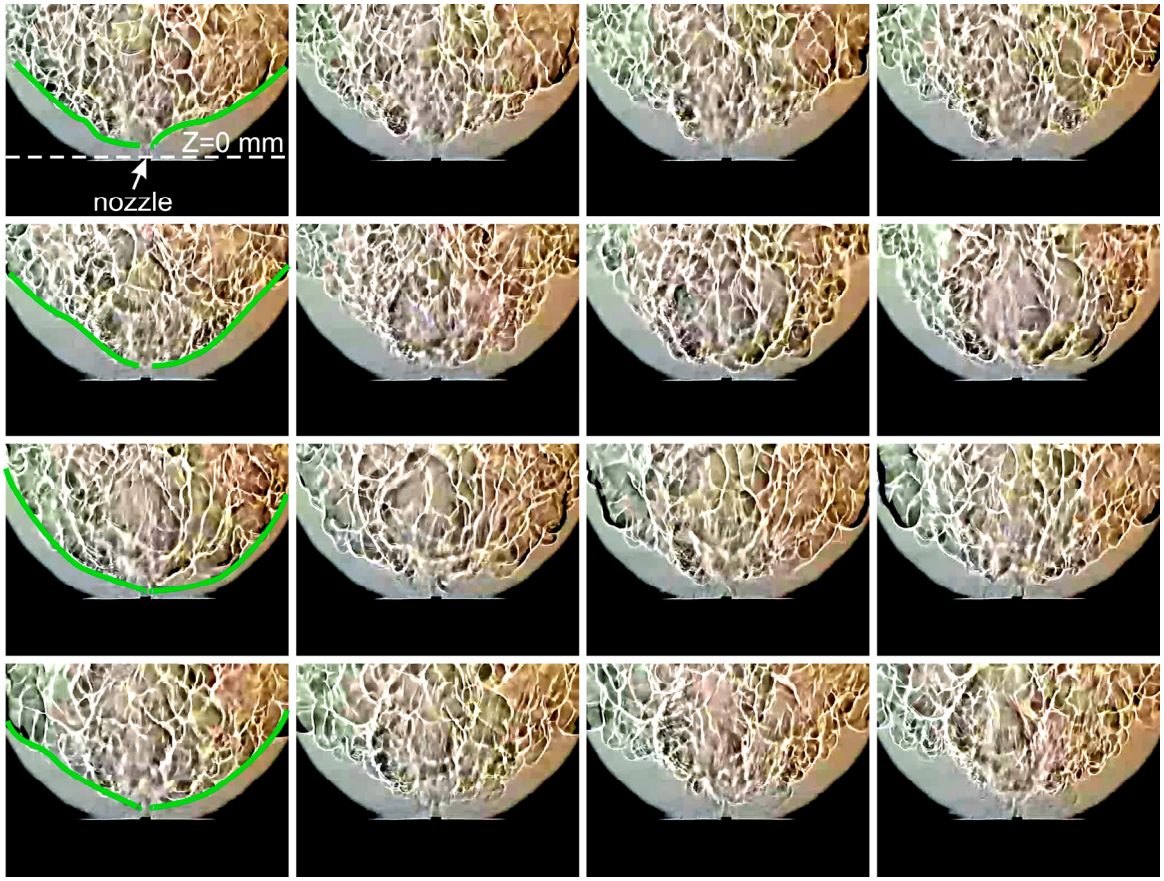

Figure 68: Series of schlieren images (line wise from top left to bottom right) recorded with a high-speed camera (CASIO EXILIM F1) at a recording speed of 300 fps. The time difference between two adjacent frames is 0.0066 s and the series covers a period of 0.01 s. The density gradients caused by the hot combustion structures are marked by a green line in selected images.

Anyhow, due to the high temporal resolution of the schlieren images strong fluctuations in the density field caused by fluctuations in the overall heat release rate are revealed. The combustion process alters the density field in the main part of the pictures above the nozzle exit; at higher heights the density is changed along the complete width of the image. Starting at the nozzle exit and the first image in figure 68, the field of visible density gradients is more or less conical shaped and changes over time. Strong variations in the lateral dimensions of the visible density gradients (marked by green lines in figure 68) can be seen and the profile changes from a conical-shaped to a more convex-shaped profile. This increase in the volume, where the density is changed due to the combustion process, indicates a rise in the overall heat release rate. The maximum expansion of the combustion gases is seen in the first image of the third line. Afterwards the volume decreases, indicating a decrease in the overall heat release rate, until a minimum is reached in the last image (bottom right), which is almost identical to the first image of the series. Since the combustion process was stable in this case, no pronounced periodicity in the fluctuation was found.

Figure 69 illustrates schlieren images with the flame chemiluminescence emissions also visible. The chemiluminescence emissions determine the position of the flame and indicate the main combustion zone, whereas the Schlieren images represent the influence of the combustion process on the density field. The main combustion zone is rather small, compared to the size of the Schlieren that represent the hot combustion gases. The intensity of the chemiluminescence emissions allows a qualitative estimation in the overall heat release rate and indicates temporal fluctuations in the overall heat release rate.

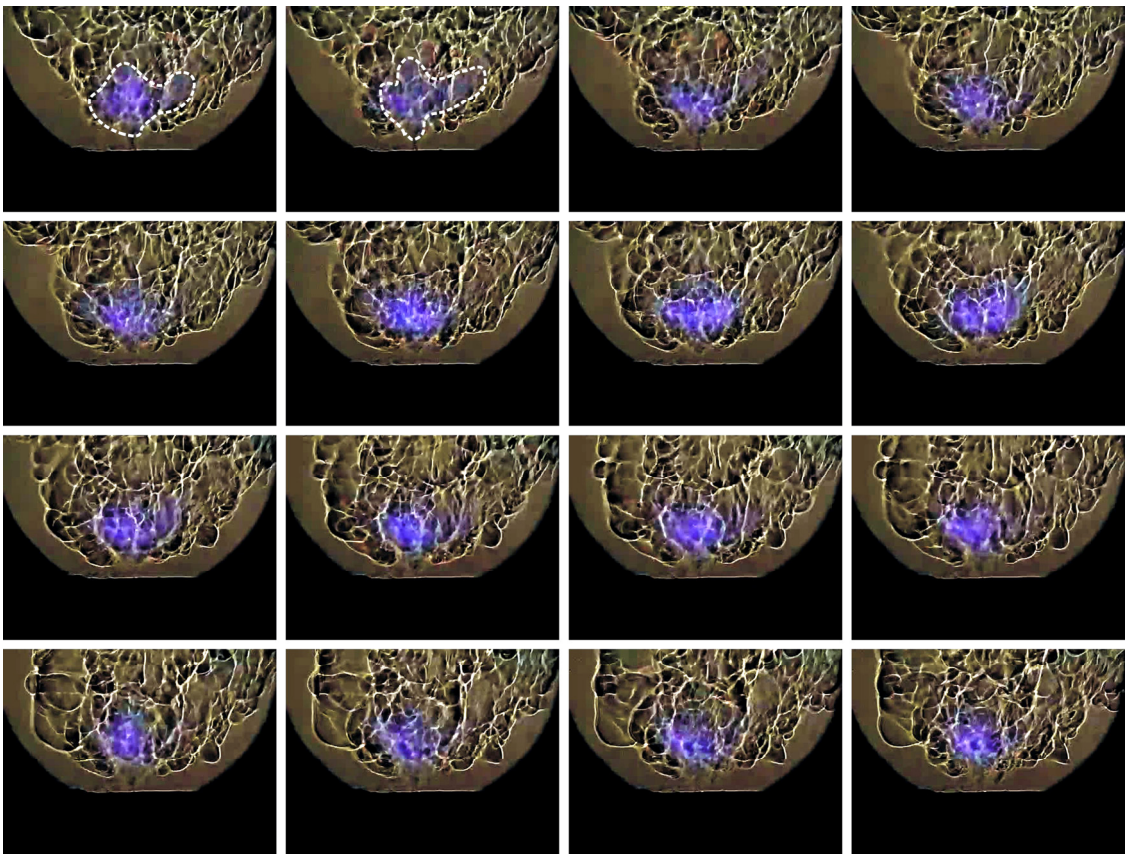

Figure 69: Series of Schlieren images (line wise from top left to bottom right) with chemiluminescence emissions visible. Images recorded at 300 fps. In frame 1 and 2 the position of the flame is marked by the dashed, white line.

Thereby a correlation between the intensity of the chemiluminescence emissions and the schlieren images can be found. If chemiluminescence emissions are high in the image, the area, where schlieren can be found is also increased, compared to images with lower chemiluminescence emissions. The sequence of images presented in figure 69 covers a time period of approximately 0.01 s and is therefore equivalent to 10 Hz. Since the combustion process was stable in this case, no periodicity in the fluctuation of the chemiluminescence emissions at a distinct frequency was found in the schlieren images. Fluctuations in the intensity of the chemiluminescence emissions and in the size of the Schlieren volume are therefore of stochastic nature, but are more likely to happen in the low frequency range.

To receive more detailed information on the fluctuation of the overall heat release rate, a FFT was applied to the time signal of overall chemiluminescence emissions, resulting in an amplitude spectrum presented in figure 70(b). Temporal fluctuations in the time signal of the overall chemiluminescence emissions are clearly visible in figure 70(a), resulting in peaks in the amplitude at lower frequencies. Distinct peaks are present at approximately 10 Hz and at 30 Hz in the amplitude spectrum; however these results are gained only from one sample with 4096 values and present only an estimation of the overall heat release rate fluctuations. For more reliable results, long-time-averaged measurements are indispensable.

Spatially-resolved and averaged chemiluminescence emissions of the premixed swirl-stabilized flame are shown in figure 71. Projection chemiluminescence emission data (images, blue colour separation), were taken from 12 different directions and a tomographic reconstruction technique (algebraic reconstruction technique, ART) was applied to these integral data sets to obtain local data of chemiluminescence emissions, using the IDEA software (Graz University of Technology freeware, available from www.optics-tugraz.at) for the tomographic reconstruction.

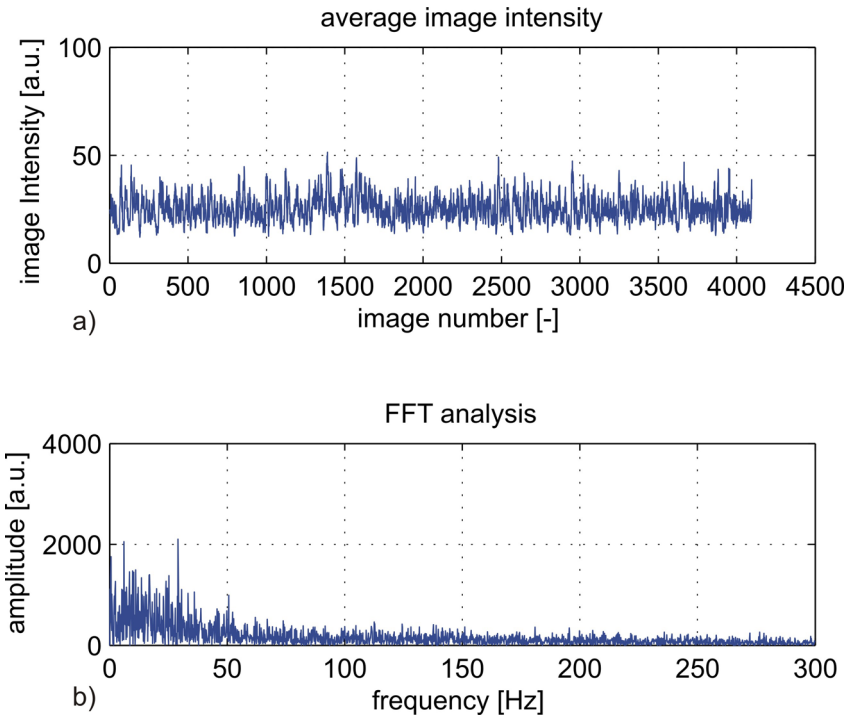

Figure 70: Time signal of the overall intensity of chemiluminescence emissions (a) for 4096 subsequent single frames with (b) the corresponding amplitude spectrum.

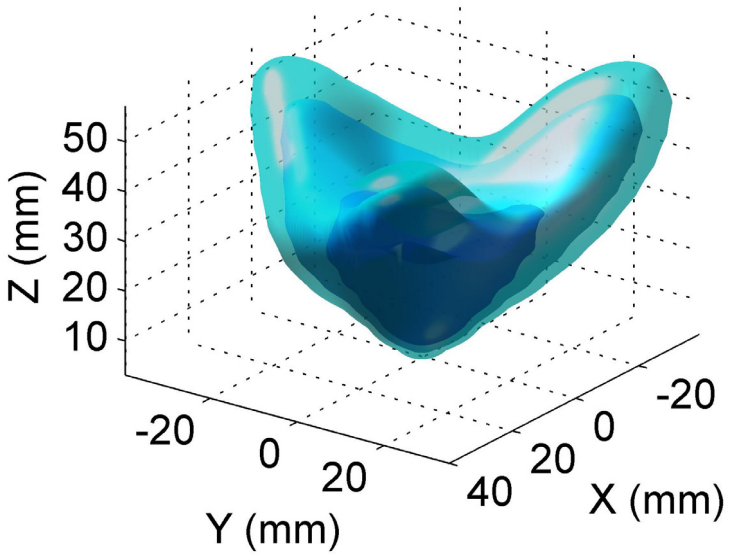

Figure 71: Isosurfaces of local and temporal-averaged chemiluminescence emissions obtained from a tomographic reconstruction applied to projection data recorded from 12 different directions (long-exposure images, blue colour separation). The local distribution of chemiluminescence emissions intensity represents local heat release rates, if fuel-to-air-ratio is constant, and serves as a marker for the main combustion zone.

The single-injection combustion module provided a nearly conical shaped flame near the exit plane of the nozzle. This conical shaped flame breaks up with increasing height into three slightly swirled arms of higher luminosity connected to each other via combustion zones of lower intensity in chemiluminescence emissions (figure 71). This indicates that the main combustion process took place in the bottom region and in the three twisted arms of the flame. As these data are gained from recordings with a long exposure time, they represent averaged data of the local chemiluminescence emissions (and therefore information on the averaged, local heat release rates), but do not provide information on the fluctuation of chemiluminescence emissions intensity and fluctuations in the heat release rate.

In order to get information on the fluctuating component of chemiluminescence emissions, high-speed recordings are indispensable. Figure 72 presents normalized line of sight data (projections) of the mean (a) and fluctuating (b) chemiluminescence emissions calculated from 6000 single frames recorded by a high-speed camera. The peak values of the mean chemiluminescence emission data are located at a height around Z = 40 mm and can be ascribed to the superposition of two arms of the flame. Chemiluminescence emissions from two arms are added along the line of sight and for this reason the highest values of chemiluminescence emissions are found in this region.

Comparing the normalized data of the mean chemiluminescence emissions to the data of the fluctuating component of chemiluminescence emissions similar distributions are found. The mean distribution (time-averaged) of chemiluminescence emission displays the main combustion zone and the zones of major heat release in space, whereas the lateral and vertical motion

of the flame and temporal oscillations in the heat release rate are characterized by the distribution of the fluctuating chemiluminescence emission data in figure 72. This result indicates that both (averaged and fluctuating) components are linked to each other in this type of premixed flame.

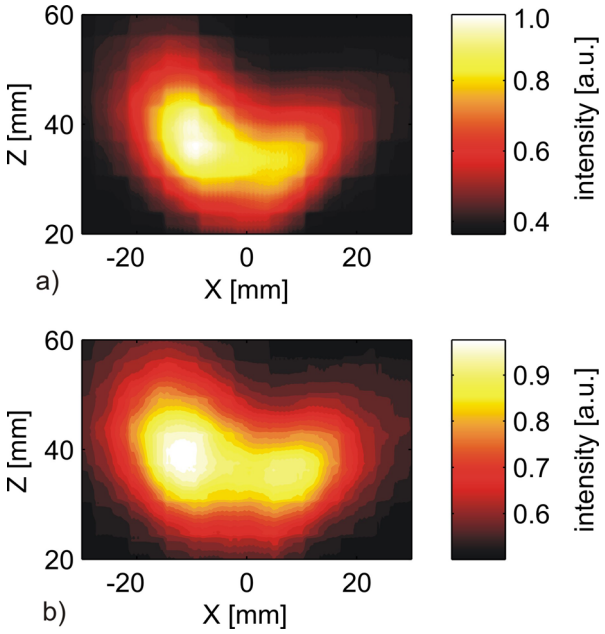

Figure 72: Line of sight data of the mean (a) and fluctuating (b) chemiluminescence emissions, recorded at a projection angle of 35°. Data calculated from 6000 subsequent single frames recorded at 600 fps and normalized by the maximum values found in each distribution.

The challenge in the application of dual LV measurements on the premixed, swirl-stabilized flame was on the one hand the enhanced level of turbulence and the higher complexity in the flame shape, and on the other hand the reduced number of single-spectra for the calculation of the averaged cross-spectrum for each scanning direction due to the increased number of measurement positions in the measurement grid. A reduction in the number of single-spectra leads to an enhanced uncertainty/noise level and therefore reduces the reliability of the measurement results obtained.

To judge the quality of measurement results based on the total number of single-spectra, a critical value for the relative correlation was defined, according to (Hampel 2005), which considers the statistical uncertainty in the calculation of the averaged cross-spectrum. In areas, where the relative correlation falls below this limit, the measurement results obtained for the averaged cross-spectrum cannot be trusted any more, as the signal values could be simply caused by noise. For the 366 single-spectra recorded in this experiment, the critical value for the relative correlation was 0.046, based on equation (87).

$$K = \frac{0.888}{\sqrt{n}} \tag{87}$$

Local distribution of the physical cross-spectrum, the corresponding relative correlation and the phase distribution for two different scanning directions at 0° and 45° are presented in figure 73 for a frequency of 20 Hz and a cross-section of the flame at Z = 55 mm . In dual-LV the correlation of two laser beams, crossed at 90°, is calculated by cross-correlation of the two signals. This is the cross-spectrum for one observation direction (e.g. 0°). Then the dual-LV system was rotated for 45° and the measurement repeated, resulting in 45° cross-sprectra for the field scanned and presented in figure 73. Comparing the magnitude of the physical cross-spectra for both scanning directions (top, figure 73) reveals, that low values of the cross-spectrum can be found in both plots near the origin of the coordinate system. This indicates that density structures recorded at 20 Hz are rather found in the outer region of the flame, but not in the centre. The time series of schlieren images in figure 68 and figure 69 already stated the same. Although, significant differences in the location of the peak values in the contour plots can be found between the two scanning directions. At some positions, elevated values of the cross-spectrum are present in both plots, e.g. at X = -40 mm and Y = -40 mm but generally the peak values do not coincide, indicating the presence of artefacts. These artefacts are

caused by large coherent density structures that are shed more or less periodically in the flame. Due to the high correlation within their dimensions and their large dimensions, it is very likely that both laser beams pass through the same structures beside their point of intersection and attribute the signal contained in both beams to the point scanned at this moment.

A closer look to the distribution of the relative correlation (figure 73, middle) supports the theory of large coherent structures in the flow-field. High values of correlation K can be found around the centre-region in both plots, and therefore the presence of artefacts is very likely. Values for the phase distribution are generally around zero in areas, where the relative correlation and the magnitude of the cross-spectrum are high (figure 73, bottom). In this case the application of the phase filter might not lead to a significant improvement of the results. The only way to improve the measurement results can be done by averaging of field scans obtained from several scanning directions with different scanning angles. Before presenting a field averaged from multiple scans, lets us first discuss the results at higher frequencies.

In figure 74, the local distribution of the physical cross-spectrum, the relative correlation and the spatially-resolved phase distribution are shown for a frequency of 120 Hz for scanning directions 0° and 45°. Compared to the cross-spectrum at 20 Hz, the location of the peak values for the cross-spectrum are different at 120 Hz (figure 74, top). Three areas of higher magnitudes of the cross-spectrum can be identified nearly at the same positions in both plots at 120 Hz. This indicates a reduced probability for artefacts at this frequency and therefore a better measurement result, even without phase filtering and averaging of measurement results obtained from several scanning directions. Furthermore, increased values of the cross-spectrum at 120 Hz are bonded to areas of low values of magnitude in the cross-spectrum at 20 Hz. The maximum correlation for the 120 Hz is significantly lower than the maximum value of the correlation for the 20 Hz, and the phase distributions at 120 Hz seems to be more arbitrary compared to the phase distribution at 20 Hz. Both facts indicating lower probability of artefacts by large scaled coherent structures.

In a next step measurement results obtained for the different scanning directions were averaged to damp potential artefacts. The results are shown in figure 75 for density fluctuations at frequencies of 20, 30, 120, 160, 240 and 500 Hz. Up to now the main focus in the discussion of measurement results for the distinct scanning directions was set on the evaluation process and the judgement of data quality based on the relative correlation and the phase distribution. For the further discussion of the combustion process in the premixed, swirl-stabilized burner, only the averaged distribution of the cross-spectra is taken into account.

At low frequencies (20 and 30 Hz) the averaged cross-spectra denotes the presence of large coherent structures, surrounding all structures at higher frequencies. These structures are more or less triangular-shaped, with the values of magnitude for the cross-spectrum being low in the centre-region, and high values of the cross-spectrum at the circumference of the triangle. For the 20 Hz plot, three peaks are present at the circumference, spatially located between the peak values at higher frequencies (e.g. 120 Hz or 240 Hz). The distribution of the cross-spectrum at 30 Hz is similar to the distribution at 20 Hz, but peak values are generally more distributed along the circumference of the structure.

According to the schlieren visualization, density fluctuations in the low frequency range can be attributed to density changes resulting from sudden lateral expansion or contraction of local volumes filled with hot combustion gases. As the hot combustion gases can only expand in the outward direction, no density fluctuations can be found in the centre-region at low frequencies, where the main combustion zone is located.

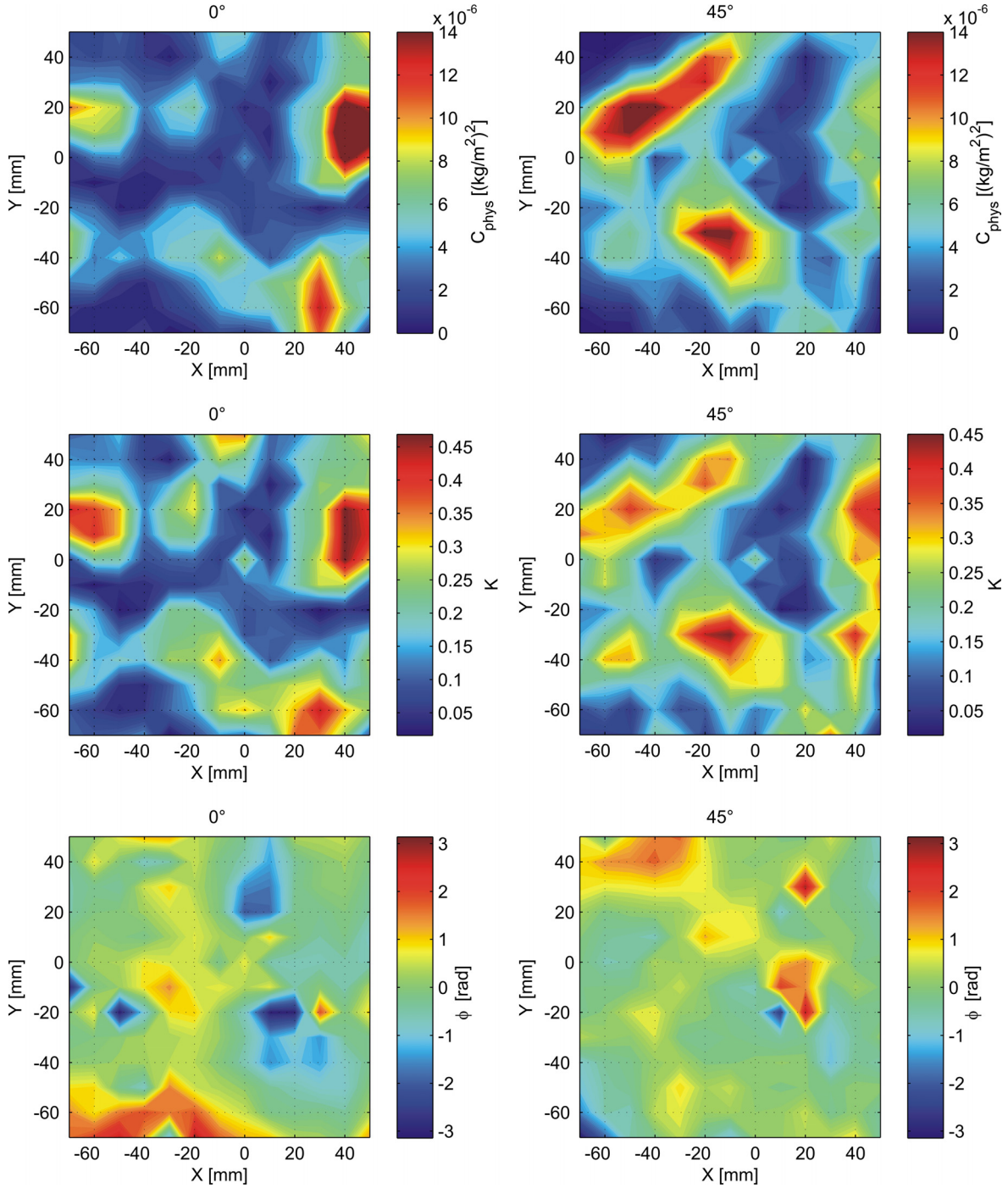

Figure 73: Measurement results dual-LV for two different scanning directions at scanning angles of 0° and 45°. Results presented are for a frequency of 20 Hz and illustrate the distribution of the physical cross-spectrum (top), the corresponding degree of correlation (middle) and the corresponding phase distribution (bottom). All data presented were recorded at a height of Z = 55 mm above the nozzle exit plane.

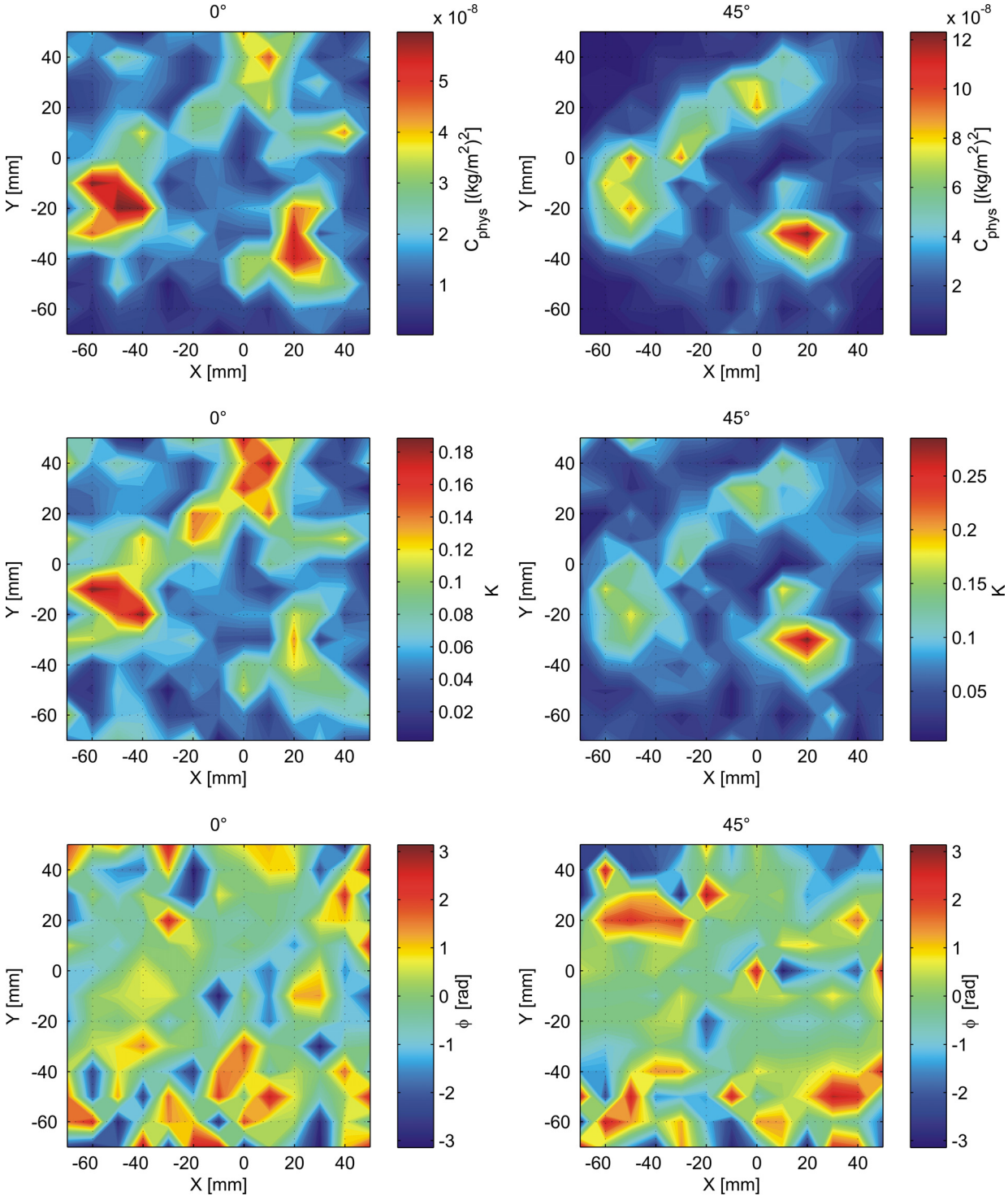

Figure 74: Measurement results obtained by dual-LV for 120 Hz for two different scanning directions. The physical cross-spectrum (top), the degree of correlation (middle) and the phase distribution (bottom) are presented at a height of Z = 55 mm above the nozzle exit plane.

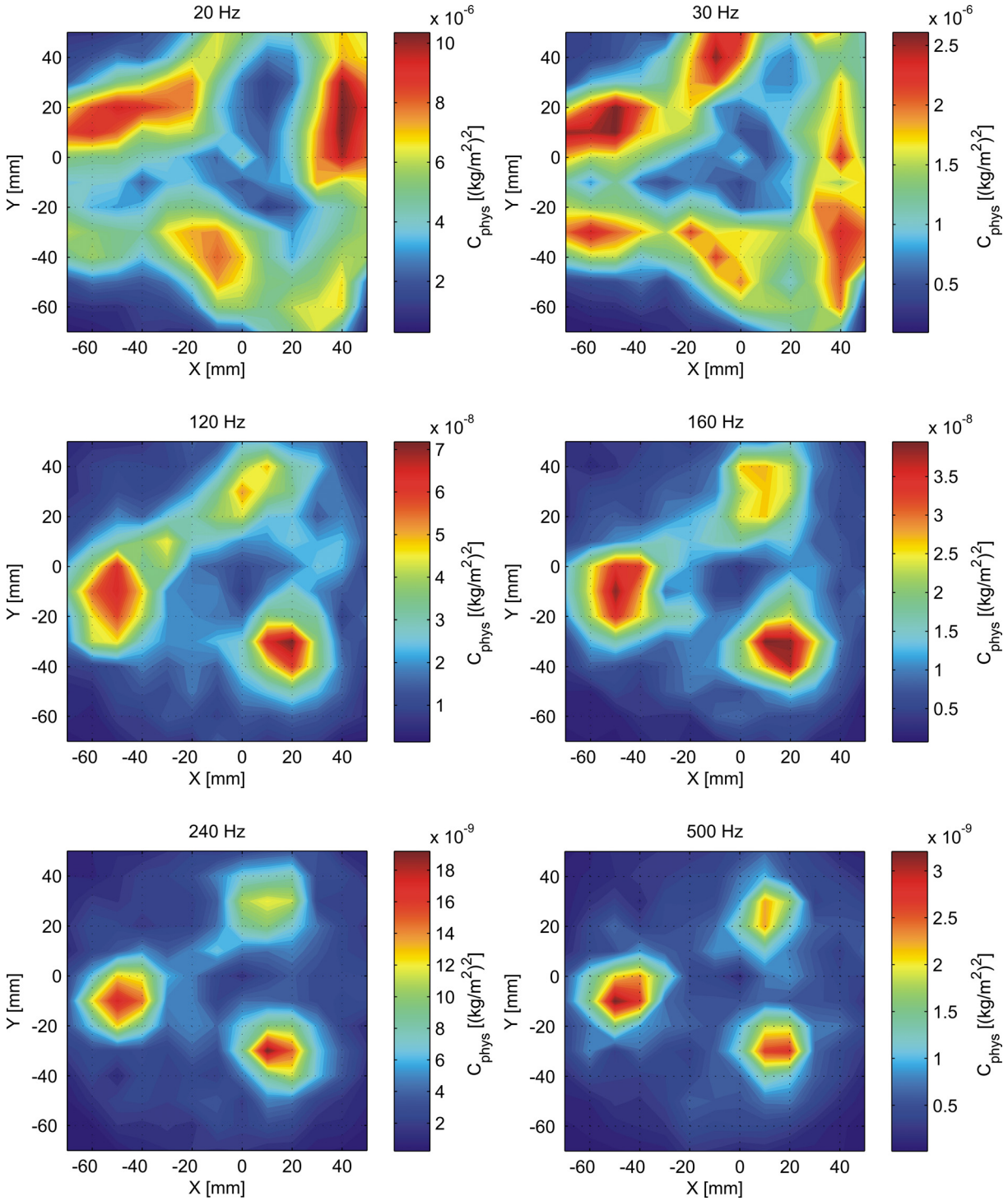

Figure 75: Local distribution of the cross-spectrum for different frequencies at a height of Z = 55 mm above the nozzle exit plane. To damp artefacts, averaging of 6 scan directions was done.

With increasing frequencies the distribution of the peak values for the averaged cross-spectra changes significantly. Furthermore the position of the peak values at higher frequencies do not vary in their positions with increasing frequencies, only the lateral dimensions of the individual peaks decrease at higher frequencies. At 120 Hz and 160 Hz the three areas of high density fluctuations are connected via sections of lower density fluctuations, while in the centre-region almost no fluctuations at these frequencies are observed. The sectors of density fluctuations between the areas of maximal values are getting weaker with increasing frequencies and almost vanish at 500 Hz.

In figure 76 the averaged cross-spectra are illustrated for the same frequencies, but now a phase filter with bandwidth $\Delta\varphi$=1 rad was applied to the data. The distributions of the cross-spectra remain almost the same and no significant differences between unfiltered and filtered results can be found. This implies that the averaging process over a number of measurements recorded at different viewing angles already improved the measurement results and damped artefacts, especially at low frequencies, and therefore the phase filtering does not improve the quality of the measurement results.

For the analysis of the premixed, swirl-stabilized flame the changes in the distribution of density fluctuations recorded at low frequencies and density fluctuations at higher frequencies are of special interest. Taking a closer look at the magnitude of the cross-spectra at different frequencies reveals that high values for the density fluctuation's cross-spectra are found in the low-frequency range and that the maximal magnitude within the field scanned declines with an increase in the frequency. Since the magnitude of the cross-spectra has the same physical unit as the power spectrum, this implies that density fluctuations of large amplitude are limited to the low frequency range, whereas density fluctuations at higher frequencies posses lower amplitudes.

The local distribution of chemiluminescence emission, on the other hand, indicates that the main combustion process takes place in the bottom region and in the three slightly twisted arms of higher luminosity at increased heights. This implies that the major heat release and therefore most of the energy conversion takes place in these areas. Figure 77 illustrates isosurfaces of the spatially-resolved chemiluminescence emissions and the local distribution of chemiluminescence emissions in the cross-section of the flame at Z = 55 mm. At this height, maximum values for the chemiluminescence emission intensity (and therefore local heat release rates) are found in three areas, forming a triangular shape. The distribution of the chemiluminescence emissions seems to coincide with the local distribution of the density fluctuations at higher frequencies, recorded by the dual LV technique. This indicates that density fluctuations at higher frequencies can be attributed to the combustion process directly and can be linked to the high heat release rates, whereas density fluctuations in the lower frequency range are also due to the combustion process, but cannot be attributed to the local heat release rates directly, as they are located besides areas of high chemiluminescence emissions. Thus density fluctuations in the low frequency range must be rather caused by the heat transfer due to conduction, convection and radiation, and its impact on the flow-field.

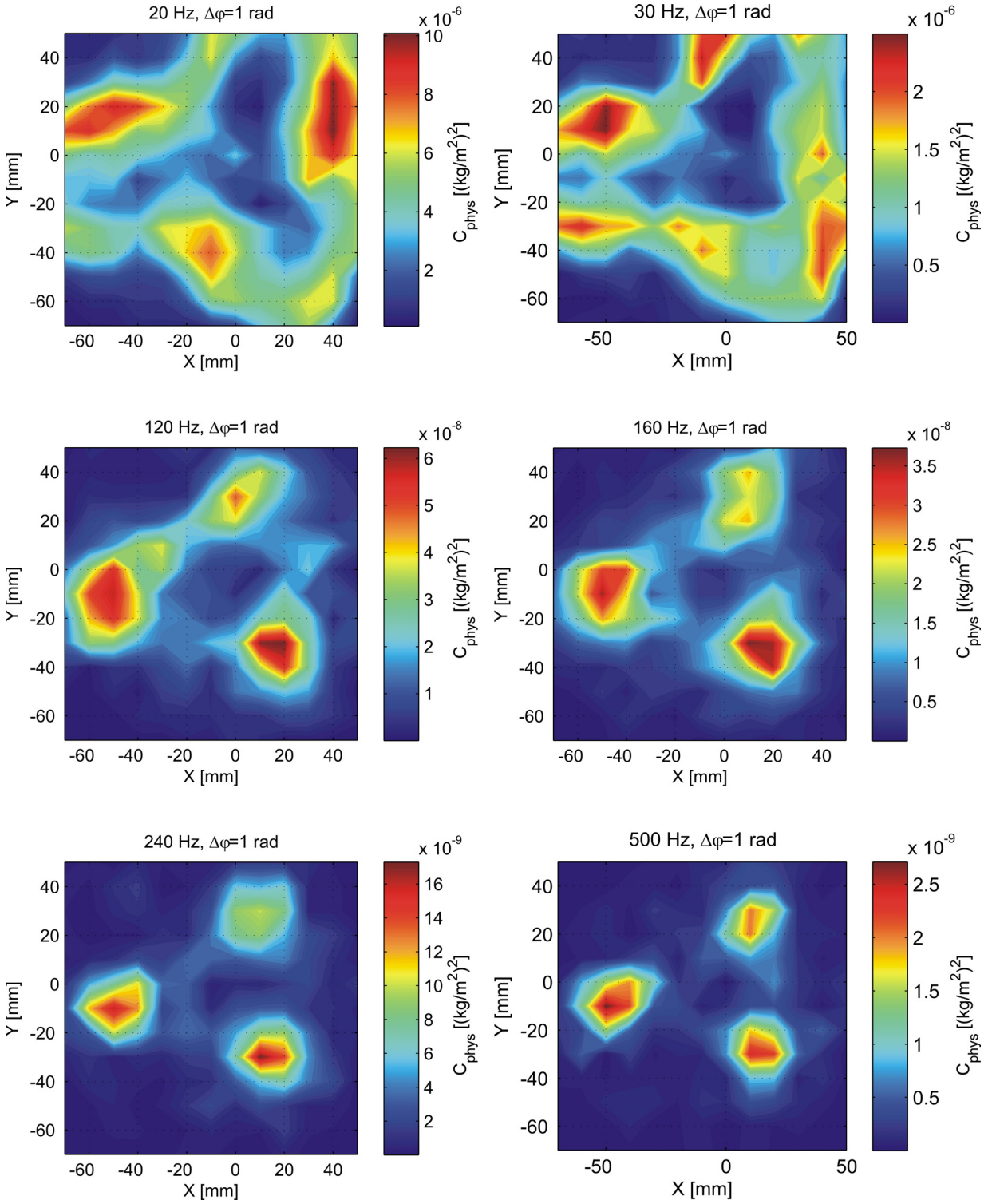

Figure 76: Local distribution of the filtered cross-spectrum at several frequencies at a height of Z = 55 mm above the nozzle exit plane. Averaging of 6 different directions and the application of a filter fuction with bandwidth Δφ=1 rad was performed.

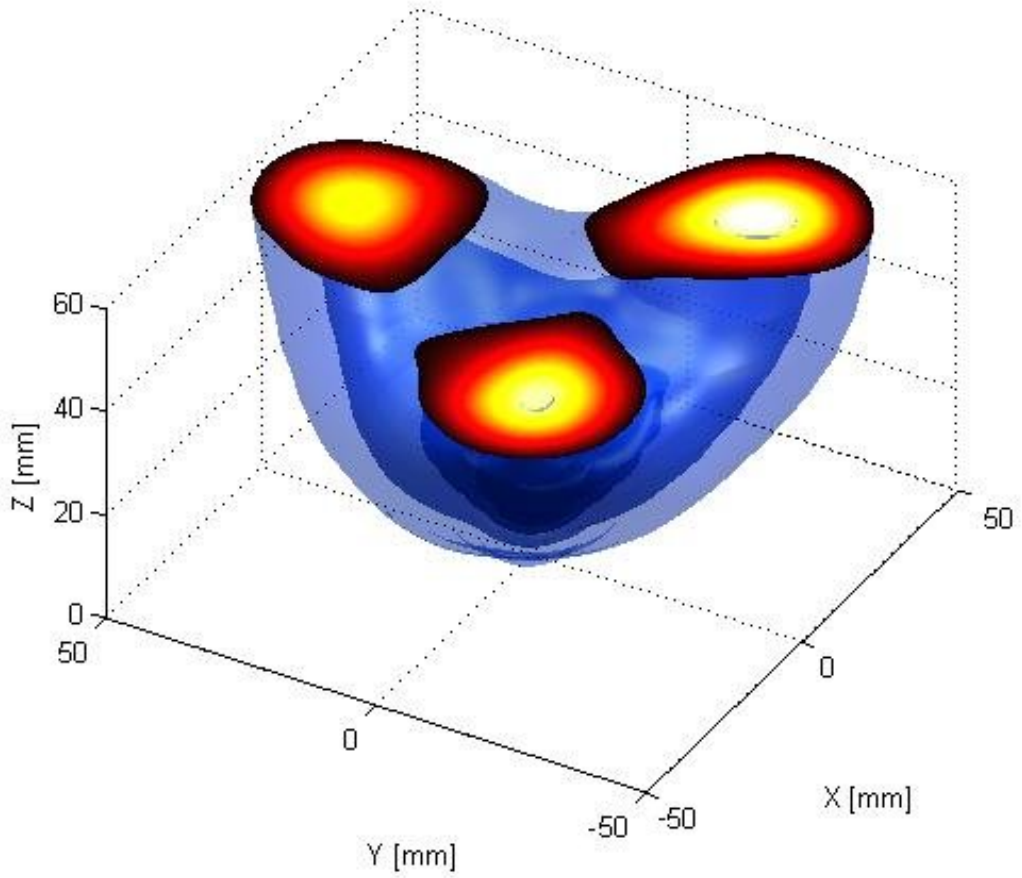

Figure 77: Isosurface of local chemiluminescence emissions and corresponding distribution in a cross-section at a height of Z = 55 mm (height above the nozzle). In this plane at Z = 55 mm the distribution of local chemiluminescence emissions features a triangular-shape, with the three peaks located at each corner.

According to equation (1) (Dowling and Morgans 2005), the time derivative of density fluctuations are proportional to the time derivative of pressure fluctuations and the unsteady heat release. Calculating the frequency-resolved spectra of the time derivative of density fluctuations alters the ratio in the magnitude between low frequencies and higher frequencies. In the frequency domain the time derivative of a complex spectrum equals a simple multiplication of this spectrum by a factor of $2\pi fi$ and therefore, the main contribution to the overall spectrum shifts from lower frequencies to higher frequencies. The higher frequencies now have a higher contribution compared to the lower frequencies with respect to their magnitude. Figure 78(a) and (b) present local data of the time derivative of density fluctuations integrated over all frequencies for the unfiltered data set (a) and the filtered data set (b) with the bandwidth of the filter function set to $\Delta\varphi$=1 rad.

The distributions of the time derivative of density fluctuations almost look alike and small differences in the magnitude between the time derivatives of density fluctuations in figure 78(a) and (b) are due to the filtering process reducing artefacts. The distribution of the time derivatives of density fluctuations, integrated over all frequencies, coincides with the local distribution of the chemiluminescence emissions, which are time-averaged (mean) data.

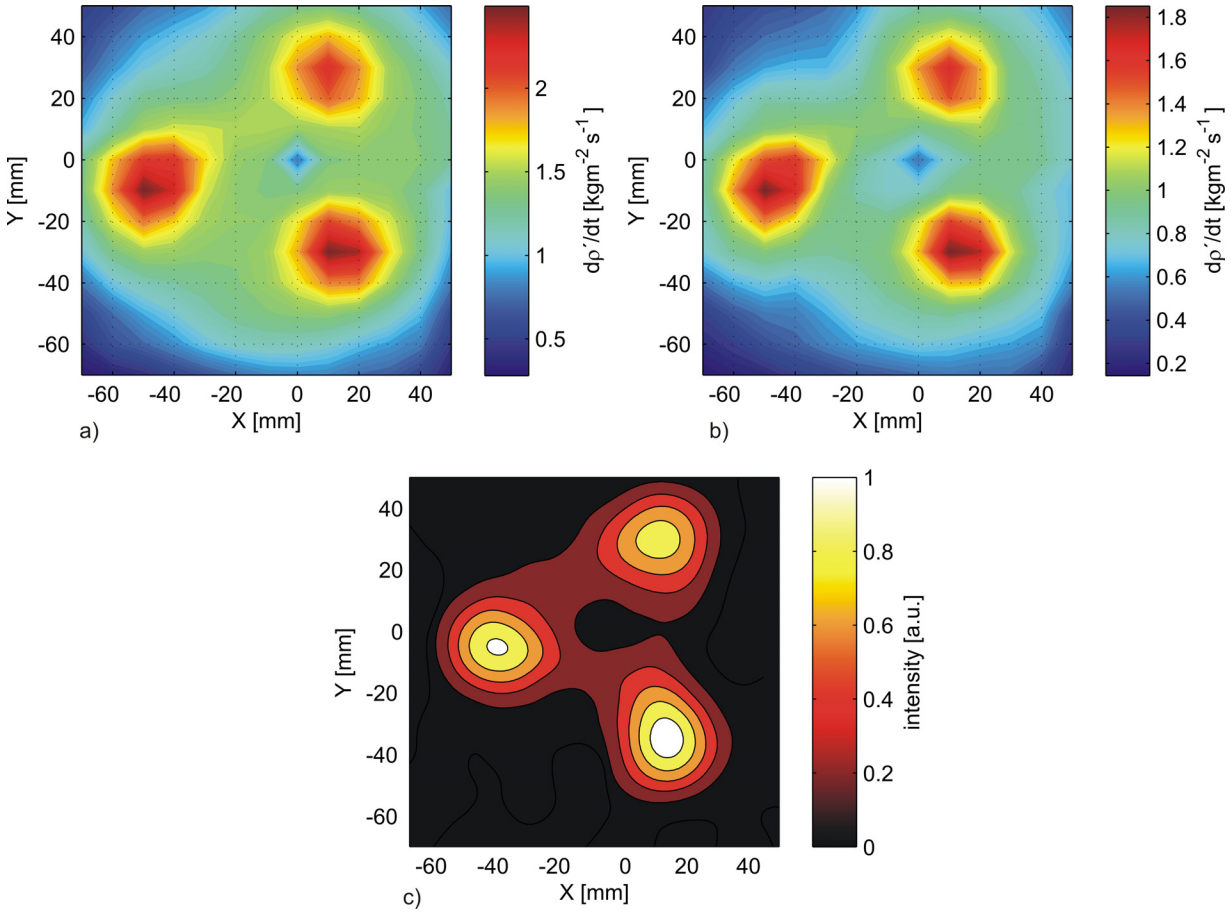

Figure 78: Local data of the time derivative of density fluctuations integrated over all frequencies for the unfiltered data set (a) and the filtered data set (b), and local chemiluminescence emissions (c) for Z = 55 mm.

For a detailed comparison the fluctuating component of the chemiluminescence emissions should be rather taken into account, as they present the fluctuations of the local heat release rates which contribute to equation (1). As was shown in figure 72 above, in this special flame mean and fluctuating components are closely linked to each other with distributions alike.

In a stable combustion process at atmospheric pressure conditions, pressure fluctuations are thought to be small compared to the heat release fluctuations caused by the combustion process. This implies that density fluctuation data recorded by the laser vibrometer are directly proportional to the heat release fluctuations, since the small amplitude pressure fluctuations can be neglected.

For the fluctuating component of the chemiluminescence emissions, only line of sight data were available. Thus, from the fields displayed in figure 78, local data of the time derivative of density fluctuations were integrated along the line of sight. The comparison of integral projection data of the time derivative of density fluctuations and the line of sight data of the fluctuating chemiluminescence emissions, recorded at a projection angle of 35° (figure 79), supports the assumption that the pressure fluctuations are small compared to the heat release fluctuations in a stable combustion process. The slope of the normalized fluctuating chemiluminescence emission data and the integral data of the time derivative of density fluctuations match quite well.

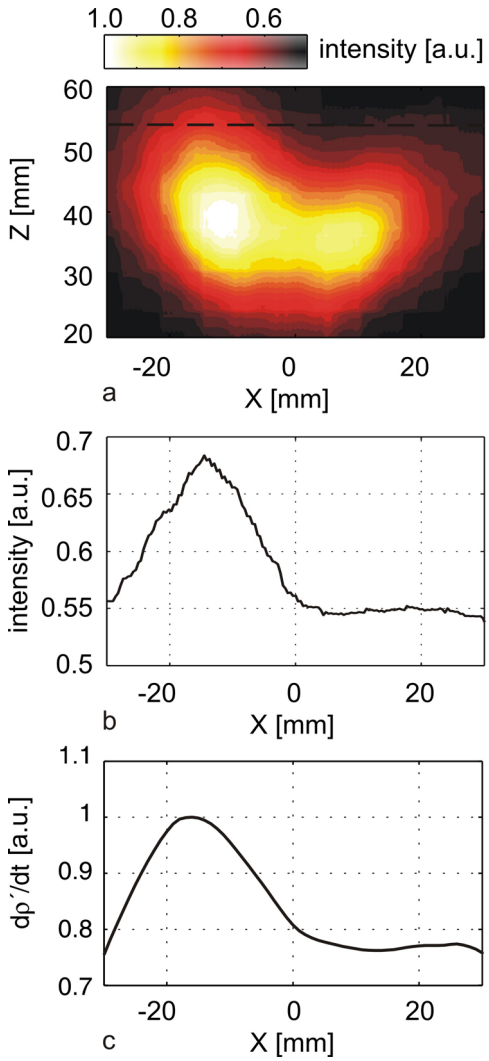

Figure 79: Comparison between projection data of the time derivative of density fluctuations and fluctuating chemiluminescence emissions at Z = 55 mm in the unconfined single swirl-stabilized flame. Integral and time-averaged data.

6 Experimental investigations in a gas turbine model combustor with self-excited combustion instabilities

6.1 Combustor design and operating conditions

In the following section a multi-flame gas-turbine model combustor will be investigated using the measurement techniques presented and discussed in the previous chapters. This multi-flame combustor consisted of three single injection modules, providing three premixed swirl-stabilized flames. A schematic view of the combustor is shown in figure 80. The injection modules were arranged along a line with a spacing of 60 mm between adjacent injection modules. Each module consisted of an axial swirler and a pipe system for fuel- and primary-air supply. Gaseous fuel (natural gas) was injected into the primary air-flow via a nozzle 0.34 m upstream of the swirler exit plane to ensure good premixing of the fuel and the primary air. The fuel-flow as well as the primary air-flow were controlled separately for each injection module. The axial swirler, designed at Graz University of Technology (Lang et al. 2008), was mounted at the end of each injection module and consisted of three blades with an axial swirl angle of 30°. Additionally, the swirler was shaped conically, resulting in a tapering flow cross section along the swirler axis. Thus, the fuel-air mixture passing through the swirler was accelerated due to the Venturi effect, preventing a flashback from the combustion chamber.

The combustion chamber (liner) had a 240 x 180 mm^2 cross section with a length of 345 mm. The four side walls of the chamber were made of stainless steel with a thickness of 1 mm. Optical access was provided by a cut-out in each side wall, which was sealed by 5 mm thick quartz plates. The dimensions for the optical accesses were 190 x 110 mm^2 and 190 x 180 mm^2 in correspondence to the respective sidewall dimensions. This design allowed optical access from all four directions perpendicular to the flames.

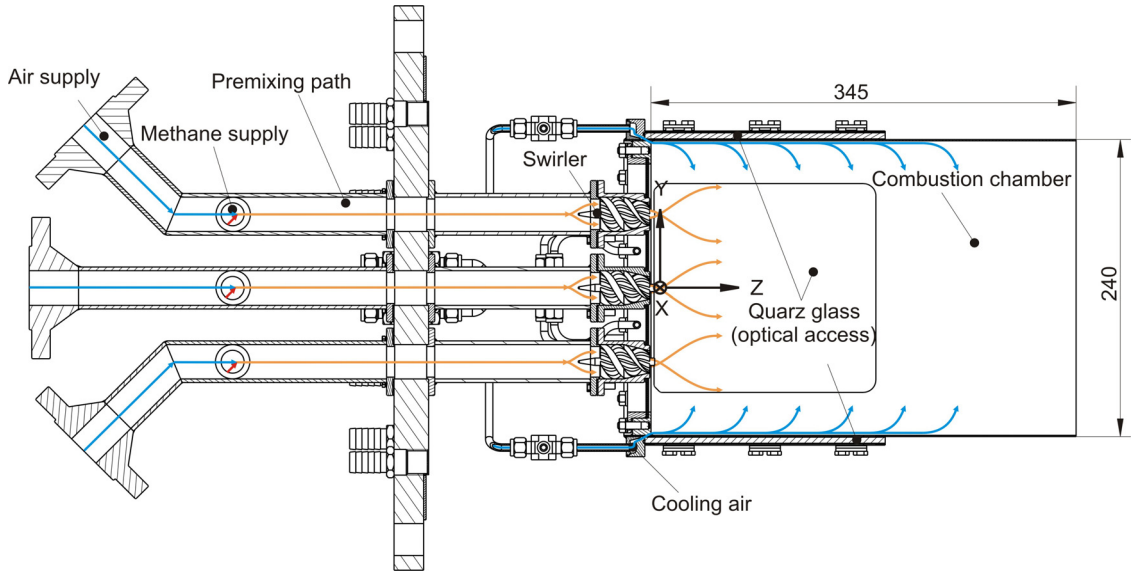

Figure 80: Schematic view of multi-flame combustor. Red: fuel-flow, blue: air-flow, orange: premixed fuel/air-flow.

Additionally to the primary air-flow, secondary air was injected for cooling purposes into the combustion chamber from four slots between the sidewall and the quartz plate near the front plate (see figure 80). The slot widths were adapted to the width of the respective quartz plates and therefore had a width of either 180 mm or 110 mm. The height of the slots was approximately 1 mm. This design provided a cooling film for each quartz plate to prevent them from overheating. This secondary air-flow was adjusted separately from the primary air-flow.

The liner of the combustion chamber, consisting of the four side walls and the quartz-plates, could be removed to allow preliminary investigations on the unconfined flames at atmospheric pressure conditions. In this case the three injection modules, the corresponding fuel- and air-supply and the front plate of the combustor comprised the burner.

For the main investigations the combustor, including the liner, was mounted and operated in the test facility for combustion chambers at the Institute for Thermal Turbomachinery and Machine Dynamics at Graz University of Technology (figure 81). For the experimental investigations presented in this work, the combustor was operated at atmospheric pressure conditions with natural gas as fuel. Operating the combustor in the test rig, the flames exhibited strong acoustic oscillations at different frequencies and operating conditions. For the results presented in here experiments were performed only at one operating point, where the strongest acoustic oscillations occurred. For this condition, mass-flows for fuel and air were 0.22 gs^{-1} and 2.6 gs^{-1}, respectively, for each injection module. The mass-flow for secondary air was 46.4 gs^{-1} resulting in an overall air mass-flow of 54.2 gs^{-1} in the combustion chamber at a thermal power of approximately 27 kW (all three flames). At this operating point, the flames exhibit a strong acoustic oscillation at a frequency of about 147 Hz.

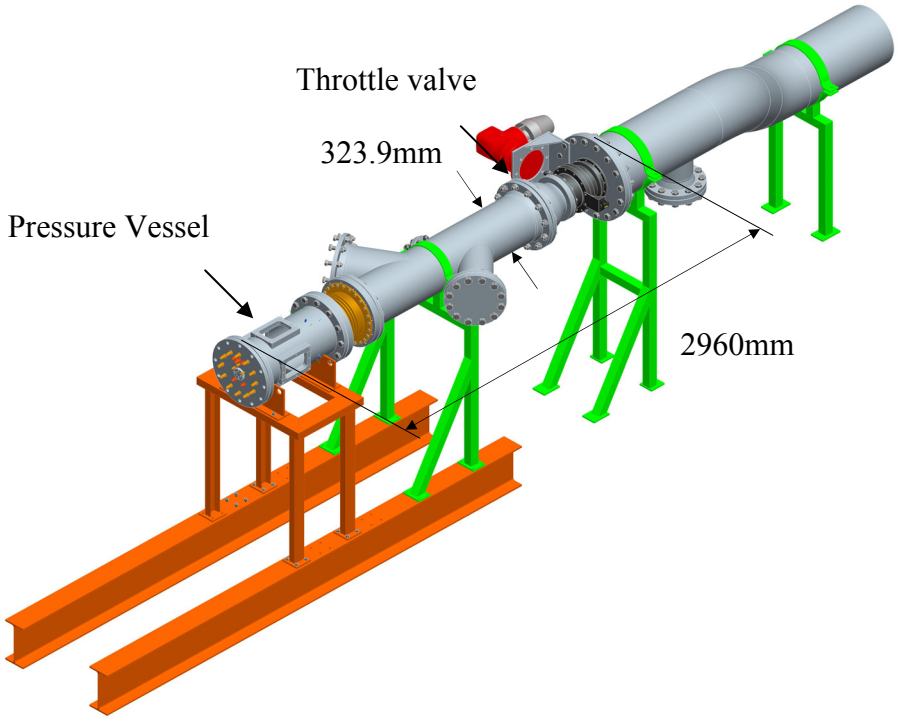

Figure 81: Combustion test rig at the Institute for Thermal Turbomachinery and Machine Dynamics. The multi-flame combustor was mounted into the pressure vessel and operated under atmospheric conditions. The pressure vessel possesses for windows and enables optical access from 4 directions. (Leitgeb 2009)

6.2 Applied measurement techniques and experimental setups

6.2.1 Chemiluminescence emission measurements

To visualize and analyse the flame dynamics qualitatively a high-speed camera (CASIO EXILIM F1, Casio, Tokyo, Japan) was used. The camera enabled the recording of high-speed movies with three different recording speeds of 300 fps, 600 fps and 1200 fps with respective resolutions of 512 x 384, 432 x 192 and 336 x 96 pixels. For the experiments presented in this work the chemiluminescence emission intensity from the combustion zone was recorded by the high-speed camera at two recording speeds, 600 fps and 1200 fps. For the evaluation process only the blue colour separation of the recorded intensity from chemiluminescence emissions was taken into account. For further data analysis two different evaluation processes were applied to these raw data.

In a first step the overall intensity of the chemiluminescence emissions was analyzed to gain information on the fluctuation of the overall heat release rate. Therefore, the overall intensity of chemiluminescence emissions was calculated for each single frame by adding up the single values of intensity for all pixels in the frame, leading to a time signal of overall emission intensities. Each data set consisted of intensity values calculated from 1024 sequent single frames. Performing a FFT with time samples containing 1024 values recorded at 600 fps then resulted in an amplitude spectrum with a frequency resolution of 0.59 Hz. The frequency resolution for time samples recorded at 1200 fps was 1.17 Hz. The calculation of the intensity for each frame, the colour separation and filtering of the blue channel and the FFT were performed in MATLAB vR2007b (The MathWorks, Natick, MA). The data obtained in this way provided information on the fluctuation of the overall heat release rate to a certain degree, but did not provide any information on the fluctuations of the local heat release rates.

To gain spatially-resolved data of the heat release rates, the intensities of the chemiluminescence emissions were now analyzed pixel-wise in the single frames. Therefore a time signal of the chemiluminescence emissions intensity was created for each pixel, consisting of the intensity values for a certain pixel from a number of sequent frames. For this setup a recording speed of 600 fps and a recording duration of 10 s were chosen. Performing a FFT with time samples containing 64 values resulted in 93 spectra with a frequency resolution of 9.375 Hz. The FFT, the calculation and averaging of the spectra were done in MATLAB vR2007b, as well. This resulted in spatially-and frequency-resolved spectra of integral fluctuations in the local heat release rate integrated along the line of sight.

Using the chemiluminescence emissions to estimate local and overall heat release rates in an unstable combustion process one must be aware of the restrictions of this measurement technique. The relationship between the local chemiluminescence emission I_{local}, per unit flame area [Wm^{-2}] and the local rate of heat release $H_{R,local}$, per unit flame area [Wm^{-2}] is characterized by a power law (equation (28),chapter 3.4.1 "*Analysis of flame dynamics by means of chemiluminescence emission*"), where the exponent α depends on the flame temperature and on the effects of unsteady strain and flame curvature (Lee and Santavicca 2003).

The flame temperature itself is a function of the equivalence ratio, unburned gas temperature, dilution, and radiation losses in the flame. Especially the dependency on the equivalence ratio is critical if the overall chemiluminescence emissions are used to investigate the overall heat release rate in an unstable combustion process. Changes in the fuel flow rate and changes in the equivalence ratio alter the chemiluminescence emissions independently, but only a varying fuel flow rate alters the overall heat release rate. Fluctuations in the equivalence ratio are

particularly critical if quantitative data about the amplitude and the phase of the overall heat release rate fluctuations are evaluated (Lee and Santavicca 2003).

In this work the risks of a fluctuating equivalence ratio was minimized due to the premixing of fuel and air at certain distance away from the swirler, additionally chemiluminescence emissions were used only as a qualitative measure for local and overall heat release rates and to characterize temporal fluctuations in the overall heat release rate qualitatively in combustion processes in terms of frequency spectra.

6.2.2 Dual laser vibrometry

The setup for the dual LV measurement technique almost remained unchanged, compared to the measurement setup employed for the previous investigation of density fluctuations in the reference flame and the premixed, swirl-stabilized flame. The calibration factor was set to 5 mm/s/V for both vibrometers again and a low-pass filter of 20 kHz was chosen throughout all the measurements. The measurement plane was placed perpendicular to the main flow direction at a distance of 30 mm above the central burner nozzle (figure 82). In contrast to the measurements performed previously, measurements were performed only from 1 viewing direction due to the limited optical access in the combustion test rig. Since no measurements from several viewing angles were available, no averaging could be performed to damp potential artefacts. The measurement grid for the dual laser vibrometry consisted of a total number of 121 measuring positions, which were equally spaced with a distance of 10 mm in between adjacent positions. This resulted in a rectangular grid with overall dimensions of 110 x 90 mm^2, which can be seen in figure 82(b).

The setup for data acquisition remained unchanged compared to the setup for the investigation of the reference burner and the premixed, swirl-stabilized burner. The voltage signal from each vibrometer was digitalized by the National Instruments PXI-1033 chassis and a NI 4452 A/D converter board (National Instruments Germany GmbH, München, Germany). Both signals were recorded simultaneously by a user-defined routine developed using National Instruments LABVIEW 8.0, which also controlled the traversing system to automate the LV measurements. A sample rate of 40.96 kHz and a recording duration of 120 s per measurement point were chosen. Performing a FFT with time samples containing 2048 values then resulted in 2440 spectra with a frequency resolution of 20 Hz. The post processing of the data, e.g. the FFT, calculation and averaging of the cross-spectra, was done in MATLAB vR2007b.

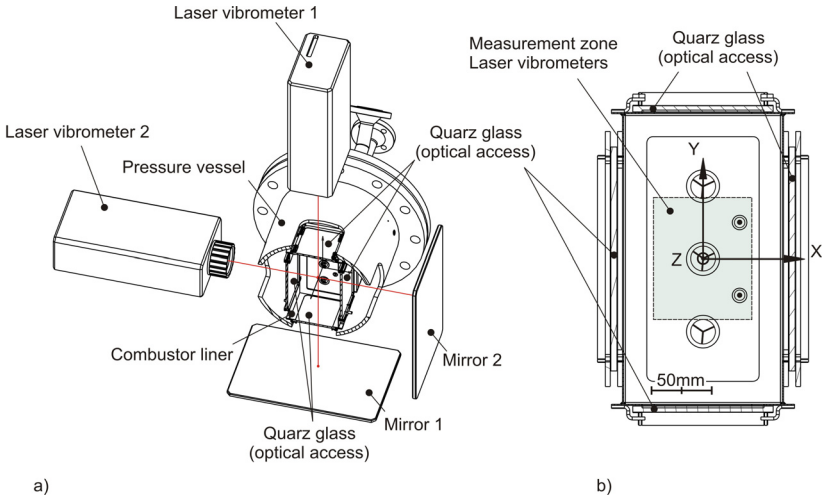

Figure 82: Experimental setup for dual laser vibrometry. Measurements were performed in a plane perpendicular to the x-y-plane at a height of Z = 30 mm above the nozzle exit.

6.3 Results and discussion

First investigations were performed on the unconfined flames, operating the burner in a single flame mode, where only one injection module was operated, and a multi-flame mode, with all three injection modules operated simultaneously, to gather information on the flame shapes and the flame behaviour outside the combustion test rig. The results for the unconfined, single flame have been discussed in the previous chapter. Figure 83(a) and (b) show the spatially-resolved and averaged chemiluminescence emissions of the unconfined combustor operated in the single flame mode (a) and the multi flame mode (b). For these tomographic reconstructions, single projections, providing integral chemiluminescence emission data, were taken from 12 different directions and a tomographic reconstruction technique (algebraic reconstruction technique, ART) was applied to these integral data sets to obtain local data of chemiluminescence emissions, using the IDEA software (Graz University of Technology freeware, available from www.optics-tugraz.at) for the tomographic reconstruction. A detailed description of the tomographic routines can be found in (Hipp et al. 1999; Hipp et al. 2004).

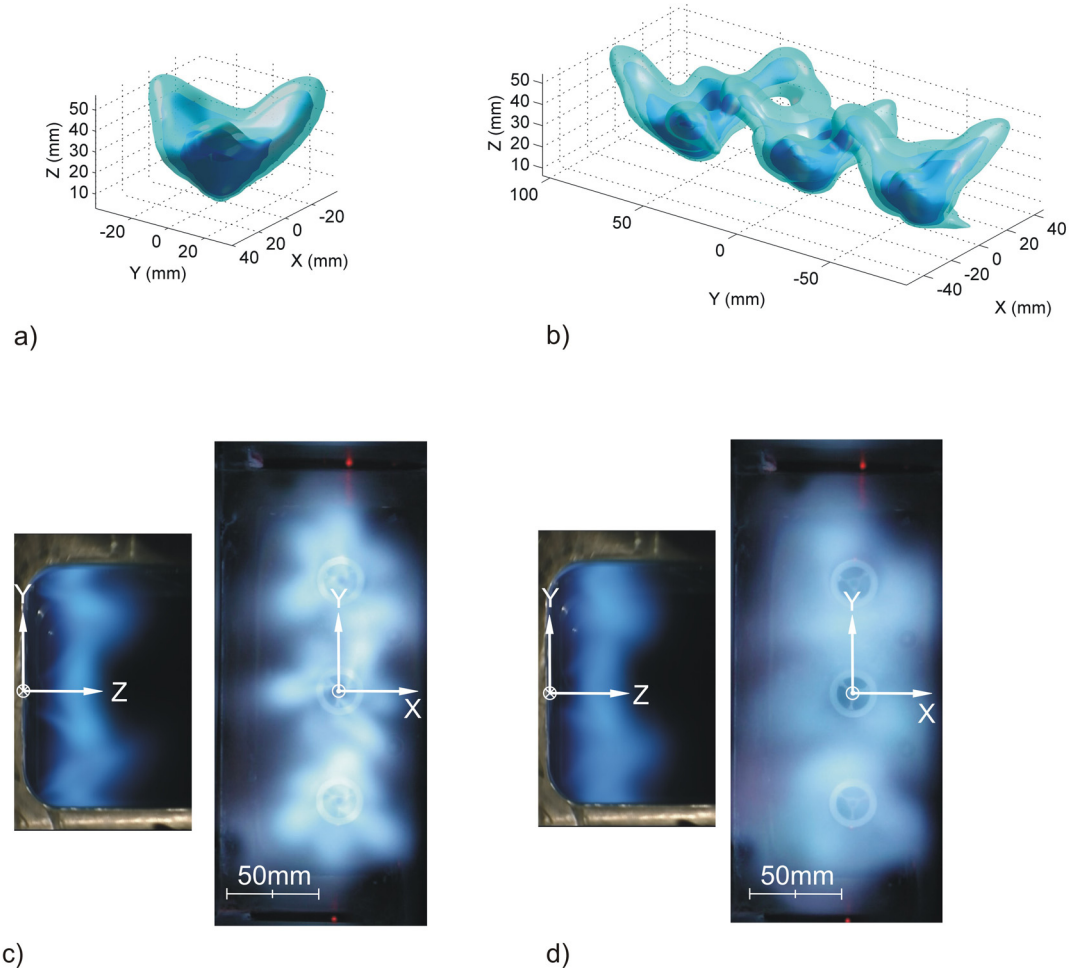

Figure 83: Tomographic reconstruction of chemiluminescence emissions of steady unconfined single flame (a) and steady unconfined multi-flame (b). Photographs of confined steady (c) and oscillating flames (d) with the combustor mounted in the test rig (1 second exposure time).

Figure 83(b) presents the spatially-resolved chemiluminescence emissions of the combustor in the unconfined multi-flame mode. Each single flame is characterized by the conical flame shape near the exit plane and the three twisted arms at higher heights again. Furthermore, the local distribution of the chemiluminescence emissions shows that the individual flames start to bond and interact via these arms at certain heights. The single flames might influence one another especially via these connections in the multi-flame mode.

Since the optical access in the combustion test rig was limited to the dimensions of the quartz windows, no tomographic reconstruction technique was applied to the chemiluminescence emissions data recorded in the confined combustor and therefore only integral line of sight data are available for this configuration. These integral sets of data display the central flame completely (figure 83(c) and (d)).

Figure 83(c) and (d) present two photographs of the combustion chamber operated in the multi-flame mode in the test rig, (c) at a stable operating point, and (d) with strong self-excited oscillations at a frequency of 147 Hz. When the combustor enters the oscillating mode, the visible appearance of the flames changes and the flames seem to be blurred at the boundaries, especially in the regions between the individual injection modules near the front plate of the combustor. In the oscillating mode the individual flames from each injection module can hardly be distinguished with the eye, thus high-speed visualization of chemiluminescence emissions were used, see figure 84.

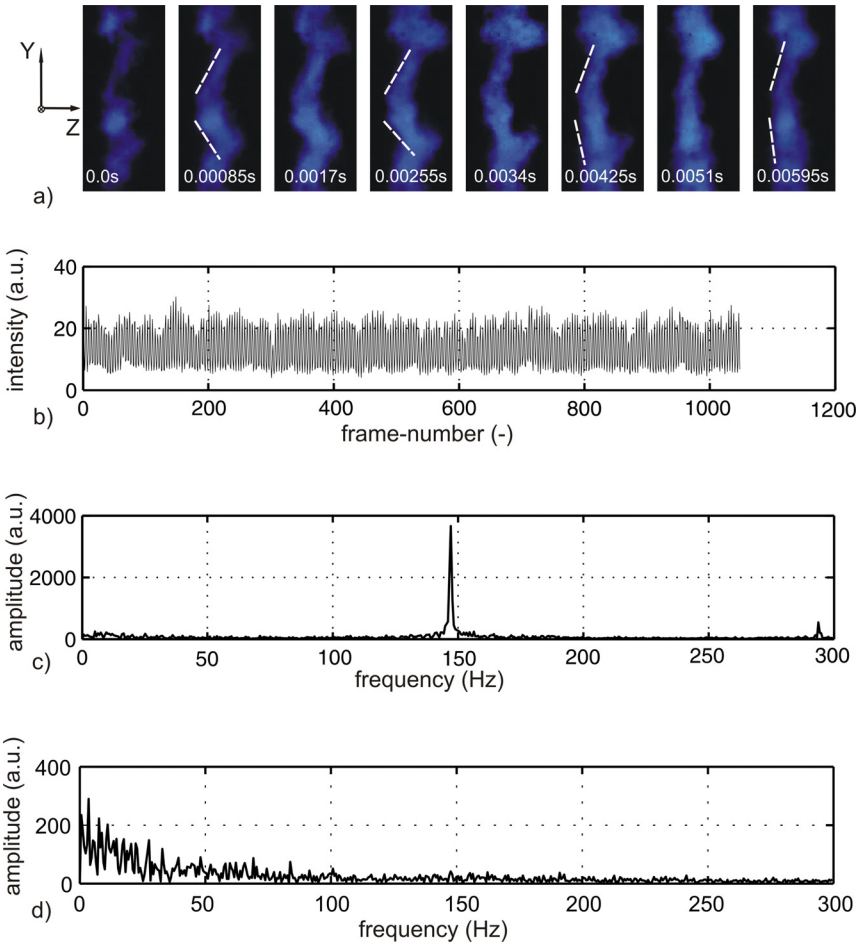

Figure 84: Time series of phase-averaged single frames (a) for one oscillation period (dashed lines indicating changes in the flame front position) and (b) time signal of the overall intensity of chemiluminescence emissions for 1024 frames with the corresponding amplitude spectrum (c). The amplitude spectrum for the same observation direction for the unconfined flames, without self-excited oscillations is shown in (d).

The investigations of the combustion chamber in the test rig started with an analysis of the chemiluminescence emissions. Figure 84(a) presents a time series of phase-averaged single frames of the flames recorded at 1200 fps in the combustion test rig operating the combustor in the oscillating mode. The time series covers one period of the oscillation. A strong fluctuation of the chemiluminescence emissions intensity is clearly visible during one oscillation period, indicating a strong variation of the overall heat release rate. Additionally to the intensity variation significant changes in the position and the shape of the flames can be observed.

At the beginning of the oscillation cycle the flame front has a serrated profile, which is composed of the overlap of the conical shaped flame in the centre-region, corresponding to the central injection module, and parts of the conical shaped flames from the other injection modules at the top and the bottom. At that time, overall chemiluminescence emissions are low. With progressing time the intensity of the overall chemiluminescence emission increases, which indicates an increase in the overall heat release rate, followed by a thermal expansion of the combustion gases. With increasing overall heat release rate, the serrated flame front flattens and parts of the flame front move back towards the front plate of the combustor, indicated by dashed lines in figure 84(a). The conical shaped flame in the centre-region widens more and more, until it turns into an almost flat surface and the intensity of chemiluminescence emission decreases, indicating a decrease in the overall heat release rate at the end of the oscillation cycle.

Figure 84(b) shows the time signal of the overall intensity of chemiluminescence emissions and figure 84(c) presents the amplitude spectrum of the overall intensity of chemiluminescence emissions for a sequence of 1024 frames. A significant peak in the amplitude spectrum can be found at 147 Hz, the oscillating frequency of the combustor. A smaller peak in the amplitude spectrum is also visible at around 290-300 Hz and characterizes the first harmonic oscillation frequency, related to the fundamental oscillation frequency at 147 Hz. Figure 84(d) finally presents the amplitude spectrum for the same observation direction for the unconfined flames, without self-excited and periodic combustion instabilities.

The strong self-excited oscillations in the combustion process also lead to strong acoustic oscillations in the whole test facility and excited forced vibrations at the test setup. Especially the forced surface vibrations of the mirrors used for the dual laser vibrometry had an unwanted, negative impact on the measurement results. Due to the surface vibrations of the mirror, the laser vibrometer did not only record the density fluctuations along the line of sight within the combustion chamber, but the signal also contained the velocity of the vibrating surface in the vibrometer mode used (velocity decoder). To investigate the influence of the surface vibrations on the measurement results, a third vibrometer was employed (figure 85) and the measurement setup was slightly altered. The third vibrometer was arranged behind the surface mirror in a way that the laser beams of vibrometer 2 and vibrometer 3 recorded data from the same point on the mirror surface, but from opposite sides. Vibrometer 2 now recorded the density fluctuations in the measurement volume and the superimposed vibrations of the mirror surface, whereas vibrometer 3 recorded only the forced vibrations of the mirror.

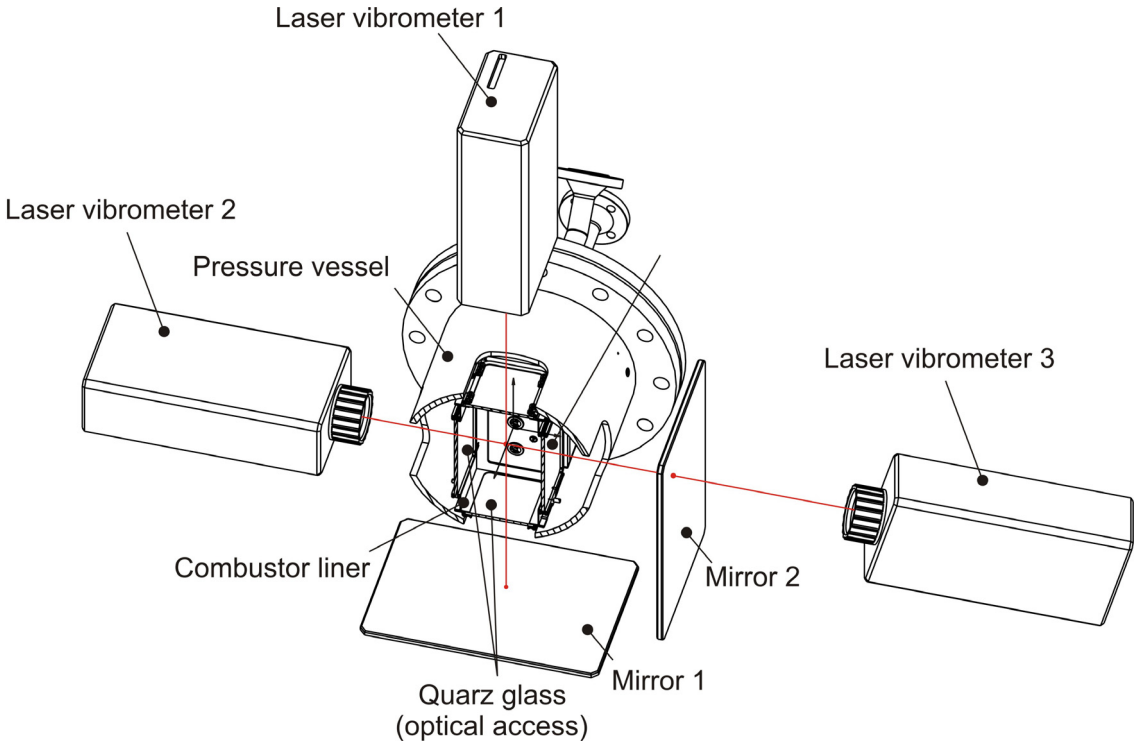

Figure 85: Dual laser vibrometry setup for the investigation of the mirror vibrations caused by the oscillating flame. A third vibrometer was applied to measure the surface vibrations and to investigate the influence of the vibrating surface on the measurement results obtained in the flame (laser vibrometer 2).

Figure 86(a) presents integral data of density fluctuations recorded by vibrometer 2 in a plane perpendicular to the x-y-plane at a height of Z = 10 mm. These data also contain the "erroneous" density fluctuations due to the vibrating mirror surface. In figure 86(b) the corresponding data for the mirror vibrations can be found. These mirror vibrations were recorded by vibrometer 3 and converted to density fluctuation data to allow a direct comparison to the data recorded by laser vibrometer 2. In both figures highest values for the density fluctuations are present at 150 Hz, near the oscillation frequency (147 Hz) of the combustion instability. In figure 86(a) higher values of density fluctuations are also visible beside the 150 Hz line, whereas in figure 86(b) the "density fluctuations" are limited almost to the 150 Hz line. These results indicate that the integral laser vibrometer measurements were falsified at 150 Hz, whereas at frequencies besides the oscillation frequency, the influence of the vibrating surface mirror on the density fluctuations recorded in the measurement volume can be neglected. At 150 Hz the integral density fluctuations recorded by vibrometer 2 are falsified significantly, as the recorded surface vibrations in figure 86(b) and the density fluctuations in figure 86(a) are in the same order of magnitude. Thus a proper interpretation of line of sight data of density fluctuations at 150 Hz can not be done in this case and no reasonable statements on the integral density fluctuations caused by the instable combustion mode can be given.

The dual laser vibrometry technique on the other hand provides a tool to extract the local data of density fluctuations, using two integral sets of data. If the surface vibrations of mirror 1 and 2 are correlated, but out of phase, the local density fluctuations can be extracted with the help of the phase filter. To investigate the surface vibrations of mirror 1 and 2 in terms of their phase relation and correlation, the laser vibrometer setup presented in figure 87 was used.

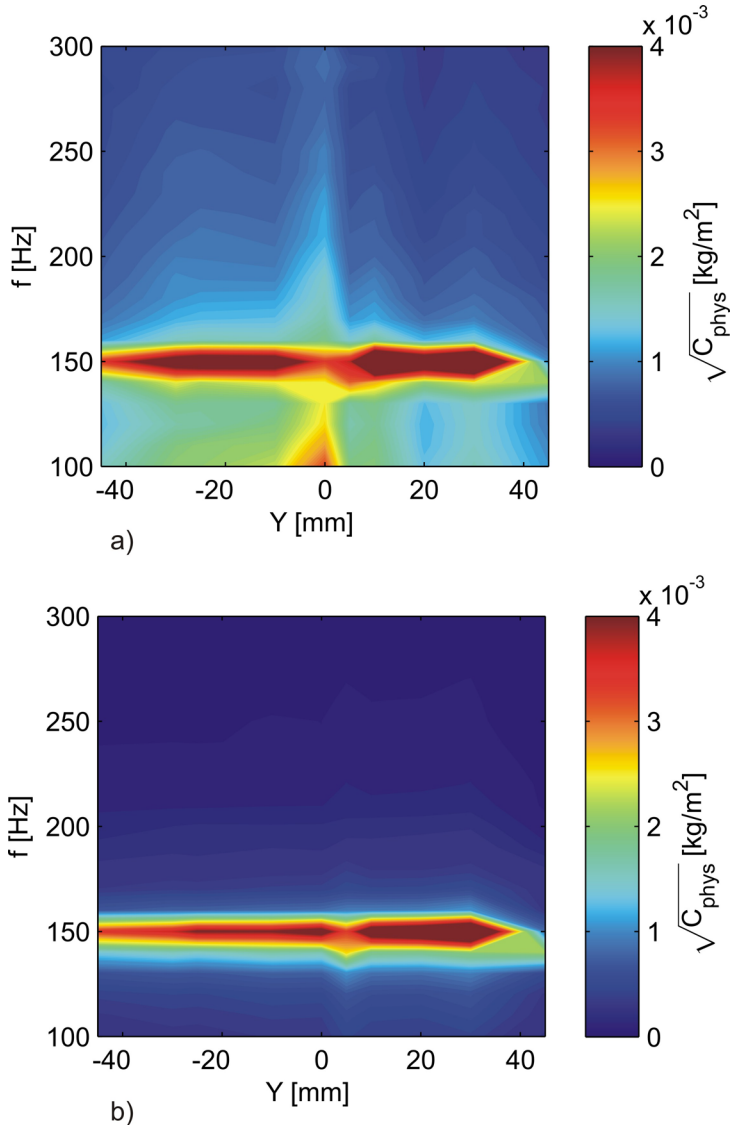

Figure 86: Comparison between (a) integral data of density fluctuations recorded by laser vibrometer 2 (density fluctuations caused by the flame and "erroneous" density fluctuations due to the vibrating mirror) and (b) surface vibrations of the mirror. The vibrations recorded by laser vibrometer 3 were converted into density fluctuations to allow a direct comparison with data recorded by laser vibrometer 2. Data were recorded in a plane perpendicular to the x-y-plane at a height of Z = 10 mm in front of the three nozzles's plane.

Compared to the setup presented in figure 85, the position of laser vibrometer 1 was changed to allow the recording of the surface vibrations from mirror 1. During this experiment, the position of the laser vibrometer 1 was fixed, while laser vibrometer 3 was traversed along the y-axis at a height of Z = 0 mm. In figure 88 the phase distribution between the surface vibrations of mirror 1 and 2 is shown. Non-zero phase values are only present beside the oscillation frequency of 150 Hz, but at 150 Hz the phase values are more or less zero. This indicates that the surface vibrations of the mirrors are in phase and therefore the phase filtering will not damp the surface vibrations in the measurement signal. This result was expected, since both mirrors were mounted at the same distance away from the combustion test rig and due to the fact that the mirror vibrations were excited by the acoustic oscillation from the unstable combustion process, which stem from the same source.

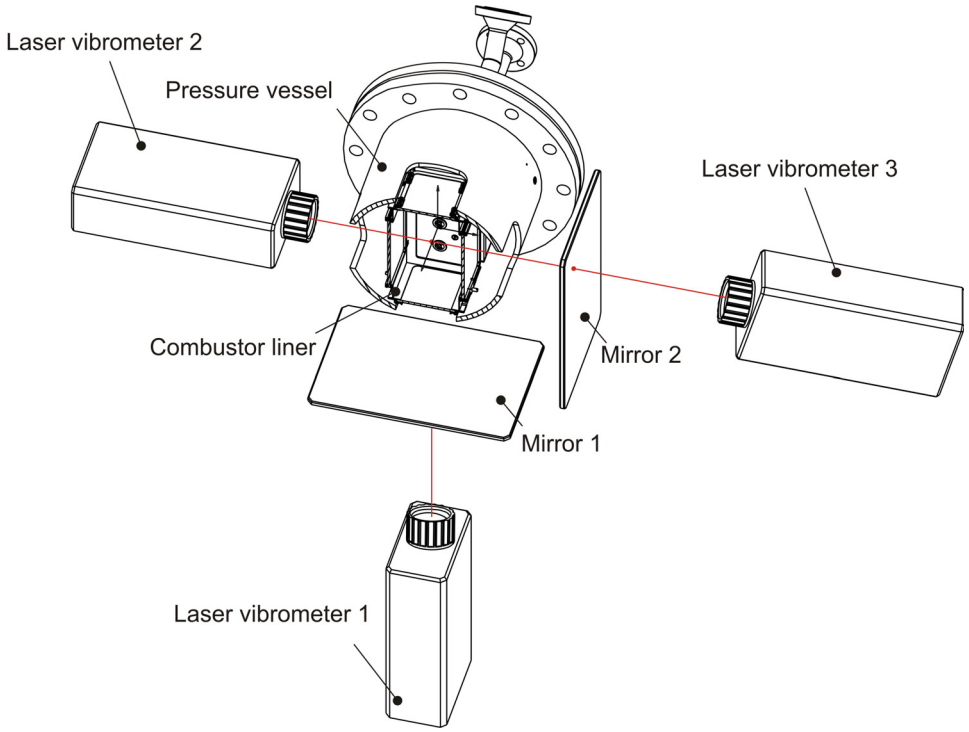

Figure 87: Dual laser vibrometer setup for the investigation of the phase between the two vibrating mirrors. For this experiment vibrometer 1 was fixed while vibrometer 3 was scanning along the y-axis at a height of Z = 0 mm in front of the three nozzles's plane.

A redesign of the mirror mountings was necessary to prevent falsified results from mirror vibrations. Therefore both mirrors were bonded to a high mass structure to damp surface vibrations caused by the strong acoustic oscillations due to the unstable combustion process. The high mass structures consisted of sectional steel with 80 x 140 x 320 mm^3 inner dimensions, filled with sand and welded on both ends. The surface mirror was then glued with its back side to the sectional steel, resulting in a mirror mounting of about 15 kg mass. On the opposite side of the steel block a reflecting foil was glued to enable vibration monitoring from this side, using a laser vibrometer (figure 89).

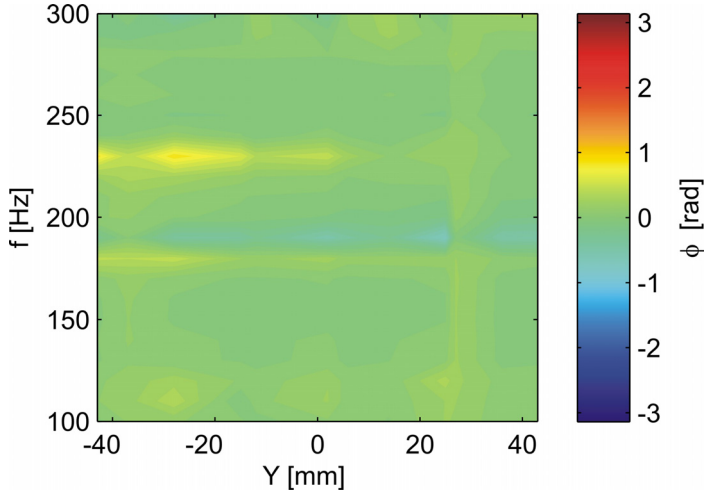

Figure 88: Relative phase distribution of the vibrating mirrors 1 and 2 at a height of Z = 0 mm. The surface vibrations of mirror 1 and 2, caused by the acoustic excitation from the combustion instabilities, are highly correlated and in phase. A redesign of the mirror mountings was necessary to prevent falsified results from mirror vibrations.

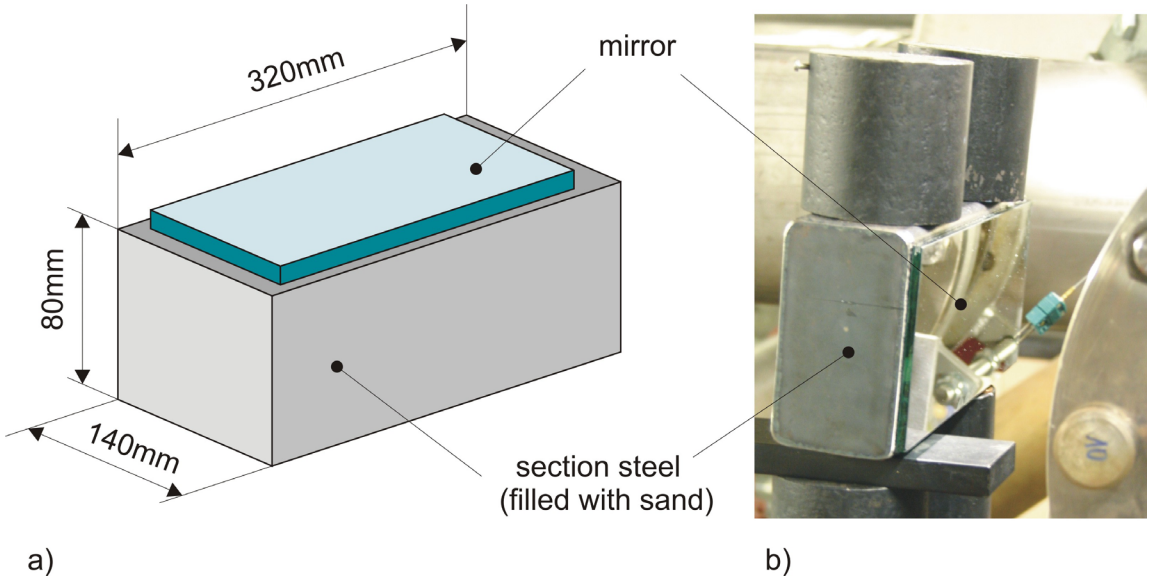

Figure 89: Model of re-designed mirror mountings (a) and photograph of one mirror mounting. The mounting consisted of sectional steel filled with sand and sealed on both ends. The surface mirror was glued with its backside to the sectional steel .This resulted in a mirror-steel block with a total mass of about 15 kg.

Figure 90 presents measurement results after the redesign of the mirror mountings. For this measurement, the laser vibrometer setup presented in figure 85 was used again, and density fluctuations in the combustion chamber and vibrations of the mirror were recorded separately. The comparison between the integral data of density fluctuations recorded by laser vibrometer 2 (figure 90(a)) and surface vibrations of the mirror recorded by laser vibrometer 3 (figure 90(b)) reveals a significant reduction of surface vibrations after the redesign of the mirror mountings. The massive structures, which carried the mirrors, damped the amplitude of the forced surface vibrations considerably due to their high mass. According to figure 90, the measurement results obtained from vibrometer 2 can be attributed solely to the density fluctuations in the combustion chamber, since the vibrations of the mirror surface are at least one order of magnitude smaller, compared to the density fluctuations in the combustion chamber. Even at 150 Hz no significantly higher values for the surface vibrations of the mirror can be found.

In a next step combustions instabilities observed at 147 Hz were investigated in detail. For a plane 30 mm in front of the three injection modules, figure 91 presents the distribution of the physical cross-spectrum, the relative correlation and the phase distribution for two different frequencies at 140 Hz and at 220 Hz. Since the frequency resolution of the FFT, applied for the data analysis of the dual laser vibrometry, was 20 Hz in this case, the frequency bin presented at 140 Hz ranges from 140-160 Hz and therefore also includes the oscillation frequency of the combustion instability at 147 Hz.

Highest values for the cross-spectrum (and therefore highest values of density fluctuations) at 140 Hz can be found in two areas ranging from X = 0 mm to 20 mm at Y = -40 mm and at X = 10 mm at Y = -10 mm (figure 91, top). Maximum values for the cross-spectrum at 220 Hz are present in the same areas, but the absolute values are one order of magnitude lower, if compared to the data obtained at 140 Hz. A closer look to the distribution of the relative correlation (figure 91, middle) reveals large differences in the absolute values between the two investigated frequencies. The relative correlation at 140 Hz (figure 91, middle) reaches values of more then 0.8, which indicates the presence of large coherent structures that are correlated over large areas in the measurement plane.

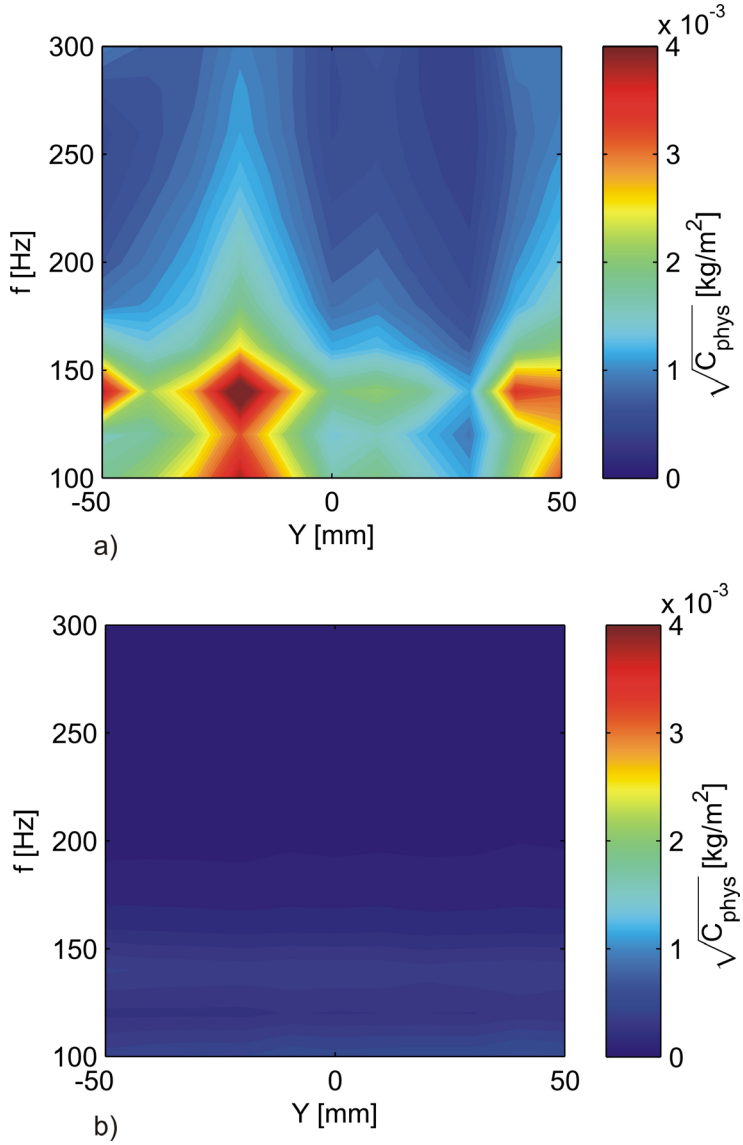

Figure 90: Comparison between (a) integral data of density fluctuations recorded by laser vibrometer 2 and (b) surface vibrations of the mirror at Z = 30 mm above the three injection modules. After the redesign of the mirror mountings, the surface vibrations were damped significantly (see figure 86) and the measurement results in (a) can be attributed to density fluctuations in the combustion chamber.

The elevated correlation can be attributed to the massive fluctuation in the heat release rate, the pressure fluctuations and the movement of the flame front (see figure 84) in the unstable combustion mode. In contrast, the highest values of the correlation at 220 Hz are around 0.12-0.14 and the distribution of the relative correlation is more heterogeneous compared to the distribution at 140 Hz. The phase distributions are nearly the same for both frequencies (figure 91, bottom) and non-zero values are present in an area at Y = 40 mm and at Y = -40 mm. At 140 Hz non-zero phase values can be found at a vertical line at X = -40 mm, but since the magnitude of the cross-spectrum is low in this area the application of the phase filter will not alter the results significantly in this region.

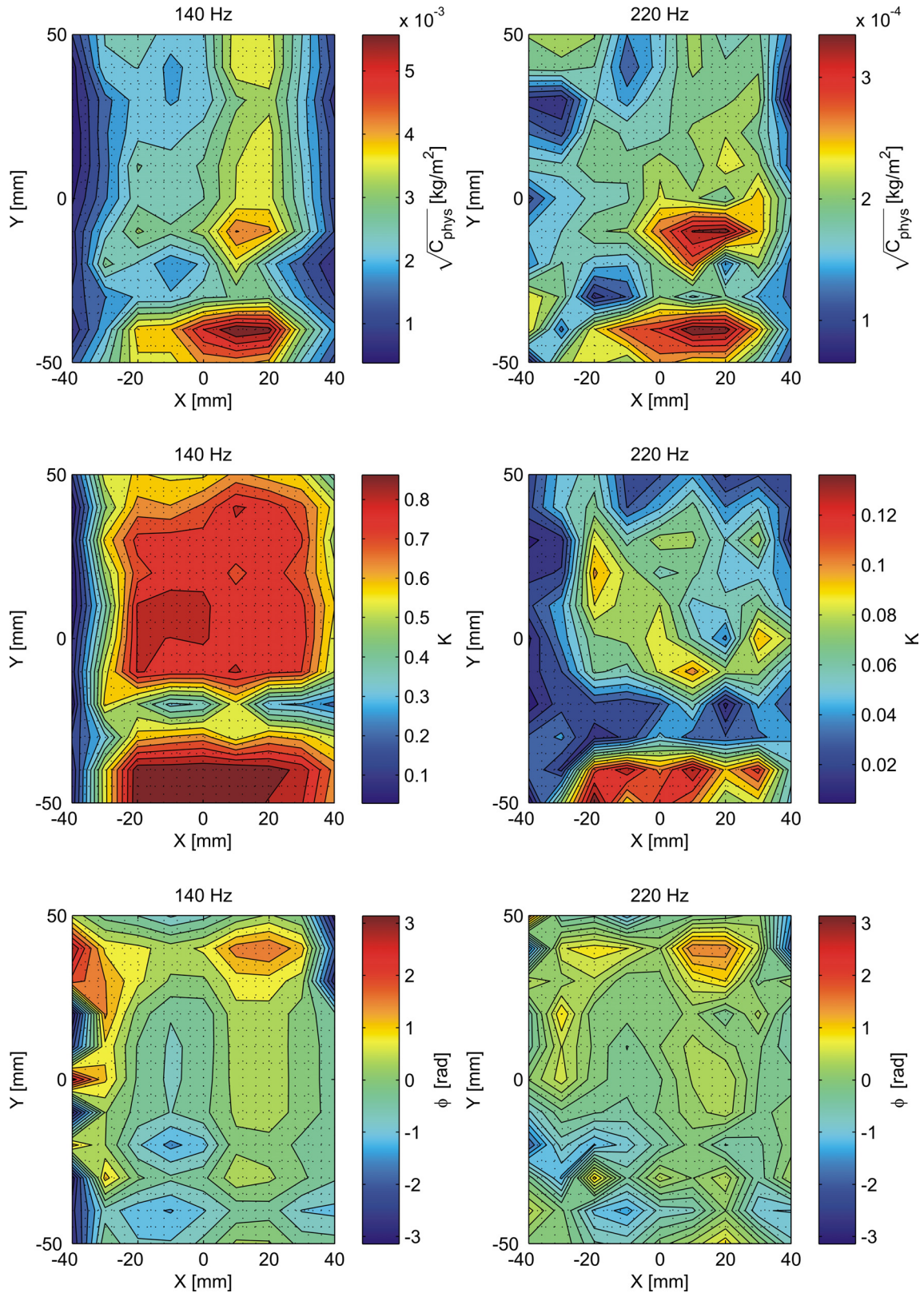

Figure 91: Comparison between the physical cross-spectrum, the relative correlation and the phase distribution for two frequencies at 140 Hz and 220 Hz at Z = 30 mm and combustions instabilities observed at 147 Hz. Significant differences between the two frequencies can be found in the magnitude of the cross-spectrum and the relative correlation. The frequency bin at 140 Hz covers the combustion instability, which is present at 147 Hz; the 220 Hz are clearly besides this frequency.

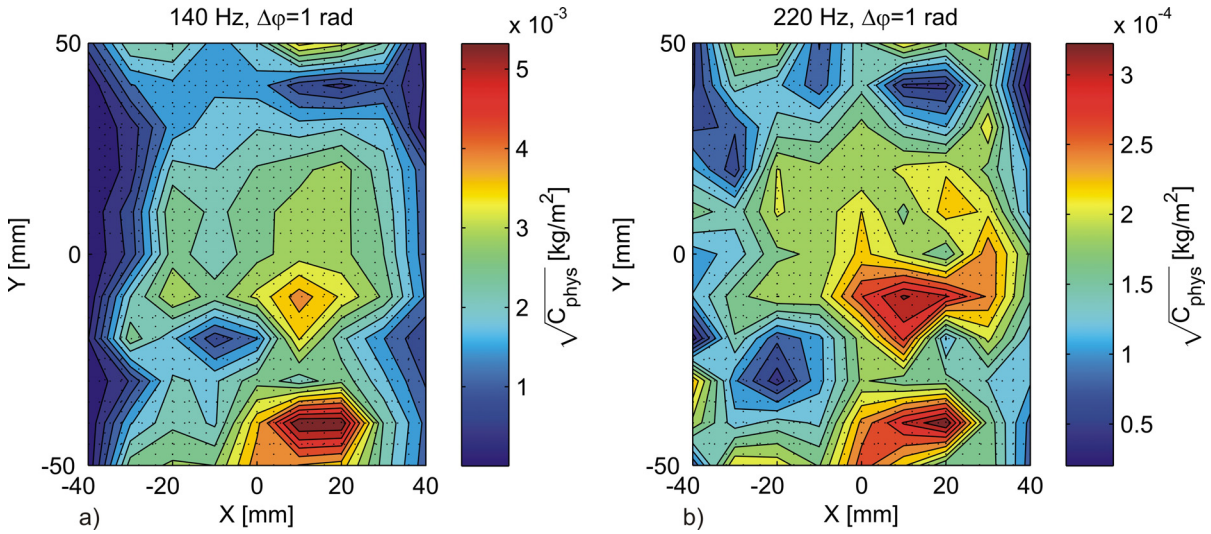

Figure 92: Comparison between (a) the filtered cross-spectrum at 140 Hz (oscillation frequency of the self-excited combustion instability) and (b) the filtered cross-spectrum at 220 Hz at a height of Z = 30 mm above the three injection modules. Density fluctuations at 140 Hz are one order of magnitude higher compared to density fluctuations at 220 Hz.

Figure 92 illustrates a comparison between the filtered cross-spectrum at 140 Hz (a) and the filtered cross-spectrum at 220 Hz (b). The density fluctuations at 140 Hz are elevated over wide areas in the measurement plane, but after the filtering process, three areas, separated by horizontal areas of lower density fluctuations at approximately Y = -25 mm and Y = 40 mm were identified. The area of higher density fluctuations in the centre-region can be attributed to the central flame, whereas the areas of higher density fluctuations at the top and at the bottom of the plot are mainly due to the second and third flame, fed by the two adjacent injection modules. At 220 Hz a similar distribution for the density fluctuations can be found, but the separations between the different areas are not so distinct, compared to the distribution of density fluctuations at 140 Hz. But again, an area of higher density fluctuations is present in the centre-region. At the top and the bottom additional areas of higher density fluctuations can be found.

In a next step the cross-spectrum, the relative correlation and the phase distribution at 300 Hz were investigated (figure 93). The 300 Hz frequency bin covers the first harmonic of the oscillation frequency and therefore the maximum values for the cross-spectrum exceed the maximum values for the 220 Hz. The density fluctuations found at 300 Hz are up to 3 times higher than the density fluctuations at 220 Hz. The distribution of the cross-spectrum and the relative correlation at 300 Hz (figure 93(a), (b)) reveal three areas of elevated values, which are clearly separated from each other. The relative correlation reaches maximum values up to 0.7, which indicates the presence of large, highly correlated density structures at this frequency. The density fluctuations at 300 Hz are triggered by the oscillation frequency of the unstable oscillation combustion mode, but the distribution of the density fluctuations at the 140 Hz and 300 Hz are different (see figure 91 top, left and figure 93(a)). The areas of higher density fluctuations at 300 Hz are considerably smaller compared to the areas of higher density fluctuations at 140 Hz. The phase distribution at 300 Hz (figure 93(c)) is also much more heterogeneous compared to the phase distribution at 140 Hz (figure 91 middle, left) and non-zero phase values are widely spread over the measurement area. This indicates a probability of potential artefacts in the non-filtered cross-spectrum, or a difference in flame oscillation (140 Hz and higher harmonics) and sound pressure modes (only at 140 Hz). To improve the results a phase filter with bandwidth Δφ=1 rad was applied and the filtered data set is shown

in figure 93(d). Higher values of density fluctuations are constrained now to three smaller areas at horizontal lines at Y = 40 mm, Y = -10 mm and Y = -40 to -50 mm. These areas coincide only in parts with areas of elevated density fluctuations at 140 Hz. Especially at Y = 40 mm density fluctuations at 140 Hz (figure 92) are rather low, whereas at 300 Hz a maximum can be found in this area.

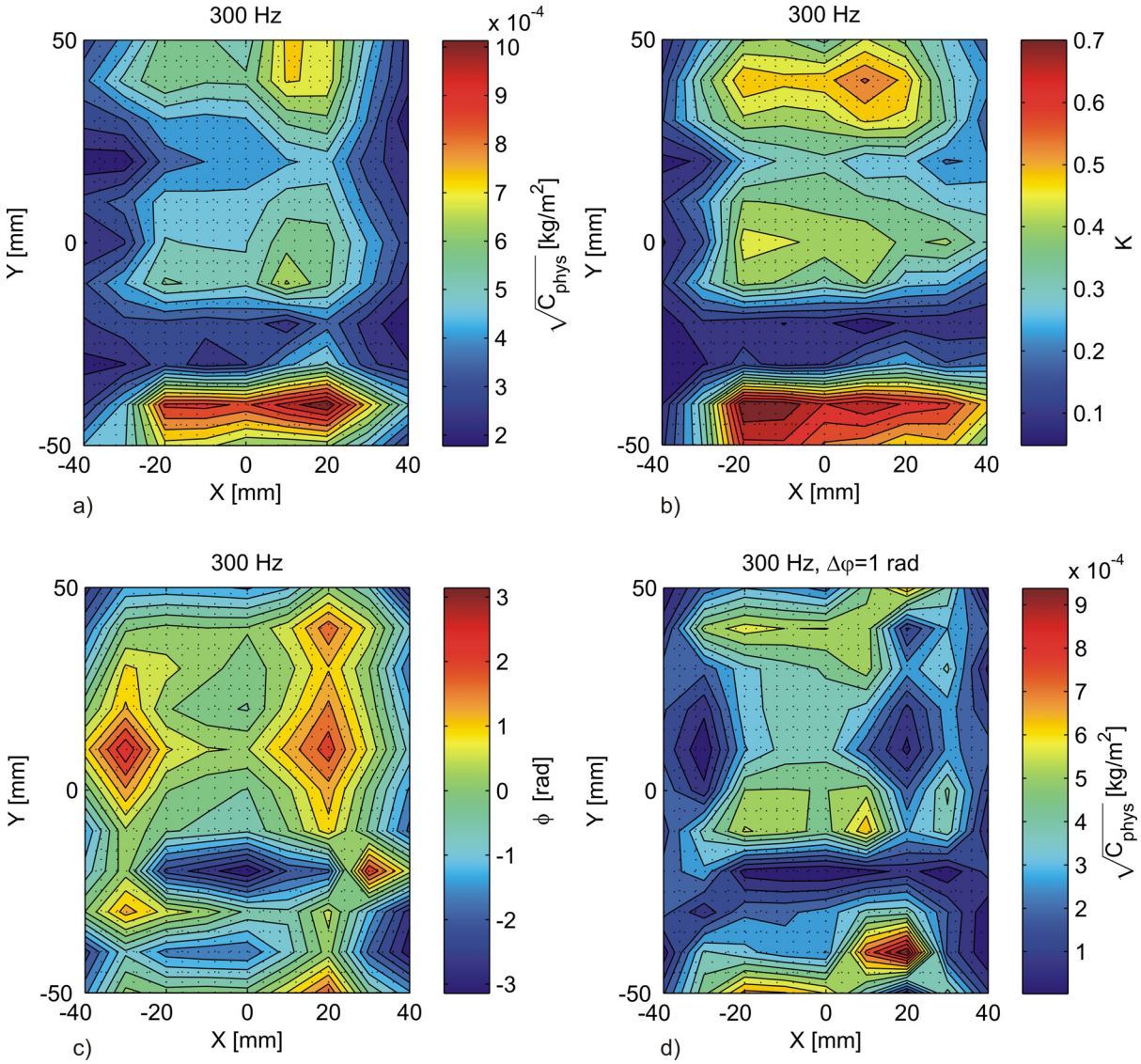

Figure 93: Distribution of the physical cross-spectrum (a), the relative correlation (b), the phase (c) and the filtered cross-spectrum (d) at a frequency of 300 Hz and a height of Z = 30 mm. The frequency bin at 300 Hz covers the first harmonic of the oscillation frequency of the combustion instability. The magnitude of the cross-spectrum exceeds the magnitude of the cross-spectrum at 220 Hz, and the relative correlation is significantly higher compared to the 220 Hz.

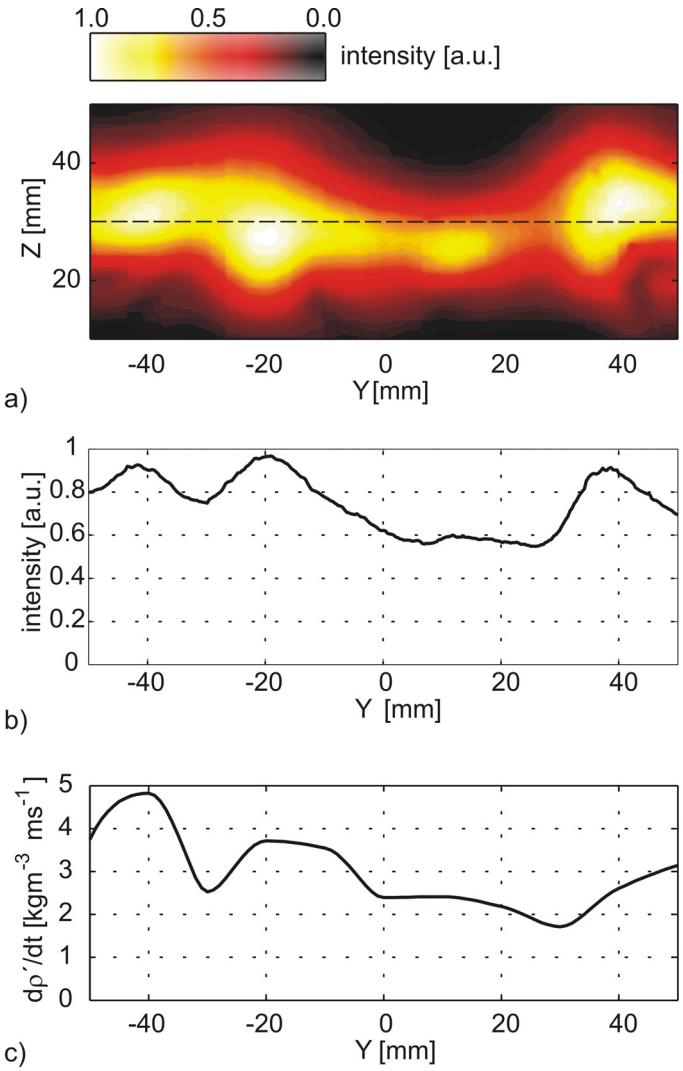

Figure 94: Integral data of normalized, fluctuating chemiluminescence emissions at a frequency of 147 Hz (a) and normalized, fluctuating chemiluminescence emissions at a frequency of 147 Hz at a height Z = 30 mm (b). In (c) the corresponding projection data of the time derivative of density fluctuations recorded by one vibrometer at Z = 30 mm are shown.

Due to the lack of measurements from several viewing angles and the accompanying loss of the averaging process, a powerful tool for the suppression of potential artefacts could not be applied in the combustion chamber. This leads to a higher probability for artefacts in the measurement results presented here, compared to the measurement results presented in the previous chapters. But since the investigations of the premixed swirl-stabilized flame (chapter 5) showed that the measurement results in the low frequency range (between 20-100 Hz) are rather prone to potential artefacts, whereas the density fluctuations recorded at higher frequencies were rather insusceptible to artefacts, the probability for falsified results in the combustion chamber at the investigated frequencies should be rather low.

In figure 94(a), the fluctuating component of the chemiluminescence emissions at a frequency of 147 Hz is shown. To obtain this result an FFT was applied to 6000 single frames with samples of 64 frames recorded at 600 fps. The data were then normalized and represent the fluctuating component of the local heat release rate when integrated along the line of sight. The highest values for the fluctuation of the chemiluminescence emissions intensity can be found at three different positions in the flame front. The strong fluctuations in these areas are in part caused by the movement of the flame front, and in part by the general variation of the intensity of the chemiluminescence emissions (heat release) during one oscillation period.

While figure 94(b) presents the fluctuating chemiluminescence emissions at a frequency of 147 Hz at a height of Z = 30 mm, figure 94(c) illustrates the corresponding projection data of the time derivative of density fluctuations recorded at the same height by one vibrometer for the same frequency.

In contrast to the stable combustion, the laser vibrometer data and the chemiluminescence data plots were not of identical shape when the combustor operates in the oscillating mode. Since density fluctuations are due to pressure fluctuations and fluctuations in the heat release

rate according to equation (1), and provided that the fluctuations of the chemiluminescence emissions are representative for fluctuations in the heat release rate, the difference between the laser vibrometer data and chemiluminescence emissions data must be due to pressure fluctuations. This indicates that the time derivatives of pressure fluctuations are in the same order of magnitude as the fluctuations of the heat release rate in an unstable combustion process. Thus, the time derivative of density fluctuations cannot be linked directly to the fluctuating heat release rate due to the high amplitude pressure fluctuations.

Additionally, figure 94(b) and (c) show that the difference between the time derivative of the density fluctuations and chemiluminescence emission data varies along with the measurement positions indicating a different amplitude of the pressure fluctuations in the central region of the combustion chamber compared to the ones close to the wall and the cooling film region.

Together with the integral data of the time-derivative of density fluctuations recorded by a single vibrometer (discussed in figure 94), the spatially-and frequency-resolved time-derivative of density fluctuations were recorded at the same height Z = 30 mm, using two laser vibrometers and a correlation technique

In figure 95, these frequency-resolved and local data of the time derivative of density fluctuations at the oscillating frequency are shown. Elevated values for the time derivative of the density fluctuations are present nearly in the whole field, except in the outer region on the left side the values tend to decrease significantly, thus indicating that the time derivatives of the pressure fluctuations and heat release fluctuations are generally low in this area, or in the same order of magnitude but out of phase.

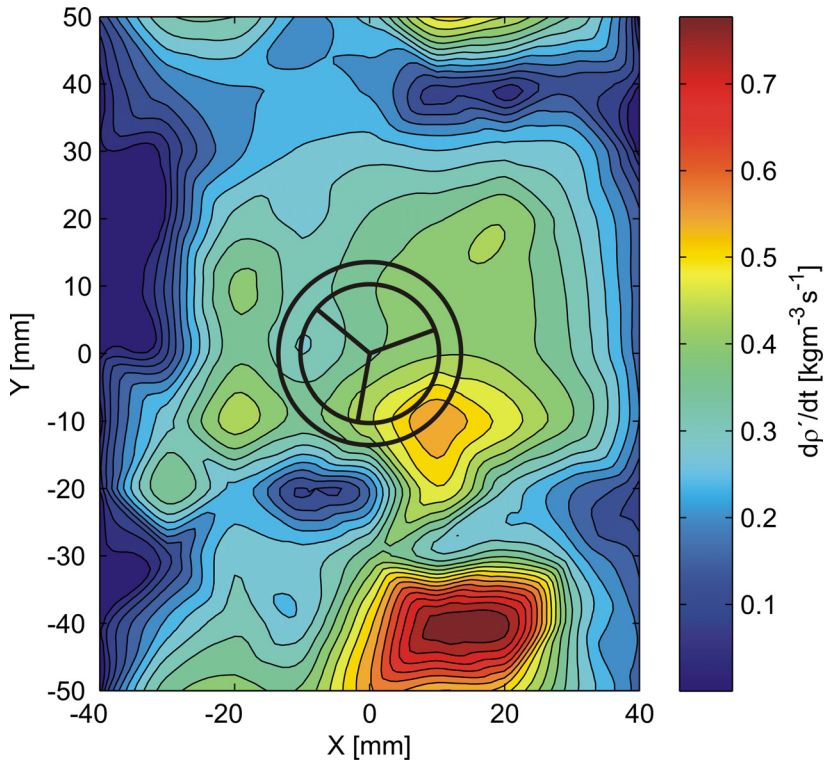

Figure 95: Time derivative of local density fluctuations at the oscillating frequency (147 Hz) at a height of Z = 30 mm above the plane of the injection modules. The position of one exit nozzle is indicated by black circles.

When compared to figure 83(d) the local distribution of the time derivative in density fluctuations confirms the connection between the single flames from the individual injection modules, but in this illustration density fluctuations can be attributed easier to the single flames. Two areas of highest values for the time derivative of the density fluctuations are found at Y = -40 mm and X = -20 to -10 mm which corresponds quite well to the integral data recorded by the single vibrometer and to the chemiluminescence emissions.

7 Summary and conclusion

In this work, a novel measurement technique for the investigation of spatially- and frequency-resolved density fluctuations in turbulent combustion processes is presented. The measurement technique has been used previously, but in this work it was applied to investigate local density fluctuations in combustion processes for the first time. Two laser vibrometers were used to measure the local magnitude of density fluctuations in different setups, starting with a circular reference flame. Further measurements were performed in a premixed, swirl-stabilized flame and a multi-flame gas turbine model combustor with self-excited combustion instabilities.

At first, the validation of the dual laser vibrometer technique for combustion analysis was done in a circular reference flame. This flame was scanned in 51 positions along the flame diameter. The beams of the two laser vibrometers crossed orthogonally in a plane perpendicular to the jet axis. The main tool of this approach is to calculate the signal cross-correlation (averaged cross-spectra) in order to obtain frequency-resolved local density fluctuations. For this methane-jet burner operating under atmospheric conditions tomographic reconstructions of integral data from single projections was also possible since no windows limited the field of view. Therefore classical interferometry (differential interferometer) and tomographic field reconstruction of single-projection laser vibrometer data were also applied to the flame and served for validation purpose.

Two main sources of error in the quantitative reconstruction of local density fluctuations by the dual laser vibrometer technique were identified. If large coherent structures are present in both laser beams at the same time, a signal correlation might be wrongly assigned to the position of the intersection of both laser beams causing a local artefact in the result. Using the phase of the cross-spectrum it is possible to distinguish between artefacts or local structures, as local structures posses no phase delay ($\varphi=0$ rad) compared to wave fields ($|\varphi|>0$ rad). Thus a phase filter can be applied to improve measurement results. Artefacts might still remain wherever the phase delay within the field is a multiple of 2π. To damp the remaining artefacts, averaging of seven different scan directions was done. In this way maps of local density fluctuations were obtained. In case of limited angle observation or large coherent structures (sound waves) the correlation coefficient K proved to be a powerful tool for error analysis and flow-field analysis. For recording quantitative data the concept of the effective measurement area A_c and its relation to velocity and frequency was discussed.

Additionally laser Doppler velocimetry measurements were performed to investigate flow velocities, Raman was done to get temperature and concentration data and differential interferometry was applied to obtain data of total density and density fluctuations in the flame. Quantitative comparison of local density fluctuations recorded by laser vibrometer measurements to data received from differential interferometry by tomographic algorithm (ART) proofed the capability of the laser vibrometer to detect density fluctuations in flames.

Furthermore preliminary investigations for the detection of combustion instabilities using the dual laser vibrometer technique were carried out. For these experiments combustion instabilities were enforced by modulating the methane-flow at a certain frequency. Due to the unsteady heat release and the pressure fluctuations, triggered by the oscillating fuel-flow, data of elevated density fluctuations were obtained at the excited frequency, which served as a marker for the enforced combustion instabilities. These experiments were accompanied by schlieren-visualizations to allow a qualitative comparison of data obtained by the dual laser vibrometry and the information on the density gradients from the schlieren technique.

In a next setup, the dual laser vibrometry was used to measure the local magnitude of density fluctuations in a premixed, swirl-stabilized flame. The flame was scanned in 169 positions in a field at $Z = 55$ mm above the burner exit plane, forming a measurement grid of 120 x 120 mm^2. Thereby the capability of the measurement technique to resolve complex shaped flames was shown. Due to the shape of the flame, averaging of measurements performed from 6 different scanning directions was applied to damp potential artefacts, and the influence of the averaging process on the quality of the obtained results was investigated. Especially for large, coherent structures, present at low frequencies, this averaging process is of great importance, as the distributions of density fluctuations varied significantly for different scanning directions, which was an indicator for the presence of artefacts. At higher frequencies, the results obtained from different scanning directions were more uniform and therefore the averaging process is no necessity. These facts are important for subsequent measurements in combustion chambers with limited optical access, where measurements can be only performed from one scanning direction.

The dual laser vibrometer measurements were accompanied by high-speed schlieren visualizations and measurements of chemiluminescence emissions. Both techniques, schlieren and chemiluminescence emission measurements, were used to validate obtained data of density fluctuations qualitatively. Special attention was paid to the comparison between the time derivative of density fluctuations integrated over all frequencies and the line of sight data of the fluctuating chemiluminescence emissions. The slopes of the time derivative of density fluctuations integrated over all frequencies and the line of sight data of the fluctuating chemiluminescence emissions coincided qualitatively very well, thus indicating the capability of the laser vibrometer to detect heat release rate fluctuations in a stable combustion process. In combination with equation (1), where the time derivative of density fluctuations is linked to the time derivative of pressure fluctuations and heat release fluctuations directly, these results lead to the assumption, that the time derivative of pressure fluctuations can be neglected in a stable combustion process, compared to the heat release fluctuations. Thus, the time derivative of density fluctuations recorded by the laser vibrometer is directly proportional to fluctuations in the heat release rate in a stable combustion process and within the flame.

In the last setup the dual laser vibrometer technique was applied to a multi-flame gas turbine model combustor operated at an unstable combustion mode, where the flames exhibited strong acoustic oscillations at a frequency of 147 Hz. The multi-flame combustion chamber was scanned in 99 positions in a field at $Z = 30$ mm above the three combustion modules, forming a measurement grid of 110 x 90 mm^2. The experiments in the combustion chamber test rig provided the most challenging environmental conditions for the dual laser vibrometer technique throughout all the measurements performed in this work. This was due to the influence of the polluted optical accesses and the influence of forced surface vibrations of the measurement setup caused by acoustic excitation in the unstable combustion mode. Since the optical access in the combustion test rig was limited to the dimensions of the quartz plates, dual laser vibrometer measurements were performed from only one viewing direction, thus no averaging of measurement results from different viewing angles was possible. Especially the surface vibrations of the mirrors had an undesirable impact on the measurement results, thus, a redesign of the mirror mountings had to be done and additionally a vibration monitoring of the mirror surface was installed.

Despite these disturbing influences, an investigation of the unstable combustion process was performed using local data of density fluctuations provided by the dual laser vibrometer technique. In addition to the dual laser vibrometry, chemiluminescence emissions were also recorded to gain information on the unsteady heat release during one oscillation period in the unstable combustion mode. A comparison between the time derivative of density fluctuations at the oscillation frequency and the line of sight data of the fluctuating chemiluminescence emissions (heat release rate fluctuations) at the oscillation frequency was done. In contrast to

the stable combustion, the laser vibrometer data and the chemiluminescence data plots were not identical in shape when the combustor operated in the oscillating mode. This indicates that the time derivatives of pressure fluctuations are in the same order of magnitude as the fluctuations of the heat release rate in an unstable oscillating combustion process and cannot be neglected any more. Thus from the difference between the time derivative of the density fluctuations and the chemiluminescence emission data, different amplitudes of the pressure fluctuations in the central region of the combustion chamber compared to the ones close to the wall and the cooling film were found.

The measurement techniques presented in this work provide local data of density fluctuations and local data of the time derivative of density fluctuations for turbulent combustion analysis. The main advantage of this measurement technique is the direct measurement of spatially- and frequency-resolved density fluctuations even if the optical access to the combustion process is limited, using two laser vibrometers, systems commonly applied to vibration diagnostics,. Furthermore the dual laser vibrometry offers the opportunity to detect combustion instabilities, as these instabilities are characterized by elevated pressure fluctuations and heat release fluctuations at certain frequencies. An additional advantage compared to other measurement techniques used to observe combustion phenomena, e.g. microphones, is the fact that dual laser vibrometry provides local data. Therefore the point of origin of instabilities and their propagation through the flow-field can be observed if phase-resolved field scans are done. The detailed information that can be obtained with this measurement technique has a high potential to improve the understanding of combustion processes and unstable combustion.

Together with measurements of chemiluminescence emissions, the dual laser vibrometry provides a powerful tool for the investigation of unstable combustion processes. Compared to other measurement techniques, e.g. laser induced fluorescence (LIF), the dual laser vibrometer technique provides a cheap alternative solution for the investigation of unstable combustion processes with a considerably lower level of complexity. A possible future application for the measurement technique could be the quantitative determination of the Rayleigh-integral for an unstable combustion process, if the dual laser vibrometry measurements are accompanied by quantitative measurements of the heat release fluctuations. However, the measurement technique is not suitable for the study of industrial combustion chambers due to the high effort in time, based on the point-wise measurements of density fluctuations, and due to the large optical access required. Nevertheless this measurement technique is an interesting alternative or addition to measurement techniques already used in combustion diagnostics.

References

Alonso M and Finn E J 1967 *Fundamental University Physics, Volume 2: Fields and Waves*, (Reading, MA: Addison-Wesley Publishing Company)

Alonso M and Finn E J 1968 *Fundamental University Physics, Volume 3: Quantum and Statistical Physics* (Reading, MA: Addison-Wesley Publishing Company)

Ayoola B O, Balachandran R, Frank J H, Mastorakos E and Kaminski C F 2006 Spatially resolved heat release rate measurements in turbulent premixed flames *Combustion and Flame* **144** 1-16

Barbosa S, Scouflaire P and Ducruix S 2009 Time resolved flowfield, flame structure and acoustic characterization of a staged multi-injection burner *Proccedings of the Combustion Institute* **32** 2965-2972

Born M and Wolf E: Principles of Optics 1980 *Electomagentic theory of propagation interference and diffraction of light* (Oxford, U.K.: Pergamon Press Ltd.)

Donges A and Noll R 1993 *Lasermesstechnik: Grundlagen und Anwendungen* (Heidelberg, Germany: Hüthig Verlag)

Dowling A P and Morgans A S 2005 Feedback control of combustion oscillations *Ann. Rev. Fluid Mech*. **37** 151–82

Gardiner W, Hidaka Y and Tanzawa T 1981 Refractivity of Combustion Gases *Combustion and Flame* **40** 213-219

Glas W, Forstner M, Kuhn K and Jaberg H 2000 Smoothing and statistical evaluation of laser-Doppler-velocimetry data of turbulent flows in rotating and reciprocating machinery *Exp. Fluids* **29** 411–7 10 xx

Giezendanner R, Weigand P, Duan X R, Meier W, Meier U, Aigner M and Lehmann B 2005 Laser-based Investigations of Periodic Combustion Instabilities in a Gas Turbine Model Combustor *Journal of Engineering for Gas Turbines and Power* **127** 492-496

Giuliani F, Leitgeb T, Durox D and Schuller T 2010 Analyse des variations de densité dans une flamme de référence en présence de couplage thermoacoustique *Recueil des actes du CFTL 2010 (Associaition Francaise de Vélocimétrie Laser, Vandoeuvre-les-Nancy)*

Giuliani F, Leitgeb T, Lang A and Woisetschläger J 2010 Mapping the density fluctuations in a pulsed air–methane flame using laser vibrometry *ASME J. Eng. Gas Turbines Power* **132** 031603

Gordon R and Herman G T 1974 Three-dimensional reconstruction from projections: a review of algorithms *Int. Rev. Cytol*. **38** 111–51

Hampel B 2005 *Ortsaufgelöste laseroptische Messungen von Dichtefluktuationen in turbinenrelevanten Gasströmungen*, PhD thesis, Institute for Thermal Turbomachinery and Machine Dynamics, Graz University of Technology, Graz

Hampel B and Woisetschläger J 2006 Frequency- and space-resolved measurement of local density fluctuations in air by laser vibrometry *Meas. Sci. Technol.* **17** 2835–42

Hassel E P and Linow S 2000 Laser diagnostics for studies of turbulent combustion *Meas. Sci. Technol.* **11** R37–57

Hayashida K, Amagai K, Sato K and Arai M 2006 Measurement of fuel concentration distribution in sooting flame through *Raman scattering JSME Int. J. B* **49** 512–7

Heimel M 2010 *Untersuchung von Flammen und Flammeninstabilitäten mittels optische Messtechnik* Diploma Thesis, Institute for Thermal Turbomachinery and Machine Dynamics, TU-Graz, Austria

Herman G T 1980 *Image reconstruction from projections* (New York: Academic Press)

Hipp M and Reiterer P 2003 *User Manual for IDEA 1.7 – Software for Interferometrical Data Evaluation.*

Hipp M, Reiterer P, Woisetschläger J, Philipp H, Pretzler G, Fliesser W and Neger T 1999 Application of interferometric fringe evaluation software at Technical University Graz *Proc. SPIE* **3745** 281–92

Hipp M, Woisetschläger J, Reiterer P and Neger T 2004 Digital evaluation of interferograms *Measurement* **36** 53–66

Joos F 2006 *Technische Verbrennung* (Berlin Heidelberg: Springer-Verlag)

Kawanabe H, Kawasaki K and Shioji M 2000 Gas-flow measurements in a jet flame using cross-correlation of high-speed-particle images *Meas. Sci. Technol.* **11** 627–32

Kee R J, Grcar J F, Smooke M D and Miller J A 1996 A Fortran Program for Modeling Steady Laminar One-Dimensional Premixed Flames *Sandia Report SAND85-8240* reprintet July 1996

Kirchweger W 2007 *Laseroptische Diagnoseverfahren zur Optimierung von Wasserstoff-DI-Brennverfahren*, Ph. D. Thesis, Institut für Verbrennungskraftmaschinen und Thermodynamik, Graz University of Technology, Graz

Kojima J, Ikeda Y and Nakajima T 2005 Basic aspects of OH(A), CH(A) and C_2(d) chemiluminescence in the reaction zone of laminar methane-air premixed flames *Combustion and Flame* **140** 34-45

Lading L, Wigley G and Buchhave P 1994 *Optical Diagnostics for Flow Processes* (New York: Plenum Press)

Lang A, Leitgeb T, Woisetschläger J, Strzelecki A, Gajan P and Giuliani F 2008 Analysis of a Pulsed Flame at Intermediate Pressure *Proceedings of the 13th International Symposium on Flow Visualization and 12th French Congress on Visualization in Fluid Mechanics (Université de Franche Comte Besancon)* paper 228-080419

Lee J G and Santavicca D A 2003 Experimental Diagnostics for the Study of Combustion Instabilities in Lean Premixed Combustors *Journal of Propulsion and Power* **19** 735-750

Leitgeb T, Giuliani F, Niederhammer A and Pirker H P 2009 Computer aided dimensioning and validation of a versatile test facility for combustion chambers and turbines *Proceedings of the ASME Turbo Expo 2009* paper GT2009-59592

Lewin A 1999 New compact laser vibrometer for industrial and medical applications *3rd Int. Conf. on Vibration Measurements by Laser Techniques, SPIE Proc. Series 3411* ed E P Tomasini pp 61–7

Lieuwen T C 2002 Experimental Investigation of Limit-Cycle Oscillations in an Unstable Gas Turbine Combustor *Journal of Propulsion and Power* **18** 61-67

Lieuwen T C 2003 Statistical characteristics of pressure oscillations in a premixed combustor *Journal of Sound and Vibration* **260** 3-17

Mayrhofer N, Lang H and Woisetschläger J 2000 Experimental investigation of turbine wake flow by interferometrically triggered LDV-measurements *Proc. 10th Int. Symp. on Application of Laser Techniques to Fluid Mechanics (Instituto Superior Tecnico, Lisboa)* paper 28-1

Mayrhofer N and Woisetschläger J 2001 Frequency analysis of turbulent compressible flows by laser vibrometry *Exp. Fluids* **21** 153–61

Meier W, Boxx I, Stöhr M and Carter C D 2010 Laser-based investigations in gas turbine model combustors *Exp. Fluids* **49** 865-882

Merzkirch W 1987 *Flow Visualization* (Orlando, FL: Academic Press)

Newland D E 1975 *Random vibrations and spectral analysis* (London: Longman Group)

Nori V N, Seitzmann J M 2009 CH* chemiluminescence modelling for combustion diagnostics *Proceedings of the Combustion Institute* **32** 895-903

Oertler H sen and Oertler H jun 1989 *Optische Strömungsmesstechnik* (Karlsruhe: G. Braun)

Phillip H, Neger T, Jäger H and Woisetschläger J 1992 Optical tomography of phase objects by holographic interferometry *Measurement* **10** 170–81

Pretzler G, Jäger H and Neger T 1993 High-accuracy differential interferometry for the investigation of phase objects *Meas. Sci. Technol.* **4** 649–58

Settles G S 2006 *Schlieren & Shadograph Techniques, 2nd edition* (Wien Heidelberg New York: Springer)

Steinberg A M, Boxx I, Stöhr M, Carter C D and Meier W 2010 Flow-flame interactions causing acoustically coupled heat release fluctuations in a thermo-acoustically unstable gas turbine model combustor *Combustion and Flame* **157** 2250-2266

Vest C M 1989 *Holographic Interferometry* (New York:Wiley)

Vukicevic D, Neger T, Jäger H and Woisetschläger J 1990 Optical tomography by heterodyne holographic interferometry *Holography eds. P Greguss T H Jeong IS9 (Bellingham: Society of Photo-Optical Instrumentation Engineers)* 160-161

Woisetschläger J, Lang H, Hampel B, Göttlich E and Heitmeir F 2003 Influence of blade passing on the stator wake in a transonic turbine stage investigated by particle image velocimetry and laser vibrometry *Proc. Inst. Mech. Eng. A* **217** 385–91

Woisetschläger J, Mayerhofer N, Hampel B, Lang H and Sanz W 2003 Laser-optical investigation of turbine wake flow *Exp. Fluids* **34** 371–8

Woisetschläger J, Pretzler G, Jericha H, Mayrhofer N and Pirker H P 1998 Differential interferometry with adjustable spatial carrier fringes for turbine blade cascade flow investigations *Exp. Fluids* **24** 102–9

Woisetschläger J 2010 *Laser-Optical Flow Measurement Techniques*, lecture script, Institute for Thermal Turbomachinery and Machine Dynanmics, Graz University of Technology, Graz

Zipser L, Lindner S and Behrendt R 2002 Interferometrische Messung und Visualisierung von Schallwellen und Turbulenzen *Tech. Mess.* **6** 275–81

Publications

Journal publications

Köberl S, Fontaneto F, Giuliani F and Woisetschläger J 2010 Frequency-resolved interferometric measurement of local density fluctuations for turbulent combustion analysis *Meas. Sci. Technol.* **21** 035302 (10pp)

Köberl S, Leitgeb T, Giuliani F and Woisetschläger J 2011 Optical- and laser-based investigations of periodic combustion instabilities in a multi-flame gas turbine model combustor *currently under review in Exp. Fluids*

Leitgeb T, Köberl S, Schuller T, Durox D, Woisetschläger J and Giuliani F 2011 Interferometric determination of heat release in a periodic flame *in preparation for Combustion and Flame*

Conference publications

Köberl S, Heimel M, Giuliani F, Woisetschläger J, Fontaneto F 2010 Measurement of local density fluctuations for combustion diagnostics of different flames using dual laser vibrometry *Proceedings of the 46th AIAA/ASME/SAE/ASEE Joint Propulsion Conference & Exhibit* AIAA paper 2010-6670

Köberl S, Giuliani F, Fontaneto F and Woisetschläger J 2009 Power spectra measurements for the density fluctuation in a jet flame using dual laser vibrometry *Proceedings of the European Combustion Meeting 2009* paper P811394

Appendix A

For the chemiluminescence emission measurements a high-speed camera (CASIO EXILIM F1, Casio, Tokyo, Japan) was used and therefore the camera had to be characterised. A chip characterization was performed using a diffusive light source and a number of different optical density filters. For each filter, a high-speed video was recorded and afterwards the average image intensity, calculated from a number of single frames, was determined for each filter. The recorded average image intensity was compared to the expected image intensity, based on the attenuation of the utilized filter. The recorded and expected image intensities were then plotted against each other, resulting in a calibration curve for the camera-chip.

$$OD = \log 10 \frac{P_1}{P_2} \tag{A.1}$$

Seven filters with different optical density were used during these experiments. The relation between the optical density (*OD*, also called absorbance) of the individual filter and the ratio of the transmitted light intensity P_2 and the incident light intensity P_1 can be seen in equation (A.1). The employed optical density filters and the corresponding ratios between incident and transmitted light intensity as well as the ratio between the incident light intensity and the transmitted intensity recorded by the camera can be found in table A.1. The setup for the camera calibration can be seen in figure A.1, the calibration curve in figure A.2.

Tab. A.1: Optical density of the employed filters. Additionally the calculated and measured ratios between the incident light intensity and the transmitted light intensity are displayed.

OD	P_1/P_2 (according to eq. A.1)	P_1/P_2 (Casio-Exilim)
0.1	1.2589	1.4966
0.195	1.5668	1.9474
0.290	1.9498	3.4308
0.405	2.5410	6.9950
0.480	3.0200	14.0086
0.580	3.8019	130.6257
0.675	4.7315	2.779×10^3

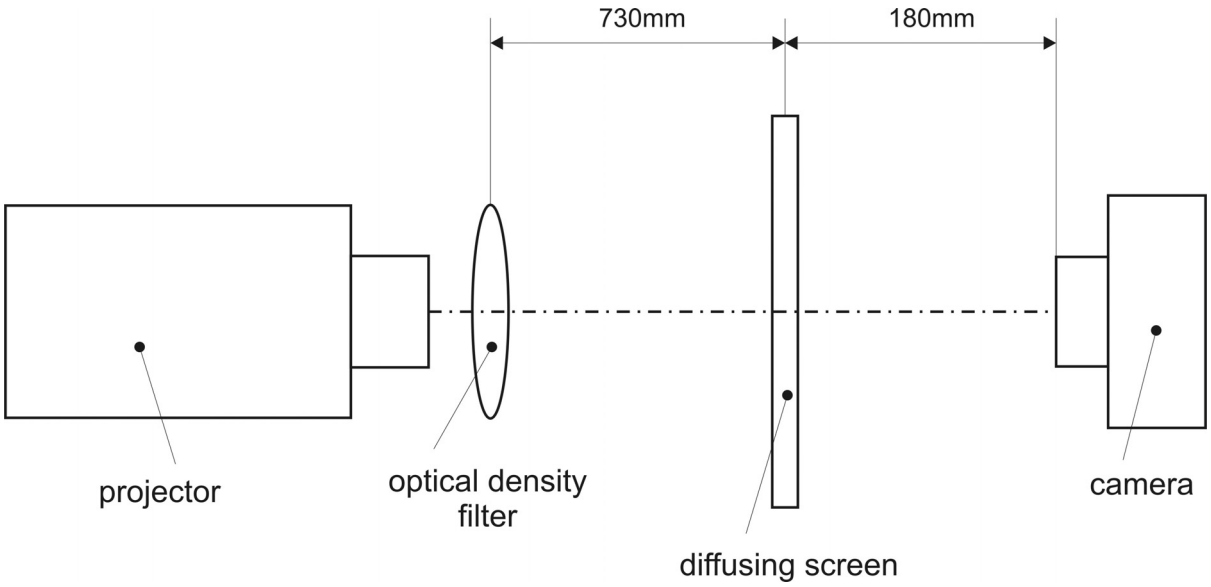

Figure A.1: Setup for camera calibration.

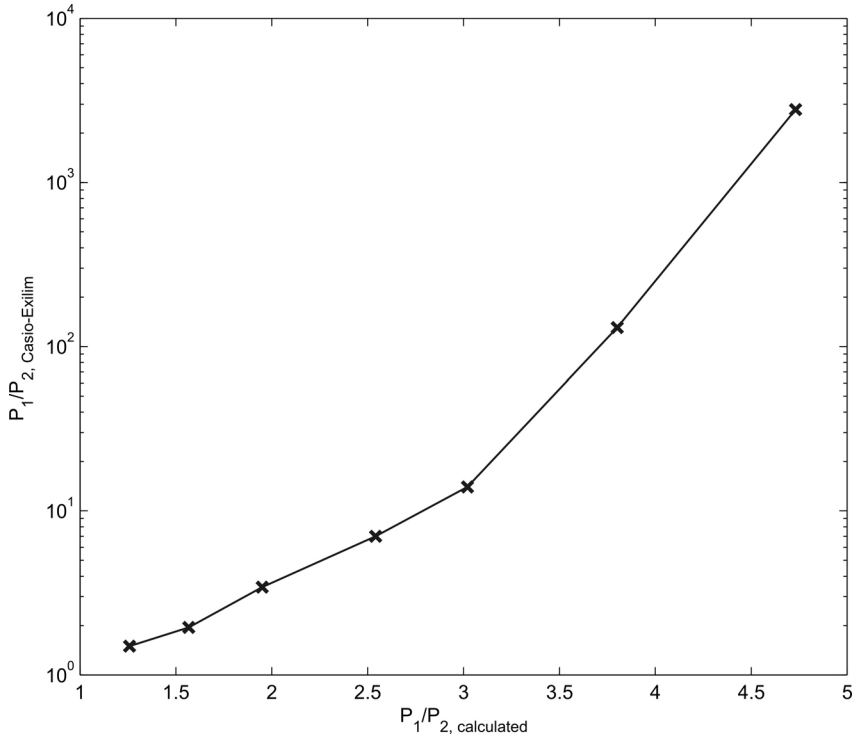

Figure A.2: Ratio between incident light P_1 and transmitted light P_2 calculated according to the optical density filters vs. ratio between P_1 and P_2 recorded by the CASIO-EXILIM F1 camera.